Dynamics of fluids and transport applied to the early Earth

Martina Ulvrová

N° attribué par la bibliothèque: 2012ENSL0750

THÈSE

en vue de l'obtention du grade de

Docteur de l'École Normale Supérieure de Lyon - Université de Lyon

Discipline : Sciences de la Terre et Univers

Laboratoire de Géologie de Lyon, Terre, Planètes, Environnement

École doctorale Matériaux

présentée et soutenue publiquement le 15 octobre 2012

par Madame **Martina ULVROVÁ**

DYNAMIQUE DES FLUIDES ET DES TRANSPORTS APPLIQUÉE À LA TERRE PRIMITIVE

Directeurs de thése :

Monsieur Stéphane LABROSSE
Monsieur Nicolas COLTICE

Aprés avis de :

Monsieur Claude JAUPART
Monsieur Christophe SOTIN

Devant la Commission d'examen formée de :

Monsieur Thierry ALBOUSSIÈRE, Président, Université Lyon 1
Monsieur Nicolas COLTICE, Directeur, Université Lyon 1
Madame Cinzia FARNETANI, Membre, Université Paris 7
Monsieur Claude JAUPART, Rapporteur, Université Paris 7
Monsieur Stéphane LABROSSE, Directeur, École Normale Supérieure de Lyon
Monsieur Christophe SOTIN, Rapporteur, California Institute of Technology

Contents

Résumé

Nous avons étudié le transfert de chaleur et de matière au cours de l'histoire de la Terre primitive à de multiples échelles en utilisant des modèles numériques. Deux systèmes différents sont abordés. Tout d'abord, nous nous concentrons sur les premiers stades de la formation du noyau terrestre lorsque le fer se sépare des silicates et descend vers l'intérieur de la planète. Au cours de la différenciation, des interactions chimiques et thermiques se produisent entre les gouttes de fer dispersées dans des silicates fondus formant un océan de magma. Nous étudions le transport chimique des éléments trace à l'intérieur et autour des gouttes. Nous tirons quelques lois d'échelle dépendantes du régime dynamique d'écoulement et montrons que le système tend à être en équilibre chimique extrêmement rapidement par rapport à l'échelle de temps de la descente de la goutte de fer.

Lors de l'accrétion de la Terre, la fusion intense de son manteau profond ainsi que la formation d'un océan de magma en surface a lieu. Comme le rayonnement de la chaleur dans l'espace est très efficace, les silicates fondus superficiels cristallisent très rapidement, en 10 Ma environ. L'histoire thermique de la couche liquide enterrée, appelée océan de magma basal (OMB), se déroule sur une longue période de temps et il est proposé que ses restes soient aujourd'hui observables sous forme de poches partiellement fondues au dessus de la frontière noyau-manteau.

Nous développons des modèles numériques décrivant la convection dans un océan de magma basal qui cristallise et déterminons les paramètres régissant ce système convectif dans lequel se produit une transition solide/liquide. Les lois d'échelle ainsi obtenues ont été appliquées à l'OMB et indiquent que la diffrence de température qui peut être maintenue dans les couches limites supérieure et inférieure de l'OMB est infime. Par conséquent, la température du noyau suit la température de liquidus à la base du manteau et ainsi la vitesse de refroidissement de l'OMB doit être la même que celle du noyau de la Terre.

Summary

We have studied the heat and mass transfer during the early Earth history at multiple scales and for multiple systems by means of numerical computing. Two different systems are approached. Firstly, we focus on the early stages of the Earth core formation when iron segregates from silicates and descends toward the interior of the planet. During the differentiation there are chemical and thermal interactions between dispersed iron blobs and surrounding molten silicates. We study the chemical transport of trace elements within and around the drops. We derive functional relations between critical parameters and show that the system tends to be in chemical equilibrium.

During the accretion process of the Earth, extensive melting of its deep interior as well as formation of shallow magma oceans occurred. As heat radiation into space happens with high efficiency, surface molten silicates crystallize very rapidly, in about 10 My. The thermal history of the buried liquid layer, called the basal magma ocean (BMO), proceeds over a long time and it is proposed that its remnants are nowadays observable as partial melts in the core-mantle boundary region.

We develop numerical models of the thermal history of the crystallizing basal magma ocean that enable to study coupling between the mantle and the core in the presence of the BMO. We derive parametrized relations for this convective system that undergoes solidification/melting. Obtained scaling equations applied to the BMO indicate that the temperature difference that can be maintained across the top and bottom boundaries of the BMO is minute. Hence, the temperature of the core follows the temperature of liquidus at the bottom of the mantle and thus the rate of the BMO cooling must be the same as that of the Earth's core.

Introduction

The present picture of the Earth and other planetary bodies is the result of several billions of years of evolution. How the Earth came to its present state depends on which conditions and processes were active during its early stages. In this thesis, two models are set up and investigated contributing to understanding the chemical and thermal history of the early Earth. Firstly, we review how the Earth was formed and describe its early evolution.

Distribution of chemical elements in the mantle reflects the most dramatic process in terms of mass redistribution within the Earth history, the metal-silicate differentiation, when iron separates from silicates and descends to form the core. This event is recorded in the silicate mantle by the abundances of trace elements. The first part of the thesis is devoted to understand the efficiency of transport of chemical elements during the core formation event.

Many heat sources, that are not active anymore, were important during the accretion of planetary bodies. These caused more or less extensive episodic melting of planets. In particular, it was suggested, that the interior of the Earth in between the silicate mantle and the metallic core ended completely molten early in the Earth history and a basal magma ocean (BMO) was formed. Since the heat evacuation from the interior of the planet is very limited by the overlying solid mantle, the crystallization time of the BMO is very long (of the order of the Earth's age). In the second part of the thesis we propose to study the BMO by means of numerical modelling. We set up a model that enables to investigate the thermal evolution of the crystallizing/melting BMO coupled with the solid mantle and that enables to infer thermal coupling between the Earth's mantle and the core in the presence of the BMO.

Chapter 1

Evolution of the Earth

The age of the Earth is approximately one third of the age of the universe and goes back about 4.54 billion years. Since the early beginning, melting and transport of magma play a crucial role in the Earth's thermal and compositional evolution.

Partial melting and volcanism in the Earth shallow mantle results in the formation of a thin crust of crystallized melt (Crisp, 1984; Schubert et al., 2001; Marsh, 2007). Creating the new crust leaves the Earth's mantle deprived in incompatible elements since they preferentially partition into the melt. Going deeper into the mantle, partial melt zones are found at the core mantle boundary (Williams and Garnero, 1996; Lay et al., 1998, 2004). These molten regions are non homogeneously distributed and very localized. They are possibly the remnants of an initially thick magma ocean that formed at the base of the mantle during the Hadean and has been slowly solidifying since (Labrosse et al., 2007). Continuing further toward the center of the planet, crystallization of the outer core (that has probably started around a billion years ago (Labrosse et al., 2001)) proceeds helping to drive the geodynamo (Figure 1.1).

Returning deeper back in time, more extensive melting of the Earth's interior is expected since core formation ultimately needs that the temperatures exceed the melting temperature of metal alloys in order to separate mantle material (silicates) from the core forming material (iron). While iron sinks to form the core (due to the high density contrast compared to the background matrix), chemical exchanges of trace elements between metal and silicates occur (equilibration process). As a result, the abundances of siderophile trace elements (iron loving elements) in the mantle might have been (at least partially) established (Rubie et al., 2007).

The subsequent crystallization of molten mantle is inevitable at some stage of the Earth evolution (there might be some periods when the Earth's mantle is actually heating up due to e.g. heat production from radiogenic elements or due to over heating of the core).

Theoretical and numerical models significantly improve the knowledge of solidification and melting processes acting in the Earth and dictating importantly the chemical composition of distinct reservoirs

as well as thermal evolution of the planet. They should describe the physics of melt as well as the solid.

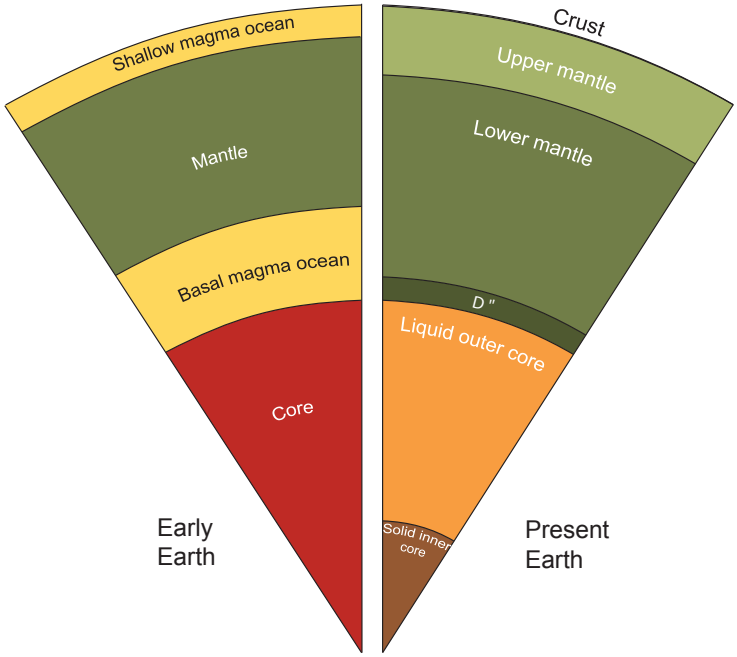

Figure 1.1: A sketch of a possible Earth's structure in the Hadean (∼4.5 Gy ago) and nowadays.

1.1 Formation and early stages

1.1.1 First cooling models and the age of the Earth

The thermal history of the Earth and its age are closely related problems. Indeed, finding physical laws that would describe the cooling of an initially hot sphere placed into a cold space was an objective of Fourier's (1822) work. His calculations later encouraged Kelvin to estimate the age of the Earth (Thompson, W. (Lord Kelvin), 1864). This was at that time an extraordinary feat since geologists were convinced that the age of the Earth was too high to be determined and might be infinite.

The basis for Kelvin's model is an estimation of the temperature gradient at the Earth's surface, that was at that time constrained to around $20\,\mathrm{K\,km^{-1}}$. He considered that the Earth was initially molten, had a uniform melting temperature $T_0 = 2000\,\mathrm{K}$, and its surface was held at constant temperature $T = 0\,^\circ\mathrm{C}$. Kelvin's work was based on two main assumptions: the cooling proceeds only by conduction and there are no heat sources. Both of these hypothesis were well justified and appropriate for that time since neither mantle convection nor radiogenic heat sources were known.

The solution for the temperature gradient at the surface is

$$\frac{\partial T}{\partial z} = \frac{T_0}{\sqrt{\pi \kappa t}}, \tag{1.1}$$

where κ is the thermal diffusivity and t the time. With $\kappa = 10^{-6}\,\mathrm{m^2 s^{-1}}$, Kelvin estimated that the time needed to drop the temperature gradient to the observed value was around 100 My.

Small improvements can be made to Kelvin's model to obtain estimations much closer to today's value. For example, considering that the gradient of melting temperature increases with the depth results to the age over 1 Gy (Jeffreys, 1942).

Nowadays, we know that the largest shortcoming of the Kelvin's model is that he did not consider convective transport (England, 2007). Indeed, convection maintains high temperature gradients at the surface during the time significantly higher than that obtained by Kelvin. The effect of convection can be seen through a simple pure conducive model that contains a variable thermal conductivity k. Efficient convective heat transport can be simulated, to a certain degree, by considering a high k. Passing from a region with small k into a material that possesses a high k causes a discontinuity in the thermal gradient at the boundary in order to satisfy the continuity of the heat flux $q = k\,\partial T/\partial z$. Consider that the Earth is approximated by a semi infinite space that is made up of two layers with different k, let's say a thin crust and deep interior. Approximate estimation leads to n times higher surface temperature gradients when using n times higher k in the lower layer. Thus, using n times higher k compared to the surface value, we obtain that the Earth is n^2 times older than estimated by Kelvin, cf. Eq.(1.1). The influence of variable material properties have been already discussed and the age of the Earth re-estimated by Perry (1895a,b) or Heaviside (1899).

Later, radioactivity was discoverer. This has only a secondary effect for the Kelvin's calculations but extends its significance by providing an independent chronometer for dating the age of the Earth (Burchfield, 1975). Besides, geologists challenged the age given by Kelvin. By estimating the rate of sedimentation and erosion they showed that the Earth must be much older than that.

Kelvin laid the foundations of modern geophysics. One of the most intriguing questions we want to answer about the Earth and planetary bodies is to reconstruct their thermal and chemical histories from the very beginning and describe how these objects came to their present state. As we will see further, melting is inevitable at some stage during the evolution of planetary objects. And as we presented above, the idea of the extensive melting of the Earth (or that the Earth started from a completely molten state) came already from Kelvin and actually it was proposed even earlier, at the turn of the seventeenth and eighteenth century (Deparis and Legros, 2000). At the time of Kelvin this had neither observational nor theoretical support and it was not until the second half of the 20^{th} century that this theory had been reopened and finally resumed (Wood et al., 1970; Wood, 1972b,a). Prior to this, it was supposed that the Earth accreted from accumulation of particles of constant size without causing any fusion.

The theory of hot start of the Earth came on the basis of observations and analysis of the Moon's samples that indicated large scale melting of its surface and formation of a lunar magma ocean (Wood et al., 1970). Later, more and more evidences were found to support this (Hostetler and Drake, 1980).

Especially large advance was made when researchers realized that not only the future planets were growing, but also the objects that were building them were also growing with time. And so the model of violent accretion causing extensive melting was born (Safronov, 1978; Kaula, 1979; Wetherill, 1985; Melosh, 1990). Below we will see that there are more sources to heat and melt the young planets.

1.1.2 Making planets: accretion models and heat sources

The Earth is the third planet in the Solar System. Its structure at first order consists of a metallic core surrounded by a silicate mantle. In this configuration, the system has a minimum gravitational energy, and this is the reason for such an arrangement. The core lies 2890 km beneath the Earth surface. However, there is still no unifying model describing timescales of separation of iron and silicates and determining thermal and chemical conditions before, during and after core formation.

In order to understand which processes played a key role during the accretion and differentiation we first describe the formation of the Solar System, which birth is defined as a time when first solid grains in the nebular disk were formed. The oldest known objects (except for the presolar grains) that witnessed the origin of the Solar System are calcium-aluminum-rich inclusions (CAI), that are small fragments trapped in carbonaceous chondrite. They can be dated using ^{207}Pb-^{206}Pb isotopic system giving the age of the Solar System 4.5682 Gy (Bouvier and Wadhwa, 2010).

The formation of the Solar System can be divided into several distinct stages characterized by different time and space scales. Here, we briefly review each period one by one in order to understand which processes lead to the birth of the Earth and set thus the initial thermal and compositional states of the planet for its subsequent evolution (e.g. Chambers, 2004).

The process of accretion of planetary bodies (Safronov, 1972; Canup et al., 2000) starts in the proto-planetary disk that is composed of dense gas and dust and rotates around the proto-Sun (Figure 1.2). Gravitational instabilities and collisions between dust particles with sizes up to centimeters allowed the growth of planetesimals that are from 1 to 10 km large within 10^3 y. Further, these objects experience the mutual gravitational interactions forming from Mars to Moon sized embryos called protoplanets. This second stage occurs on the timescales of $10^5 - 10^6$ y. The final stage of accretion takes the longest time ($10 - 100$ My) and ends up with fully grown terrestrial bodies. Probabilities of a collision decrease with time as there is less and less objects in space, but individual impacts are more violent and more energetic due to the important masses involved (Melosh, 1990).

Simultaneously with accretion, differentiation, i.e. separation of iron and silicates and mantle and crust (and eventually a deep silicate reservoir), of planets occurred. There is still an ongoing debate trying to reconstruct this process. The formation of the core is often presented as a single stage event. However, it occurred certainly on multiple levels. Also, if a protoplanet encounters a collision with an already differentiated body, the merging of both cores can happen instead of emulsification of both phases (Tonks

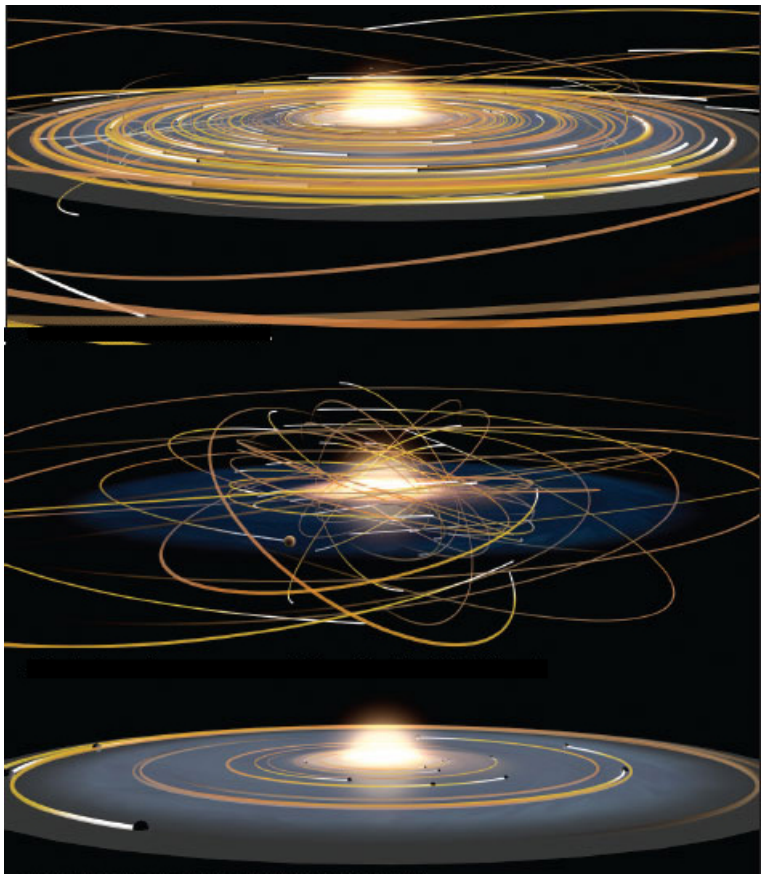

Figure 1.2: A schematic picture of planetary formation (Lin, 2008). (Top) Orbiting dust grains around the proto-Sun (In the centre) forming planetesimals. (Middle) Planetesimals grow to form planetary embryos. (Bottom) Planetary embryos gravitationally interact.

and Melosh, 1992). Then, the chemical signal of the formation of the impactor's core would be recorded in a growing planet.

A necessary condition for the separation of the distinct phases is that iron must be molten (e.g. Stevenson, 1990; Ricard et al., 2009). Several possible sources can heat up the planet. These operated on different time scales and are not important nowadays. We review them below.

Heating by impacts

As was described above, violent collisions between bodies with important sizes happened late in the accretion process. The kinetic energy of the impactor is $E_{\rm k} = 1/2 M v_{\rm imp}^2$, with M the mass of the impactor and $v_{\rm imp}$ its velocity. $v_{\rm imp}$ is comparable to the escape velocity $v_{\rm imp} = \sqrt{2gR}$, where R is the radius of the impacted body and $g = 4/3 G\pi\rho_{\rm ic} R$ the gravity ($\rho_{\rm ic}$ is the density of the impacted body and $G = 6.67 \cdot 10^{-11}\,{\rm m^3 kg^{-1} s^{-2}}$ the gravitational constant). For impactors with velocities that are large

enough, larger than the elastic velocities, the energy is buried in a spherical region where the impactor hit the growing planet (the so called isobaric core) (Croft, 1982; Pierazzo et al., 1997; Senshu et al., 2002). The kinetic energy of the impactor is transformed in heat and is partly retained by the planet (fraction f_1) and partly lost to space by radiation. Considering that the density of the impacted body is equal to the density of the impactor $\rho_{\mathrm{ic}} = \rho_{\mathrm{imp}} = \rho$, the temperature increase is

$$\Delta T = \frac{4\pi}{3} \frac{f_1}{f_2} \frac{\rho G R^2}{C_p} \,, \tag{1.2}$$

where C_p is the heat capacity and f_2 represents the heated volume, that is normalized by the volume of the impactor and is around $f_2 \sim 9$. f_1 is determined experimentally and its value lies around $f_1 \sim 0.3$ (e.g. Monteux et al., 2007). ΔT increases rapidly with the radius of the impacted body (due to the second power in Eq.(1.2)) and does not depend on the radius of the impactor. Using $C_p = 1200\,\mathrm{Jkg^{-1}K^{-1}}$, $\rho = 4000\,\mathrm{kg\,m^{-3}}$, we obtain for a Moon size protoplanet $\Delta T \sim 100\,\mathrm{K}$. For a Mars size impacted object $\Delta T \sim 360\,\mathrm{K}$, for an Earth size impacted body $\Delta T \sim 1260\,\mathrm{K}$.

Heating due to decay of radioactive nuclides

Short-lived radioactive nuclides ^{26}Al (which decays to stable ^{26}Mg) and ^{60}Fe (which decays to stable ^{60}Ni) are a significant source of heat during the first millions of years after the formation of the Solar System thus being important for small bodies (planetesimals). The thermal state of planetesimals is fundamental since the extensive melting would induce their differentiation. It is thus still not clear if the Earth (and other planetary bodies) accreted from bodies that already had a metallic cores or from undifferentiated objects. Most probably a mixture of differentiated and undifferentiated planetesimals contributed to the formation of planets, depending on their size and formation history (Šrámek et al., 2012).

We now estimate the temperature increase ΔT due to decay of radioactive nuclides as

$$\Delta T = \frac{f C_i E_{\mathrm{D}}}{C_p} \,, \tag{1.3}$$

where f is the initial fraction of radioactive isotope (i.e. $^{\mathrm{rad}}\mathrm{X/X}$ where X is Al or Fe), C_i the concentration of the stable element, E_{D} the nuclear decay energy released into heat within the whole history and C_p is the heat capacity (Rubie et al., 2007). For the ^{26}Al system (half-life $\tau = 0.74\,\mathrm{My}$) $E_{\mathrm{D}} = 1.16 \cdot 10^{13}\,\mathrm{Jkg^{-1}}$ and $f = 5 \cdot 10^{-5}$ at the beginning of the Solar System (CAI time). The abundance of ^{27}Al stable isotope is taken to be chondritic 0.865 wt.%. Using $C_p = 1200\,\mathrm{Jkg^{-1}K^{-1}}$ results in a temperature rise of 4180 K. Supposing, that the body was formed 3 My later, the fraction of the radioactive nuclide would decrease after the decay law $f(t) = f_0 \exp(-\ln 2\, t/\tau)$, where f_0 is a fraction of radioactive element at time 0 (CAI time). Hence, $f(t = 3\,\mathrm{My}) = 3.01 \cdot 10^{-6}$ resulting in $\Delta T = 252\,\mathrm{K}$.

For the ^{60}Fe system $E_{\mathrm{D}} = 4.43 \cdot 10^{12}\,\mathrm{Jkg^{-1}}$ and the half-life of decaying atoms is $\tau = 2.6\,\mathrm{My}$ (Rugel et al., 2009) (note that this value differs from $\tau = 1.5\,\mathrm{My}$ used prior to 2009). The initial isotopic fraction for this system is still highly debated and recently it has been suggested that its distribution

has been non-homogenous in the early Solar System due to incomplete isotopic mixing (Quitté et al., 2007, 2010). f is usually estimated either around $f(t = \mathrm{CAI}) = 8 \cdot 10^{-9}$ (Quitté et al., 2010, 2011) or $f(t = \mathrm{CAI}) = 4 \cdot 10^{-7}$ (Quitté et al., 2007). The former concentration is so low, that the temperature increase due to radioactive decay would be minimal at any time (inferior to 5 K). Considering the chondritic composition of stable iron isotope ^{56}Fe 18.2 wt.% results in $\Delta T = 268\,\mathrm{K}$ at CAI time and 120 K 3 My later.

These estimations of the temperature increase were done with an assumption that the body is isolated. In reality, a fraction of this energy is lost to space. Also, they are valid only for large planetary bodies where diffusion is negligible. For smaller bodies with radius inferior to diffusion length the temperature in the centre of the planet is controlled by diffusion. Simple estimates show that these objects, with kilometer scale sizes, are unaffected by the radioactivity (Šrámek et al., 2012). Hence, the radioactive decay of short lived nuclides is an important heat source only for larger bodies that have accreted rapidly while the system was alive.

As an example of a differentiated small planetary body, an asteroid Vesta is considered. Vesta (diameter about 525 km) can be found between Mars and Jupiter and it is supposed that a meteoritic group Howardite Eucrite Digenite (HED) found on Earth comes from this parent body. Isotopic measurements of these meteorites indicate that Vesta was formed during the first 20 million years of the Solar System. Spectral measurements reveal that radioactive nuclides provided enough heat to differentiate the object (probably by the decay of ^{26}Al (Ghosh and McSween, 1998)) forming metallic core, silicate mantle and crust, early after its formation (between 4 and 16 My after the CAI formation) (Lee and Halliday, 1997; Kleine et al., 2002).

Heating due to differentiation

An accreted undifferentiated planet (density $\bar{\rho}$) is a mixture of silicates (density ρ_{sil}) and metal (density ρ_{met}). Several physical processes lead to the separation of the two major phases and their redistribution so that the silicates envelop the metallic core. The change in mass distribution is accompanied by a change of gravitational potential energy, that is driving the system toward a lower state and is converted into heat by viscous friction. The amount of energy liberated depends only on the final and initial states of the planet and is irrespective of the manner the final state was achieved. The temperature increase ΔT due to differentiation is (Flasar and Birch, 1973; Solomon, 1979; Ricard et al., 2009)

$$\Delta T = \frac{4G\pi R^2}{5\bar{\rho}C_p}\left(\bar{\rho}^2 - \rho_{\mathrm{met}}^2 b^5 - \rho_{\mathrm{sil}}^2\left(1-b^5\right) - \frac{5}{2}\left(\rho_{\mathrm{met}} - \rho_{\mathrm{sil}}\right)\rho_{\mathrm{sil}} b^3\left(1-b^2\right)\right), \tag{1.4}$$

where b is the ratio between the size of the core R_{core} and the total radius of the planet R, G the gravitational constant and C_p the heat capacity. The average density can be expresses as $\bar{\rho} = b^3\rho_{\mathrm{met}} + (1-b^3)\rho_{\mathrm{sil}}$. Note that zero temperature difference is obtained when there is no segregation, i.e. $b = 1$ if the planet is formed only by metal, $b = 0$ is the planet is composed entirely of silicates or $\rho_{\mathrm{sil}} = \rho_{\mathrm{met}}$.

Typically, for a planet with radius $R = 3000\,\mathrm{km}$ and the core size $R_{\mathrm{core}} = 1500\,\mathrm{km}$, the temperature increase due to segregation of metal into the centre is 250 K (using $\rho_{\mathrm{met}} = 7000\,\mathrm{kg\,m^{-3}}$, $\rho_{\mathrm{sil}} = 3500\,\mathrm{kg\,m^{-3}}$ and $C_p = 1200\,\mathrm{Jkg^{-1}K^{-1}}$). Monteux et al. (2009) show that the thermal energy released during the segregation of metal on growing planets is comparable to the thermal energy buried during the impact. Contrary to the energy brought by impacts, the gravitational energy is transformed into heat within the Earth interior and is not readily lost to space. However, its partitioning between the silicate and the metal is still unclear. The work of Ricard et al. (2009) predicts a significant temperature increase in both the proto-core and the shallow mantle, but leaves a rather cold deep mantle (that remains undifferentiated in their model). At the end of segregation process, the proto-core has a temperature around 1800 K and stays thermally insulated due to low temperatures in the deep interior of the planet while the upper part cools by convection. Overheating in the core might have caused melting of the lowermost mantle.

Samuel et al. (2010) studied core formation by negative diapirism and the associated gravitational heat release. The result strongly depends on the size distribution of diapirs and leads to two distinct states: a relatively cold core is formed when a small number of large diapirs deliver the metal in the centre while a relatively hot core is produced with a large number of small metallic diapirs. In any case, the lowermost mantle is left with higher temperatures compared to its shallow parts that can further enhance the extensive melting of deep mantle.

1.1.3 Crystallization of the Earth mantle

As we saw in the previous section, multiple heat sources operated during the early evolution of the Earth resulting in episodic melting and leaving eventually the Earth's mantle completely molten. This is crucial since the subsequent Earth history follows from these initial conditions.

Whether inevitable crystallization of the magma ocean proceeds from the bottom, the middle or the top can be inferred by comparing the liquidus curve with the mantle temperature profile. The latter can be also linked to the thermodynamic quantity γ, the Grüneisen parameter. For an isentrope in the magma ocean it holds

$$\gamma = \left(\frac{\partial(\log T)}{\partial(\log \rho)} \right)_{\mathrm{S}} , \tag{1.5}$$

where T is the temperature and ρ the density. The subscript S signifies that the derivative is at constant entropy. A high γ would then imply a relatively high temperature gradients in the convecting magma ocean.

The classical view is that the crystallization of a deep magma ocean starts from the bottom advancing upward (e.g. Abe, 1997; Solomatov, 2000, 2007). This has been recently challenged by a new model of Mosenfelder et al. (2007) and Mosenfelder et al. (2009) based on shock experiments. They suggest that due to the high Grüneisen parameter γ of the Earth's interior, the crystallization of the mantle starts at the surface or in the middle of the mantle, cf. Figure 1.3. Increase of γ for silicate liquid in

Earth's lower mantle is also supported by the first principles molecular-dynamics simulations (Stixrude and Karki, 2005; Stixrude et al., 2009).

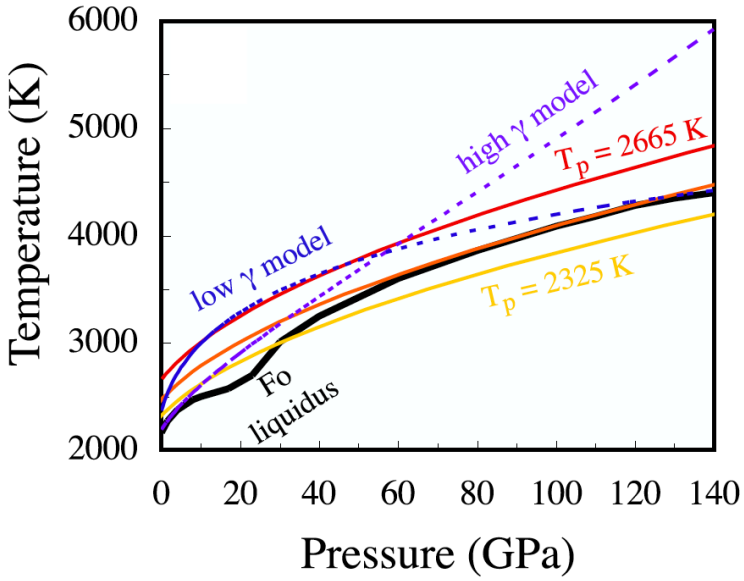

Figure 1.3: The liquidus curve (black solid thick line) is compared with several isentropic profiles for Mg_2SiO_4 composition. Considering thermal evolution described by three adiabats represented by colored solid lines, the crystallization would proceed from the bottom (high pressures and temperatures). The model with low Grüneisen parameter γ (one of the blue dashed lines) would give the same evolution. But the new shock wave experiments (Mosenfelder et al., 2009) predict an increase of the Grüneisen parameters of the melts upon compression implying adiabat with higher temperature gradient (dashed blue line - high γ model). This would mean that the magma ocean would solidify from the middle of the mantle. (Figure taken from Mosenfelder et al. (2009).)

1.1.4 Equilibration process during Earth's core formation

An important indicator on the formation of the core is provided by abundances of chemical elements in the mantle (Figure 1.4). Elements with relatively low condensation temperature (volatiles) are depleted in the mantle relative to chondritic concentrations. This is because they can be more easily lost when temperatures get high such as during the accretion. Refractory elements that have a high condensation temperature are thus more suitable for documentation of the early state of planets.

Elements that dissolve more easily in metal (siderophile elements) are also depleted in the mantle relative to chondrites (Figure 1.4). This is because they were preferentially partitioned into the metal during formation of the core and were delivered to the center of the Earth.

Elements that have not been affected by the differentiation belong to the refractory litophile (preferentially dissolves in silicates) group. Indeed, we note that their abundances match the chondritic ones (Figure 1.4).

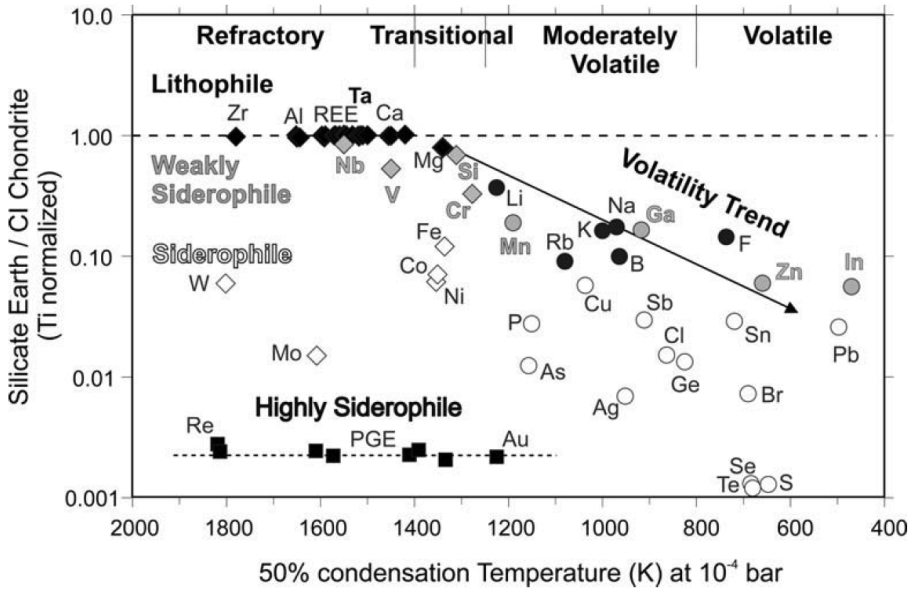

Figure 1.4: Element abundances in the Earth mantle (normalized to CI chondrite and Ti) as a function of the condensation temperature. Two phenomenons are reported by the concentration depletion. Volatile elements (circles, right half of the figure) are depleted because the temperature at which they evaporate is low and thus they have been partly lost during accretion. Siderophile elements (black squares, dissolve readily in iron) are depleted because they have partitioned into iron rich metal during core formation. Note that elements that are lithophile (dissolve readily in silicates) and refractory (high condensation temperatures) (black diamond symbols) have the same concentrations in the Earth and in the chondrites. Reproduced from Mann et al. (2009).

Timescales of differentiation are constrained by the Hf-W isotopic system. Hafnium ^{182}Hf is a radioactive nuclide that decays to a stable isotope tungsten ^{182}W with a half-life 8.9 My. Both, ^{182}Hf and ^{182}W, are refractory elements, but Hf is lithophile while W is siderophile. If the core formed early during the half-life of hafnium, ^{182}Hf would be left in the mantle and the ratio of radiogenic and nonradiogenic tungsten, ^{182}W and ^{183}W, would be high. While if the core forms tardily when ^{182}Hf is already extinct, ^{183}W would be removed to the core resulting in the low ^{182}W/^{183}W ratio. It has been shown that the Earth's mantle shows an excess in radiogenic tungsten compared to undifferentiated chondrites indicating that the Earth's core must have formed earlier than $\sim$ 30 My after the Solar System was formed (Kleine et al., 2004). Core formation and accretion were thus probably processes that happened simultaneously (Stevenson, 1990).

As mentioned above, siderophile elements are depleted in the mantle. Assuming equilibrium model for core-mantle differentiation (and here we consider only this model), the degree of depletion is given by a partition coefficient K that is the ratio between concentrations of an element i in the metal and silicates at equilibrium, i.e. $K = C_i^{\text{metal}}/C_i^{\text{silicates}}$. However, experimentally determined partition coefficients at low pressure predict much lower concentrations of siderophile elements in the mantle (e.g Wood et al.,

2006). This overabundance gives us an insight into the conditions under which segregation of metal from silicates occurred.

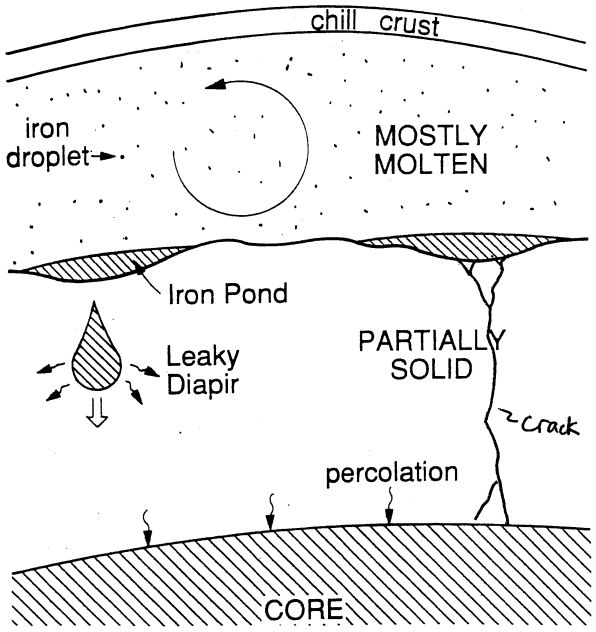

Figure 1.5: Schematic cartoon representing different processes acting during the core formation. The shallow part of the planet is molten. In this upper magma ocean, that is probably vigorously convecting, separation of the metal and silicates occurs. Iron forms a small droplets and sinks to a rheological boundary between the liquid and solid. After a certain amount of iron was accumulated, it descends toward the center of the planet in large diapirs to form the core. After Stevenson (1990).

A range of observed concentrations can be explained by equilibration between metal and silicate at high pressure and temperature conditions. As metal sinks into the centre of the planet, pressure and temperature increase and the partition coefficient generally decrease. Subsequent reequilibration at new conditions occurs. During the differentiation of the planet, shallow magma oceans were formed and small droplets of metals sink due to density excess and deliver metal toward the centre. Metallic blobs accumulate at a rheological boundary between the molten and solid mantle (marked as 60% melt fraction) and further descend to form the core having a form of large diapirs (Stevenson, 1990; Karato and Murthy, 1997; Murthy and Karato, 1997). This canonical model (Figure 1.5) is probably very simplistic but provides a good first order approach to be considered. Using this scenario, concentrations of elements in the silicate mantle result from equilibration at the base of the shallow magma ocean. This requires inefficient equilibration between the mantle and large diapirs (due to large spatial dimension and small temporal scale) while very efficient equilibration must proceed between the dispersed iron drops and liquid silicates (Rubie et al., 2003; Ulvrová et al., 2011; Samuel, 2012). Whether equilibration process of small droplets of iron is efficient (and to which extent) is an object of the first part of this thesis and is detailed further in this chapter. Many studies of the partitioning behaviour have been conducted to infer pressure and temperature conditions at the base of the shallow magma ocean (e.g Li and Agee,

2001; Chabot et al., 2005; Righter, 2011; Siebert et al., 2012) and a very broad interval of equilibration conditions have been given, 30-60 GPa for pressure and 2000-4200 K for temperature (Rubie et al., 2007).

1.2 Article: Compositional and thermal equilibration of particles, drops, and diapirs in geophysical flows

In order to quantify the efficiency of chemical equilibration between dispersed iron droplets and background silicate matrix during the core formation, we propose to study a single liquid drop falling in liquid silicates. Assuming that the system is initially at non-equilibrium, we derive scalings predicting how fast it takes to get into equilibrium state considering the flow structure outside as well as inside the drop.

Our results were published in a peer reviewed journal Geochemistry, Geophysics, Geosystems and the paper follows below (Ulvrová et al., 2011).

Geochemistry Geophysics Geosystems G3

Article
Volume 12, Number 10
20 October 2011
Q10014, doi:10.1029/2011GC003757
ISSN: 1525-2027

Published by AGU and the Geochemical Society

Compositional and thermal equilibration of particles, drops, and diapirs in geophysical flows

M. Ulvrová
Laboratoire de Géologie de Lyon, École Normale Supérieure de Lyon, 46, Allée d'Italie, F-69364 Lyon CEDEX 07, France (martina.ulvrova@ens-lyon.fr)

N. Coltice and Y. Ricard
Laboratoire de Géologie de Lyon, Université de Lyon 1, Bat Geode, 43 Boulevard du 11 Novembre 1918, F-69100 Villeurbanne, France (nicolas.coltice@univ-lyon1.fr; ricard@ens-lyon.fr)

S. Labrosse
Laboratoire de Géologie de Lyon, École Normale Supérieure de Lyon, 46, Allée d'Italie, F-69364 Lyon CEDEX 07, France (stephane.labrosse@ens-lyon.fr)

F. Dubuffet
Laboratoire de Géologie de Lyon, Université de Lyon 1, Bat Geode, 43 Boulevard du 11 Novembre 1918, F-69100 Villeurbanne, France (fabien.dubuffet@univ-lyon1.fr)

J. Velímský
Department of Geophysics, Faculty of Mathematics and Physics, Charles University, V Holešovičkách 2, 180 00 Prague 8, Czech Republic (velimsky@karel.troja.mff.cuni.cz)

O. Šrámek
Department of Physics, University of Colorado at Boulder, 390 UCB, Boulder, Colorado 80309-0390, USA (ondrej.sramek@colorado.edu)

[1] Core formation, crystal/melt separation, mingling of immiscible magmas, and diapirism are fundamental geological processes that involve differential motions driven by gravity. Diffusion modifies the composition or/and temperature of the considered phases while they travel. Solid particles, liquid drops and viscous diapirs equilibrate while sinking/rising through their surroundings with a time scale that depends on the physics of the flow and the material properties. In particular, the internal circulation within a liquid drop or a diapir favors the diffusive exchange at the interface. To evaluate time scales of chemical/thermal equilibration between a material falling/rising through a deformable medium, we propose analytical laws that can be used at multiple scales. They depend mostly on the non-dimensional Péclet and Reynolds numbers, and are consistent with numerical simulations. We show that equilibration between a particle, drop or diapir and its host needs to be considered in light of the flow structure complexity. It is of fundamental importance to identify the dynamic regime of the flow and take into account the role of the inner circulation within drops and diapirs, as well as inertia that reduces the thickness of boundary layers and enhances exchange through the interface. The scaling laws are applied to predict nickel equilibration between metals and silicates that occurs within 130 m of fall in about 4 minutes during the metal rain stage of the Earth's core formation. For a mafic blob (10 cm diameter) sinking into a felsic melt, trace element equilibration would occur over 4500 m and in about 3 years.

Components: 6500 words, 5 figures, 1 table.

Keywords: equilibration; fluid mechanics; magma; mixing; modeling; segregation.

Index Terms: 1009 Geochemistry: Geochemical modeling (3610, 8410); 1043 Geochemistry: Fluid and melt inclusion geochemistry; 8145 Tectonophysics: Physics of magma and magma bodies.

Received 15 June 2011; **Revised** 29 August 2011; **Accepted** 30 August 2011; **Published** 20 October 2011.

Ulvrová, M., N. Coltice, Y. Ricard, S. Labrosse, F. Dubuffet, J. Velímský, and O. Šrámek (2011), Compositional and thermal equilibration of particles, drops, and diapirs in geophysical flows, *Geochem. Geophys. Geosyst.*, *12*, Q10014, doi:10.1029/2011GC003757.

1. Introduction

[2] Bubbles and crystals travel through differentiating magmas; metal drops and diapirs fell through molten silicates during the formation of Earth's core [*Stevenson*, 1990; *Rubie et al.*, 2003; *Samuel and Tackley*, 2008; *Monteux et al.*, 2009]; and sometimes, coexistent immiscible magmas or metals separate to reach gravitational equilibrium [*Dawson and Hawthorne*, 1973; *Dasgupta et al.*, 2006, 2009; *Morard and Katsura*, 2010]. Differential motion driven by gravity is a prerequisite for planetary differentiation at all scales. While a phase travels through and deforms the other, chemical and thermal diffusion proceed towards thermodynamic equilibrium. Depending on material and flow dynamics, non-equilibrium fractionation could result from inefficient mass/heat transfer from one phase to the other during travel. In order to quantify the time scale of thermodynamic equilibration, it is necessary to model deformation of both phases and transport dynamics.

[3] A generic physical description of these differentiation mechanisms can be formulated by the rise/fall of chemically (or thermally) distinct particles, drops or diapirs through a viscously deforming medium. In this paper, the term particle refers to a small self-contained body significantly more viscous than the surroundings and possibly solid, while drop and diapir are defined by self-contained bodies as viscous or less viscous than the surroundings and possibly inviscid. A diapir is a large-scale body with approximate sphericity, and we use the term of drop for small-scale body, when surface tension controls the sphericity. The purpose of this paper is to review and propose analytical laws that describe the chemical/thermal equilibration of a traveling particle, drop or diapir, that can be used at multiple scales and applied to a variety of geological problems. This chemical equilibration is that of minor or trace elements, migrating across the surface of the traveling sphere, assuming that the major element mineralogies, inside and outside the sphere, do not change. We first draw attention to results that are often overlooked in the geoscience literature though acknowledged in engineering and mass/heat transfer communities. Indeed, the mass and heat transfer between a liquid drop/solid particle and a viscous surrounding medium has been described for various industrial purposes [*Clift et al.*, 1978]. We then extend their use and couple them to concentration models inside and around the spherical body. We propose scaling laws for the time of equilibration for 4 different regimes: a particle with and without inertia, a drop/diapir with and without inertia. Then, we propose times of chemical equilibration during core formation and silicate melt differentiation.

2. Models for the Equilibration of Rising/Falling Particles, Drops, and Diapirs

2.1. Chemical and Thermal Transfer From a Sphere

[4] We restrict ourselves to the study of an individual spherical particle, drop or diapir of radius R in steady-state motion with terminal velocity U_t. In the following, the subscript "o" denotes the properties outside the sphere and "i" inside the sphere. The viscosity ratio between the falling/rising body and its host liquid is $\mathcal{R}_\mu = \mu_i/\mu_o$ and we speak of "particles" when $\mathcal{R}_\mu = \mu_i/\mu_o \gg 1$ and "drops" or "diapirs" when $\mathcal{R}_\mu = \mu_i/\mu_o \lesssim 1$. All the notations and parameters can be found in Table 1.

[5] In order for the dispersed phase to keep its sphericity, the interfacial force has to exceed disrupting forces, i.e. the viscous force and inertia, that tend to deform the sphere. The smallest drops or diapirs coalesce (they are swept by larger spheres traveling faster), the largest deform, stretch and eventually break-up. For highly viscous flows, the capillary number $\mathrm{Ca} = \mu_o U_t/\gamma$ (γ is interfacial tension), being the ratio between the viscous stresses and the interfacial tension, reaches a critical value for break-up conditions that depends on

Table 1. Variables and Parameters of the Studied System Together With Expressions for the Proposed Equilibration Times τ

Parameter	Notation	Unit
Viscosity of the host liquid	μ_o	Pa s
Viscosity inside the sphere	μ_i	Pa s
Diffusivity of the host liquid	D_o	$m^2\ s^{-1}$
Diffusivity inside the sphere	D_i	$m^2\ s^{-1}$
Density of the host liquid	ρ_o	$kg\ m^{-3}$
Density of the sphere	ρ_i	$kg\ m^{-3}$
Radius of the sphere	R	m
Terminal velocity	U_t	$m\ s^{-1}$
Initial concentration within the sphere	c_0	$mol\ m^{-3}$
Concentration at infinity	c_∞	$mol\ m^{-3}$
Dimensionless Number	**Notation**	**Expression**
Viscosity ratio	$\mathcal{R}_\mu$	μ_i/μ_o
Diffusivity ratio	$\mathcal{R}_D$	D_i/D_o
Reynolds number	Re	$RU_t\rho_o/\mu_o$
Peclet number	Pe	RU_t/D_o
Schmidt number	Sc	$Pe/Re = \mu_o/(\rho_o D_o)$
Sherwood number	Sh	$-\langle \nabla C_o^{surf}\rangle/\langle C_o^{surf}\rangle$
Regime		**Equilibrium Timescale**
Drop: low Re, low $\mathcal{R}_\mu$		$\tau = \frac{Pe}{3}\left(\frac{K}{0.461\left(1+\mathcal{R}_\mu\right)^{-1/2}Pe^{1/2}} + \frac{1}{10\,\mathcal{R}_D}\right)$
Drop: high Re, low $\mathcal{R}_\mu$		$\tau = \frac{Pe}{3}\left(\frac{K}{0.79\,Pe^{1/2}} + \frac{1}{10\,\mathcal{R}_D}\right)$
Particle: low Re, high $\mathcal{R}_\mu$		$\tau = \frac{Pe}{3}\left(\frac{K}{0.64\,Pe^{1/3}} + \frac{3}{\pi^2\mathcal{R}_D}\right)$
Particle: high Re, high $\mathcal{R}_\mu$		$\tau = \frac{Pe}{3}\left(\frac{K}{0.6\,Pe^{1/3}Re^{1/6}} + \frac{3}{\pi^2\mathcal{R}_D}\right)$

the viscosity ratio $\mathcal{R}_\mu$ across the surface. This critical capillarity number Ca is about 0.1 for high viscosity ratios and larger for low viscosity ratios, for which the drop/diapir stretches and forms a slender shaped body difficult to fragment (see *Stone* [1994] for a review). For low viscosity flows, perturbations of the interface generate Rayleigh-Taylor and Kelvin-Helmoltz instabilities that ultimately break up the drops [*Kitscha and Kocamustafaogullari*, 1989]. This situation happens when the Weber number $We = \rho_o U_t^2 R/\gamma$ (ρ_o is external density), which is the ratio between inertia and interfacial tension, reaches values around 10 [*Wierzba*, 1990].

[6] For a body sinking or rising through a viscous medium, two non-dimensional numbers control the dynamics of chemical equilibration of the traveling sphere with its surroundings: (1) the Reynolds number $Re = RU_t\rho_o/\mu_o$ that describes the effect of inertia to viscous force and (2) the Péclet number $Pe = RU_t/D_o$ that relates the diffusion time to the advection time in the host liquid, D standing for chemical diffusivity. As both Re and Pe include the terminal velocity, it may be confusing to use simultaneously the two numbers and we introduce their ratio, also called the Schmidt number $Sc = Pe/Re = \mu_o/(\rho_o D_o)$. When the spherical body and its host liquid have different physical properties, the ratios of internal to external diffusivities $\mathcal{R}_D = D_i/D_o$ and viscosities $\mathcal{R}_\mu = \mu_i/\mu_o$, have to be considered.

[7] Starting from non equilibrium initial conditions, the sphere and its surroundings tend to chemically equilibrate by microscopic diffusion and macroscopic stirring. The stirring, i.e., the advection of concentration by the flow, occurs outside and possibly inside the sphere, due to the circulation forced by the shear stress at the surface of the drop.

[8] We assume that the initial concentration c of some trace element outside the sphere is uniform and equal to c_∞ while the concentration inside the drop is equal to c_0. The dimensionless transport equation governing this process, assuming materials are incompressible, is written as

$$\frac{\partial C}{\partial t} = \nabla \cdot \left(\frac{\mathcal{D}}{Pe}\nabla C - \mathbf{v}C\right), \tag{1}$$

where C stands for the normalized concentration of any minor element of interest, i.e., $C = (c - c_\infty)/(c_0 - c_\infty)$ and $\mathcal{D}$ for the dimensionless diffusion coefficient being 1 outside the drop and $\mathcal{R}_D = D_i/D_o$ inside. To scale the quantities back to numbers with dimensions, the dimensionless distance has to be multiplied by the radius of the sphere R, and the time by the advection time R/U_t. The initial non-dimensional concentrations are one inside and zero outside.

[9] The local chemical equilibrium implies that the concentration c_i^{surf} on the inner side of the sphere is controlled by thermodynamics to be Kc_o^{surf}, where K is the partition coefficient at the surface ($K = c_i^{surf}/c_o^{surf}$). The final equilibrium is reached when the outside concentration is homogeneous and equal to c_∞ and the inside concentration also homogeneous but equal to Kc_∞. The normalized concentration inside the sphere, C_i, evolves therefore from 1 to $(K-1)c_\infty/(c_0 - c_\infty)$.

[10] The chemical and thermal diffusion of a traveling sphere is the subject of numerous studies in the chemical/heat transfer literature [e.g., *Clift et al.*, 1978; *Levich*, 1962] that we can only briefly introduce here. Usually the mass transfer coefficient of the sphere is defined as the Sherwood number:

$$\mathrm{Sh} = -R\frac{\langle \nabla c_o^{surf}\rangle}{\langle c_o^{surf}\rangle - c_\infty} = -\frac{\langle \nabla C_o^{surf}\rangle}{\langle C_o^{surf}\rangle}, \qquad (2)$$

where $\langle c_o^{surf}\rangle$ and $\langle C_o^{surf}\rangle$, and $\langle \nabla c_o^{surf}\rangle$ and $\langle \nabla C_o^{surf}\rangle$ are the average concentrations at the surface of the sphere and average gradients of concentration normal to it, with and without dimensions. The minus sign in equation (2) insures the positivity of Sh. Notice also that although the gradient of concentration $\langle \nabla c_o^{surf}\rangle$ can have any sign, the normalized gradient $\langle \nabla C_o^{surf}\rangle$ is always negative. Because of the similarity of heat and diffusion equations, all the results on diffusion relating Schmidt and Sherwood numbers have thermal counterparts where the mass flux is equivalent to the Nusselt number $\mathrm{Nu} = -R\nabla T_{surf}/(T_{surf} - T_\infty)$, and the Schmidt number to the Prandtl number $\mathrm{Pr} = \mu_o/(\rho_o\kappa_o)$, where T is temperature and κ thermal diffusivity.

[11] A very large number of semi-empirical equations predicting Sh, can be found in the literature, based on experiments and physical analysis. However, simple boundary layer theories can be developed to quantitatively describe mass fluxes at the interface in the different flow regimes. The general method is to express the velocity at the surface of the sphere, estimate the shape of the diffusion layer and perform careful averaging over the sphere [*Levich*, 1962; *Ribe*, 2007]. The general results for high enough Pe can be written in the form

$$\mathrm{Sh} = a\,\mathrm{Sc}^m\mathrm{Pe}^n = a\,\mathrm{Sc}^{m+n}\mathrm{Re}^n, \qquad (3)$$

where a, m and n are constants for a given regime. The exponents can be found by scaling arguments as summarized hereafter and the prefactor estimated analytically, numerically or experimentally:

[12] 1. When $\mathcal{R}_\mu \lesssim 1$, i.e., in the case where the internal viscosity is of the same order or smaller than the external viscosity, the external flow experiences the surface of the drop/diapir as a free-slip boundary condition. The surface velocity in the reference frame of the drop/diapir is therefore of order U_t, the transport term of the advection-diffusion equation $v.\nabla C$ is of order U_tC/R (transport along the surface of the sphere) and is balanced by a diffusion term $D_o\nabla^2 C$ of order D_oC/δ^2 across a diffusion boundary layer of thickness δ (diffusion perpendicular to the surface of the sphere). Therefore the diffusion boundary layer is of order $(\delta/R)^2 \propto 1/\mathrm{Pe}$, and, as $\mathrm{Sh} = R/\delta$

$$\mathrm{Sh} = a\,\mathrm{Pe}^{1/2} = a\,\mathrm{Sc}^{1/2}\mathrm{Re}^{1/2}. \qquad (4)$$

The details of the external velocity field control the diffusion layer and hence the expression of the constant a. (1) For low Re flows, inertia is negligible, the external velocity is given analytically by the Rybczynski-Hadamard expression [*Acrivos and Goddard*, 1965] and following *Levich* [1962] we obtain

$$a = 0.461\sqrt{\frac{1}{1+\mathcal{R}_\mu}}. \qquad (5)$$

(2) At very large Re, the flow becomes irrotational and the analytical expression of the potential flow yields $a = 0.79$ [*Clift et al.*, 1978].

[13] 2. When $\mathcal{R}_\mu \gg 1$, the sphere behaves rigidly. In its own reference frame, the surface velocity is zero then increases away to U_t. Two cases must then be considered. First, at low Re, there is no viscous boundary layer as viscous forces dominate everywhere in the domain. As a consequence the velocity increases from 0 to U_t over the distance R so that the velocity is of order $U_t\delta/R$ at the distance δ. The balance between advection and diffusion now gives $(U_t\delta/R)(C/R) \propto D_oC/\delta^2$, which leads to $(\delta/R)^3 \propto 1/\mathrm{Pe}$ and thus to

$$\mathrm{Sh} = a\,\mathrm{Pe}^{1/3} = a\,\mathrm{Sc}^{1/3}\mathrm{Re}^{1/3}, \qquad (6)$$

where $a = 0.64$ [*Levich*, 1962]. Second, at large Re, the situation is more complex. In this case, there is a viscous boundary layer of thickness δ' where the inertia term of the Navier-Stokes equation $\rho_o U_t^2/R$ is balanced by the viscosity $\mu_o U_t/\delta'^2$. The diffusive boundary layer is therefore embedded in a viscous layer of thickness $\delta' \propto R\ \mathrm{Re}^{-1/2}$. The velocity at the distance δ of the particle surface is of order $U_t\delta/\delta' = U_t\delta\mathrm{Re}^{1/2}/R$. The balance between diffusion and advection is now $(U_t\delta\mathrm{Re}^{1/2}/R)(C/R) \propto D_o C/\delta^2$ which leads to $(\delta/R)^3 \propto 1/(\mathrm{Re}^{1/2}\mathrm{Pe})$ and thus to

$$\mathrm{Sh} = a\,\mathrm{Re}^{1/6}\mathrm{Pe}^{1/3} = a\,\mathrm{Sc}^{-1/6}\mathrm{Pe}^{1/2} = a\,\mathrm{Sc}^{1/3}\mathrm{Re}^{1/2}, \quad (7)$$

where $a = 0.6$ [*Ranz and Marshall*, 1952].

[14] 3. For a non moving body, the diffusion equation can be solved exactly and Sh = 1. This is a special case, that does not obey the asymptotic equation (3) valid for high Pe. In the intermediate regime where Pe is small, various empirical expressions for each specific case can be found in the literature. For example, for $\mathrm{Re} \ll 1$, *Clift et al.* [1978] propose $\mathrm{Sh} = 1 + (1 + a^{4/3}\mathrm{Pe}^{2/3})^{3/4}$ in the case $\mathcal{R}_\mu \lesssim 1$ (which generalizes equation (4)) and $\mathrm{Sh} = 1 + (1 + a^3\mathrm{Pe})^{1/3}$ in the case $\mathcal{R}_\mu \gg 1$ (which generalizes equation (6)). These expressions are cumbersome and the cases where diffusion dominates advection not very interesting physically. For numerical applications, the reader should use the maximum of the asymptotic equation (3) and of the diffusive limit Sh = 1.

2.2. Equilibration Time Scales

[15] Once the Sherwood number is known (the average concentration gradient), to compute the evolution of the concentration within the sphere, we must now relate $\langle C_o^{\mathrm{surf}}\rangle$ to $\langle C_i\rangle$, the average concentration of the spherical body. Hence we integrate the diffusion equation (1) to get

$$\frac{\partial\langle C_i\rangle}{\partial t} = \frac{3}{\mathrm{Pe}}\langle \boldsymbol{\nabla} C_o^{\mathrm{surf}}\rangle = -3\frac{\mathrm{Sh}}{\mathrm{Pe}}\langle C_o^{\mathrm{surf}}\rangle. \quad (8)$$

The thermodynamic equilibrium at the surface implies $c_i^{\mathrm{surf}} = K c_o^{\mathrm{surf}}$, or in term of normalized concentrations,

$$C_i^{\mathrm{surf}} = K C_o^{\mathrm{surf}} + (K-1)\frac{c_\infty}{c_0 - c_\infty}. \quad (9)$$

[16] The concentration diffuses from the surface where the concentration gradient is $\langle \boldsymbol{\nabla} C_o^{\mathrm{surf}}\rangle/\mathcal{R}_D$. Therefore a reasonable profile for the radial concentration inside the drop is

$$C_i(r) = \langle C_i^{\mathrm{surf}}\rangle + \frac{\langle \boldsymbol{\nabla} C_o^{\mathrm{surf}}\rangle}{\mathcal{R}_D} f(r). \quad (10)$$

The function $f(r)$ characterizes the concentration profile and verifies the conditions at the surface and the center of the sphere: $f(1) = 0$, $f'(1) = 1$ and $f'(0) = 0$. This function should also satisfy some positivity constraint as the real concentration $c_i(r)$ should be everywhere positive. We do not impose such a condition. Our models implies that the concentration near the surface of the sphere is always positive and this controls the average concentration (related to the integral of $C_i(r)r^2$) which is always positive as we see below.

[17] Equation (10), averaged over the volume of the sphere, gives for the radial average concentration

$$\langle C_i\rangle = \langle C_i^{\mathrm{surf}}\rangle - \frac{\langle \boldsymbol{\nabla} C_o^{\mathrm{surf}}\rangle}{b\,\mathcal{R}_D} = \langle C_o^{\mathrm{surf}}\rangle\left(K + \frac{\mathrm{Sh}}{b\,\mathcal{R}_D}\right) + (K-1)\frac{c_\infty}{c_0 - c_\infty}, \quad (11)$$

where the second equality uses averaged equation (9), and where b is positive and given by

$$\frac{1}{b} = -3\int_0^1 f(r)r^2\mathrm{d}r. \quad (12)$$

[18] Combining equations (8) and (11) we predict an exponential homogenization of the concentration

$$\frac{\partial\langle C_i\rangle}{\partial t} = -\frac{1}{\tau}\left(\langle C_i\rangle - (K-1)\frac{c_\infty}{c_0 - c_\infty}\right) \quad \text{with} \quad \tau = \frac{\mathrm{Pe}}{3}\left(\frac{K}{\mathrm{Sh}} + \frac{1}{b\mathcal{R}_D}\right). \quad (13)$$

With real dimensions, the solution is simply

$$\langle c_i(t)\rangle = c_0\exp\left(-\frac{U_t}{R\tau}t\right) + Kc_\infty\left(1 - \exp\left(-\frac{U_t}{R\tau}t\right)\right). \quad (14)$$

These last expressions show that the average concentration in the sphere reaches exponentially the asymptotic equilibrium value and provides an estimate of the characteristic homogenization time τ as a function of K, Pe, Re, $\mathcal{R}_D$ and $\mathcal{R}_\mu$ (which controls the appropriate expression of Sh). It also shows that the average concentration is always positive, independently of the choice of $f(r)$, hence b, that we estimate for two limiting cases:

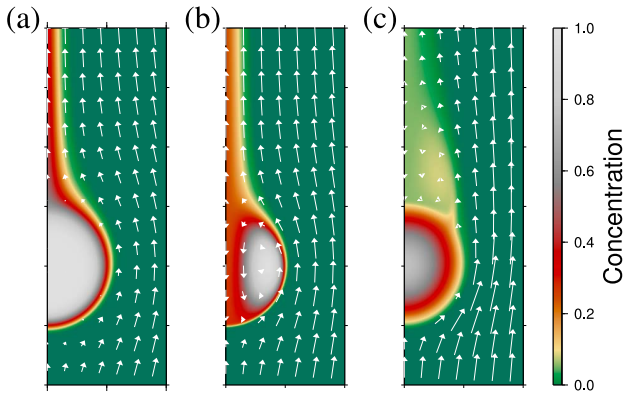

Figure 1. Maps (close-ups) of the nondimensional velocity relative to the average drop velocity (arrows) and concentration (color) for falling (a) particle in Re < 1 flow, (b) drop in Re < 1 flow (in to out viscosity ratio $\mathcal{R}_\mu = 10^{-3}$) and (c) particle in a higher Re flow (being 50 here). The spheres fall under their own weight and start with a composition of 1 (light grey) and the surrounding material has a zero concentration initially (green). All models have Péclet number Pe = 2800 and equal diffusivity in and out of the sphere ($\mathcal{R}_D = 1$). Snapshots are taken after a falling distance of 36 (Figure 1a), 41 (Figure 1b) and 283 (Figure 1c), times the sphere radius.

[19] 1. When $\mathcal{R}_\mu \gg 1$, there is no recirculation inside the sphere. When diffusivity of the outer material is large, $1/(b\mathcal{R}_D) \gg K/\mathrm{Sh}$, the time of equilibration in dimensional quantities is $\tau = R^2/(3bD_i)$, which is the same as the classical value obtained for diffusion in a sphere with imposed surface concentration $R^2/(\pi^2 D_i)$ [*Carslaw and Jaeger*, 1959], when $b = \pi^2/3$. This is obtained for $f(r) = -\sin(\pi r)/(\pi r)$, which indeed verifies $f'(0) = f(1) = 0$, and $f'(1) = 1$. In our equilibration experiments, the concentration is not imposed at the sphere surface but at infinity. The diffusion toward the sphere must also proceeds outside the sphere and using equation (13) with Sh = 1 we predict for the equilibration time of a static sphere (with real dimension)

$$\tau_s = K\frac{R^2}{3D_o} + \frac{R^2}{\pi^2 D_i}. \qquad (15)$$

The equilibration of a sphere with concentration maintained at infinity is indeed slower than when this concentration is imposed at the surface and depends on internal and external diffusivities and on the partition coefficient.

[20] 2. When $\mathcal{R}_\mu \lesssim 1$, there is an internal recirculation inside the drop/diapir, the concentration at the center is close to the concentration at the surface because of the efficient inner transport. Thus, the radial concentration profile within the fluid sphere must also satisfy $f(0) = 0$. The simplest polynomial function that verifies all four conditions $f(0) = f'(0) = f(1) = 0$, and $f'(1) = 1$ is $f(r) = r^2(r-1)$ which results in $b = 10$.

[21] For the convenience of the reader, the expressions for the equilibration times in the different regimes are summarized in Table 1.

3. Numerical Examples

[22] The goal of this section is to compare full numerical solutions for the time of equilibration with the analytical laws proposed above. Hence we run 2D axisymmetric numerical simulations of the incompressible Navier-Stokes equation coupled with the mass transfer equation. The experiments are performed using the finite element method (FEM) implemented in the Elmer open software (CSC IT–Center for Science, 2010, available at http://www.csc.fi/english/pages/elmer). The computing domain consists of an axisymmetrical cylinder with height and diameter of 40 R. In the center of the cylinder is a motionless sphere of radius R. Constant inflow of magnitude U_t parallel to the axis of symmetry together with zero concentration boundary condition are prescribed at the bottom of the cylinder, neglecting thus the influence of other drops. Free-slip boundary condition for velocity, and zero concentration are imposed at the sides of the cylinder. At the top, a flow parallel to the symmetry axis is forced, and a Neumann boundary condition of zero concentration gradient is prescribed. Finally, at the surface of the sphere, zero normal velocity and zero tangent traction are prescribed. A jump in concentration is imposed according to the choice of the partition coefficient, while the concentration flux remains continuous.

[23] Using FEM allows us to refine the mesh in the boundary layer around the sphere in order to have a good resolution for the velocity and transport equations, together with the refinement in the wake where more complicated structures of the flow appear at high Re. We use up to 80 000 mesh nodes. For each of the simulations, the time of equilibration τ is computed through a least-squares fit of the time series of $\langle C_i(t)\rangle$. We explore its dependence on the non-dimensional numbers Pe in the range 10^2–10^5, Re in the range 0–170 and diffusivity and viscosity ratios $\mathcal{R}_D$ and $\mathcal{R}_\mu$, in the range 10^{-1}–10^3 and 10^{-3}–10^3, respectively.

[24] Typical flows are shown in Figure 1 (velocity in the sphere reference frame is depicted by arrows, concentration by color scale). For a rigid sphere and low Reynolds number (panel a, $\mathcal{R}_\mu$ = 100, Re = 0.1), the flow is a typical Stokes flow, homogenization proceeds from the surface, and a tail is emitted in the wake of the sphere. When the internal viscosity is reduced keeping the same low Reynolds number (panel b, $\mathcal{R}_\mu = 10^{-3}$, Re = 0.1), a circulation is induced within the drop with velocities comparable to the terminal velocity, and we note two minima for the concentration, along the symmetry axis and at the surface. As Re increases (panel c, $\mathcal{R}_\mu = 10^4$, Re = 50), the symmetry of the flow breaks down and a vortex is generated behind the sphere. The variety of flows, within and outside the sphere, is the expression of the diversity of regimes for chemical and heat transfer. The transition from the drop/diapir case, in which the inner circulation is pronounced, and the particle case, where the sphere acts as a solid, occurs for $\mathcal{R}_\mu$ between 1 and 500 in our calculations.

[25] In Figure 2 we depict the average radial concentrations corresponding to cases with and without internal recirculation, for the situations and times of the cases in Figures 1b and 1c (the case in Figure 1a, without recirculation is comparable to the case in Figure 1c for what concerns the average radial concentration). Although the fits are not perfect, the analytical profiles capture the behavior of the numerical solutions. The quality of the approximations are increasing with time, as equilibration proceeds. As the average concentrations in the sphere involves $C_i(r)r^2$, and are therefore mostly controlled by the concentration near r = 1, more accurate fits are not needed.

[26] To benchmark the quality of the predictive laws proposed above, we compute the evolutions of the concentrations in numerical simulations. These evolutions can be closely matched by exponentials, as predicted. In Figure 3, the Pe dependence proposed above reproduces the results of the simulations in the various cases, at low and high Re. The proposed analytical expressions are in very good agreement with the numerical experiments. For the drop/diapir case, the analytical model with inviscid flow gives a lower bound for the time of equilibration since viscosity should slow motion in boundary layers. In Figure 3, the role of the circulation within the drop/diapir is expressed by the shorter equilibration time for the fluid sphere case relative to the solid case. Indeed, the circulation within the sphere produces efficient stirring that generates stronger chemical/thermal gradients which diffuse away more rapidly. As Pe increases, the non-dimensional time of equilibration increases. To keep the same reference time scale for the non-dimensionalization (fixing the values for U_t and R) while increasing Pe implies that diffusivity has to be decreased. It is then expected that keeping the velocity constant and decreasing the diffusivity thwarts equilibration.

[27] The observed role of Re in the simulations is also consistent with our predictions with and without internal circulation, as seen in Figure 4. Increasing Re leads to a decrease of the dimensionless time of equilibration. At high Re, velocities can be larger and stronger velocity gradients are allowed which favor a faster mixing. Indeed, the higher the Re the thinner the boundary layer around the sphere, and thus the more efficient the diffusion across the drop interface. However, this mechanism is somewhat modest since a limited reduction of the equilibration time by a factor of 2 requires more than 3 order of magnitude higher Re. The onset of the wake instability does not generate significant changes in the equilibration style mostly because the flux of elements/heat is dominated by the fluxes at the front of the sphere while it remains close to zero in the wake.

[28] Figure 5 shows τ as a function of $\mathcal{R}_D$ for a fixed Pe for the drop/diapir and particle cases at low and high Re. Again the numerical results show a good agreement with our theoretical predictions: when $\mathcal{R}_D > 1$, diffusion inside the sphere is more efficient than outside. Hence, diffusion in the host liquid is the limiting parameter for equilibration and τ does not depend on $\mathcal{R}_D$, cf. equation (13). For $\mathcal{R}_D < 1$, diffusion in the sphere is the limiting parameter and as a consequence τ decreases with $\mathcal{R}_D$. As explained above, the analytical model for the

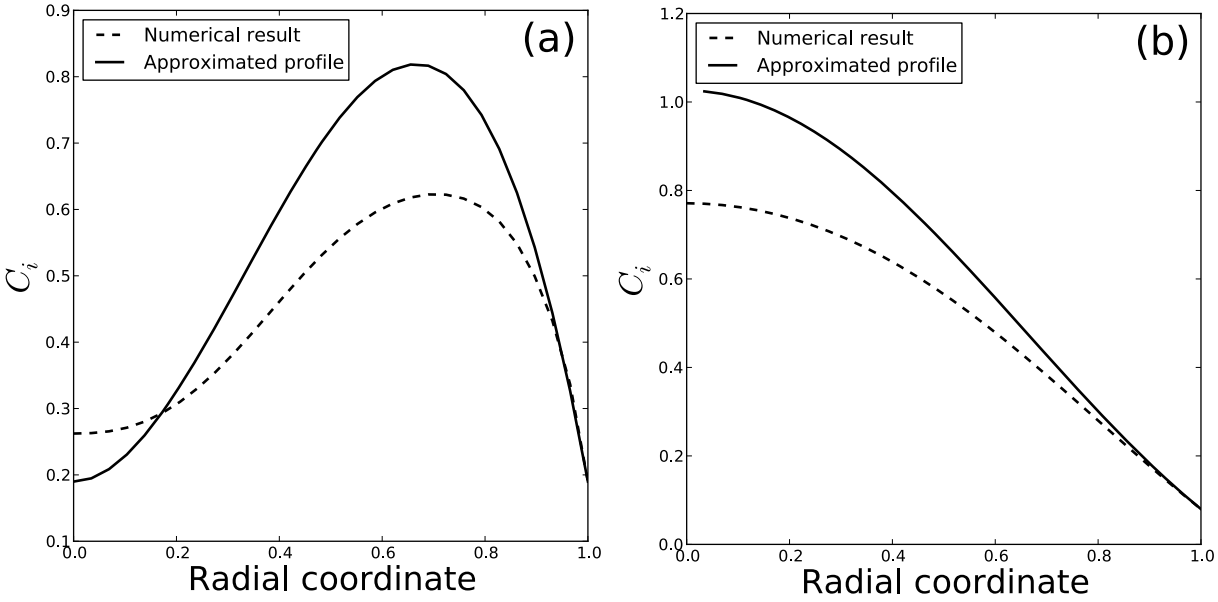

Figure 2. Average concentrations in the sphere as a function of normalized radius, corresponding to the cases in Figures 1b and 1c (solid lines). The profile approximations (dashed lines), equation (10) with $f(r) = r^2(r - 1)$ and $f(r) = -\sin(\pi r)/(\pi r)$, are in reasonable agreement with the simulations, particularly near $r = 1$.

high Re drop regime represents a lower bound for the analytical model since inviscid fluid is considered.

4. Discussion and Conclusions

[29] We presented approximate analytical models to predict equilibration times for spherical particles, drops and diapirs traveling through a viscously deforming surroundings due to buoyancy forces. Numerical simulations for a wide range of parameters confirm our predictive laws that can be used in geophysical problems at any scale. Small differences between analytical and numerical predictions can however be noticed (particularly visible in Figure 4 where we use a vertical linear scale). This might be due to the several assumptions of the analytical models (asymptotic expressions and choices of simple radial profiles) or of the numerical simulations (finite size of the computation domain).

[30] We showed that it is fundamental to take into account the flow structure and hence evaluate the correct regime for a given situation. The existence of an internal circulation within the spherical body is essential since it significantly reduces the time needed for equilibration. Compared to the purely diffusive systems, advective motion gives rise to thinner boundary layers and thus raises concentration gradients. Consequently, diffusion transport inside the spherical body and whole equilibration are more efficient than for a particle or motionless drop/diapir. When inertia dominates over the viscous forces, the boundary layer is even thinner speeding up further diffusion across the rim. Concerning the role of diffusivity and viscosity, a high diffusion rate of the surrounding host liquid always favors a rapid equilibration. The role of the external viscosity is more complex. The time of equilibration decreases both when the external viscosity is too low (in which case no stirring occurs within the drop) and when it is too large (in which case the terminal velocity and the internal velocities also decrease). The cases where the internal and external viscosities are close, i.e., the transition between drops (internal recirculation) and particles (no internal recirculation), are difficult to predict analytically. In the low Re number limit, the flow can be expressed as a function of $\mathcal{R}_\mu$ by the Rybczynski-Hadamard formulae but a choice has to be made for the value of b ($b = 10$ for a drop, $b = \pi^2/3$ for a particle). The situation is even more complex at high Re numbers where the real solution lies in between the two analytical cases.

[31] The predictive laws are scale-independent and can be applied to various geophysical settings without computing the full mass transfer problems. A small scale problem is hybridization of mafic blob falling in a more silicic melt. We choose typical numbers as those of *Grasset and Albarède* [1994]: 200 kg m^{-3} density excess than the felsic surroundings [*Huppert et al.*, 1982], viscosities of 500 Pa s

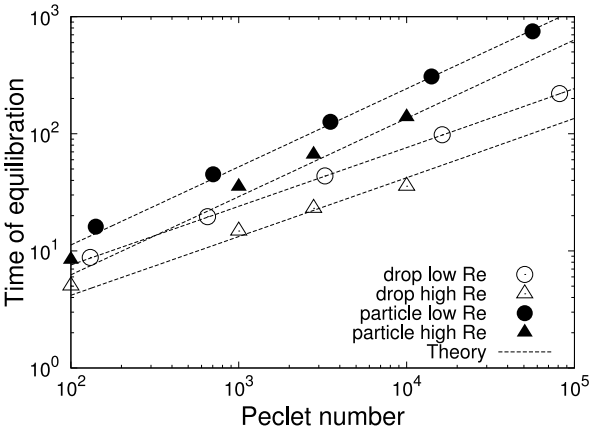

Figure 3. Nondimensional time of equilibration as a function of Péclet number (Pe) for drops and particles, at Re = 0 and Re = 50. In these simulations, the ratio of internal to external diffusivity is $\mathcal{R}_D$ = 1000 and for the drop $\mathcal{R}_\mu$ = 0.1. The analytical relationships are depicted by dashed lines.

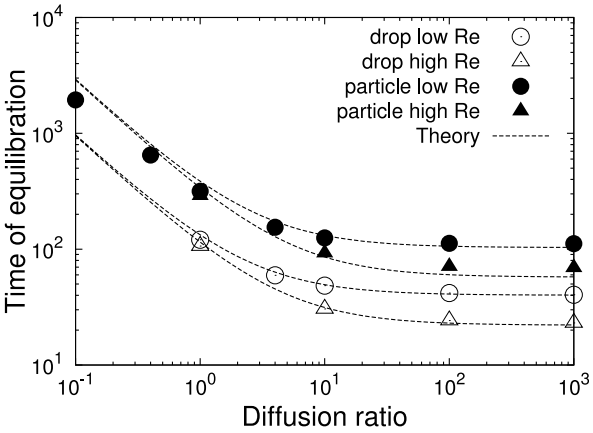

Figure 5. Nondimensional equilibration time as a function of diffusivity ratio $\mathcal{R}_D$ for drops and particles, at low and higher Reynolds number Re (Re = 0 and 50 here). In these simulations the Péclet number is Pe = 2800 and for the drop viscosity ratio $\mathcal{R}_\mu$ = 0.1. The analytical relationships are depicted by dashed lines.

and 25000 Pa s for the mafic blob and host silicic melt and viscosity, respectively, and 10 cm for the blob diameter. The Rybczynski-Hadamard formula gives a terminal velocity of $U_t = 5.3 \cdot 10^{-5}$ m s^{-1} which implies Re = $2 \cdot 10^{-7}$. The corresponding dynamic regime is that of a drop traveling at low Re. To compute the time of equilibration we use typical

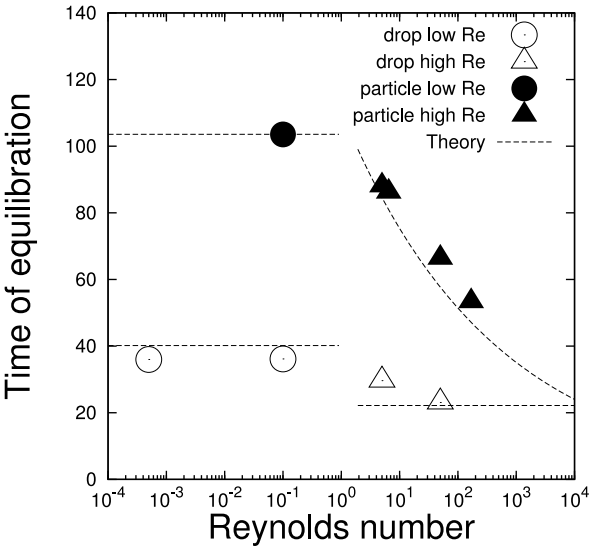

Figure 4. Nondimensional time of equilibration as a function of Re for drops and particles. In these simulations the Péclet number is Pe = 2800, ratio of internal to external diffusivity is $\mathcal{R}_D$ = 1000 and for the drop case, ratio of in and out viscosities is $\mathcal{R}_\mu$ = 0.1. The analytical relationships for low and high Re are depicted by dashed lines. The transition from low to high Re regime happens around Re = 1.

diffusion coefficients of 10^{-12} m^2 s^{-1} for trace elements for both liquids. As a consequence, Pe is about $2.7 \cdot 10^6$. We arbitrarily choose a partition coefficient of 2 between the two melts which means that a trace element will be twice more abundant in the mafic enclave than in the silicic melt after full equilibration. The mafic blob is much less viscous than the surrounding melt. Stirring inside the body thus enhances the hybridization rate and the characteristic time of equilibration is 2.7 years corresponding to a falling distance of 4535 m. This is a significantly shorter time than if equilibration proceeded only by static diffusion obtained from equation (15). Without any movement the equilibration could be attained in about 60 years. Notice, that many people would use the classical expression $\tau = R^2/(\pi^2 D_i)$ that gives for this case an equilibration time of 8 years, but is physically inappropriate as it neglects the diffusion in the surroundings of the sphere and the partition coefficient.

[32] For small iron droplets falling through a silicate magma ocean during early planetary differentiation, we use values similar to those given by *Rubie et al.* [2003], with a drop size of R = 0.5 cm. The most uncertain and critical parameter is the viscosity of molten silicates composing the magma ocean ranging in a wide interval 10^{-4}–100 Pa s. Choosing 0.01 Pa s gives us a terminal velocity U_t = 0.6 m s^{-1} using the work of *Brown and Lawler* [2003] for high Re flows. The viscosity of iron droplets is fixed at μ_i = 0.01 Pa s [*Vočadlo et al.*, 2000] and we choose a partition coefficient of K = 30, which would be that for nickel at a pres-

sure of 50 GPa [*Li and Agee*, 2001]. The diffusivity of nickel in liquid iron is set to $D_i = 10^{-8}$ m^2 s^{-1} which is estimated from self-diffusion in liquid Fe at high pressure [*Dobson*, 2002]. The diffusion coefficient in molten silicate is chosen to be $D_o = 10^{-9}$ m^2 s^{-1}, imposing a diffusion ratio of 10. Using parameters above results in Pe, Re, and $\mathcal{R}_\mu$ of 3×10^6, 1000, and 1, respectively. Hence, the regime is that of a drop in a high Re fluid. In this case equilibration should be attained in 4 minutes with a traveled distance around 126 m. This distance is certainly shorter than the depth of a magma ocean that could be generated from an impact with a Mars-sized object [*Tonks and Melosh*, 1992]. Our predictions are of the same order of magnitude as the results obtained by *Rubie et al.* [2003] considering the uncertainties on the parameters. However, our theory takes into account the flow within the drop and effect of high Re, and thus proposes an intrinsically faster time of equilibration and shorter distance than *Rubie et al.* [2003].

[33] Further applications can be made (crystal settling in granitoids or ignimbrites, immiscible silicate and carbonatitic melts segregation etc…) using the correct proposed predictive relationships. However, we have made 3 main assumptions that have to be considered as limitations:

[34] 1. First, sphericity was assumed, which is known to be matched for drops when the surface tension dominates and for low Re, and for solids having a spheroidal shape. The deformation of diapirs and drops by viscous stresses along the boundaries can lead to peculiar shapes possibly skirted and with instabilities leading to break-up. More complex calculations have to be performed to follow the shape evolution in such case.

[35] 2. A second assumption involves non-interacting bodies. In the case of the previously advocated metallic rain in magma oceans the coalescence and influence of neighboring droplets have to be taken into account [*Ichikawa et al.*, 2010].

[36] 3. Third, we assumed pure buoyancy driven flow. The settling of particles and drops can be influenced by the effect of rotation or other forces that we have not considered in the present study.

Acknowledgments

[37] This work has been supported by the Agence Nationale de la Recherche under grant ANR-08-JCJC-0084-01 (Dyn-BMO). J.V. acknowledges the support of the Grant Agency of the Czech Republic, project P210/11/1366. Numerical models where performed using the free FEM software Elmer, from CSC. This paper also benefited from LaTeX, GMT and Gnuplot magic. We thank J. Rudge and P. J. Tackley for constructive reviews.

References

Acrivos, A., and J. Goddard (1965), Asymptotic expansions for laminar forced-convection heat and mass transfer, *J. Fluid Mech.*, *23*, 273–291.

Brown, P. P., and D. Lawler (2003), Sphere drag and settling velocity revisited, *J. Environ. Eng.*, *129*, 222–231.

Carslaw, H. S., and J. C. Jaeger (1959), *Conduction of Heat in Solids*, Clarendon, Oxford, U. K.

Clift, R., J. R. Grace, and M. Weber (1978), *Bubbles, Drops, and Particles*, Academic, New York.

Dasgupta, R., M. Hirschmann, and K. Stalker (2006), Immiscible transition from carbonate-rich to silicate-rich melts in the 3 GPa melting interval of eclogite plus CO_2 and genesis of silica-undersaturated ocean island lavas, *J. Petrol.*, *47*, 647–671.

Dasgupta, R., A. Buono, G. Whelan, and D. Walker (2009), High-pressure melting relations in Fe-C-S systems: Implications for formation, evolution, and structure of metallic cores in planetary bodies, *Geochim. Cosmochim. Acta*, *73*(21), 6678–6691.

Dawson, J., and J. Hawthorne (1973), Magmatic sedimentation and carbonatitic differentiation in kimberlite sills at Benfontein, South Africa, *J. Geol. Soc. London*, *129*, 61–85.

Dobson, D. (2002), Self-diffusion in liquid Fe at high pressure, *Phys. Earth Planet. Inter.*, *130*, 271–284.

Grasset, O., and F. Albarède (1994), Hybridization of mingling magmas with different densities, *Earth Planet. Sci. Lett.*, *121*(3–4), 327–332.

Huppert, H., J. Turner, and R. Sparks (1982), Replenished magma chambers—Effects of compositional zonation and input rates, *Earth Planet. Sci. Lett.*, *57*(2), 345–357.

Ichikawa, H., S. Labrosse, and K. Kurita (2010), Direct numerical simulation of an iron rain in the magma ocean, *J. Geophys. Res.*, *115*, B01404, doi:10.1029/2009JB006427.

Kitscha, J., and G. Kocamustafaogullari (1989), Breakup criteria for fluid particles, *Int. J. Multiphase Flow*, *15*(4), 573–588.

Levich, V. (1962), *Physicochemical Hydrodynamics*, Prentice-Hall, Englewood Cliffs, N. J.

Li, J., and C. Agee (2001), The effect of pressure, temperature, oxygen fugacity and composition on partitioning of nickel and cobalt between liquid Fe-Ni-S alloy and liquid silicate: Implications for the Earth's core formation, *Geochim. Cosmochim. Acta*, *65*, 1821–1832.

Monteux, J., Y. Ricard, N. Coltice, F. Dubuffet, and M. Ulvrova (2009), A model of metal-silicate separation on growing planets, *Earth Planet. Sci. Lett.*, *287*(3–4), 353–362.

Morard, G., and T. Katsura (2010), Pressure-temperature cartography of Fe-S-Si immiscible system, *Geochim. Cosmochim. Acta*, *74*, 3659–3667.

Ranz, W., and W. Marshall (1952), Evaporation from drops. 1, *Chem. Eng. Prog.*, *48*(3), 141–146.

Ribe, N. (2007), Analytical approaches to mantle dynamics, in *Treatise on Geophysics*, edited by G. Schubert, pp. 167–226, Elsevier, Amsterdam, doi:10.1016/B978-044452748-6.00117-6.

Rubie, D., H. Melosh, J. Reid, C. Liebske, and K. Righter (2003), Mechanisms of metal-silicate equilibration in the terrestrial magma ocean, *Earth Planet. Sci. Lett.*, *205*, 239–255.

Samuel, H., and P. J. Tackley (2008), Dynamics of core formation and equilibration by negative diapirism, *Geochem. Geophys. Geosyst.*, *9*, Q06011, doi:10.1029/2007GC001896.

Stevenson, D. (1990), Fluid dynamics of core formation, in *Origin of the Earth*, edited by H. E. Newsom and J. H. Jones, pp. 231–249, Oxford Univ. Press, New York.

Stone, H. (1994), Dynamics of drop deformation and breakup in viscous fluids, *Annu. Rev. Fluid Mech.*, *26*, 65–102.

Tonks, W., and H. Melosh (1992), Core formation by giant impacts, *Icarus*, *100*(2), 326–346.

Vočadlo, L., J. Brodholt, D. Alfe, M. Gillan, and G. Price (2000), Ab initio free energy calculations on the polymorphs of iron at core conditions, *Phys. Earth Planet. Inter.*, *117*, 123–137.

Wierzba, A. (1990), Deformation and breakup of liquid-drops in a gas-stream at nearly critical Weber numbers, *Exp. Fluids*, *9*(1–2), 59–64.

1.3 Melt in the lowermost mantle

1.3.1 Core mantle boundary (CMB) region

The interface between the core and the mantle is the most important boundary inside the Earth with large density contrasts across it. A detailed picture of the core mantle region, that is probably as complex as the shallow parts of the Earth (the crust and lithosphere), has been gathered in large part by seismology.

Seismic tomography is a technique that reveals 3D images of the Earth's present state. It uses travel times of seismic waves propagating through the Earth to reconstruct its structure. Wave velocities depend on the thermal and chemical properties of the material they are passing through. A seismic wave propagates slower through hot regions while it travels faster through cold areas at the same depth.

At the base of the mantle two large provinces with reduced shear wave velocities have been detected, one under the Pacific and one under south Africa continent (e.g. Ritsema et al., 1999; Romanowicz, 2003; Ritsema et al., 2004). Whereas under the central America lies an area where waves travel faster. As the seismic wave velocity increase with decreasing temperature, correlation between this anomaly and arriving cold slab has been made. Large low velocity seismic anomalies can not be simply associated only with thermal variations alone and it is necessary to consider chemical effects. Mantle models with heterogeneous composition associated these structures to thermochemical piles with high density (e.g. Kellogg et al., 1999; Davaille, 1999a; Jellinek and Manga, 2002; Tackley, 2002; McNamara and Zhong, 2005). Due to the increased density these patches persist to be entrained by mantle convective currents and stay at the bottom of the CMB. Gravitational stability and elevated temperatures favor that these regions give rise to the origin of plume clusters.

A seismic discontinuity has been observed in the lowermost mantle. Similar discontinuities are also detected in the upper parts of the mantle and are attributed to the solid-solid phase transitions. Solid-solid phase change has been thus debated to explain the seismic observations deep in the mantle. It was not until recently, that this hypothesis has been verified and a new phase change transition has been indeed discovered under the extreme pressure and temperature conditions at the CMB (pressures around 125 GPa and temperatures above 2500 K). Experimental work of Murakami et al. (2004) and *ab-initio* calculations by Oganov and Ono (2004) show that the structure of $MgSiO_3$ perovskite, the most abundant mineral in the lower mantle, transforms to a high pressure form, post-perovskite. The transition is accompanied by a slight increase in density of 1.0 to 1.2% and has been associated to an upper limit of D" layer. Since the discovery of the new mineral phase, many studies have been initiated to explain the bottom mantle observations, cf. e.g. Hernlund et al. (2005); Hernlund and Labrosse (2007); Lay et al. (2006) and a review study by Tackley (2012).

The fine structure of the core mantle boundary has been further constrained by seismology that detected small regions of very reduced seismic wave velocities, the so called ultra low velocity zones (ULVZ). These are described in detail in the next section.

The resulting picture of the core mantle boundary of the present-day Earth is given by a schematic cartoon in Figure 1.6.

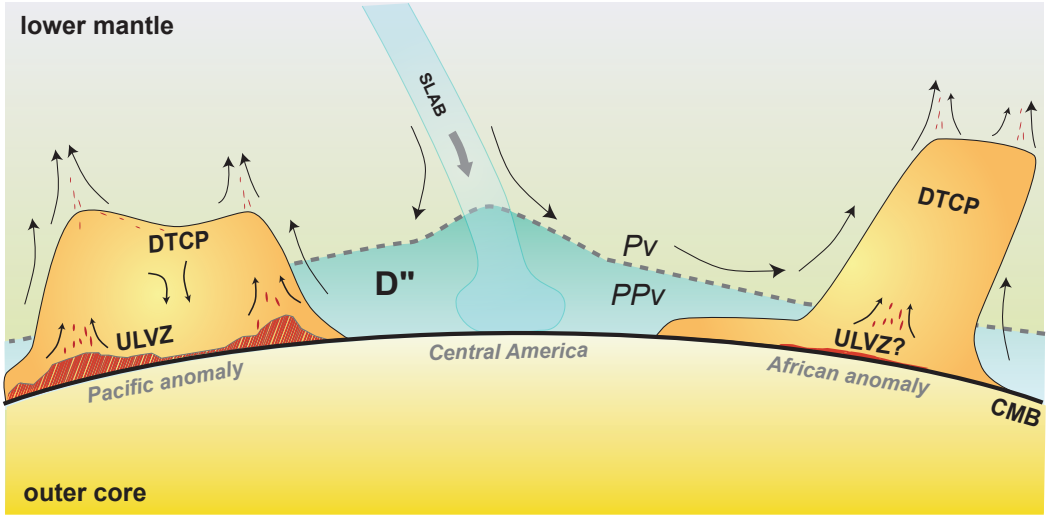

Figure 1.6: A sketch of the lowermost mantle structure. Dense thermochemical piles (DTCP) are associated with low-velocity seismic anomalies beneath Africa and the Pacific Ocean. Cold descending slab reaching the bottom mantle has been correlated with fast velocity seismic anomaly beneath central America. Phase transition between perovskite (Pv) and post-perovskite (PPv) is depicted by a shadow dashed line and it limits the upper extent of the D" layer. Finally, zones with ultra low seismic wave velocities (ultra low velocity zones, ULVZ) are depicted. Picture taken from Garnero et al. (2007).

1.3.2 Ultra Low Velocity Zones (ULVZ): possible insight into the past

Regions with ultra low wave velocities at the core mantle boundary have been discovered by seismology (Mori and Helmberger, 1995; Garnero and Helmberger, 1996). Estimates of ULVZ thickness are of the order of 5-40 km. The vertical limit for the zone to be detectable seismologically is 3-5 km. Horizontally, the extent is estimated to be of the order of 100 km. A significant reduction of compressional (P) and shear (S) wave velocities has been observed (10% for P wave and up to 30% for S wave), being thus the largest seismic anomaly in the mantle. The absolute change in P and S wave velocities is about a factor of two and five, respectively, greater than that observed near major mantle discontinuities (i.e. solid-solid phase transitions at 440 and 660 km in the upper mantle and perovskite post-perovskite in the deepest mantle). Because the reduction of S wave velocity is more pronounced than that of P wave, it has been suggested that ULVZ results from partial melting (e.g Williams and Garnero, 1996).

Since the original discovery of ULVZs (Garnero and Helmberger, 1996; Wen and Helmberger, 1998; Garnero et al., 1998; Garnero and Vidale, 1999) many studies have been devoted to explore their exact positions as well as their characteristics. A very heterogeneous distribution has been observed (Figure 1.7). Moreover, these seismic anomalies are extremely localized (e.g. Russell et al., 1998; Rost et al., 2005) and it has been suggested that they are preferentially found at the edges of large compositional piles (McNamara et al., 2010) introduced in the previous section.

In order to be gravitationally stable on the lifetime of the Earth, the molten zones must be dense enough. Numerous numerical and experimental studies were devoted to determine the necessary density

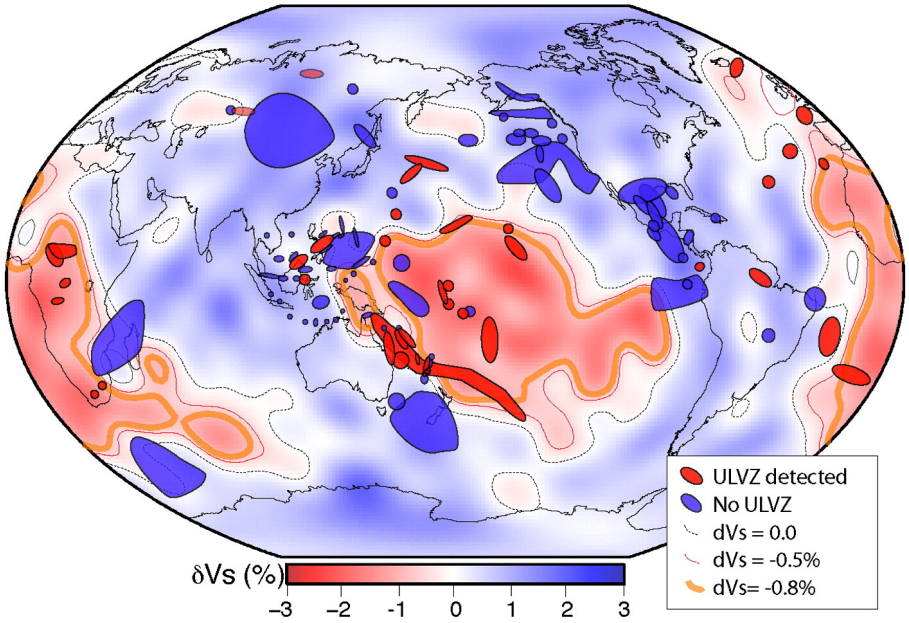

Figure 1.7: Distribution of ultra low velocity zones (ULVZ) at the CMB from a number of available seismic studies (compilation done by McNamara et al. (2010)). Saturated blue corresponds to places where no ULVZs were detected. Saturated red patches correspond to regions with detected ULVZs. Note the heterogeneous ULVZs distribution. Background colors represent seismic shear velocity anomalies at the lowermost mantle from the seismic tomography model by Ritsema et al. (2004). Picture from McNamara et al. (2010).

difference between the partial melt and the density of the lowermost mantle $\delta\rho_{\mathrm{ULVZ}}$ and the rate of entrainment (e.g Davaille, 1999b; Zhong and Hager, 2003). It seems that the chemical density contrast of around 2% is needed for the layer to be stable through time (cf. Tackley (2012) for a review). This result can slightly decrease if the dense zone has a much lower viscosity (Tackley, 1998). Seismologically, a much higher $\delta\rho_{\mathrm{ULVZ}}$, around 10%, has been estimated (Rost et al., 2005). Recently, partitioning of iron between the solid and the liquid silicates has been measured over the entire mantle pressure range using laser-heated diamond-anvil cell (Nomura et al., 2011). A sharp change in the partitioning behaviour has been observed and associated with a spin crossover of iron (from high-spin to low-spin) in the silicate melt (Figure 1.8 (left)). At pressures greater than ~ 76 GPa (corresponding to a depth around 1800 km), heavy element iron enters more easily into melt. As a result, Nomura et al. (2011) deduce that the melt becomes more dense than solids due to higher iron content (Figure 1.8 (right)). Hence, the liquid forming above a depth of ~ 1800 km is lighter than the background solid and rises upward whereas below this limit, forming melt is iron rich and sinks downward. This is consistent with seismological observations detailed above. Iron enrichment in the lowermost mantle is also supported by measurements of the sound velocities of (Mg,Fe)O by x-ray scattering. Wicks et al. (2010) showed that only a small amount of iron-rich (Mg,Fe)O can reduce the average sound velocity, implying that this oxide can be a candidate for a chemically distinct ULVZ at the core mantle boundary.

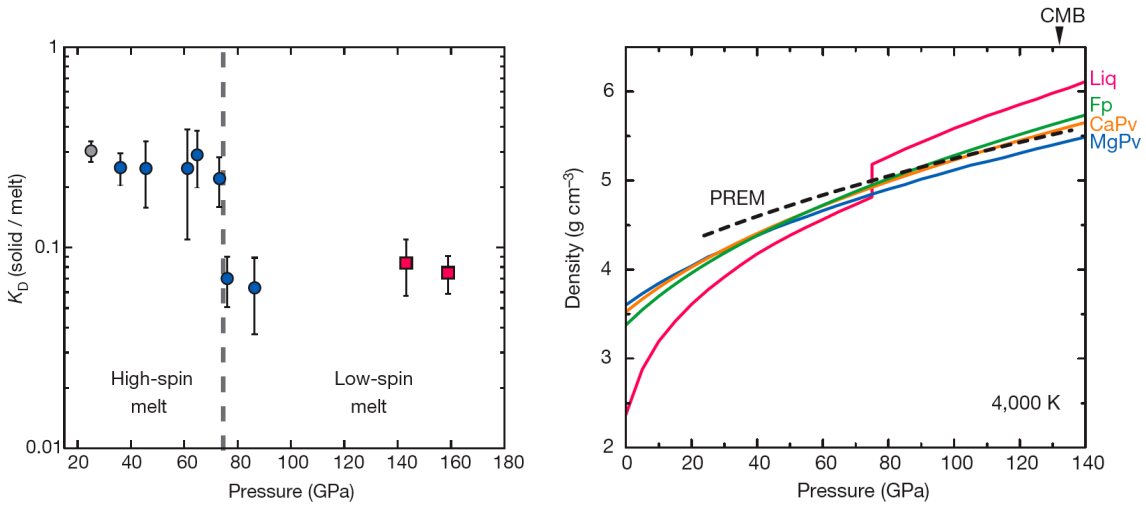

Figure 1.8: (left) Partition coefficient K_D between perovskite (blue circles) or post-perovskite (red squares) and melt. K_D changes abruptly at pressure around 76 GPa (the limit denoted by a dashed vertical line, corresponds to a depth around 1800 km). This change is associated with the spin crossover of iron in silicates. (right) The density of the liquid (red solid line) calculated for 4000 K using the new partitioning data. Density profile of the mean mantle is represented by PREM model (Dziewonski and Anderson, 1981) shown in dashed line. The liquid at great depth has a higher density than solid. Pictures taken from Nomura et al. (2011).

1.3.3 Model of a long term evolution of the deep mantle

Above we described the present state of the deep interior of the Earth mainly based on seismic observations and supported by experimental work. In order to test the feasibility of a scenario to explain the present observations, one needs a realistic evolutionary model to get the Earth to the present state. In this effort the Earth has to be considered in its totality since individual reservoirs form a system that is not independent. Strong coupling between rheologically distinct parts exists. Indeed, the heat flux evacuated from the core is limited by what can be accepted by the mantle and thus the mantle controls core cooling. Records of existing geomagnetic field during at least the last 3 Gy indicate efficient heat escape from the core since convection in the core is ultimately needed for the geodynamo to run (Labrosse, 2003). The temperature of the core mantle boundary is thus increasing when going back in time and thus more important melting is expected to be present in the past. Recently, the existence of a basal magma ocean (BMO) was proposed (Labrosse et al., 2007). In this scenario the mantle starts from a largely molten state and crystallization begins from the middle, forming thus two magma oceans, one at the surface and one buried deep in the Earth's interior. Due to radiation to space, a very efficient way of heat loss, the shallow magma layer crystallizes rapidly (e.g. Abe, 1997). On the other hand, the cooling of the BMO is limited by heat transfer through the solid mantle and so its decay time is of order 1 Gy. This means that extensive melting has been present in the deep mantle throughout its whole history whose remnants are nowadays observable as pockets of partial melt, the ULVZs, discussed before. The slow fractional crystallization would then determine the composition and thermal evolution of the planet. Schematically,

the model is depicted in Figure 1.9.

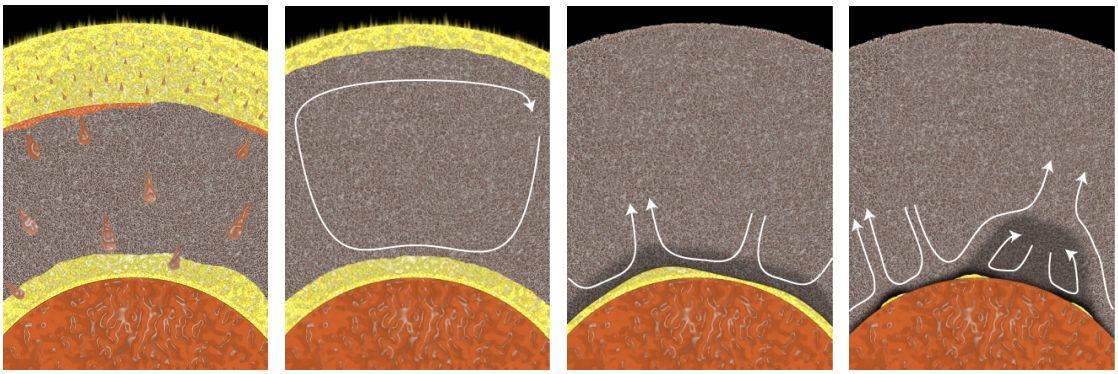

Figure 1.9: A schematic model of the Earth evolution depicting four different stages during the Earth's history (on the left and the right hand sides are the most ancient and the present state, respectively). (left) The early Earth mantle (grey) is supposed to be totally or at least extensively molten resulting in the presence of two magma oceans (yellow): the shallow magma ocean at the surface and the basal magma ocean (BMO) buried deep in the interior. (middle left) As cooling proceeds, the upper liquid layer crystallizes much faster than the melt enveloping the core (orange) due to efficient heat radiation to the space. A large scale convection sets up in the solid mantle (depicted by the white arrow). (middle right) Slow fractional crystallization of the deep liquid layer results in the lower mantle that is enriched in iron (depicted by dark grey). (right) Solidification of the BMO proceeds and the lower mantle is more and more enriched in iron with time and becomes gravitationally stable forming distinctive patches of dense material that resist entrainment by convection in the mantle. A scenario proposed by Labrosse et al. (2007).

Alternatively, other processes have been suggested to explain the observations at the CMB. In particular, the presence of dense piles can be attributed to the segregation of subducted mid-ocean rich basalt (MORB) (Christensen and Hofmann, 1994; Coltice and Ricard, 1999; Nakagawa and Tackley, 2010). Many studies have been devoted to explore this scenario (cf. Tackley (2012) for a review) and it is still not clear whether the oceanic crust, that would have accumulated at the base of the mantle since the plate tectonics has been active, can match the observed density and compositional constrains. Also, they could melt and join the ULVZs.

1.3.4 Deep differentiation and fractionation processes narrated by geochemistry

Previously, we discussed mainly geodynamical side of the presence of the BMO and compatibility of the model with experimental results and seismic observations. In this part we focus on compositional aspects of the BMO and the solid mantle. A distribution of the chemical elements will be largely affected by a slow fractional crystallization of the initially thick liquid layer lying above the core.

Viscosity estimations of the molten deep magma ocean at high pressure and high temperature conditions have been given using first-principles molecular dynamics calculations by Karki and Stixrude (2010). These are very low and do not exceed 0.1 Pa s (to comparison, viscosity of the outer core is assumed to be of the order of 10^{-3} Pa s, similar to that of water). Further, as was discussed earlier, due to high content in iron, a high density is presumed for the melt. The result is that the BMO resists entrainment by large scale convective currents in the mantle and thus remains unsampled. Yet, its chemical signatures can be seen through the dense piles forming by accumulation of solid crystals that are dense enough to be gravitationally stable (having the density difference about 2% compared to the background solid mantle).

So far, these systems recording the BMO crystallization have been addressed: concentrations of incompatible elements and rare gas isotopic systems of helium and neon (He and Ne) (Labrosse et al., 2007; Coltice et al., 2011). Here, we summarize their most important findings.

Taking a chemical composition of the continental crust that is enriched in incompatible elements, one can compute the volume of the mantle that must be depleted to balance for the crust's incompatible element enrichment (taking chondrites as a reference). It turns out, that about 20-30% of the mantle is estimated to be depleted, leaving thus the rest for a 'hidden reservoir' occupying the lowermost mantle (Hofmann, 1997). The BMO was suggested to represent this hidden unsampled mantle (Labrosse et al., 2007).

Using the BMO scenario, Labrosse et al. (2007) computed the present-day composition of the melt that has resulted by fractional crystallization from initially 850 km thick melt layer. They show that the remaining melt is slightly enriched in incompatible elements compared to the continental crust. Applying the mass balance for the resident melt and the crust, they then predict a composition of the remaining solid mantle that is consistent with estimations for the shallow mantle composition.

Presence of a hidden unsampled layer is also supported by noble gases concentrations measured in the ocean island basalts (OIB) in hotspots. In particular, a high $^3He/^4He$ isotopic ratio has been observed in many OIBs. ^3He is a stable isotope that is easily degassed into the atmosphere at the surface of the Earth. Thus, high $^3He/^4He$ ratio indicates the source provenance from deep primordial regions that are not degassed. Coltice et al. (2011) show that the concentrations of helium recorded in OIBs can be a signal sampling the stable chemical piles (formed by crystallization of the BMO) in case that the solid-melt partition coefficients of He are high enough (higher than 0.01).

1.4 Conclusions

Many theoretical and numerical models have been developed in order to determine the thermal and chemical history of the Earth and other planetary bodies. Abundances of chemical elements are observations that need to be understand by these models and that provide an insight into the formation and subsequent evolution of these bodies. In particular, a depletion of measured concentrations of siderophile elements in the Earth's mantle can be explained by efficient equilibration between iron and silicates at high pressure

and temperature conditions during core formation event. We further explore the equilibration process that occurred between a single falling metal droplet and background liquid in order to quantifies characteristic timescales of equilibration for which we propose scaling laws. Derived parametrized equations depends on the dynamic regime of the flow outside drop as well as inner circulation. We show that the equilibration was very efficient and thus the drops are in permanent equilibrium with surroundings.

Present day structure of the Earth reveals deep melting at the core mantle boundary. More extensive melting has been necessarily presented in the early days of the planet and we reviewed several sources of heat acting at that time. The existence of a deep molten layer, called a basal magma ocean (BMO), was proposed. The BMO is crystallizing over a long time (order Gy) and is highly convecting.

Questions that are addressed in our work refer to the thermal evolution of the BMO. What is the coupling between the Earth's mantle and the core when a convecting liquid layer is found in between? What is the dynamics of the solidification of a melt layer coupled with convective flow?

Chapter 2

Thermal convection and solid/liquid phase change

More than a century ago, Bénard (1900a,b) performed one of the first quantitative studies of convective transport. His work later initiated exploring, theoretically as well as experimentally, the process of convection. Bénard (1900a,b) heated a thin liquid layer with a thickness of the order of a millimeter and with a free upper surface. He observed the formation of stable regulars cells, now called Bénard cells, with polygonal shapes, predominantly hexagonal, cf. Figure 2.1. Initially it was thought that these instabilities were buoyancy driven. Purely thermally driven flow has been examined theoretically by Rayleigh (1916) who was excited by the Bénard regular hexagonal cells and genuinely interested in explaining his results. Rayleigh (1916) investigated a fluid layer subjected to an unstable vertical temperature gradient, i.e. imposing a bottom temperature superior to the top temperature. He determined a critical temperature difference across the liquid necessary for the convective motion to start. Using a stability analysis, Rayleigh (1916) also obtained a critical wavelength of convective cells. He, however, noticed that his theory did not match quantitatively the results of Bénard.

It was not until the second half of the 20^{th} century that Bénard's (1900a,b) observations have been explained in the works of Block (1956), Pearson (1958) and Nield (1964). The convective motion in a layer with free surface was caused by the thermally induced surface tension gradients (the Marangoni effect).

Convection occurring in a horizontal layer heated from below is now called Rayleigh-Bénard convection and in this chapter we present its governing equations and recall its different aspects relevant to the system under study, the basal magma ocean (BMO).

Our ultimate goal is to investigate thermal convection coupled with the solid-liquid phase transformation. Solidification was first studied by Stefan, when exploring the formation of ice in the polar seas. Stefan (1891) gives a mathematical description of the freezing problem and compares his model with experimental data. The task includes the determination of the phase change front position at each time. Nowadays, problems with free or moving boundary problems are called Stefan problems. However,

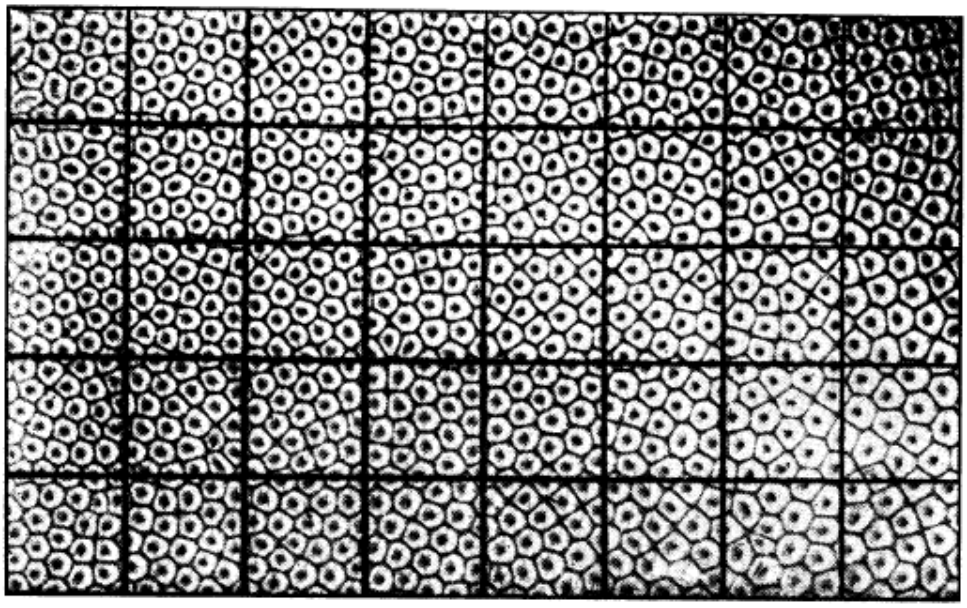

Figure 2.1: Stabilized regular polygonal convective patterns observed by Bénard (1900a). Thin liquid layer (thickess of the order of milimeter) is heated from below with free upper surface. A network of squares with surface $1\,\mathrm{cm}^2$ is plotted in the image.

we note also that a similar problem had been already treated previously by Lamé and Clapeyron (1831) and the mathematical solution given by Stefan (1891) had been already discovered by Neumann several decades earlier.

The process of solidification and melting is described later in this chapter. We present the governing equations and further focus on the coupled problem of phase change with convective motion.

2.1 Physical model for Rayleigh-Bénard convection

2.1.1 General governing equations

The dynamics of the fluid is described by the basic set of conservation equations (e.g. Landau and Lifshitz, 1959) that are recalled here.

Conservation of mass is expressed by

$$\frac{\mathrm{D}\rho}{\mathrm{D}t} + \rho \boldsymbol{\nabla} \cdot \boldsymbol{v} = 0\,, \tag{2.1}$$

where ρ is the density, t is the time and $\boldsymbol{v}$ is the velocity. The symbol $\mathrm{D}\bullet/\mathrm{D}t$ represents total derivation. Its definition depends on the chosen reference frame. Adapting the Euler perspective where the observer

is standing at a fixed point from which a moving particle is seen, we obtain

$$\frac{\mathrm{D}}{\mathrm{D}t}\bullet = \frac{\partial}{\partial t}\bullet + \boldsymbol{v}\boldsymbol{\nabla}\bullet \,. \tag{2.2}$$

Lagrangian specification is a way of looking at fluid motion where an observer is riding on the particle. In this case, the rate of change seen by an observer is simply

$$\frac{\mathrm{D}}{\mathrm{D}t}\bullet = \frac{\mathrm{d}}{\mathrm{d}t}\bullet \,. \tag{2.3}$$

Momentum conservation reads as

$$\rho\frac{\mathrm{D}\boldsymbol{v}}{\mathrm{D}t} = -\boldsymbol{\nabla}P + \boldsymbol{\nabla}\cdot\boldsymbol{\tau} + \rho\boldsymbol{g}\,, \tag{2.4}$$

with $\boldsymbol{g}$ the gravitational acceleration, $\boldsymbol{\tau}$ the deviatoric stress tensor that depends on velocity and P the thermodynamic pressure.

Conservation of energy is

$$\rho C_\mathrm{P}\frac{\mathrm{D}T}{\mathrm{D}t} = -\boldsymbol{\nabla}\cdot(k\boldsymbol{\nabla}T) + \alpha T\frac{\mathrm{D}P}{\mathrm{D}t} + \boldsymbol{\tau}:\boldsymbol{\nabla}\boldsymbol{v} + \rho\mathcal{H}\,, \tag{2.5}$$

where T is the temperature, C_P is the heat capacity at constant pressure, k is the thermal conductivity, α is the coefficient of thermal expansion and $\mathcal{H}$ is the heat production per unit mass, owing to radioactive decay.

2.1.2 Approximations and nondimensionalization

First, we assume the incompressibility of the flow, i.e. the density is constant when following a fluid parcel, i.e. $\mathrm{D}\rho/\mathrm{D}t = 0$, and thus Eq. (2.1) can be simplified to

$$\boldsymbol{\nabla}\cdot\boldsymbol{v} = 0\,, \tag{2.6}$$

known as the continuity equation.

Considering a Newtonian viscous rheology for incompressible flow

$$\boldsymbol{\tau} = \eta\left(\boldsymbol{\nabla}\boldsymbol{v} + (\boldsymbol{\nabla}\boldsymbol{v})^T\right)\,, \tag{2.7}$$

where $(\cdot)^T$ is a tensor transposition, Eq. (2.4) turns to

$$\rho\frac{\mathrm{D}\boldsymbol{v}}{\mathrm{D}t} = -\boldsymbol{\nabla}P + \boldsymbol{\nabla}\cdot\left(\eta\left(\boldsymbol{\nabla}\boldsymbol{v} + (\boldsymbol{\nabla}\boldsymbol{v})^\mathrm{T}\right)\right) + \boldsymbol{g}\rho\,, \tag{2.8}$$

known as the Navier-Stokes equation.

In order to solve Eq. (2.8) we need an equation of state (EoS). We assume that the density varies linearly with temperature T, i.e.

$$\rho = \rho_0\left(1 - \alpha(T - T_\mathrm{c})\right)\,, \tag{2.9}$$

Variable	Scaling	
Length	L	Thickness of the system under study
Time	L^2/κ_L	Conduction time over the thickness L
Velocity	κ_L/L	Velocity over diffusive time
Pressure	$P_0 = \kappa_\mathrm{L}\eta_\mathrm{L}/L^2$	Reference pressure
Temperature	$\frac{T-T_\mathrm{c}}{T_\mathrm{h}-T_\mathrm{c}}$	Superisentropic temperature difference across L

Table 2.1: Scaling parameters of different variables.

where T_c is a reference temperature at which the density is ρ_0. In our case the reference temperature is the temperature of the cold wall. Effects of pressure and composition are neglected in this EoS.

Considering that pressure P consists of dynamic pressure p and hydrostatic pressure P_H, i.e. $P = p + P_\mathrm{H}$, using the equation for hydrostatic equilibrium $\boldsymbol{\nabla} P_\mathrm{H} = g\rho_0$, using Eq. (2.9) and considering the Boussinesq approximation, i.e. we neglect the density variations except in the body force therm (e.g. Ricard, 2007), we can rewrite Eq. (2.8)

$$\rho_0 \frac{\mathrm{D}\boldsymbol{v}}{\mathrm{D}t} = -\boldsymbol{\nabla} p + \boldsymbol{\nabla} \cdot \left(\eta \left(\boldsymbol{\nabla}\boldsymbol{v} + (\boldsymbol{\nabla}\boldsymbol{v})^\mathrm{T}\right)\right) - \rho_0 \alpha (T - T_\mathrm{c})\boldsymbol{g}\,. \tag{2.10}$$

Heating due to decompression/compression (the term $\alpha T \frac{\mathrm{D}P}{\mathrm{D}t}$) and viscous heating (the term $\tau : \boldsymbol{\nabla}\boldsymbol{v}$) are neglected in Eq.(2.5) since we consider incompressibility of the flow and Boussinesq approximation, respectively (e.g. Ricard, 2007). In addition, internal heating due to the presence of radioactive elements is also neglected. Assuming the thermal conductivity to be constant, the energy conservation equation has a form

$$\frac{\mathrm{D}T}{\mathrm{D}t} = \kappa \nabla^2 T\,, \tag{2.11}$$

where the thermal diffusivity κ has been introduced

$$\kappa = \frac{k}{\rho_0 C_\mathrm{P}}\,. \tag{2.12}$$

In fluid dynamics we want to determine parameters controlling the system and their functional relations (e.g. Landau and Lifshitz, 1959; Batchelor, 1967; Ribe, 2007). We thus proceed here with the dimensional analysis and transform the governing equations into a dimensionless system.

A suitable transformation is employed. Several choices of scaling parameters can be found in the literature and we use the following transformations for the length $\boldsymbol{\nabla} = \boldsymbol{\nabla}^*/L$, the time $t = h^2/\kappa_\mathrm{L}\, t^*$, the temperature $T = (T_\mathrm{h} - T_\mathrm{c})\, T^* + T_\mathrm{c}$, the velocity $v = \kappa_\mathrm{L}/L v^*$, the pressure $p = P_0\, p^* = \kappa\eta_\mathrm{L}/L^2\, p^*$ with P_0 the reference pressure, and the viscosity $\eta = \eta_\mathrm{L}\, \eta^*$ with η_L the viscosity of liquid. Dimensionless temperature and length are thus bounded between 1 and 0 in the computational domain. Star denotes a variable without physical thickness and we drop it immediately for the sake of simplicity. All scaling parameters are given in Tab. 2.1.

Conservation equations, Eqs. (2.6), (2.10) and (2.11), in dimensionless form are

$$\boldsymbol{\nabla}\cdot\boldsymbol{v} = 0\,, \tag{2.13}$$

$$\frac{1}{\mathrm{Pr}}\frac{\mathrm{D}\boldsymbol{v}}{\mathrm{D}t} = -\boldsymbol{\nabla}p+\boldsymbol{\nabla}\cdot\left(\eta\left(\boldsymbol{\nabla}\boldsymbol{v}+(\boldsymbol{\nabla}\boldsymbol{v})^{\mathrm{T}}\right)\right)+\mathrm{Ra}\,T\boldsymbol{e}_{\mathrm{z}}\,, \tag{2.14}$$

$$\frac{\mathrm{D}T}{\mathrm{D}t} = \nabla^2 T\,. \tag{2.15}$$

Two dimensionless numbers were introduced, the Prandtl number Pr that relates the fluid viscosity to the thermal diffusivity

$$\mathrm{Pr}=\frac{\eta_{\mathrm{L}}}{\rho_0\kappa_{\mathrm{L}}}\,, \tag{2.16}$$

and the Rayleigh number Ra that compares the driving mechanisms (buoyancy) to dissipative processes (dissipation of heat and momentum)

$$\mathrm{Ra}=\frac{\mathrm{g}\alpha\mathrm{L}^3\rho_0(\mathrm{T_h}-\mathrm{T_c})}{\kappa_{\mathrm{L}}\eta_{\mathrm{L}}}\,. \tag{2.17}$$

A value of the Prandtl number (for a given fluid) is based only on its physical properties. Rayleigh number on the other hand depends on the parameters of the system like its thickness.

Typical values of Rayleigh and Prandtl numbers for the Earth's core, the mantle and the BMO are given in Table 2.2. Parameters of these systems are listed in Table 2.3. As there is a large uncertainty on the BMO parameters, large intervals are given for the nondimensional numbers. Moreover, Ra is very sensitive to the physical dimension of the system, that, for the BMO, must have varied for more than two orders of magnitude from 1000 km to roughly 10 km. Estimations of Ra are depicted in Figure 2.2 as a function of most uncertain parameters, the viscosity and superisentropic temperature difference maintained across the BMO.

		Mantle	BMO	Core
Rayleigh number	Ra	$4\cdot10^7$	$10^{15}-10^{25}$	$10^{27\,\dagger}$
Prandtl number	Pr	$3\cdot10^{23}$	$1-10^3$	10^{-2}

Table 2.2: Nondimensional numbers for the mantle, the BMO and the core (for the BMO values see also Figure 2.2). † In order to give the Rayleigh number of the core, nonadiabatic temperature difference 1 K was used (Ricard, 2007), that is highly uncertain and still unknown parameter. Thus, please note, that this value is only a raugh estimate.

Parameter	Notation	Mantle	BMO	Outer core	Units
Density	ρ_0	4000	5500	11000	$\mathrm{kg\,m^{-3}}$
Viscosity	η_0	10^{21}	$10^{-2}-10$	10^{-3}	Pa s
Size	L	2890	$10-1000$	2260	km
Gravity	g	10	10	5	$\mathrm{m\,s^{-2}}$

Table 2.3: Parameters of the system

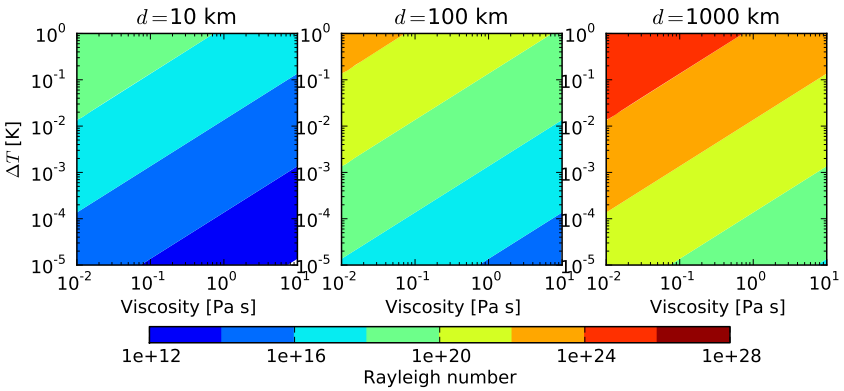

Figure 2.2: Rayleigh number of the BMO as a function of the viscosity and superisentropic temperature jump maintained across the system for three different BMO thicknesses.

2.2 Isoviscous Rayleigh-Bénard convection

The state of a liquid horizontal layer with constant properties subjected to a given vertical unstable temperature gradient is fully determined by two nondimensional parameters, the Rayleigh number Ra and the Prandtl number Pr. If the Rayleigh number of the fluid is lower than a certain critical value (denoted $\mathrm{Ra_c}$), no movement develops and the heat transfer proceeds by conduction. The velocity stays null everywhere and a linear temperature profile is established in the system.

$\mathrm{Ra_c}$ is independent of Pr and is different for different boundary conditions imposed (e.g Chandrasekhar, 1961). If the top and bottom boundaries are no-slip surfaces (velocity vanishes at the limits) $\mathrm{Ra_c} = 1708$. For mixed boundary conditions (one boundary is rigid, one free) $\mathrm{Ra_c} = 1101$. With both boundaries free-slip (zero shear stress at the limits) $\mathrm{Ra_c} = 657$.

Once Ra exceeds $\mathrm{Ra_c}$, convection develops. At moderate Ra stable convective patterns are established and variables such as temperature and velocity reach a steady state. Increasing Ra leads to the formation of instabilities and the flow starts to be time dependent. Temperature and velocity fields fluctuate around mean values reaching a statistically steady states. And thus, Ra is a measure of convective vigour of the flow.

Pr compares viscous and heat dissipations. The relative size of mechanical and thermal boundary layers is controlled by the magnitude of the Prandtl number. The thickness of the thermal boundary layer is set by the Rayleigh number and then the thickness of the mechanical boundary layer is set relative to that as a function of Pr. The smaller Pr, the thinner the mechanical boundary layer. A particular case occurs for very large Pr. If the Prandtl number is large, the inertia term on the left hand side of Eq.(2.14) can be omitted. Neglecting the inertia force implies that if the driving force is switched off, the system would stop immediately to move. This can be considered for the Earth's mantle convection - as

an example we can take an abrupt change in motion in the Pacific where the Hawaiian chain of islands gives us a possible insight into the structure of the mantle flow. But it is more questionable for the BMO as Pr lies somewhere between 1 and 1000 for the BMO (depending on the ill constrained viscosity parameter), cf. Table 2.2.

Systematically, the (Ra,Pr) parameter space has been investigated in laboratory experiments by Krishnamurti (1970a), cf. Fig. 2.3. Krishnamurti (1970a) reported that changes between different convective modes happen at the same Ra for Pr > 100. However, one must not forget that these results are dependent on the boundary conditions employed (no-slip in case of Krishnamurti (1970a) experiments) and might change with the size of the convecting system.

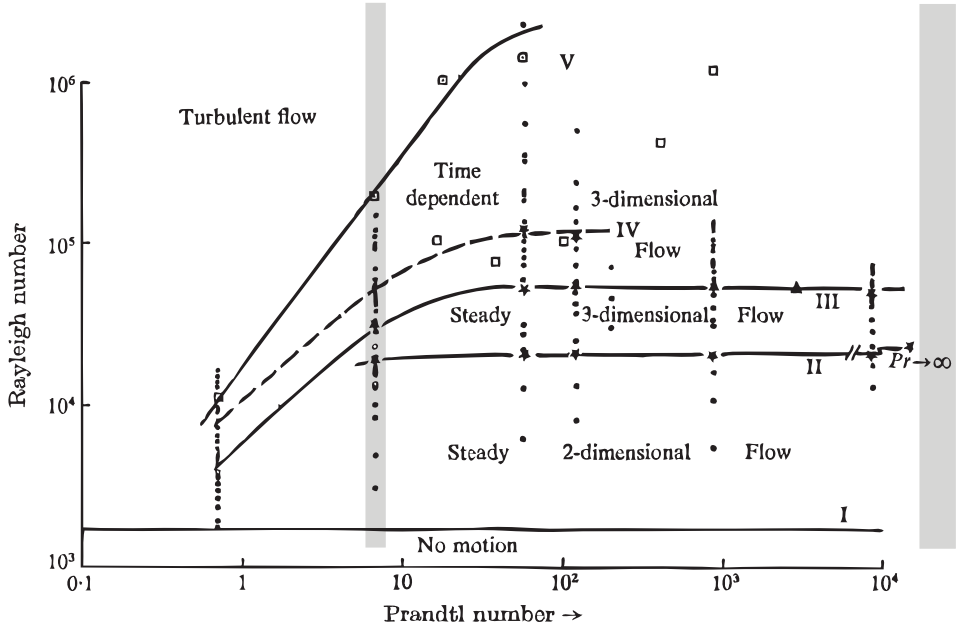

Figure 2.3: Different types of convection as a function of the Rayleigh and Prandtl numbers. Shaded areas represent domains of our study (Pr = 7 and Pr = ∞). After Krishnamurti (1970b).

In order to ascertain the transfer of heat through planetary mantles, the relationship between the Nusselt number (dimensionless heat flux density) and the Rayleigh and Prandtl numbers must be determined. Thus, finding a functional relationship Nu = Nu(Ra, Pr) have been always in the centre of attention. The Nusselt number is a nondimensional parameter describing the efficiency of heat transfer. It is defined as a ratio between the convective heat flux q (heat transported by convection and conduction) and the heat flux that would be transported by conduction alone

$$\mathrm{Nu} = \frac{\mathrm{q}}{\frac{\mathrm{k}(\mathrm{T_h}-\mathrm{T_c})}{\mathrm{L}}} \,. \tag{2.18}$$

Reference	Fluid	Pr	Ra explored	Scaling law
Rossby (1969)	Silicone oil	200	$4 \cdot 10^3 < \mathrm{Ra} < 3.5 \cdot 10^6$	$0.184\,\mathrm{Ra}^{0.281}$
Rossby (1969)	Water	7	$3.4 \cdot 10^4 < \mathrm{Ra} < 3 \cdot 10^6$	$0.131\,\mathrm{Ra}^{0.30}$
Rossby (1969)	Mercury	0.025	$2 \cdot 10^4 < \mathrm{Ra} < 5 \cdot 10^5$	$0.147\,\mathrm{Ra}^{0.257}$
Niemela et al. (2000)	Helium	$0.68 - 13$	$10^6 < \mathrm{Ra} < 10^{17}$	$0.124\,\mathrm{Ra}^{0.309}$
King et al. (2012)	Water/sucrose solution	$4.5 - 11$	$10^6 < \mathrm{Ra} < 10^{10}$	$0.16\,\mathrm{Ra}^{2/7}(0.16\,\mathrm{Ra}^{0.286})$

Table 2.4: Compilation of functional relations obtained experimentaly between the Nusselt (Nu) and Rayleigh (Ra) numbers.

A general relation between the Nusselt and Rayleigh numbers is usually sought in the form

$$\mathrm{Nu} = \beta_1 \mathrm{Ra}^{\beta_2}\,, \tag{2.19}$$

with two unknown coefficients β_1 and β_2. β_1 might or might not be a function of Pr. This is still unclear and debated (Grossmann and Lohse, 2000; King et al., 2012). For large enough Pr (roughly larger than unity), the coefficient β_2 is generally close to 1/3 and does not depend on Pr. Hence, in infinite Prandtl number approximation Nu is only a function of Ra. So far, no general consensus has been established and different authors report different relations. Table 2.4 gives a summary of proposed parametrizations.

2.3 Convection with temperature dependent viscosity

The problem of convection with a temperature dependent viscosity has been extensively studied because many geophysical systems exhibit this characteristic. Temperature differences across the Earth's mantle as well as in magma chambers are large and imply large variations in viscosity. Theoretical studies (Fowler, 1985b,a; Solomatov, 1995), laboratory experiments (Nataf and Richter, 1982; White, 1988; Davaille and Jaupart, 1993), and numerical models (Christensen, 1984; Jaupart and Parsons, 1985; Moresi and Solomatov, 1995; Tackley, 1996; Solomatov and Moresi, 1997) approached this problem.

The temperature dependence of the viscosity is often considered to involve an exponential function whose general expression can be written as

$$\eta = \eta_0 e^{f(T)}\,. \tag{2.20}$$

Due to its exponential character, even small temperature variations imply large viscosity variations. The total viscosity contrast, a nondimensional parameter of the system defined as the ratio between viscosity of the cold boundary (temperature T_c) and the hot boundary (temperature T_h), is

$$\mathcal{R}_\eta = \frac{\eta(T_\mathrm{c})}{\eta(T_\mathrm{h})} = e^{f(T_\mathrm{c}) - f(T_\mathrm{h})}\,. \tag{2.21}$$

At small supercritical Rayleigh numbers and with a constant viscosity, the motion of the system is prone to have a form of two-dimensional rolls. The temperature dependence of the viscosity (or any other

physical parameter) causes a break in symmetry between the hot and the cold plate and change in the stable convective pattern is observed. As the viscosity ratio increases, hexagonal convective cells are stable marginal modes. This has been explained theoretically by Palm (1960) and observed experimentally by e.g. Richter (1978) or Oliver and Booker (1983). Although already Bénard (1900a) obtained hexagonal cells in his laboratory experiments, their origin was hidden in surface instabilities driven by the variability in surface tension. His experiments were driven from one boundary only, and are therefore non-symmetric, irrespective of the physical parameters being constant or not.

The first study that systematically explored the preferential patterns for the temperature dependent viscosity convection was done by White (1988). By imposing a controlled initial temperature conditions he forced selective patterns to be developed. These are then subjected to stability study. The resulting phase diagram is reproduced in Figure 2.4 that shows a chart of stable patterns as a function of the Rayleigh number and viscosity ratio. At all Rayleigh numbers studied and viscosity ratios higher than 40, rolls become unstable modes and are replaced by hexagonal and square patterns.

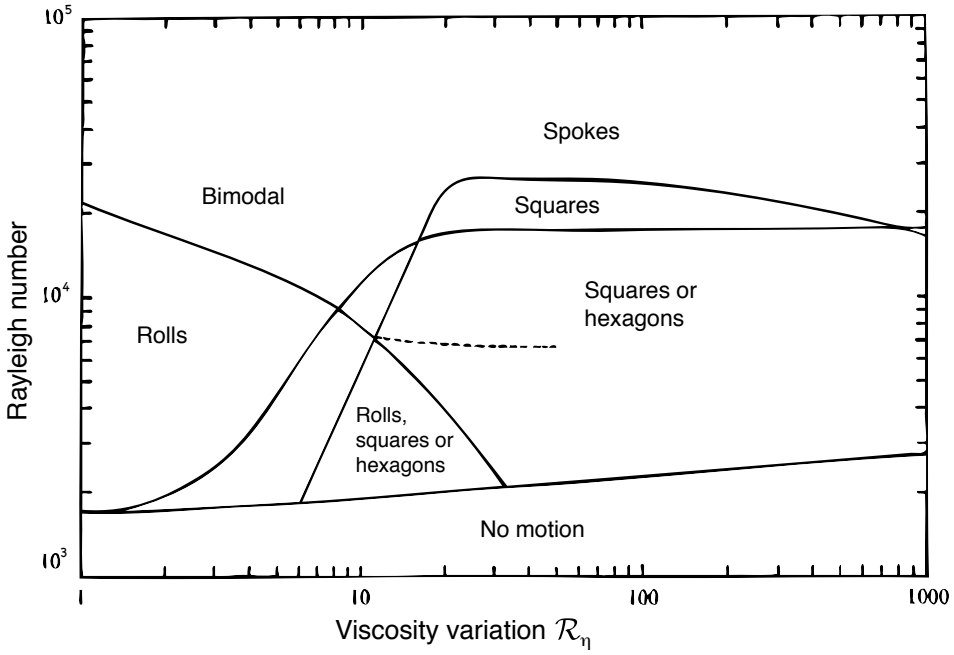

Figure 2.4: Stability of the different convective patterns as a function of the Rayleigh number and the viscosity ratio $\mathcal{R}_\eta = \eta_{\max}/\eta_{\min}$. An experimental results were obtained with a fluid with Prandtl number varying from $\sim 10^3$ to $\sim 10^7$ (White, 1988).

The thermal structure of a convecting layer with uniform physical parameters that is heated from below and cooled from above consists of an isothermic core and two symmetric boundary layers at the top and bottom. Imposing a temperature dependent viscosity results in creating a stagnant lid (in case that the viscosity ratio and the Rayleigh number are high enough, cf. e.g. Solomatov and Moresi (1997)) where upper boundary layer is not involved in the conventing motion. This can, to a certain degree, meet

characteristics of a convecting layer under a solid cap. Though in case of freezing and melting there are other physical complications like latent heat release/consumption.

2.4 Effects of rotation on convection

The Earth is spinning around its own axis with angular speed $\Omega = 2\pi\,\mathrm{rad}/1\,\mathrm{day} \sim 10^{-4}\mathrm{rad\,s^{-1}}$. This brings additional forces in the problem. In particular, one must take into consideration the Coriolis acceleration F_c (often called Coriolis force),

$$F_\mathrm{c} = 2\,\boldsymbol{\Omega} \times \boldsymbol{v}\,, \tag{2.22}$$

where Ω is the angular velocity with which a convecting system rotates. In order to estimate the importance of the Coriolis force for the Earth's systems, a comparison to the viscous force is performed. The nondimensional parameter that measures the ratio of the two forces is called the Ekman number,

$$\mathrm{Ek} = \frac{\text{viscosity}}{\text{Coriolis}} = \frac{\nu}{2\Omega \mathrm{a}^2}\,, \tag{2.23}$$

where a is the characteristic size of the system and ν the kinematic viscosity $\nu = \eta/\rho$. In the literature, one can also find the Taylor number Ta used by many authors that is equivalent to the Ekman number. The relation between these two dimensionless numbers is

$$\mathrm{Ta} = \frac{4\Omega^2 \mathrm{a}^4}{\nu^2} = \frac{1}{\mathrm{Ek}^2}\,. \tag{2.24}$$

For the Earth's mantle ($a \sim 3000\,\mathrm{km}$ and $\nu = \eta/\rho \sim 10^{21}\mathrm{Pa\,s}/4000\mathrm{kg\,m^{-3}} \sim 10^{17}\mathrm{m^2\,s^{-1}}$) we obtain $\mathrm{Ek} \sim 10^8$. Immediately we can see, that the viscous force dominates over the Coriolis force and hence the rotation effects on convection in the mantle can be ignored.

In order to make the same estimation for the BMO, we choose $a = 100\,\mathrm{km}$, $\eta = 1\,\mathrm{Pa\,s}$ and $\rho = 5500\,\mathrm{kg\,m^{-3}}$, thus taking $\nu \sim 2 \times 10^{-4}$. These parameters give us $\mathrm{Ek} \sim 10^{-10}$ for the BMO with thickness 100 km. The variation of the Ekman number with uncertain parameters, i.e. with viscosity and layer thickness, is shown in Fig. 2.5(left). $\mathrm{Ek} \ll 1$ for the BMO, this suggests that rotation might be important and the question needs further consideration.

Rotating convective systems have been studied for a long time, owing to their importance in the dynamics of oceans and atmospheres. One of the first laboratory experiments exploring Rayleigh-Bénard convection with and without rotation were done by Rossby (1969). He showed that the stability of rotating fluid is described by three nondimensional parameters, the Rayleigh number, the Taylor number and the Prandtl number and that the linear theory is insufficient to describe the fluid's state. Rossby (1969) also brings some photos of visual observations of rotating convection.

In rotating systems, fluid velocities tend to be uniform along any parallel line to the axis of rotation. This is stated by the Taylor-Proudman theorem (Chandrasekhar, 1961). Larger buoyancy forces compared to non-rotating system are required in order to perturb the flow and let the buoyancy instabilities develop.

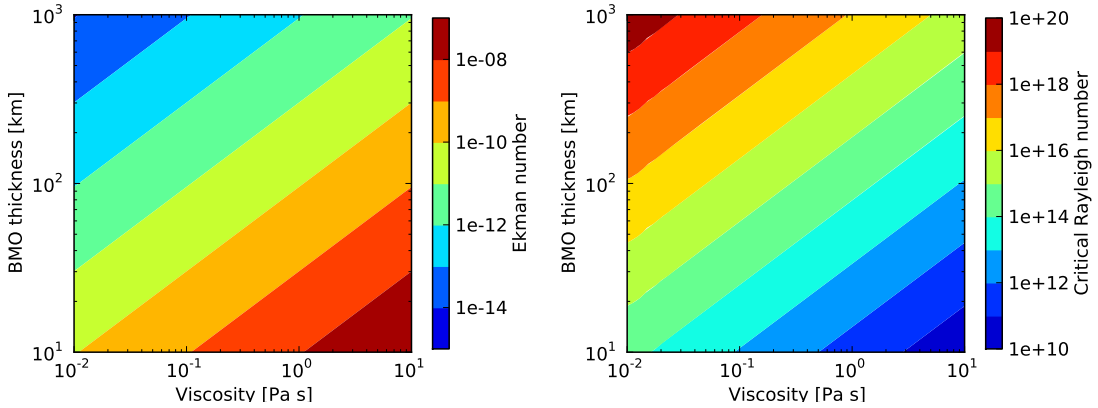

Figure 2.5: (left) Ek estimations for the BMO as a function of viscosity and magma ocean's thickness. (right) Critical Rayleigh number estimations for the BMO as a function of viscosity and magma ocean's depth

The higher the angular speed, the more difficult it is to start convecting. In other words, the critical Rayleigh number increases with the rate of rotation. Considering the asymptotic limit of rapid rotation ($\mathrm{Ta} \to \infty$), the critical Rayleigh number varies with the Taylor number as $\mathrm{Ra_c} \sim \mathrm{Ta}^{2/3}$ (Chandrasekhar, 1961). This is only a limiting case and many studies were devoted to estimate the criterion for the onset of thermal convection in rotating spherical shells depending e.g. on the Prandtl number or Taylor number and for different configurations (different boundary conditions or the presence of heat sources) (e.g. Yano, 1992; Jones et al., 2000; Dormy et al., 2004). Fig. 2.5(right) shows the estimated values of $\mathrm{Ra_c}$ using the asymptotic solution as a function of viscosity and the BMO thickness.

Once the rotating convection is set up, time dependent flows develop at a lower supercritical limit $\mathrm{Ra}/\mathrm{Ra_c}$. At Ra that are large enough, heat transfer in the turbulent rotating Bénard convection follows the classical scaling relation $\mathrm{Nu} \sim \mathrm{Ra}^{1/3}$ that is the same law as for the system with absence of rotation (e.g King et al., 2012). Here, we consider the 1/3 power law functional relationship although the precise value of the coefficient is still debated and no common consensus has been established so far as was discussed early in this chapter.

The transition between a high Ra regime where rotation effects are negligible and a regime whose dynamics is dominated by rotation occurs when the heat fluxes given by the two scaling laws (that for rotating and non-rotating systems) are approximately equal, cf. Fig. 2.6. Canuto and Dubovikov (1998) argued that this occurs at a limit Rayleigh number Ra_* for which holds $\mathrm{Ra}_* \sim \mathrm{Ta}^{3/4} = \mathrm{Ta}^{0.75}$. More recently, it has been argued that the relative thickness of rotating (Ekman) and non-rotating (thermal) boundary layers controls the effect of rotation (King et al., 2009, 2012). Comparing the two boundary layers yields for the transition between the two regimes (rotationally controlled and non-rotating) $\mathrm{Ra}_* \sim \mathrm{Ta}^{7/8} = \mathrm{Ta}^{0.875}$, that holds for $\mathrm{Ta} \geq 10^6$ and $1 \leq \mathrm{Pr} \leq 100$ (King et al., 2009).

Considering that the thickness of the BMO is 100 km results in $\mathrm{Ta} \sim 10^{20}$ for $\eta = 1\,\mathrm{Pa\,s}$ and thus we obtain $\mathrm{Ra}_* \sim 10^{18}$ using the 3/4 power law or $\mathrm{Ra}_* \sim 10^{15}$ using the 7/8 scaling (Ra_* would be higher for

larger BMO thicknesses). This might be of the same order as the BMO Rayleigh number, cf. Fig. 2.2. Thus, rotation could effect the heat transfer across the BMO at certain conditions. However, here we neglect it, for the sake of somplicity.

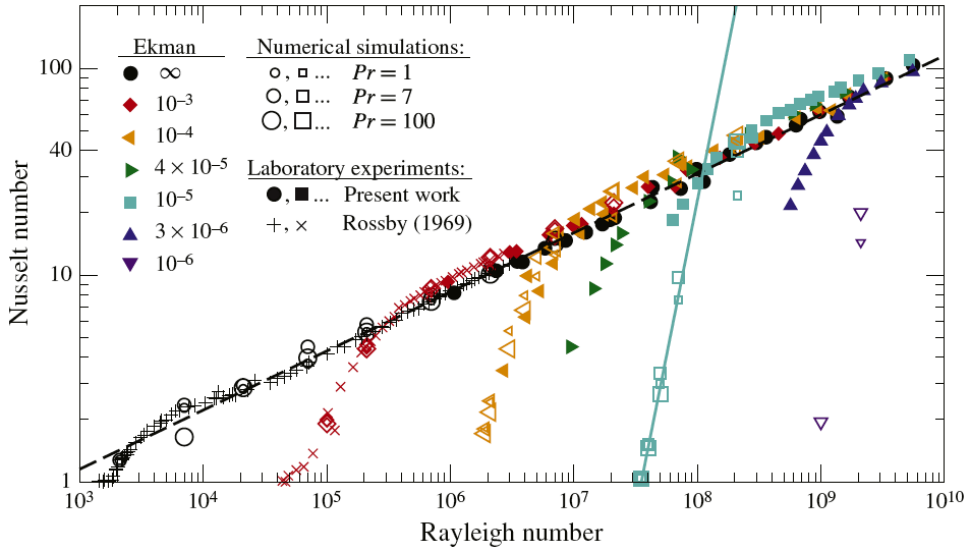

Figure 2.6: Nusselt number versus Rayleigh number. Black dashed line represents a scaling law $\mathrm{Nu} \sim \mathrm{Ra}^{2/7}$ for convection without rotation ($\mathrm{Ek} = \infty$). Cyan solid line represents the rotationally controlled scaling law. The transition between the two regimes (dynamics dominated by non-rotating or rotating effects) occurs at $\mathrm{Ra}_* \sim \mathrm{Ek}^{-7/4}$ depending on the relative thickness of the thermal and Ekman boundary layers. After King et al. (2012).

2.5 Solidification and melting

Melting and crystallization have been always important in the Earth's history. Creation of continents or freezing of the inner core belong to processes ultimately shaping the present state of the planet. In Chapter 1 we saw that extensive melting of the Earth's deep interior is present since the early beginning of the Earth's history.

Changing a state between the liquid and solid phase is a physical problem where the melting front behaves like a free moving boundary. At the melting front, latent heat is liberated/consumed and diffused away from the boundary. Balancing the heat flux at the interface gives us direction and speed of the phase limit.

Freezing of liquids consisting of more substances gives rise to intrinsic interface instabilities depending on the structure and dynamics of the thermal and solutal boundary layers (Huppert and Sparks, 1988; Huppert, 1990; Davis, 2001). When an alloy is solidifying at a moderate speed, dendritic structure of the frozen substance is created resulting in the formation of a mushy layer with characteristics chimneys. In our work we consider the crystallization/melting of a pure pole. Hence neglecting all compositional effects.

In addition, if the solidification occurs in a gravitational field, more complexities emerge as the thermal gradients can induce a buoyancy driven flow. Coupling between the convecting motion and interface instabilities then changes the interface morphology and is at the centre of our focus.

Theoretical and experimental studies of conditions for formation of instabilities leading to convection in a pure melt undergoing a phase transformation were carried out by Davis et al. (1984) and Dietsche and Müller (1985). They considered a horizontal liquid layer of cyclohexane, a single component liquid, that was from below. The top boundary was kept at a temperature inferior to the melting temperature and adjusted so that the phase change interface stayed frozen in the upper part of the enclosure. Davis et al. (1984) performed a weakly nonlinear analysis in order to determine the stable interfacial patterns as a function of solid thickness. To characterize the system they use a parameter $\mathcal{A}$

$$\mathcal{A} = \frac{L - h_{\mathrm{cond}}}{h_{\mathrm{cond}}} = \frac{T_{\mathrm{M}} - T_{\mathrm{c}}}{T_{\mathrm{h}} - T_{\mathrm{M}}}\,, \tag{2.25}$$

that is a ratio of solid and liquid depths in static equilibrium with h_{cond} the liquid height for pure heat conduction. The Rayleigh number they use is also based on h_{cond} and the temperature difference across the melt

$$\mathcal{R} = \frac{g\alpha h_{\mathrm{cond}}^3 \rho_0 (T_{\mathrm{h}} - T_{\mathrm{M}})}{\kappa_{\mathrm{L}} \eta_{\mathrm{L}}}\,. \tag{2.26}$$

In their experiments they keep T_{h} and T_{M} constant. $\mathcal{R}$ thus changes through h_{cond} that also implies the change in $\mathcal{A}$. They show that two-dimensional rolls are formed when the solid is thin and hexagonal planform is obtained when the solid is thick. Their stability diagram is reproduced in Figure 2.7. However, they do not consider that there are alternative mechanisms that can lead to formation of hexagonal patterns. In particular, as we saw previously, considering temperature dependent viscosity would predict hexagons without any dependence on the solid thickness.

Dietsche and Müller (1985) investigated initiation of convective instabilities around the critical Rayleigh number. They reported a hysteresis loop of the liquid layer height. When the liquid layer is progressively increased convection sets up around $\mathcal{R} = 1450$. Reversing the experiment and progressively decreasing the thickness of the liquid by decreasing T_{c}, convection persists in the melt for Rayleigh numbers lower than the critical value, around $\mathcal{R} = 1100$ (corresponding to $\mathrm{Ra}_{\mathrm{eff}} = 5500$). Dietsche and Müller (1985) also shows that there exists several possible stable solutions depending on whether they were obtained by increasing or decreasing the liquid height, cf. Figure 2.8. They argue that the particular convective pattern becomes 'frozen' by the interfacial corrugations. Thus, the steady solution obtained at small Rayleigh numbers may be dependent on initial conditions.

In the next sections we present a physical model enabling to describe the coupled problem of solidification and melting with microscale fluid flow.

There are two basic mathematical models approaching the coupled physics of convection with solidification/melting. The first one solves for the conservative equations in each of the phases separately and couples them by the conditions prescribed at the melting front. Alternatively, in the so called enthalpy method, governing equations are employed in the whole system comprising the solid and the liquid together. Latent heat effects are then accounted for by imposing a suitable liquid fraction function being

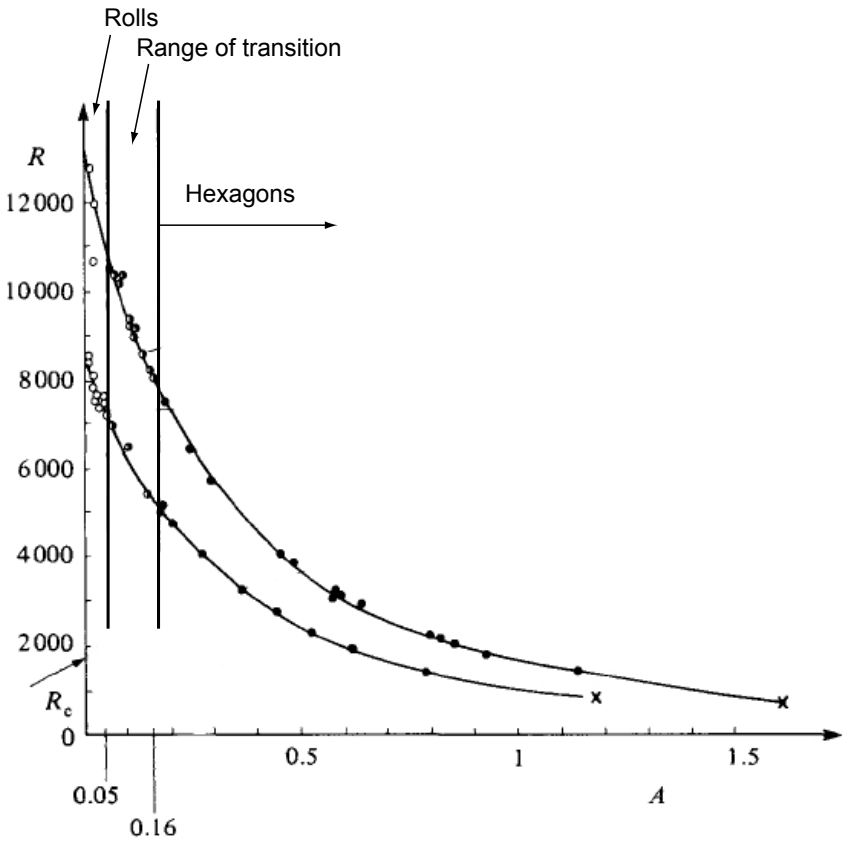

Figure 2.7: Pattern stability diagram in single-component Rayleigh Bénard system coupled with solidification. The two curves represent two runs fo experiments for two different total layer thicknesses. Modified from Davis et al. (1984).

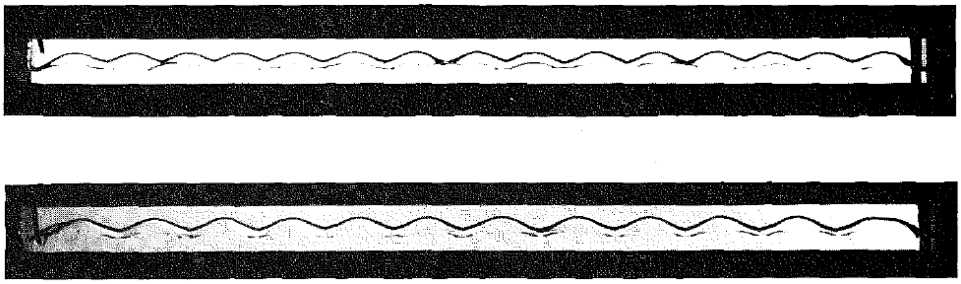

Figure 2.8: Different steady roll pattern at $\mathcal{R} = 5100$ and $\mathcal{A} = 2.67$. (top) 15-roll pattern obtained in an experiment where the liquid height was progressively increased (bottom) 12-roll steady pattern obtained in an experiment where the liquid height was decreased. Reproduced from Dietsche and Müller (1985).

one in the liquid and zero in the solid. Mechanical conditions are fulfilled by an eligible choice of the

viscosity function that is low enough in the liquid (in order to allow convection) and high enough in the solid (in order to prevent deformation). The former method is described in Section 2.5.1, the latter one in Section 2.5.2.

2.5.1 Coupling between the solid and convecting liquid

The melting front represents a free moving boundary in a given system. In order to determine its speed and position, heat and mass balances across it must be considered.

Temperature is continuous across the phase change and equal to the melting temperature T_{M}. Strictly speaking, T_{M} should be a function of pressure (depth) in the mantle. However, for the BMO, as will be shown later in Chapter 4, the topography of the boundary should be negligible. Pressure variation at which the phase transition happens is thus also negligible and T_{M} can be considered pressure independent. This is true on short timescales. On the long term, the BMO thickness changes significantly and thus the melting temperature should also vary. However, we assume that there is a good separation of long and short time scales so that the long term evolution can be modeled using the short timescale laws when the melting temperature stays in a restricted depth interval. This can be violated when considering lateral temperature variations in the mantle, which can induce important large scale interface deflections. The pressure range over which the phase transformation happens is then large and the approximation of constant melting temperature with depth less valid. Including the depth dependence of the melting temperature poses no technical difficulty but is left aside for the moment in the interest of simplicity.

The two conditions holding at the melting front can be written as

$$[T]_{-}^{+} = 0\,, \quad \text{and} \quad T = T_{\mathrm{M}}\,, \tag{2.27}$$

where the brackets $[\ ]_{-}^{+}$ indicate the jump of a given quantity across the phase interface.

Second, the condition for flux (Davis, 2001) (known as the Stefan condition) is

$$\rho\mathcal{L}\,\boldsymbol{u}\cdot\boldsymbol{n} = [k\boldsymbol{\nabla}T\cdot\boldsymbol{n}]_{-}^{+}\,, \tag{2.28}$$

and expresses conservation of energy while the interface moves. $\boldsymbol{u}$ is the velocity of the interface, and $\boldsymbol{n}$ is a unit normal vector to the phase interface pointing toward the liquid. We assumed that the volume changes on melting are negligible, i.e. $\rho_{\mathrm{L}} = \rho_{\mathrm{S}} = \rho$. Its form without dimensions reads as

$$\mathrm{St}\,\boldsymbol{u}\cdot\boldsymbol{n} = [\boldsymbol{\nabla}\mathrm{T}\cdot\boldsymbol{n}]_{-}^{+}\,, \tag{2.29}$$

with the Stefan number

$$\mathrm{St} = \frac{\mathcal{L}}{C_P\Delta T_{\mathrm{tot}}}\,. \tag{2.30}$$

In order to show the nonlinearity hidden in Eq.(2.28), consider its 1D form (with $u = \frac{\partial h_{\mathrm{m}}}{\partial t}$ where h_{m} is the position of the melting front) (Carslaw and Jaeger, 1959)

$$\rho\mathcal{L}\frac{\partial h_{\mathrm{m}}}{\partial t} = k_{\mathrm{L}}\frac{\partial T_{\mathrm{L}}}{\partial z} - k_{\mathrm{S}}\frac{\partial T_{\mathrm{S}}}{\partial z}\,, \tag{2.31}$$

and assume an isotherm in the liquid $T_{\mathrm{L}}(z,t) = \mathrm{const}$. Then, we write

$$\mathrm{d}T_{\mathrm{L}}(z,t) = \frac{\partial T_{\mathrm{L}}}{\partial z}\,\mathrm{d}z + \frac{\partial T_{\mathrm{L}}}{\partial t}\,\mathrm{d}t = 0\,, \tag{2.32}$$

and at the phase interface $z = h_{\mathrm{m}}$

$$\left.\frac{\mathrm{d}z}{\mathrm{d}t}\right|_{z=h_{\mathrm{m}}} = -\frac{\frac{\partial T_{\mathrm{L}}}{\partial t}}{\frac{\partial T_{\mathrm{L}}}{\partial z}}\,. \tag{2.33}$$

Introducing equation above in Eq.(2.31) we obtain

$$-\rho\mathcal{L}\frac{\frac{\partial T_{\mathrm{L}}}{\partial t}}{\frac{\partial T_{\mathrm{L}}}{\partial z}} = k_{\mathrm{L}}\frac{\partial T_{\mathrm{L}}}{\partial z} - k_{\mathrm{S}}\frac{\partial T_{\mathrm{S}}}{\partial z}\,. \tag{2.34}$$

From this form it is obvious, that the boundary condition (2.28) prescribed at the melting front is nonlinear. Similarly, it can be generalized in more dimensions.

We presented the thermal boundary conditions at the phase interface. What remains to be determined are the mechanical conditions at the freezing front that must hold for the velocity $\boldsymbol{v} = (v_{\mathrm{x}}, v_{\mathrm{z}})$. Following Davis (2001), we carry out the mass balance in the control volume $\mathcal{V}$ spanning the phase front, cf. Figure 2.9. Mass conservation for a pure pole that undergoes a solid-liquid phase transition and allows for changes in density between the solid and liquid $\Delta\rho = \rho_{\mathrm{S}} - \rho_{\mathrm{L}}$ is (assuming there is no flow in the solid)

$$\begin{aligned}[\rho_{\mathrm{S}} - \rho_{\mathrm{L}}]\frac{\partial h_{\mathrm{m}}}{\partial t}\,\mathrm{d}x \quad &= \quad \rho_{\mathrm{L}}\Big\{(v_{\mathrm{z}}(z+\mathrm{d}z)\,\mathrm{d}x - v_{\mathrm{x}}(x)[z+\mathrm{d}z-h_{\mathrm{m}}(x)] \\ &\quad + v_{\mathrm{x}}(x+\mathrm{d}x)[z+\mathrm{d}z-h_{\mathrm{m}}(x+\mathrm{d}x)]\Big\}\,,\end{aligned} \tag{2.35}$$

that can be rearranged as

$$\frac{\rho_{\mathrm{S}} - \rho_{\mathrm{L}}}{\rho_{\mathrm{L}}}\frac{\partial h_{\mathrm{m}}}{\partial t} = v_{\mathrm{z}}(z+\mathrm{d}z) - \frac{v_{\mathrm{x}}(x+\mathrm{d}x)h_{\mathrm{m}}(x+\mathrm{d}x) - v_{\mathrm{x}}(x)h_{\mathrm{m}}(x)}{\mathrm{d}x} + [z+\mathrm{d}z]\frac{v_{\mathrm{x}}(x+\mathrm{d}x) - v_{\mathrm{x}}(x)}{\mathrm{d}x}\,. \tag{2.36}$$

Reducing the control volume to zero, i.e. $\mathcal{V} \to 0$, that is equivalent to $\mathrm{d}x \to 0$ and $\mathrm{d}z \to 0$, partial derivatives appear on the right hand side of Eq.(2.36) and we can write

$$\frac{\rho_{\mathrm{S}} - \rho_{\mathrm{L}}}{\rho_{\mathrm{L}}}\frac{\partial h_{\mathrm{m}}}{\partial t} = v_{\mathrm{z}}(h_{\mathrm{m}}) - \frac{\partial(v_{\mathrm{x}}h_{\mathrm{m}})}{\partial x} + h_{\mathrm{m}}\frac{\partial v_{\mathrm{x}}}{\partial x}\,, \tag{2.37}$$

that finally results in

$$\frac{\rho_{\mathrm{S}} - \rho_{\mathrm{L}}}{\rho_{\mathrm{L}}}\frac{\partial h_{\mathrm{m}}}{\partial t} = v_{\mathrm{z}} - v_{\mathrm{x}}\frac{\partial h_{\mathrm{m}}}{\partial x}\,. \tag{2.38}$$

We add a condition, that the melting front is a no-slip surface, that is

$$0 = \boldsymbol{v}\cdot\boldsymbol{t} = v_{\mathrm{x}}t_{\mathrm{x}} + v_{\mathrm{z}}t_{\mathrm{z}}\,, \tag{2.39}$$

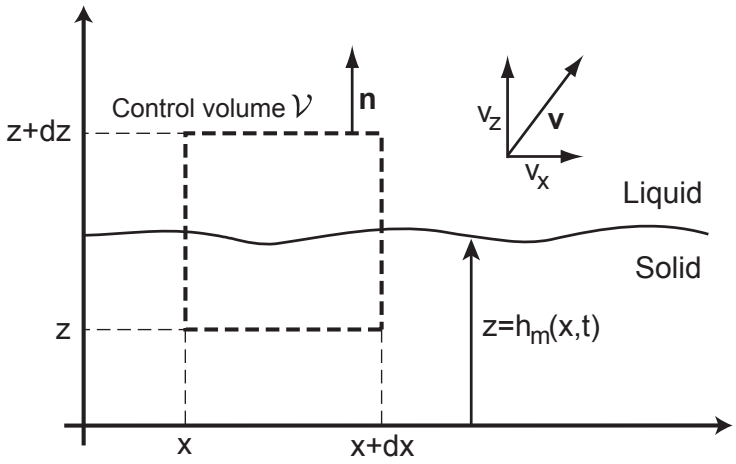

Figure 2.9: Schematic picture of the control volume used to derive the velocity boundary conditions at the phase change interface.

with the tangent $\boldsymbol{t} = (t_\mathrm{x}, t_\mathrm{z}) = 1/\sqrt{(1 + \left(\frac{\partial h_\mathrm{m}}{\partial x}\right)^2)}(1, \frac{\partial h_\mathrm{m}}{\partial x})$. It implies that

$$0 = v_\mathrm{x}\left(1 + \left(\frac{\partial h_\mathrm{m}}{\partial x}\right)^2\right) . \tag{2.40}$$

This condition is satisfied if and only if $v_\mathrm{x} = 0$. Introducing $v_\mathrm{x} = 0$ into Eq.(2.38) results in the final condition for the horizontal velocity

$$v_\mathrm{z} = \frac{\Delta\rho}{\rho_\mathrm{L}}\frac{\partial h_\mathrm{m}}{\partial t} , \tag{2.41}$$

that reduces to

$$v_\mathrm{z} = 0 , \tag{2.42}$$

in our particular case since we consider that there is no density difference between the two phases, i.e. $\Delta\rho = 0$.

2.5.2 Enthalpy method

The equation of the energy conservation (Eq.(2.11)) can be formulated using the enthalpy variable H

$$\frac{\mathrm{D}H}{\mathrm{D}t} = k\nabla^2 T , \tag{2.43}$$

where $H = \int_0^T \rho c_\mathrm{p}\,\mathrm{d}\lambda + \rho\mathcal{L}f_\mathrm{L} = \rho c_\mathrm{p} T + \rho\mathcal{L}f_\mathrm{L}$ and f_L is the liquid fraction (assuming that ρ and c_p are constant). Since we can write for the total differential

$$\frac{\mathrm{D}f_\mathrm{L}}{\mathrm{D}t} = \frac{\mathrm{d}f_\mathrm{L}}{\mathrm{d}T}\frac{\mathrm{D}T}{\mathrm{D}t} , \tag{2.44}$$

Eq. (2.43) can be transformed into

$$\left(\rho c_{\mathrm{p}} + \rho\mathcal{L}\frac{\partial f_{\mathrm{L}}}{\partial T}\right)\left(\frac{\partial T}{\partial t} + \boldsymbol{v}\nabla T\right) = k\nabla^2 T\,, \tag{2.45}$$

that gives after nondimensionalization

$$\left(1 + \mathrm{St}\frac{\partial \mathrm{f_L}}{\partial \mathrm{T}}\right)\frac{\mathrm{D}T}{\mathrm{D}t} = \nabla^2 T\,. \tag{2.46}$$

In order to solve Eq.(2.46) we have to prescribe the liquid fraction, that is a temperature dependent function. Taking f_{L} as the Heaviside step function recovers the condition for the heat balance at the melting front, Eq. (2.28), and leads to the discontinuous enthalpy. Here, we choose

$$f_{\mathrm{L}} = \frac{1}{2}\left(1 - \tanh\left(\frac{T_{\mathrm{M}} - T}{\epsilon}\right)\right)\,. \tag{2.47}$$

ϵ is a regularization parameter. Hence, the phase change is not sharp but happens over a mushy region of finite thickness.

In order to fulfil the mechanical conditions, a temperature dependent viscosity must be prescribed. The solid should not deform, contrary to the liquid where convection is desirable. Correspondingly to liquid fraction we choose the viscosity as

$$\eta = \exp\left(B(1 - f_{\mathrm{L}})\right) = \exp\left\{\frac{B}{2}\left(\tanh\left(\frac{T_{\mathrm{M}} - T}{\epsilon}\right) + 1\right)\right\}\,. \tag{2.48}$$

2.6 Conclusions

Due to small viscosity and large thickness of the BMO, the system is supposed to be vigorously convecting while it is crystallizing. In order to understand its thermal evolution, our ultimate goal here, we need to understand how the heat is transfered through a convecting layer whose dynamics is closely coupled with solidification/melting processes.

Functional relations that describe the efficiency of heat transported in the Rayleigh-Bénard convection have been extensively studied and are still discussed. These have started as a simple models with constant physical properties and got more complicated with time as they included more physics, in particular temperature dependent viscosity.

Here, we propose to study convection coupled with liquid-solid phase change transformation. In this chapter we presented governing equations of the problem. In the next, we construct numerical models that let us to derive functional relations for the heat flux and allow us to ascertain the coupling between the BMO and the Earth's core.

Chapter 3

Numerical models of convection coupled with liquid-solid phase transition

In this chapter we propose a numerical model eligible for the convecting system undergoing a liquid-solid phase change in order to determine its thermal characteristics. In particular, we intend to simulate the dynamics and thermal evolution of the basal magma ocean together with the solid boundary layer representing the lowermost mantle.

3.1 Physical model

In Chapter 2 we presented and discussed the equations governing the dynamics of convection coupled with a solid-liquid phase transition. These are recalled here in their dimensionless form.

Dimensionless equations governing the dynamics of the liquid are

$$\boldsymbol{\nabla}\cdot\boldsymbol{v} = 0\,, \tag{3.1}$$

$$\frac{1}{\mathrm{Pr}}\frac{\mathrm{D}\boldsymbol{v}}{\mathrm{D}t} = -\boldsymbol{\nabla}p + \boldsymbol{\nabla}\cdot\left(\eta\left(\boldsymbol{\nabla}\boldsymbol{v} + (\boldsymbol{\nabla}\boldsymbol{v})^{\mathrm{T}}\right)\right) + \mathrm{Ra}\,T\boldsymbol{e}_z\,, \tag{3.2}$$

$$\frac{\mathrm{D}T}{\mathrm{D}t} = \nabla^2 T\,, \tag{3.3}$$

and the solid is

$$\frac{\partial T}{\partial t} = \nabla^2 T\,. \tag{3.4}$$

$\boldsymbol{v}$ is the liquid velocity, p the dynamic pressure, η the dimensionless viscosity, T the temperature, $\boldsymbol{e}_z$ a unit vector pointing up in the vertical direction.

At the phase change interface, that is a sharp boundary interface, following conditions must be fulfilled

$$
\begin{aligned}
[\boldsymbol{\nabla} T \cdot \boldsymbol{n}]_{-}^{+} &= \mathrm{St}\, \boldsymbol{u} \cdot \boldsymbol{n}\,, && (3.5)\\
[T]_{-}^{+} &= 0\,, && (3.6)\\
T &= T_{\mathrm{M}}\,, && (3.7)\\
\boldsymbol{v} &= \boldsymbol{0}\,, && (3.8)
\end{aligned}
$$

where $\boldsymbol{u}$ is the velocity of the interface and $\boldsymbol{n}$ its unit normal vector pointing toward the liquid.

Alternatively, Eqs.(3.1)-(3.8) can be recast in a system of equations holding for both, the solid and the liquid,

$$
\begin{aligned}
\boldsymbol{\nabla} \cdot \boldsymbol{v} &= 0\,, && (3.9)\\
\frac{1}{\mathrm{Pr}} \frac{\mathrm{D}\boldsymbol{v}}{\mathrm{D}t} &= -\boldsymbol{\nabla} p + \boldsymbol{\nabla} \cdot \left(\eta \left(\boldsymbol{\nabla}\boldsymbol{v} + (\boldsymbol{\nabla}\boldsymbol{v})^{\mathrm{T}}\right)\right) + \mathrm{Ra}\, T \boldsymbol{e}_{\mathrm{z}}\,, && (3.10)\\
\left(1 + \mathrm{St} \frac{\partial \mathrm{f_L}}{\partial \mathrm{T}}\right) \frac{\mathrm{D}T}{\mathrm{D}t} &= \nabla^2 T\,, && (3.11)
\end{aligned}
$$

implicitly including the latent heat effects. Using this formulation, the phase change is not sharp but happens over a mushy region of finite thickness. The liquid fraction f_{L} and the viscosity η are functions of temperature and have been chosen

$$
\begin{aligned}
f_{\mathrm{L}} &= \frac{1}{2}\left(1 - \tanh\left(\frac{T_{\mathrm{M}} - T}{\epsilon}\right)\right)\,, && (3.12)\\
\eta &= \exp\left(B(1 - f_{\mathrm{L}})\right)\,. && (3.13)
\end{aligned}
$$

A parameter ϵ can be seen as a physical parameter linked to the width of the mushy region. B is a parameter that defines the ratio between the viscosity of the solid and the liquid.

We are interested in the dynamics and heat characteristics of the solidifying basal magma ocean, whose physical model was retrieved in this section. The large uncertainties in ill constrained BMO properties result in a wide interval of parameters decisive for its time evolution, cf. Table 2.2 and Figure 2.2. In order to explore the parameter space we decide to perform numerical experiments at finite and infinite Prandtl numbers. For that we use two different codes, Elmer and StagYY, each of them using a different solidification model. In the first model the inertia force is included (limited Prandtl number) and the latent heat effects are treated as a boundary condition. In the second model the inertia force is neglected (the infinite Prandtl number approximation) and the latent heat effects are implicitly included in the heat equation. This allows us to study the system with and without inertia (both cases being applicable for the BMO) but also determine the suitability of different numerical techniques for the liquid/solid phase transition coupled with a fluid flow that can be useful for other geological systems such as magma chambers. The methods as well as numerical techniques are presented in detail in the paper that follows this chapter. Here, we briefly recall them and also present additional benchmarks.

3.2 Numerical method - finite element code Elmer

The system of equations (3.1)-(3.4) together with conditions (3.5)-(3.8) are solved in the liquid and solid with the finite element method using Elmer (CSC – IT Center for Science, 2010). A cartesian 2D geometry is considered.

On a single timestep level, Eqs. (3.2) and (3.3) are coupled via a time derivative (in addition to temperature and velocity) as we consider the inertia term in the Navier-Stokes equation. Also, the interfacial condition Eq. (3.5) is a time evolution equation. There are several possible strategies to solve the coupled system including the monolithic algorithm. This algorithm yields (after discretization of all governing equations) to a single system of equations to be solved at each time step. Instead, our strategy considers a weak coupling where each equation is solved separately and the result is used immediately. Common iterations can be employed on a single time level, but we use no system coupled iterations. The time discretization of equations is thus of the first order precision.

The phase change interface is always described by the same nodes. This implies that the solid and liquid domains are present during the whole simulation preventing to perform the solidification or melting of the whole cavity. Once the interface moves, mesh nodes have to follow this displacement. This is done by solving a nonphysical elastic equation with boundary conditions given by the interface position, as if stretching an elastic membrane containing grid nodes. The mesh is never regenerated entirely. Instead, nodes are displaced relative to the old position, which reduces considerably computation time. However, there is no way to ensure that the new mesh stays valid and it might lead to simulation crash. An example of corrupted mesh is shown in Figure 3.2.

Further details of the solving procedure with careful description and thorough discussion of the method are described in the paper following this chapter.

3.3 Numerical method - finite volume/finite difference code StagYY

We also use a different strategy to solve Eqs.(3.9)-(3.13) using StagYY (Tackley, 1993, 1996, 2008) where we implemented the liquid-solid phase transition. In this case, an infinite Prandtl approximation is considered and thus we neglect a term on the right hand side of Eq.(3.10). Eqs.(3.9)-(3.13) are solved in the whole cavity, implicitly including the latent heat effects. A temperature field is obtained as a solution, that is used to reconstruct the position of the phase change interface a posteriori. A cartesian 2D or 3D geometry is considered. The algorithm consists of two steps: finding a solution of pressure and velocity (solving Eqs.(3.1) and (3.10)) and taking a timestep (solving Eq.(3.11)).

To solve the equations of fluid flow, a finite difference multigrid method for primitive variables (pressure and velocity) on a staggered grid is used (Patankar, 1980) and multigrid F-cycles are employed.

The advection term in the heat equation is solved using the explicit MPDATA (Multidimensional Positive Definite Advection Transport Algorithm) scheme (Smolarkiewicz, 1998) that iteratively calls donor-cell scheme to obtain more accurate solution of the second order precision. Typically, we use 3 iterations. The diffusion term is computed with the explicit Euler method in time and second-order

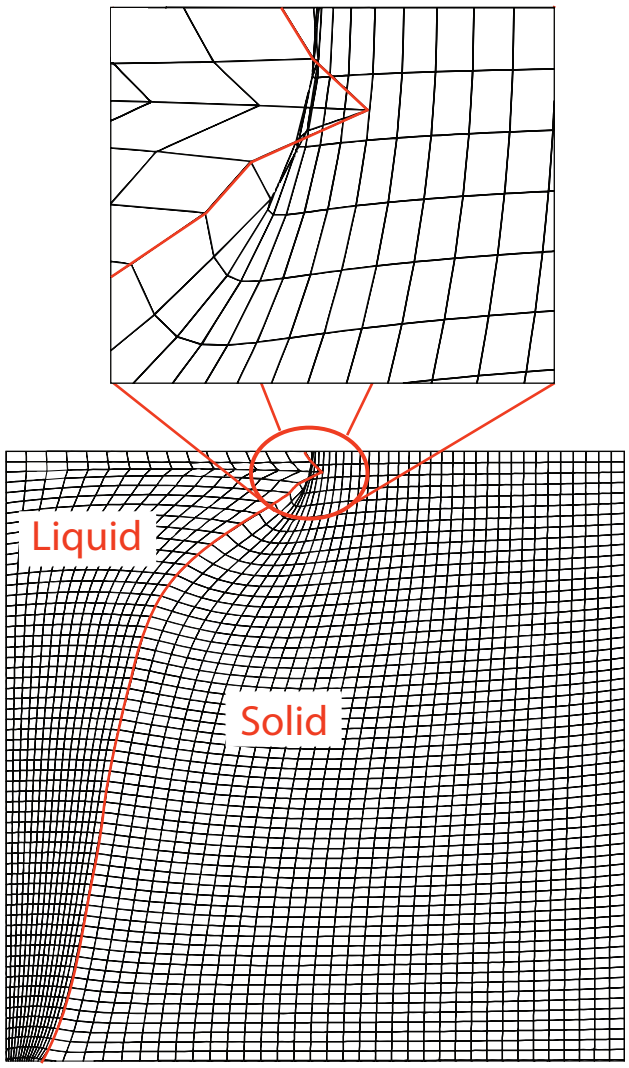

Figure 3.1: Corrupted mesh obtained for a simulation of melting from left vertical wall with a zoom around the corrupted elements (top picture). Displacement of node corresponding to the phase front was larger than a distance to the nearest node in the solid region. Solid red line represents the phase change interface between the liquid (left part of the cavity) and solid (right part of the cavity).

finite-differences in space. Time steps are computed to get a unity Courant number for cases with a small Rayleigh number that lead to steady state solution, and are decreased to a Courant number of 0.6 for higher Ra numbers.

The detailed solution strategy is described in the paper following this chapter.

3.4 Benchmarking the numerical model

In order to evaluate the precision and quality of the numerical solution we perform several benchmarks. There is no analytical solution for the coupled problem, but only for a purely conductive solid/liquid undergoing a phase transformation in simple 1D geometry. Besides, a limited boundary condition (fixed temperature) must be employed because again no analytical work can be derived for more complicated cases such as constant heat flux. This exercise is presented in Section 3.4.1.

In addition to analytical comparison, numerical solutions can be used to verify the numerical solution. Works of Blankenbach et al. (1989) or Busse et al. (1994) provide a reference solution for convection codes at infinite Prandtl number and in Cartesian geometry. Unfortunately, such a benchmark comparison does not exist for coupled system of convective motion and solid-liquid phase transformation. In the past, there has been several attempts to remedy this. The work of Bertrand et al. (1999) proposes four test cases to be examined. However, all contributors show significant differences between their numerical solutions so that no reference is given after all. Nevertheless, we compare our solutions with their outcome (Section 3.4.2).

Finally, we perform qualitative comparison with laboratory experiments of solidification done by Davis et al. (1984) and Hill (1996).

3.4.1 One dimensional freezing

Numerical resolution of the heat equation, solidification and mesh regeneration is tested here against an analytical solution for a simple case of solidifying pure melt in 1D semi-infinite space. This situation does not involve any fluid flow but allows to test the treatment of the diffusion equation coupled with the phase change.

Consider a liquid occupying a space $z \in [0, \infty]$ with zero initial undercooling, i.e. the fluid is initially at the melting temperature $T(t = 0) = T_{\mathrm{M}}$ everywhere. At time $t = 0$ the temperature of the boundary ($z = 0$) is dropped to T_{c} so that undercooling arises $\Delta T = T_{\mathrm{M}} - T_{\mathrm{c}} > 0$. Consequently, phase change transformation initially adjacent to the boundary is created at $h(t)$.

With the initial conditions chosen, the temperature of the liquid does not change and remains at all times at the melting temperature, $T^{\mathrm{an}} = T_{\mathrm{M}}$. In the solid, heat conduction equation holds

$$\frac{\partial T}{\partial t} = \kappa \frac{\partial^2 T}{\partial z^2}\,, \tag{3.14}$$

with κ the thermal diffusivity. Eq.(3.14) can be solved for a given auxiliary conditions. At the melting front a constant temperature that is equal to the melting temperature is prescribed, $T(z = h) = T_{\mathrm{M}}$, and the heat flux balance must hold

$$\left(\frac{\partial T}{\partial z}\right)_{z=h} = \mathrm{St}\frac{\partial \mathrm{h}}{\partial \mathrm{t}}\,. \tag{3.15}$$

The so-called Neumann solution for temperature distribution in the solid phase is (e.g. Davis, 2001)

$$T^{\mathrm{an}} = \frac{\mathrm{erf}\left(\frac{z}{2\sqrt{\kappa t}}\right)}{\mathrm{erf}\left(\Lambda\right)}\,, \tag{3.16}$$

where Λ is a parameter that characterizes the solution and is determined by

$$\sqrt{\pi}\Lambda e^{\Lambda^2}\,\mathrm{erf}(\Lambda) = \mathrm{St}^{-1}\,. \tag{3.17}$$

A bijection between undercooling and interface speed exists, cf. Fig. 3.2.

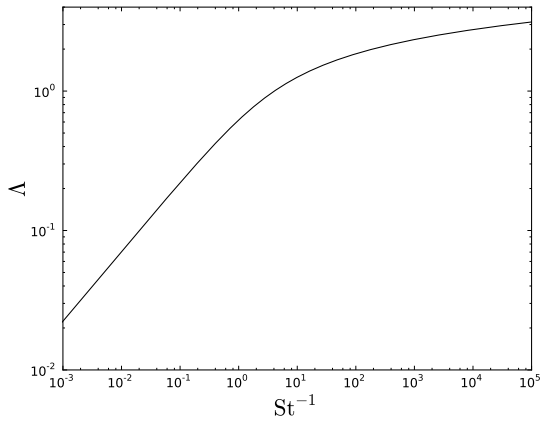

Figure 3.2: Analytical solution for Λ as a function of the undercooling St^{-1}.

As a part of the solution, the position of the phase front is ascertained as a function of time and is

$$h^{\mathrm{an}}(t) = 2\Lambda\sqrt{\kappa t}\,. \tag{3.18}$$

Due to the absence of thermal diffusion in the liquid, the semi-infinite space can be replaced by a 2D square cavity with constant temperature condition at the top wall equal to the melting temperature, cf. Figure 3.3. The bottom boundary has a temperature T_{c}. Vertical walls must be insulating to prevent any lateral diffusion so that the solution does not depend on the horizontal coordinate.

Numerical solutions of the vertical temperature distribution T^{num} in the cavity and position of the phase interface h^{num} (both as a function of time) are then compared to analytical solutions. The root mean square error for the temperature distribution is

$$\delta T = \sqrt{\frac{\sum_{i=1}^{N}\left(T^{\mathrm{num}}(z_i) - T^{\mathrm{an}}(z_i)\right)^2}{N}}\,, \tag{3.19}$$

where the sum is over the nodal points in the vertical direction with the totality of N nodes. The relative error for the phase front position is then

$$\delta h = \frac{h^{\mathrm{num}} - h^{an}}{h^{an}}\,. \tag{3.20}$$

The exercise is performed with Elmer. We thus need to start from a solution that already contains the solid and liquid domains. As an initial condition we take an analytical solution for the temperature

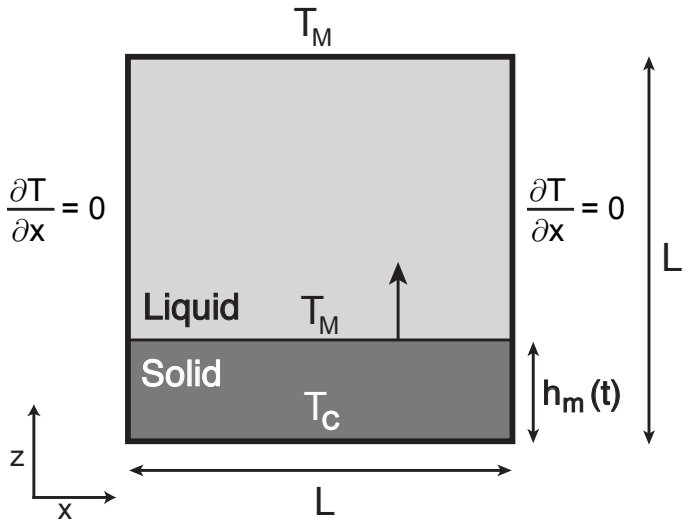

Figure 3.3: Set up for the benchmark comparison: solidification of a pure substance from a cold boundary. The interface between the liquid and solid stays planar at all times as no convective motion is involved and its position is at $h(t)$. The temperature in the liquid is constant with time as temperature gradients are absent, $T(z = h) = T_{\mathrm{M}}$ and $T(z = L) = T_{\mathrm{M}}$.

distribution and the phase front position obtained after a time $t_{\mathrm{init}} = 0.05$ has elapsed. A unity Stefan number is chosen. Using Eq.(3.17) gives us $\Lambda = 0.620$. The initial position of the melting front is thus $h = 0.277$.

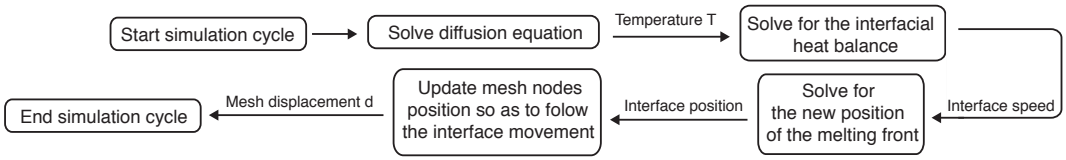

Figure 3.4: Flowchart of Elmer solving strategy for freezing from bottom boundary without any flow. See Figure 3.3 for the set up.

The algorithm is depicted on Figure 3.4.1. A weak coupling of the system is employed with no coupled iterations so that results of individual solvers are used immediately.

Several numerical aspects of Elmer solution are tested. Below, we evaluate the impact of the choice of the time-stepping strategy and we verify the time and space discretization.

Benchmarking the time-stepping method

There exist many methods for discretization of temporal derivatives. In order to determine their suitability for our particular problem we test them against analytical solutions. In particular we compare results of the benchmark test obtained using the Crank-Nicolson method and the Backward Differences Formulae (BDF) of several orders. Results are depicted in Figures (3.5) and (3.6). As we can see, the

Crank-Nicolson method and BDF of order 1 give satisfactory results. The BDF method of higher orders is not suitable, at least without performing coupled iterations. We choose to use the Crank-Nicolson hereafter.

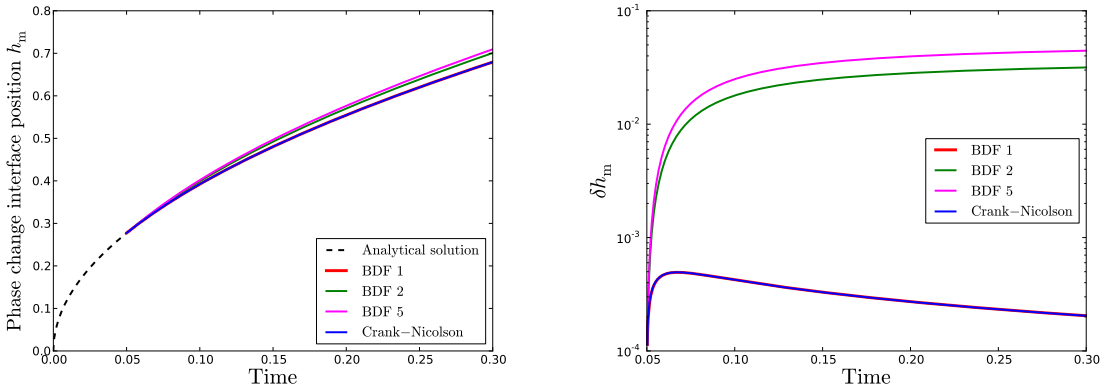

Figure 3.5: Comparison of numerical and analytical solutions for different time-stepping methods employed. Crank-Nicolson and Backward Differences (BDF) of different orders is tested (orders 1, 2 and 5 are used). (Left) Time evolution of the interface position. (Right) Relative error between the analytical and numerical solutions.

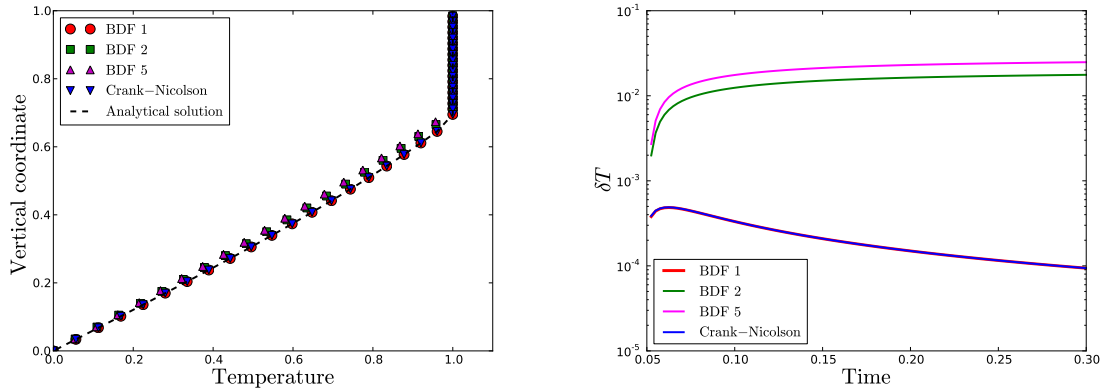

Figure 3.6: (Left) Vertical profile of temperature in the cavity at time $t = 0.3$. (Right) Root mean square error of the temperature solution as a function of time.

Time resolution

In order to verify the time resolution of equations we compare the relative error between analytical and numerical solution of phase position at time $t = 0.3$ for different values of the timestep. Figure 3.4.1 shows

the results. We can see that for a coarse mesh with resolution $10 \times (10 + 10)$ elements in the horizontal and vertical (solid+liquid) directions, the error decreases till timestep is around 10^{-4} and then reaches a plateau. This is because for small timesteps the error is dominated by the effect of spatial resolution. Results with a finer mesh $(100 \times (100 + 100))$ elements in horizontal and vertical (solid+liquid) direction) decrease at all timesteps. If you decrease a timestep by a factor of 10, the error decreases ten times. This shows that the time accuracy of the solution is of the first order precision.

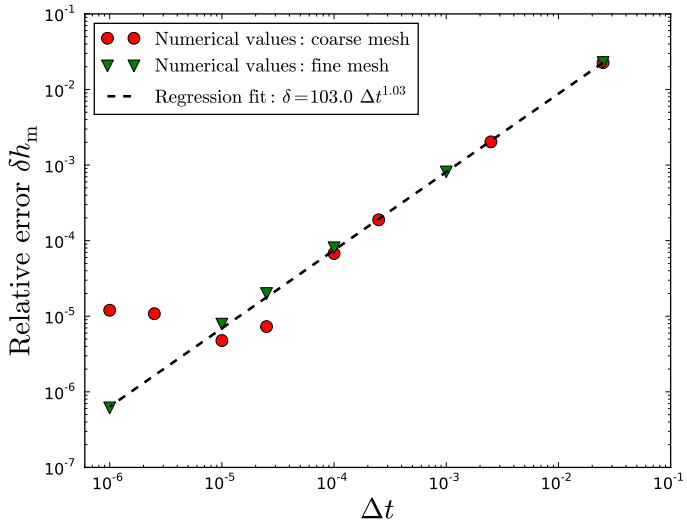

Figure 3.7: Relative error between the numerical and analytical solutions for the phase change position at time $t = 0.3$ as a function of timestep Δt. Two different meshes are used: a coarse mesh with spatial discretization of $10 \times (10 + 10)$ elements in the horizontal and vertical (solid+liquid) directions and fine mesh with a resolution of $100 \times (100 + 100)$ elements.

3.4.2 Melting from vertical wall

In order to verify the flow solver coupled with the heat transfer and solidification/melting, we perform an exercise where initially a solid cavity is heated from the left vertical wall and progressively melts. This comparison exercise was proposed by Bertrand et al. (1999) in the ultimate goal to give a reference solution for convection interacting with a melting and solidification interface. Yet, the thirteen contributions reported significant differences and thus no reference solution is given. This emphasizes that improvements of such numerical models are still needed.

Description of the exercise

Initially the cavity is kept at the melting temperature T_M. Bottom and top horizontal walls are insulating boundaries with zero velocity conditions. Right vertical wall ($x = 1$) is kept at the melting temperature T_M. At time $t = 0$ the temperature of the left vertical wall ($x = 0$) is increased to a temperature

$T_h > T_M$. The phase interface originally contiguous to the cavity's boundary ($x = 0$) arises and starts to move horizontally. Progressive melting proceeds through several stages: a pure conductive stage with a planar interface is established at the beginning. Later, convection sets up in the liquid and prevails over conduction. This stage is characterised by the formation of interface corrugations due to different temperature gradients in the vicinity of the melting front.

Bertrand et al. (1999) suggested to investigate two different systems with low and high Prandtl numbers (Pr = 0.02 and Pr = 50), namely melting of pure tin (metal) and octadecane (paraffin wax). We performed the proposed exercise for high Prandtl number with the two methods, the finite element method and the finite volumes method. Results and a careful discussion are included in the paper that follows this chapter. Results for the test case at small Prandtl number performed with the moving mesh method can be found below.

Results for small Pr number

The exercise at Pr = 0.02 and Ra = 2.5×10^5 is carried out with the finite element code Elmer using a mesh with resolution $(20 + 40) \times 60$ elements in the horizontal (melt+solid) and vertical directions. The timestep size is kept constant and equal to 0.0001 throughout the simulation. We start from a conduction temperature profile after the time $t_{\text{init}} = 0.1$ has elapsed. With a given Stefan number St = 100 this results in $\Lambda = 0.0706$ and $h_{\text{init}} = 0.0446$. The simulation runs for the total time 10. Snapshots of temperature and velocity fields are depicted in Figure 3.8. The mesh at time $t = 0.1$ and $t = 4$ is shown in Figure 3.9.

The time evolution of the Nusselt number over the left vertical wall in comparison with results of other contributors to this benchmark (Gobin and Le Quéré, 2000) is depicted in Figure 3.10. Our results are in excellent agreement with published solutions being closest to the simulation done by Wintruff. Oscillatory instabilities of the system are observed after the time $t = 4$. Indeed, it was noted by Le Quéré and Gobin (1999) that the system in consideration is prone to the multicellular instability for sufficiently high Rayleigh numbers. These are not observed for high Prandtl number fluids.

Figure 3.11 shows a comparison of the position of the melting front at time $t = 4$ with results published by Gobin and Le Quéré (2000). Certain contributors observed one convective cell. This is probably due to insufficient time resolution. We observe two main rolls that later merges into one cell. Our results are in excellent agreement with solutions obtained by Wintruff or Médale.

The comparison exercise is in very good agreement with previously published results and we conclude that the moving mesh method implemented in Elmer is suitable and accurate for systems with low Prandtl number.

3.4.3 Qualitative comparison with 3D laboratory experiments

Our numerical tools have been subjected to thorough evaluations against analytical and numerical solutions. In addition, comparison to 3D analogical experiments can be made. However, these can only be qualitative as several experimental conditions cannot be exactly matched, at least with the present model.

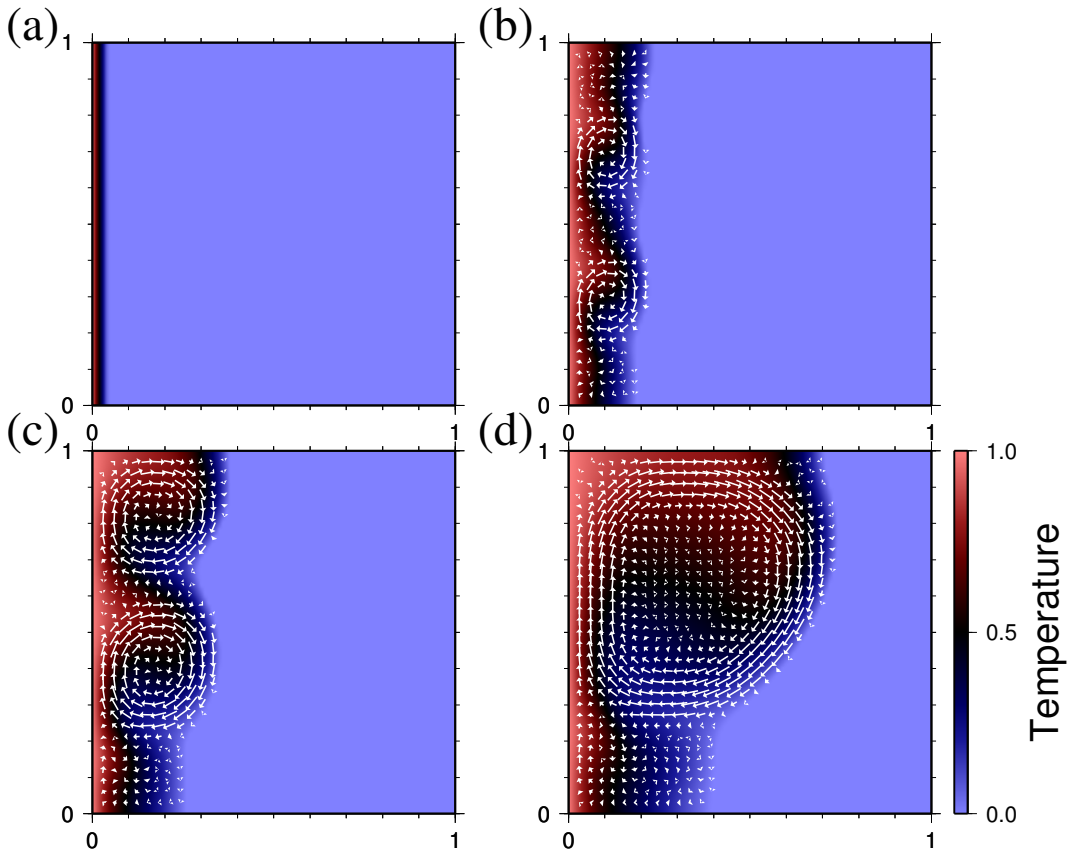

Figure 3.8: Snapshots of temperature (color scale) and velocity (vectors) fields at times (a) $t = 0.1$ (b) $t = 2.0$ (c) $t = 4.0$ (d) $t = 10.0$ for the melting exercise from vertical wall proposed in Bertrand et al. (1999). (Case with $\mathrm{Pr} = 0.02$, $\mathrm{Ra} = 2.5 \cdot 10^5$ and $\mathrm{St} = 100$.)

Davis et al. (1984) experimentally examined a single-component liquid that solidifies/melts in a plane layer heated from below and cooled from above. The upper part of the layer is frozen while the lower one is convecting. Different morphologies of the phase change interface were observed depending on the ratio of solid to liquid thicknesses $\mathcal{A}$ and the Rayleigh number $\mathcal{R}$. Davis et al. (1984) chose to relate all results to a purely conductive state in which the interface is planar. Thus, $\mathcal{A}$ is the ratio of the two heights in the case where only heat conduction proceeds and $\mathcal{R}$ is defined using the liquid height for pure heat conduction and temperature difference across the liquid layer. Small solid thickness (small $\mathcal{A}$) leads to roll-like convective pattern selection whereas large thickness of the solid (large $\mathcal{A}$) results in hexagonal convection pattern in the liquid. Figure 3.12 shows two dimensional and hexagonal convective patterns in melting experiments in comparison with results of Davis et al. (1984). Predicted morphologies of the phase change interface were successfully observed. Parameters and resulting wavenumbers of convective cells k are given in Table 3.1 together with results obtained by Davis et al. (1984).

In the same geometry, Hill (1996) observed in his laboratory experiments square interfacial corrugations at $\mathrm{Ra}_{\mathrm{eff}} = 3.3 \cdot 10^4$. These have been also successfully reproduced (cf. Figure 3.13) although

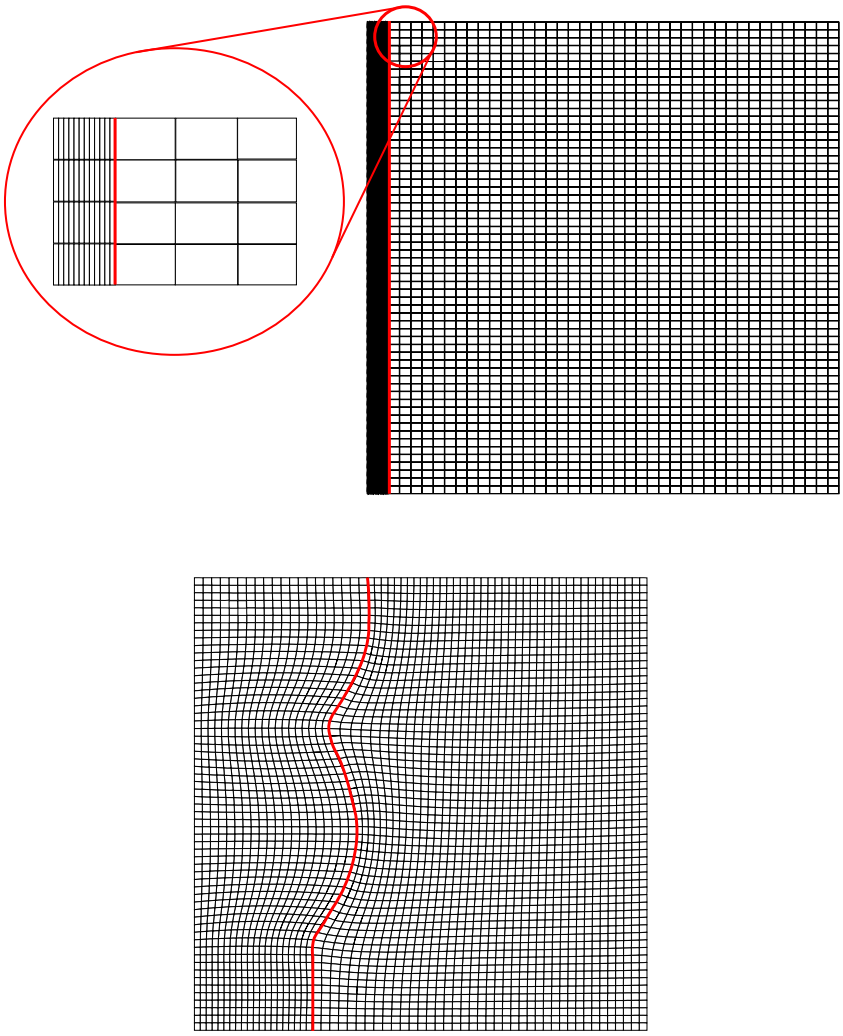

Figure 3.9: Mesh corresponding to snapshots (top) Fig. 3.8(a) and (bottom) Fig. 3.8(c). The number of elements in the liquid and the solid is constant at each time. The red line represents the phase change front.

the effective Rayleigh numbers are not exactly the same ($\mathrm{Ra}_{\mathrm{eff}} = 1.4 \cdot 10^4$ in our case). Hill (1996) uses a cavity with dimensions $320 \times 320 \times 80\,\mathrm{mm}$ that corresponds to the aspect ratio 4 in both horizontal directions and we kept the same aspect ratio in our experiment. We observe regular square patterns that have a wavelength λ_c around 1.8 (adimensionalized with the liquid thickness). This agrees very well with a value given by Hill (1996) $\lambda_c = 1.55$. Albeit a difference in the solid thickness is observed (Hill (1996) reported $h_S = 0.65$ and in our experiment $h_S = 0.38$), in both cases the solid is thick ($\mathcal{A} = 2.8$ and $\mathcal{A} = 1.4$ for laboratory and numerical experiments, respectively).

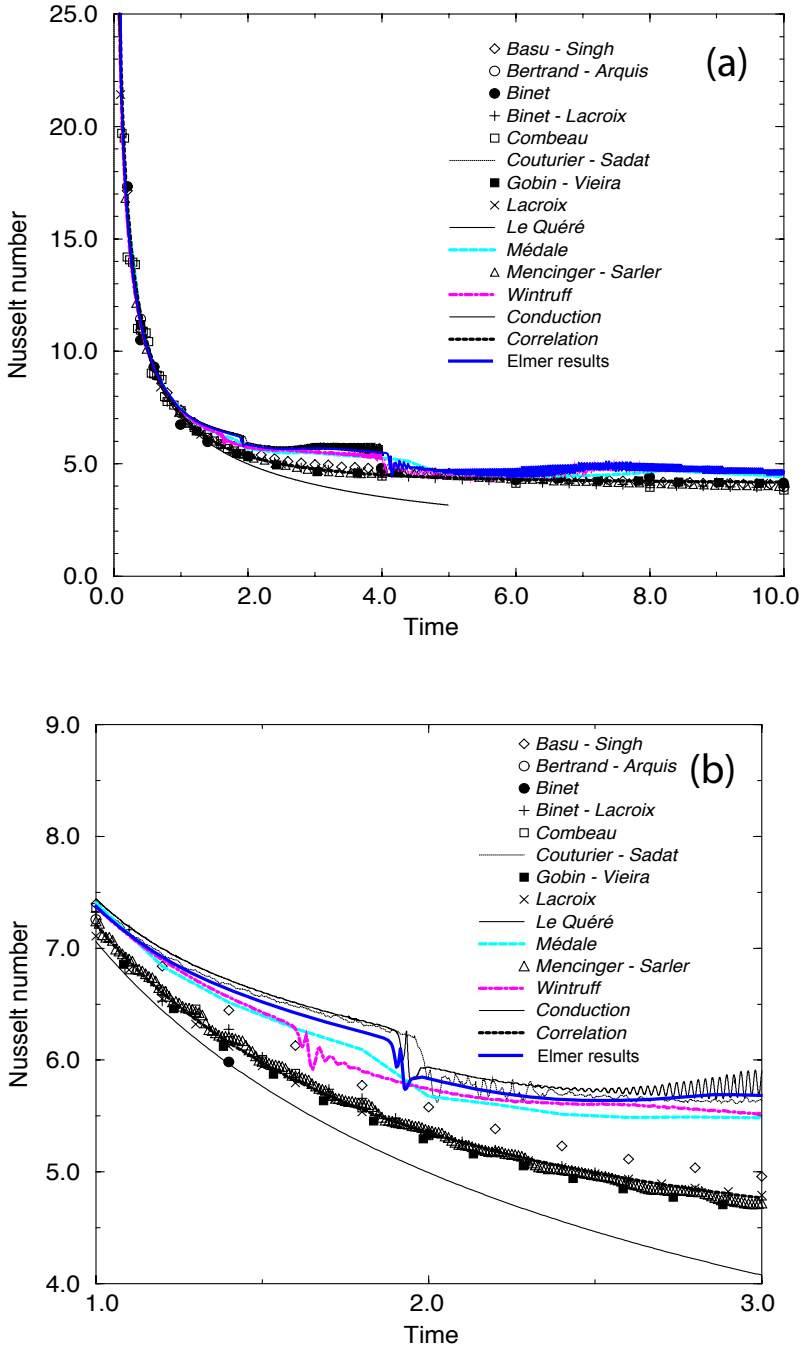

Figure 3.10: Nusselt number over the left vertical wall as a function of time. Our numerical results are compared with results published in Gobin and Le Quéré (2000). (a) The whole time interval studied. After the time $t = 4$ oscillations of the system are observed. (b) Zoom over time $t \in (1, 3)$. Our results are closest to simulations done by Wintruff. (Case with $\mathrm{Pr} = 0.02$, $\mathrm{Ra} = 2.5 \cdot 10^5$ and $\mathrm{St} = 100$.)

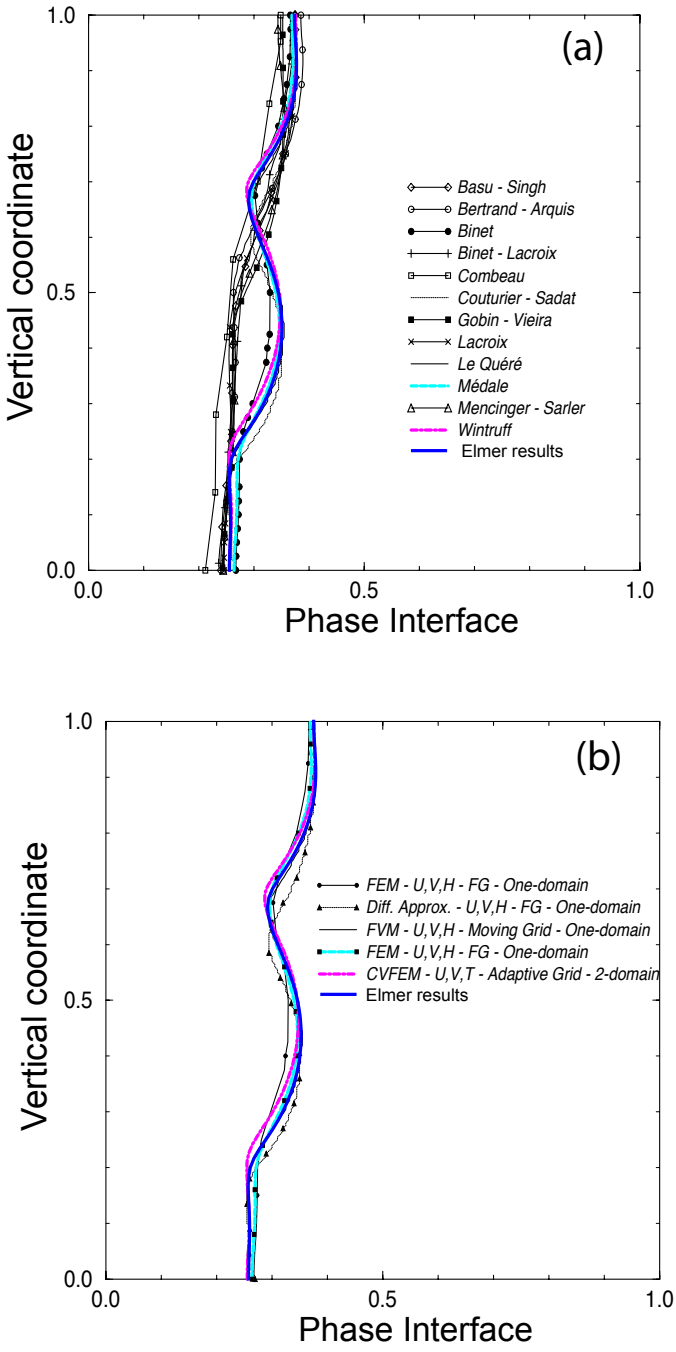

Figure 3.11: Position of the phase change interface at time $t = 4$ compared with results published in Gobin and Le Quéré (2000). (a) All simulations. (b) Simulations that observed multicellular flow. Best agreement is attained with results of Médale and Wintruff. (Case with $\mathrm{Pr} = 0.02$, $\mathrm{Ra} = 2.5 \cdot 10^5$ and $\mathrm{St} = 100$.)

$\mathcal{R}$	$\mathcal{A}$	$k^{\dagger}$	Patterns†	$k^{\ddagger}$	$\mathrm{Ra}_{\mathrm{eff}}^{\ddagger}$	Patterns‡
3300	0.36	3.0	hexagons	1.9	$5 \cdot 10^3$	hexagons
7500	0.03	2.5	rolls	2.9	$8 \cdot 10^3$	rolls

Table 3.1: Benchmark comparison with 3D laboratory experiments. For a given $\mathcal{R}$ and $\mathcal{A}$ different convective patterns were observed. † Results obtained by Davis et al. (1984). ‡ Our results.

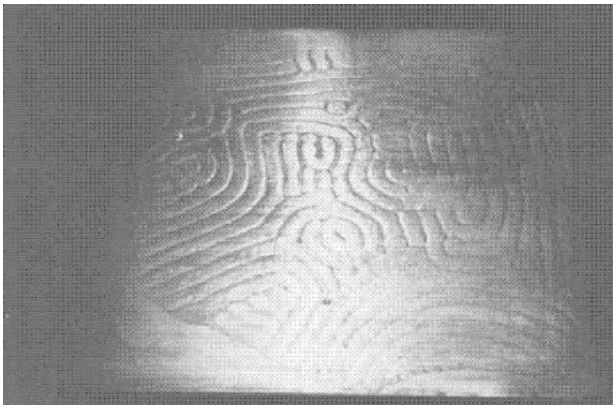

(a) Two dimensional corrugations resulting in an experiment when the solid layer is thin.

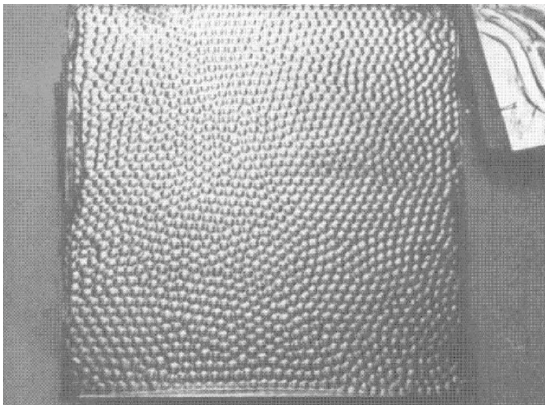

(b) Formation of hexagonal interfacial corrugation when the solid layer is thick.

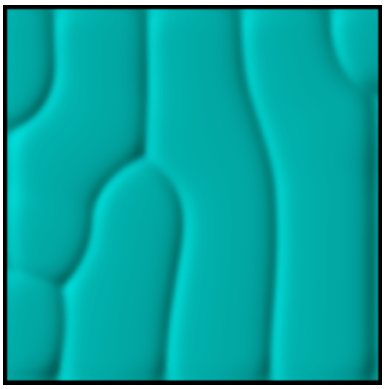

(c) Roll-like patterns.

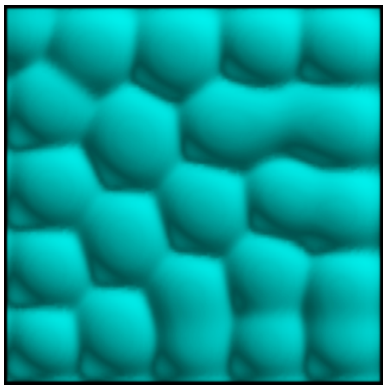

(d) Hexagonal patterns.

Figure 3.12: Morphology of the phase change interface. Laboratory experiments, pictures (a) and (b), of horizontal layer that is heated from below and cooled from above performed by Davis et al. (1984). Numerical results, pictures (c) and (d), were computed with the StagYY code in a cavity with an aspect ratio of 8 in both horizontal directions for $\mathrm{St} = 1$ and (c) $\mathrm{Ra} = 8.4 \cdot 10^3$ ($\mathrm{Ra}_{\mathrm{eff}} = 8 \cdot 10^3$) (d) $\mathrm{Ra} = 1.1 \cdot 10^4$ ($\mathrm{Ra}_{\mathrm{eff}} = 5 \cdot 10^3$).

3.5 Conclusions

Dynamics of solidification coupled with convective flow represents a problem where free moving boundary is present and thus it requires specific numerical methods to track the phase boundary. We presented and tested two different numerical frameworks that are described in more detail in the paper that fol-

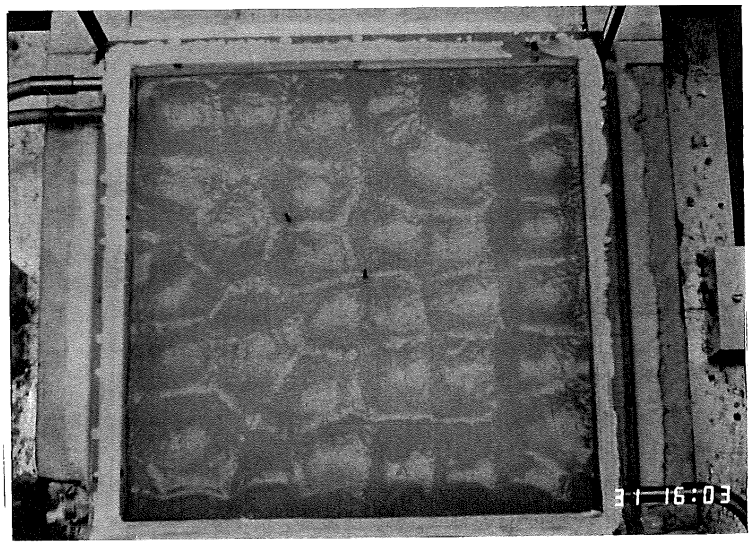

(a) Square and pentagonal patterns are observed in laboratory experiment of solidification coupled with convection (Hill, 1996) (case with $\mathrm{Pr} = 10^4$, $\mathrm{Ra_{eff}} = 3.3 \cdot 10^4$ and $\mathrm{St} = 1.7$).

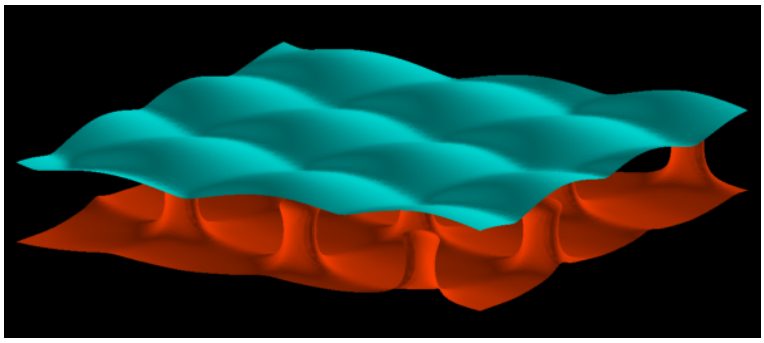

(b) Numerical simulations done with StagYY. Two isotherms are displayed: $T = T_{\mathrm{M}}$ corresponding to the phase change interface (cyan) and $T = 0.9$ for hot upwellings (red). (Case with $\mathrm{Pr} = \infty$, $\mathrm{Ra_{eff}} = 1.4 \cdot 10^4$ and $\mathrm{St} = 0.1$.)

Figure 3.13: Square patterns observed in morphology of the phase change interface. Qualitative comparison of laboratory experiments and numerical simulations.

lows (Ulvrová et al., 2012). A very good agreement in the benchmark tests was observed.

These numerical tools are then used to infer heat transfer characteristics of a melting/freezing convecting layer with an application to the thermal evolution of the basal magma ocean, see Chapter 4.

Article: Numerical modeling of convection interacting with a melting and solidification front: application to the thermal evolution of the basal magma ocean.

Following paper has been published in the Physics of the Earth and Planetary Interior journal (Ulvrová et al., 2012).

Numerical modeling of convection interacting with a melting and solidification front: application to the thermal evolution of the basal magma ocean.

M. Ulvrová[a], S. Labrosse[a,b], N. Coltice[a,b], P. Råback[c], P. J. Tackley[d]

[a] *Laboratoire de Géologie de Lyon ; Université de Lyon; Université Lyon 1; Ecole Normale Supérieure de Lyon; CNRS, Lyon, France.*
[b] *Institut Universitaire de France, France.*
[c] *CSC – IT Center for Science, Espoo, Finland.*
[d] *ETH Zurich, Switzerland.*

Abstract

Melting and solidification are fundamental to geodynamical processes like inner core growth, magma chamber dynamics, and ice and lava lake evolution. Very often, the thermal history of these systems is controlled by convective motions in the melt. Computing the evolution of convection with a solid-liquid phase change requires specific numerical methods to track the phase boundary and resolve the heat transfer within and between the two separate phases. Here we present two classes of method to model the phase transition coupled with convection. The first, referred to as the moving boundary method, uses the finite element method and treats the liquid and the solid as two distinct grid domains. In the second approach, based on the enthalpy method, the governing equations are solved on a regular rectangular grid with the finite volume method. In this case, the solid and the liquid are regarded as one domain in which the phase change is incorporated implicitly by imposing the liquid fraction f_{L} as a function of temperature and a viscosity that varies strongly with f_{L}. We subject the two modelling frameworks to thor-

ough evaluation by performing benchmarks, in order to ascertain their range of applicability. With these tools we perform a systematic study to infer heat transfer characteristics of a solidifying convecting layer. Parametrized relations are then used to estimate the super-isentropic temperature difference maintained across a basal magma ocean (BMO) (Labrosse et al., 2007), which happens to be minute ($< 0.1\,\mathrm{K}$), implying that the Earth's core must cool at the same pace as the BMO.

Keywords: Melting, Solidification, Stefan problem, Phase change, Moving boundary, Convection, Core-Mantle dynamics

1. Introduction

Solidification and melting dynamics have always attracted a lot of attention, particularly for practical applications: industrial engineering including metal processing, solidification of castings, or welding, as well as environmental and food engineering. Yet, changing phase state - tightly linked with mechanics - also plays a fundamental role in Earth and planetary evolution. Crystallization in magma chambers (Brandeis and Jaupart, 1986; Brandeis and Marsh, 1989) as well as inner core growth (Alboussière et al., 2010) are examples of geodynamic processes that have shaped the state of our planet.

A recent model suggests that after formation of the core, a basal magma ocean (BMO) was formed at the bottom of Earth's mantle and has slowly solidified since (Labrosse et al., 2007; Coltice et al., 2011). Remnants may be seismically observed as partially molten regions at the core mantle boundary (CMB) (Williams and Garnero, 1996). The BMO, the initial thickness of which could have been 1000 km, slowly cooled down while vigorously

convecting because of its high temperature and low viscosity. On a small scale, the process of solidification coupled with convective flow has been observed in lava lakes (Worster et al., 1993; Jellinek and Kerr, 2001) or ice lakes (Notz and Worster, 2006). However, suitable models capturing melting/solidification coupled with convective motions need to be developed.

Analytical works conducted in early years contain mainly mathematical solutions for one dimensional diffusion problems in an infinite or semi-infinite domain and for problems with simple initial and boundary conditions (Crank, 1984; Davis, 2001). More complex systems in terms of geometry or thermochemical parameters require numerical solutions. Including a transformation between solid and liquid phases presents a challenging numerical task since the position of the melting/freezing front is a part of the solution and so the moving boundary needs to be determined in space at each time.

A number of numerical methods for treating the moving boundary due to solidification or melting, and also being capable of handling convection in the melt, have been proposed (Crank, 1984, and reference therein). These can be divided into two main groups: moving mesh front tracking methods and fixed grid numerical techniques. The former group solves different governing equations in each of the phases and latent heat effects enter via the heat balance boundary condition at the melting/freezing front. The latter group uses a static mesh and the same differential equations are applied in both phases. The position of the phase interface is then recovered from the temperature solution and the phase diagram.

The goal of this paper is to propose, implement and critically test suitable numerical tools for simulating a solidifying/melting system whose dynamics is

closely coupled with convection in the melt. We start from two different codes that solve motion in a fluid: the finite element open source code Elmer (CSC – IT Center for Science, 2010), in which we use the formulation for a moving grid method, and the finite volume code `StagYY` (Tackley, 1993, 1996, 2008), in which we implemented the dynamic treatment of melting/solidification on a fixed grid.

These numerical tools are subsequently applied to benchmark test cases. We present a detailed comparison of heat flow, phase change front tracking and the nature of convection. The applicability of the different approaches is carefully analyzed and discussed.

In addition, we present a qualitative comparison of the three dimensional numerical results with experimental work of Davis et al. (1984).

Finally, we focus on the thermal evolution of the magma ocean solidifying in the deep mantle during early Earth's history. We derive scaling relations for the heat transfer and apply these scalings to the BMO.

2. Physical model

In this section we describe the physics of a pure substance undergoing a crystallization/melting phase change. A Newtonian incompressible liquid in a domain $\Omega \in \mathbb{R}^2$ changes phase at a fixed temperature T_M. In the molten region, density differences due to temperature gradients induce convection through a buoyancy force term.

The basic set of conservation equations for mass and momentum in the Boussinesq approximation holds in the liquid:

$$\boldsymbol{\nabla} \cdot \boldsymbol{v} = 0\,, \tag{1}$$

$$\frac{1}{\mathrm{Pr}}\frac{\mathrm{D}\boldsymbol{v}}{\mathrm{D}t} = -\boldsymbol{\nabla}p + \boldsymbol{\nabla}\cdot\left(\eta\left(\boldsymbol{\nabla}\boldsymbol{v} + (\boldsymbol{\nabla}\boldsymbol{v})^{\mathrm{T}}\right)\right) + \mathrm{Ra}\,T\boldsymbol{e}_{\mathrm{z}}\,, \tag{2}$$

written in a dimensionless form. Length is scaled by the vertical thickness of the whole domain L, velocity vector $\boldsymbol{v}$ by κ/L, with κ the thermal diffusivity, time t by the diffusion time L^2/κ and pressure p by $\kappa\,\eta_{\mathrm{L}}/L^2$ with η_{L} the dynamic viscosity of the liquid. $\boldsymbol{e}_{\mathrm{z}}$ is a unit vector along a vertical direction pointing upward and η the dimensionless viscosity scaled by η_{L}. The solid is considered to be a non deformable medium with zero velocity everywhere.

The definition of the total time derivative $\frac{\mathrm{D}\bullet}{\mathrm{D}t}$ depends on the chosen reference frame. For the Eulerian description of motion $\frac{\mathrm{D}\bullet}{\mathrm{D}t} = \frac{\partial\bullet}{\partial t} + (\boldsymbol{v}\nabla)\bullet$, which reduces to $\frac{\mathrm{D}\bullet}{\mathrm{D}t} = \frac{\mathrm{d}\bullet}{\mathrm{d}t}$ when using the Lagrangian description of motion.

There are two dimensionless numbers appearing from the normalisation of the conservation equations. The first one is the Prandtl number Pr, which is the ratio between momentum diffusion and thermal diffusion,

$$\mathrm{Pr} = \frac{\eta_{\mathrm{L}}}{\rho_0\kappa}\,, \tag{3}$$

where ρ_0 is the density at the temperature of the coldest wall. The second is the Rayleigh number, which relates the driving forces to the resistive mechanisms,

$$\mathrm{Ra} = \frac{g\alpha L^3\rho_0\Delta T_{\mathrm{t}}}{\kappa\eta_{\mathrm{L}}}\,, \tag{4}$$

where g is the gravitational acceleration and α is the thermal expansion coefficient. $\Delta T_{\mathrm{t}} = T'_{\mathrm{C}} - T'_{\mathrm{H}}$ is the total super-isentropic temperature difference between the hot ($T' = T'_{\mathrm{H}}$) and the cold ($T' = T'_{\mathrm{C}}$) boundaries (prime denotes physical dimension).

The third governing equation applying to liquid and solid, energy conservation without any volumetric heat source, is written as

$$\frac{\mathrm{D}T}{\mathrm{D}t} = \nabla^2 T \,. \tag{5}$$

The temperature field T is scaled as $T = (T' - T'_{\mathrm{C}})/(T'_{\mathrm{H}} - T'_{\mathrm{C}})$. Normalized temperature T is thus bounded by 0 and 1 in the computational cavity.

Thermodynamical properties (thermal diffusivity κ, heat capacity at constant pressure C_{P}, thermal conductivity k) are considered to be constant and independent of temperature, and are the same for the liquid and solid. Density is also taken to be constant and the same for both phases following the Boussinesq approximation (density variations due to temperature gradients are only considered in the buoyancy term).

At the phase change interface, the following conditions must be verified. There are three requirements on temperature: continuity of temperature that is equal to the melting temperature, $[T]^+_- = 0$, and $T = T_{\mathrm{M}}$, and a jump in the heat flux corresponding to the release or consumption of latent heat $\mathcal{L}$ (Crank, 1984; Davis, 2001),

$$[\boldsymbol{\nabla} T \cdot \boldsymbol{n}]^+_- = \mathrm{St}\, \boldsymbol{u} \cdot \boldsymbol{n} \,. \tag{6}$$

The brackets $[\ ]^+_-$ indicate the jump of a given quantity over the phase interface. $\boldsymbol{u} = (u_{\mathrm{x}}, u_{\mathrm{z}})$ is the velocity of the phase change boundary and $\boldsymbol{n} = (n_{\mathrm{x}}, n_{\mathrm{z}})$ its unit normal vector pointing toward the liquid, cf. Fig.1. The Stefan number St is

$$\mathrm{St} = \frac{\mathcal{L}}{C_{\mathrm{P}} \Delta T_{\mathrm{t}}} \,. \tag{7}$$

It compares the latent heat to the specific heat C_{P}. The larger St, the more important latent heat effects are and thus the slower the interface moves.

In terms of velocity constraints, the melting front is a no-slip boundary, i.e., for a unit tangent vector $\boldsymbol{t}$, the condition $\boldsymbol{v} \cdot \boldsymbol{t} = 0$ must be fulfilled. The next condition results from mass balance allowing the density change over the phase transition. Suppose that the geometry of the solidifying system is as in Fig.1, with the position of the interface described by the function $z = h(x, t)$. Then the vertical velocity of the interface, u_{z}, must satisfy (Davis, 2001)

$$\Delta\rho \, u_{\mathrm{z}} = \rho_{\mathrm{L}} \left(v_{\mathrm{z}} - v_{\mathrm{x}} \frac{\partial h}{\partial x} \right) , \tag{8}$$

where $\Delta\rho$ is the difference between the densities of solid and liquid, $\Delta\rho = \rho_{\mathrm{S}} - \rho_{\mathrm{L}}$, and v_{x} and v_{z} are the horizontal and vertical components of the fluid velocity vector $\boldsymbol{v} = (v_{\mathrm{x}}, v_{\mathrm{z}})$. In our case $\Delta\rho = 0$, thus the above two conditions are satisfied if and only if $\boldsymbol{v} = \boldsymbol{0}$ at the melting front.

3. Front tracking method

The first numerical approach for the solidification/melting process with fluid flow in the melt involves treating the solid and the liquid as distinct domains coupled by the boundary conditions at the phase change front. At each time the position of the boundary is explicitly computed. In order to account for its motion, either mesh deformation or a suitable mapping that transforms the problem on a fixed mesh is required. This strategy is suitable for the isothermal phase change of a pure substance and might not be accurate enough when the state transformation happens over a finite temperature interval. Solving for proper equations, Eqs.(1), (2) and (5), involves finding the velocity field in the liquid and the temperature field in the solid and the liquid. As a part of the solution, the position of the melting/freezing front arises as it is not known a priori.

The finite element (FE) free software Elmer (CSC – IT Center for Science, 2010) is used to numerically solve the equations described above. First, the energy equation is solved using the velocity field from the previous timestep to give the new temperature distribution. Next, the Navier-Stokes equation is solved in order to determine the new velocity. The temperature field explicitly defines the new position of the melting/freezing front and the mesh nodes must be redistributed so as to follow the interface movement. The solution of the problem thus involves four steps, four particular solvers, that are weakly coupled. The linear systems related to different physical phenomena are solved one-by-one (using iterative or direct methods, cf. below) without any common iterations.

3.1. Navier-Stokes and heat equations

The classical Galerkin method (e.g. Hughes, 1987) implemented for simulations of natural convection often results in spurious oscillations whose origin is in the advection terms. Thus, several stabilization methods have been developed to overcome this problem including the residual free bubbles method (Baiocchi et al., 1993) or using Taylor-Hood elements (Taylor and Hood, 1973). In our simulations the stabilization scheme proposed by Franca et al. (1992) and Franca and Frey (1992) is applied.

The Galerkin discretization of partial differential equations by the finite element method (FEM) is applied with subsequent linearization of the nonlinear convective term in the Navier-Stokes equation. The Picard linearization used is somewhat slower in convergence than the Newton's method, but has a larger radius of convergence.

Two main strategies in searching for the solution of the linear set of

discretized equations include direct and iterative methods. For small systems, it is desirable to use the former strategy, which finds the exact solution up to machine precision but demands a large memory usage. As a direct solver we use Unsymmetric MultiFrontal method (UMFPACK) (Davis, 2004). On the other hand, iterative solvers generate an improving approximate solution to the given problem. These are useful for 3D geometries or large 2D systems. As an iterative solver strategy, the BiConjugate Gradient Stabilised method (BiCGStab) (Van der Vorst, 1992) with incomplete LU (ILU) factorization as a preconditionner is used.

For the time-stepping strategy, the Crank-Nicolson scheme (Crank and Nicolson, 1947) is chosen. In a single time step, the coupling between individual solvers proceeds in a weak manner (computation of one step after another), thus no coupled iterations of the system are run.

3.2. Motion of the phase interface and mesh update

Eq.(6), which expresses the heat balance at the melting front, is used to obtain the velocity of the interface. Supposing that the interface moves only in the vertical direction z, its velocity in the z-direction u_z is obtained as

$$[\boldsymbol{\nabla} T \cdot \boldsymbol{n}]_-^+ = \mathrm{St}\, n_\mathrm{z} \left(u_\mathrm{z} - D_\mathrm{u} \nabla^2 u_\mathrm{z} \right) , \tag{9}$$

where an artificial diffusion D_u has been added because otherwise the algorithm is subject to numerical oscillations. In order not to significantly influence the results, the condition $D_\mathrm{u} \ll \Delta^2$ for the diffusion factor must be fulfilled, with Δ being the characteristic grid size.

In order to compute the nodal heat fluxes in Eq.(9) for the solid and the liquid, respectively, the residual of the discrete system for the heat equation

without the effects of boundary conditions is used. This procedure provides the most accurate estimate of the nodal fluxes.

The new position of the phase interface is then obtained from the computation of its motion within one time step Δt: $\delta h = u_z \Delta t$. In order to account for the movement of the melting front, which is always described by the same mesh nodes, the grid must be distorted. The new node distribution results from solving a non-physical elastic equation for the mesh displacement $\boldsymbol{d}$

$$-\nabla \cdot \left(\mu \left(\nabla \boldsymbol{d} + (\nabla \boldsymbol{d})^T \right) + \lambda \nabla \cdot \boldsymbol{d}\, I \right) = 0\,, \tag{10}$$

where I is the unity tensor. Fictive Lamé parameters μ and λ, representing the elastic properties of the mesh, are chosen arbitrarily and can eventually help to enhance the quality of the new mesh. We can express the Lamé coefficients in terms of Youngs modulus Y and Poisson ratio ν

$$\mu = \frac{Y\nu}{(1-\nu)(1-2\nu)}\,, \quad \lambda = \frac{Y}{2(1+\nu)}\,. \tag{11}$$

The larger the value of Y, the stiffer the mesh is. This might be particularly useful for adding local rigidity near singularities, i.e. around the corners. The larger the Poisson ratio, the better the elements maintain their volume until reaching the critical value of $\nu = 0.5$, when Eq.(11) becomes singular. Nevertheless, with smooth meshes these have only minor effects and we keep them constant for all numerical experiments.

Coupling between the distorted mesh and interface position comes through the Dirichlet boundary condition at the melting front where for the vertical displacement d_z the relationship $d_z = \delta h$ holds.

Using the displacement of nodes allows us to significantly reduce the computational time compared to completely regenerating the mesh at each time

step. On the other hand, there is no way to ensure that the new mesh guarantees good computational precision since elements can be strongly strained. Thus, small changes in geometry are favorable for retaining a numerically accurate mesh.

Since movement of the mesh is involved, in Eqs.(1) and (5) the mesh velocity $\boldsymbol{v}_{\mathrm{m}}$ must be accounted for. The so-called Arbitrary Lagrangian-Eulerian (ALE) description (Donea et al., 2004), in which the mesh nodes can be moved about an arbitrary distance in between nodes following the continuum movement (Lagrangian description) or being held fixed (Eulerian approach), is implemented. The total time derivative term is then

$$\frac{\mathrm{D}\bullet}{\mathrm{D}t} = \frac{\partial \bullet}{\partial t} + (\boldsymbol{c} \cdot \boldsymbol{\nabla})\bullet \,, \tag{12}$$

where $\boldsymbol{c}$ is the convective velocity, $\boldsymbol{c} = \boldsymbol{v} - \boldsymbol{v}_{\mathrm{m}}$. In Lagrangian approaches, the mesh velocity is equal to the material velocity, i.e. $\boldsymbol{c} = \boldsymbol{0}$, and the total derivative simplifies to the partial derivative. The Eulerian formulation keeps the mesh non-deformed, and thus $\boldsymbol{c} = \boldsymbol{v}$ holds. In the present model, the mesh motion is computed such that the phase change interface coincides with a mesh line.

3.3. Mesh

In 2D simulations quadrilateral bilinear elements are used. For 3D simulations, hexagonal elements with 8 nodes are used. At the beginning of the computation, the grid is composed of rectangular elements that deform with the motion of the melting front. A schematic example of a deformed mesh is depicted in Fig.2(a) with finer and coarser resolution in the liquid and solid, respectively. The red line represents the phase change front.

Input files for `Elmer` simulation together with mesh files corresponding to the simulations presented can be found at `http://perso.ens-lyon.fr/martina.ulvrova/research.php`.

4. Fixed grid method

In order to eliminate the necessity of explicitly satisfying the thermal conditions between the two phases, we can describe heat transfer in the solid and the liquid using a single governing equation for energy conservation written in terms of the enthalpy variable H on a fixed grid in an Eulerian reference frame (Crank, 1984). The system of equations (5)-(6) comprising additionally the heat balance at the melting/freezing interface is replaced by a single equation

$$\frac{\partial H}{\partial t} + \boldsymbol{v} \cdot \nabla H = \nabla^2 T \,, \tag{13}$$

implicitly containing the effect of the phase change. The total enthalpy of the system is equal to the temperature in the solid part and is increased in the liquid part by the contribution from latent heat

$$H(T) = \begin{cases} T & \text{if } T \leq T_{\mathrm{M}} \,, \\ T + \mathrm{St} & \text{if } T > T_{\mathrm{M}} \,. \end{cases} \tag{14}$$

Conditions (14) can be combined into one single equation $H = T + \mathrm{St}\, f_{\mathrm{L}}$, with f_{L} the liquid fraction. Introducing the definition of enthalpy into Eq.(13) we obtain

$$c^{\mathrm{A}} \frac{\mathrm{D}T}{\mathrm{D}t} = \nabla^2 T \,, \tag{15}$$

with the nondimensional apparent heat capacity

$$c^{\mathrm{A}} = \frac{\mathrm{d}H}{\mathrm{d}T} = 1 + \mathrm{St} \frac{\partial f_{\mathrm{L}}}{\partial T} \,. \tag{16}$$

In this case, a temperature field is obtained as a solution, which is used to reconstruct a posteriori the position of the melting/freezing front. However, the mechanical boundary condition, which requires the solid not to deform, must also be fulfilled. This is achieved by imposing a viscosity strongly dependent on the liquid fraction f_{L}. Here, we use

$$\eta = \exp\left(B(1 - f_{\mathrm{L}})\right) , \tag{17}$$

where B is a parameter that defines the viscosity ratio between the solid and the liquid. Equations for fluid flow, Eqs.(1) and (2), are then solved in the whole cavity.

Taking f_{L} as the Heaviside step function implicitly imposes the condition Eq.(9) at the solid liquid boundary. It leads to a discontinuity in the enthalpy. However, treating singularities with methods that compute derivatives using finite differences requires regularization techniques. Hence, when using the enthalpy formulation the phase change is not sharp but always happens over a mushy region of finite thickness. Thus, the enthalpy method is naturally suitable for melting/solidification processes of solids/liquids consisting of multiple components.

Several numerical approaches have been developed to solve Eq.(13) including source update methods, where the latent heat effects are put into a separate term corresponding to the source term, enthalpy linearization or using the apparent heat capacity (e.q. Voller, 1996; Voller et al., 1990; Voller, 1985). In our paper we choose the latter one, thus solving governing Eq.(15) instead of Eq.(13) together with the mass and momentum equations. The advantage is that the energy equation remains formally the same as for the standard heat transfer model and only the definition of the heat capacity

changes, which enables the phase change to be easily incorporated into an already existing convection code. On the other hand, the drawback of using a temperature dependent heat capacity c^{A} is that it forbids writing Eq.(15) in a fully conservative finite volume form. Thus, this method is more suitable for small Stefan numbers, roughly lower that 1, for which the temperature dependence of c^{A} is limited. As a remedy for high Stefan number cases, fine spatial resolution can be employed to ensure a balanced heat budget at steady state. Fine resolution is also needed in the vicinity of the phase boundary where the largest enthalpy gradient occurs.

In order to model a phase change using an effective heat capacity we have to define the liquid fraction as a function of temperature. For a sharp phase transformation this should be a step function with value one in the liquid and zero in the solid. As mentioned earlier, smoothing of the discontinuity must be incorporated in order for the system to be solved numerically. Hence, the phase change occurs over a temperature interval $2\,\epsilon$ that defines the width of a mushy region and we choose the phase fraction function to be

$$f_{\mathrm{L}} = \frac{1}{2}\left(1 - \tanh\left(\frac{T_{\mathrm{M}} - T}{\epsilon}\right)\right), \tag{18}$$

which gives us the derivative needed in Eq.(15). The parameter ϵ can be seen as a physical parameter linked to the width of the mushy region, which is observed to exist in experiments of phase changes in complex compounds. The extent of the mush also depends on the vigor of convection that determines the temperature gradients at the phase change interface.

The f_{L} function together with viscosity η are depicted in Fig.3. The critical parameters in these definitions are the temperature phase interval $2\,\epsilon$ and the parameter B that controls the viscosity values in the solid and

mushy regions.

The physical situation that we consider here is different from that of solid-solid phase transitions in the Earth's mantle, where an effective heat capacity is introduced to treat latent heat effects due to a solid-solid phase transition in mantle convection simulations (Christensen and Yuen, 1985): firstly, the dynamics associated with solid-solid phase transformations in the interior of the Earth are dominated by changes in their depth (pressure) caused by lateral temperature variations, which contrasts to melting that we here consider to be purely dependent on temperature; also, with a solid-solid phase change in the mantle, flow is allowed across the boundary which differs from our case where the solid does not deform.

We implement the liquid/solid transition into the finite volume code `StagYY`; cf. Tackley (1993, 1996, 2002, 2008) for technical details of the code, and repeat here only some of its important technical aspects.

`StagYY` is intended to model Rayleigh-Bénard convection of extremely viscous fluids in the infinite Prandtl number approximation, so the time derivative in Eq.(2) is neglected. A staggered grid discretization is used, hence velocity components are defined at cell boundaries while pressure and temperature are defined at cell centers. Of great importance is that `StagYY` is capable of handling large viscosity variations of up to 19 orders of magnitude (Tackley, 2008).

Viscosity, which is also defined in the cell center, needs to be interpolated to the cell corners (in 2-D) or cell edges (in 3-D) in order to compute the viscous shear stresses. There are several viscosity averaging strategies including harmonic mean, arithmetic mean or geometric mean. Choice of

the averaging law is particularly important in regions of abrupt viscosity change (Deubelbeiss and Kaus, 2008), i.e. in this case around the phase transition. Arithmetic averaging would give a stiffer mush while harmonic averaging would allow the mush to deform more (Schmeling et al., 2008). These differences would be noticeable only in cases where insufficient spatial resolution is employed. Geometric averaging lies in the middle of arithmetic and harmonic mean and we decide to use this for all of our experiments.

The governing Eq.(15) of the enthalpy formulation of the Stefan problem is discretized on a regular non deforming mesh and treated using the Eulerian description of motion. The position of the melting front is then read off the temperature solution. A schematic example of the grid together with the phase boundary is depicted in Fig.2(b).

5. Benchmarking both codes

In order to test our numerical solutions we performed two- and three-dimensional calculations in several different settings. Firstly, we test our tools using an exercise proposed by Bertrand et al. (1999) in which a 2D solid cavity is heated from a vertical wall so that the single component phase subsequently melts.

Secondly, we compare the two methodologies for solving the phase change problem coupled with Rayleigh-Bénard convection in the melt. The liquid layer is heated from below and cooled from above so that the melting front stays in between.

Next, we draw a qualitative comparison between our 3D numerical calculations and experimental results published in Davis et al. (1984) for a

horizontal layer heated from below.

Finally, we quantify the effects of the two parameters needed when employing the enthalpy formulation: the temperature interval $2\,\epsilon$ over which the phase transition occurs and the parameter B defining the viscosity ratio between the solid and the liquid.

5.1. Melting driven by natural convection in a square cavity

Consider a square cavity that is initially solid and maintained at an initial temperature that is equal to the melting temperature $T_{\mathrm{M}} = 0$. Insulating horizontal walls are imposed and the right vertical wall is kept at T_{M}, cf. Fig.4. Zero velocity initial conditions are prescribed and all boundaries are no-slip.

At time $t = 0$ the temperature of the left vertical wall is raised and kept at a temperature $T_{\mathrm{H}} > T_{\mathrm{M}}$, in order to allow melting to start. After the initial transient stage dominated by heat conduction, convection in the melt arises as the thickness of the liquid layer increases. Finally, heat transfer through the liquid phase is controlled by convection. The phase change interface remains planar when heat transfer occurs by conduction. As early as convection sets up, upper part of the cavity melts at higher rate due to high temperature gradients.

Numerical experiments are first performed using the `Elmer` code. As was described in Section 3, the position of the melting/freezing front is always assigned to the same mesh nodes, resulting in deformation of the grid corresponding to latent heat consumption/release. Consequently, the number of mesh nodes changes neither in the solid nor in the liquid during a simulation. Thus, for all numerical experiments, both the solid and the liquid must exist

from the beginning to the end of the run. Hence, in the set-up test case we use as initial conditions for the temperature the analytical solution of the 1D Stefan problem (Davis, 2001) resulting after time $t = 5 \cdot 10^{-3}$ has elapsed. The parameter values of the simulation correspond to Case 3 in Bertrand et al. (1999), i.e. $\mathrm{Pr} = 50$, $\mathrm{Ra} = 10^7$ and $\mathrm{St} = 10$. The initial position of the phase front is thus $x_{\mathrm{init}} = 0.0311149996856$.

The rectangular 2D mesh is composed of bilinear elements. Initial equal spacing in both directions is imposed. We use 60 elements in the vertical direction and 15 and 35 elements in the horizontal direction in the liquid and solid parts of the cavity, respectively. A fixed time step $\mathrm{d}t = 2 \cdot 10^{-5}$ is used in the Crank-Nicolson method.

Snapshots of the temperature field at four different times are depicted in Fig.5. A comparison of our solution with the results published in Bertrand et al. (1999) is plotted in Fig.7. Fig.7(a) shows the time evolution of the average Nusselt number, which is the dimensionless heat flux density, over the hot vertical wall. Fig.7(b) shows the position of the melting front at time $t = 0.1$.

Numerical results published in Gobin and Le Quéré (2000) show a large dispersion of possible solutions, e.g. in the case of melting front positions at time $t = 0.1$ (Fig.7(b)) the dispersion at $z = 1$ is around 9%. The differences are caused by the various implementations of the time and spatial resolutions and not by the mathematical formulations used (Gobin and Le Quéré, 2000). However, in the absence of an exact solution, it is hard to know which code produces the most accurate solution.

Nevertheless, our solutions lie in the region of published solutions, being

closest to the results of Le Quéré or Wintruff (Gobin and Le Quéré, 2000). The model of Le Quéré uses the enthalpy formulation. The enthalpy is approximated in this case by a continuous and piecewise linear function with phase change interval 0.001. A 2^{nd} order centred finite volume discretization is used in the spatial domain. Wintruff uses the control volume finite element approach together with a front tracking method to account for the latent heat effects; the interface position is thus calculated explicitly.

From this benchmark comparison we conclude that `Elmer` provides an accurate tool capable of handling the crystallization/melting processes closely coupled with convective motions in the liquid. The impossibility of modelling complete solidification/melting of the cavity is compensated by the small computational cost.

The same exercise was repeated with the `StagYY` code, which allows the computation of the phase transformation and convective motion in the infinite Prandtl number approximation. It is important to note that the formulation we have chosen is not suitable for this test. As all the solid is initially held at the solidification temperature, the last term in Eq.(16), which should be non-zero only in the mushy region between the solid and the liquid, contributes to the solution over the whole solid. We thus modify the phase fraction function so that the mushy region occurs mainly in the liquid by adding a shift ϵ_{S}

$$f_{\mathrm{L}} = \frac{1}{2}\left(1 - \tanh\left(\frac{T_{\mathrm{M}} + \epsilon_{\mathrm{S}} - T}{\epsilon}\right)\right), \tag{19}$$

and we use $\epsilon_{\mathrm{S}} = \epsilon$.

The computations were performed on a mesh with 256×256 finite volumes. The same initial conditions described above for Elmer were used.

Snapshots of the temperature field are shown in Fig.(6). Comparison of the interface position at time $t = 0.1$, which is in this case represented by the isotherm with the temperature value $T = T_{\mathrm{M}} + \epsilon_{\mathrm{S}}$, together with time evolution of the heat flux over the hot vertical wall, are presented in Fig.(7). While the form of the phase interface falls into the interval of solutions obtained in Gobin and Le Quéré (2000), the most significant difference is observed in the time dependence of the Nusselt number. This difference is not caused by neglecting the inertia force but rather is related to the limitation of the method implemented.

5.2. Rayleigh-Bénard convection during melting of a single component solid

As a second test case, melting in a square cavity heated from below is studied. The schematic layout is depicted in Fig.8. In a box of height L, we impose a temperature difference between the top and bottom boundaries: $T_{\mathrm{C}} = 0$ at the upper surface and $T_{\mathrm{H}} = 1$ at the lower one, so that with an imposed melting temperature of $T_{\mathrm{M}} = 0.5$ the upper region stays solid while the lower one is molten. If the Rayleigh number is high enough, Rayleigh-Bénard convection establishes itself in the liquid, which leads to the development of corrugations of the phase change interface.

Vertical walls are taken to be insulating. All boundaries are considered to be no-slip and we start from a conductive solution, $T = 1 - z$, with perturbations $P = 0.1 \sin(\pi x) \sin(2\pi z)$ in the liquid layer. With $T_{\mathrm{M}} = 0.5$, initially 50% of the computing volume is liquid. Parameters of the test case are chosen to be as follows: $\mathrm{St} = 0.1$ and $\mathrm{Ra} = 10^5$. As time increases the fluid starts to convect. Ascending current develops in the middle of the cavity and the fluid descends along the vertical walls. As a consequence, the

initially flat interface becomes corrugated due to the variable temperature gradient normal to the melting front.

The two numerical implementations differ in treating the momentum equation. In the fixed grid method, an infinite Prandtl number approximation is considered. Based on laboratory experiments, it was shown by Krishnamurti (1970a,b), that this simplification is valid for $\mathrm{Pr} > 100$. We thus use $\mathrm{Pr} = 1000$ for the distorting grid method so as to make the comparison of the two sets of results meaningful.

In the moving mesh code, the mesh used during the simulation consists of 50 elements in horizontal direction and 40 and 10 elements in vertical direction in the liquid and the solid, respectively, with the chosen timestep size equal to $2 \cdot 10^{-5}$. The enthalpy method formulation is solved on a grid consisting of 128×256 elements. The timestep is chosen so that the Courant number does not exceed 1. A clear advantage of the moving grid method appears here: very few grid points can be used in the solid since only diffusion proceeds there. Thus it allows optimization of the computational cost. On the contrary, the enthalpy method must handle large viscosity contrasts in the vicinity of the phase transition and thus requires fine mesh resolution. As a possible strategy adaptive grid refinement can be employed (e.g. Davies et al., 2011), which allows having a fine mesh resolution where needed. However, its implementation is beyond the scope of this work, and we use a static regular mesh that is dense enough to manage the large viscosity variations.

Comparison of results from the two methods is shown in Fig.9-13. Fig.9 shows the time evolution of the mean temperature in the cavity and the average Nusselt number over the hot wall. At steady state, the relative

difference between the two solutions is less than 1% for the mean temperature and around 2% for the bottom heat flux.

These differences also show up in the thermal profiles displayed in Fig.10, where vertical temperature profiles are presented at four different times at a distance $x = 0.25$ from the left boundary. The convecting core is slightly colder with the moving mesh code than with the fixed grid one. Corresponding velocity profiles are plotted in Fig.11. Convective velocities in the liquid are mildly faster for moving mesh simulations.

A comparison of the interface position obtained by the two approaches is depicted in Fig.12. In the case of the distorted grid, larger amplitudes of corrugations are obtained. Comparing the position of the melting front at time $t = 0.2$, the relative difference between the two average solutions is 0.8%. The maximum of the difference between deviations of the interface positions is 0.006.

Snapshots of the complete temperature field at four different times using both methods together with maps of their difference are depicted in Fig.13. All results show an excellent agreement in the temperature fields. The differences are concentrated around the transition between the two phases. Compared to the results of Viswanath and Jaluria (1993), the two sets of our solutions show much better agreement in terms of interface position and temperature structure. In the case of Viswanath and Jaluria (1993) the large discrepancies between the solutions might be caused mainly by the insufficient resolution they used within the enthalpy approach. In contrast to what Viswanath and Jaluria (1993) reported, the interface positions obtained by the moving mesh method are always higher than those obtained by the

enthalpy method.

5.3. Pattern selection in a crystallizing 3D convective horizontal layer

Davis et al. (1984) experimentally examined a single-component liquid that solidifies/melts in a plane layer heated from below and cooled from above. The convective pattern established (rolls or hexagons) depends on the ratio of solid to liquid thicknesses A and the Rayleigh number. Davis et al. (1984) chose to relate all results to a purely conductive state in which the interface is planar. Thus, A is the ratio of the two heights in the case where only heat conduction proceeds. Small values of A lead to roll-like convective pattern selection whereas large A results in hexagonal convection.

Here, we qualitatively study these results and show the transition between these two configurations. Numerical simulations are carried out with the `StagYY` code, which is fully parallelized using domain decomposition and the Message Passing Interface library (MPI). We use a 3D layer with an aspect ratio of 8 in both horizontal directions, and $256 \times 256 \times 128$ grid cells in the two horizontal and vertical directions, respectively. Heating from below is imposed with insulating vertical walls and zero velocities at all boundaries. We pick the same parameters used in laboratory experiments, cf. Figure 3(a) and 3(b) in Davis et al. (1984). Results of the first case, computed for $\mathrm{Ra} = 8.4 \cdot 10^3$ and $A = 0.03$, i.e. a liquid layer approximately thirty times thicker than the solid one for pure conduction, are presented in Fig.(14)(a). We show the corrugated solid-liquid interface at state close to the steady state. Indeed, we observe convective roll patterns. A second experiment is performed for $\mathrm{Ra} = 1.1 \cdot 10^4$ and $A = 0.36$, i.e. the liquid layer approximately three times as thick as the solid. Results are shown in Fig.(14)(b). In this case, hexagonal

patterns are observed, in agreement with experimental observations of Davis et al. (1984).

5.4. Choice of parameters in the enthalpy method

In order to test the influence of the two numerical parameters appearing in the enthalpy method (temperature interval $2\,\epsilon$ over which the phase transformation happens, which is related to the width of the mushy two-phase region, and the viscosity contrast B between the solid and the liquid), we perform a series of experiments with the following set-up: fixed temperatures at the bottom ($T_{\mathrm{H}} = 1$) and the top ($T_{\mathrm{C}} = 0$) are imposed together with insulating vertical walls and zero shear stress on the bottom and vertical boundaries. The velocity condition at the top boundary must be no-slip to further prevent deformation of the solid. The melting temperature is chosen to be $T_{\mathrm{M}} = 0.5$, and $\mathrm{Ra} = 3{\cdot}10^5$ and $\mathrm{St} = 0.1$ are imposed. Steady convection in a square box is then computed on a 128×128 grid.

The temperature field, together with the viscosity for two different values of parameter B, are depicted in Fig.15. The phase change temperature interval is here $\epsilon = 0.05$. Fig.15(e) shows the difference between the two solutions with the highest discrepancies around the phase transformation. This is caused by the fact that the parameter B primarily affects the viscosity gradients in the mush that in turn controls velocity values in this transition. The higher the value of B the lower the velocities in the two-phase region due to higher viscosity gradients. In the limiting case, velocities go to zero for temperatures higher than the melting temperature. However, having large viscosity gradients is numerically challenging. Thus, we determine the minimum value of B sufficient to create a stagnant solid region and being able

to sufficiently reduce the velocity values in the mush, by running a systematic investigation. The effect of B is shown in Fig.17(a) where we plot, as a function of B, the maximum of the relative difference between the temperature for the given value of B and that obtained for $B = 13$ (having a viscosity contrast of $2 \cdot 10^{11}$), chosen as a reference. The maximum relative difference can be kept below 10% if the viscosity contrast is larger than 10^3, which is the minimum to keep the solid from deforming. This is in agreement with experiments carried out for convection with strongly temperature dependent viscosity when a stagnant lid is formed for high enough viscosity ratios (Davaille and Jaupart, 1993).

The effect of the phase change interval ϵ is shown in Fig.16 where two cases with $\epsilon = 0.005$ and $\epsilon = 0.05$ are compared (with $B = 6$ for both experiments, corresponding to a viscosity contrast of $2 \cdot 10^5$). Fig.16(a) and (b) show the phase change interval in the two cases. The main effect of changing ϵ is to change the thickness of the two-phase region. This thickness ϵ_z can be related to ϵ by

$$\epsilon_z = \frac{\epsilon\, L}{\int_0^L \frac{\partial T}{\partial z}|_{\rm surf}\, {\rm d}x}\,. \tag{20}$$

As a normalization factor, the mean temperature gradient at the surface is suitable since it is approximately constant in the solid (Fig.10).

Fig.16(e) depicts the relative difference between the two temperature solutions. Again, the largest difference between solutions is found around the melting front. Results of the systematic study are displayed in Fig.17(b). As a reference solution, the case with the smallest $\epsilon = 0.001$ is taken. The relative difference is less than 1% for ϵ_z of order Δz or less and is kept below the 10% level for nearly the whole studied interval. Using a larger epsilon

amounts to treating a large two-phase region and could be a good modelling approach for a convection situation in which a thick mushy layer develops.

6. Thermal evolution of the crystallizing basal magma ocean (BMO)

In this section we use the tools developed above to conduct a series of numerical experiments to derive the heat transfer laws for the convecting liquid layer undergoing crystallization/melting. These laws are subsequently applied to the magma ocean that could have been lying between the Earth's core and solid mantle since the formation of the planet (Labrosse et al., 2007).

6.1. Heat transfer by Rayleigh-Bénard convection interacting with a freezing front

We consider the setting depicted in Fig. 1 where a liquid layer heated from below underlies the solid layer, similar to the second test case. The interface is locked in the computing box as we impose for the melting temperature $T_\mathrm{C} < T_\mathrm{M} < T_\mathrm{H}$.

The dimensionless heat flux is expressed by the Nusselt number, here termed effective since it is written with variables applying to the liquid layer,

$$\mathrm{Nu_{eff}} = \frac{\mathrm{Q}}{\frac{\mathrm{k}\Delta\mathrm{T_L}}{\langle \mathrm{h} \rangle}} \,, \tag{21}$$

where Q is the actual heat flux density coming in and out of the box, $\Delta T_\mathrm{L} = T'_\mathrm{H} - T'_\mathrm{M}$ the temperature difference across the convective zone and $\langle h \rangle$ its average thickness. We want to describe $\mathrm{Nu_{eff}}$ as a function of the effective Rayleigh number based on the temperature difference ΔT_L and $\langle h \rangle$,

$$\mathrm{Ra_{eff}} = \frac{\mathrm{g}\alpha \langle \mathrm{h} \rangle^3 \rho_0 \Delta \mathrm{T_L}}{\kappa \eta_\mathrm{L}} \,. \tag{22}$$

Combining with Eq.(4) we have $\mathrm{Ra_{eff}} = \langle \mathrm{h} \rangle^3 (1 - \mathrm{T_M})\mathrm{Ra}$. Here, $\langle h \rangle$ does not have any physical dimension. For the sake of simplicity, we use the same symbol as above in Eq.(22). In the numerical experiments $\mathrm{Ra_{eff}}$ is calculated a posteriori, Ra being imposed as an input parameter. We explore the $\mathrm{Nu_{eff}}(\mathrm{Ra_{eff}})$ relationship at two different Prandtl numbers, $\mathrm{Pr} = 7$ (equivalent to that of water) and $\mathrm{Pr} = \infty$. Clarification of the parameter choice is discussed below in Section 6.2 and is motivated by our intention to use the scaling laws for the BMO. We do not aim to simulate the long term cooling history of the system but focus on heat transfer at statistical steady-state. All experiments are thus conducted with a balanced energy budget.

Experiments at $\mathrm{Pr} = 7$ and $\mathrm{St} = 0.9$ are performed with the moving grid method. The aspect ratio of the computation domain is kept at a value of 4 but the resulting liquid layer has an aspect ratio in the range from 5 to 9. The number of finite elements in the grid depends on the value of the Rayleigh number. The finest resolution for highest Rayleigh number contains 500 elements in horizontal direction and 85 and 10 elements in the vertical direction in the solid and liquid, respectively. Most of the calculations are performed on a grid with 300 elements in the horizontal direction and 45 and 10 elements in the vertical direction in the liquid and solid, respectively. The grid is refined in the vertical direction in the thermal boundary layers in the liquid. The bottom and vertical velocity boundary conditions are free slip with thermally insulating vertical walls. The initial condition for temperature is a linearly varying profile in the solid. In the liquid for cases with small Rayleigh numbers an isothermal interior is prescribed with boundary layers at top and bottom plus small random perturbations. The phase front is

planar at the beginning of the run. Its initial position is fixed at a height of 0.6. Cases at high Rayleigh numbers were initiated from the final states of low Rayleigh number cases since the initial state has little effect on the final state for these runs.

Experiments at infinite Prandtl number where inertia is neglected and $\mathrm{St} = 0.1$ are done using the enthalpy method implemented in `StagYY`. We changed St because, for a given spatial resolution, a lower St ensures better energy conservation in the system. We compared calculations with both values using `StagYY` and found no significant effect on the dynamics of the flow and heat characteristics as both Stefan numbers are low enough.

We run experiments at aspect ratios of the computation domain 4 and 16 that give, after rescaling to the liquid layer, aspect ratio ranges $5 - 9$ and $18 - 36$, respectively. Again, the grid resolution varies with the Rayleigh number. The highest resolution cases contain 512×256 grid cells for the aspect ratio 4 and 1024×128 for the aspect ratio 16. In all experiments we independently verify that at steady state the heat flux balance is satisfied, i.e. the difference between the top and bottom heat flux does not exceed one percent. The bottom boundary is assumed to have zero shear stress and a fixed temperature. Vertical walls are periodic. The initial temperature profile is isothermal plus top and bottom boundary layers, and superimposed small random noise. Initial states for high Rayleigh number cases are derived from low Rayleigh number cases.

Fig.18 shows snapshots of the temperature field for steady and unsteady flows. At stationary state, Fig.18(a), (c) and (e), when variables such as mean temperature and heat fluxes remain constant with time, hot plumes are

centred below the highest points of the corrugated interface. This occurs at small Rayleigh numbers. At higher $\mathrm{Ra_{eff}}$, convection is oscillatory. Boundary layer instabilities develop periodically and are dragged by the main flow around convective cells (Krishnamurti, 1970b; Jarvis, 1984). Variables then oscillate evenly around a mean value.

At even higher $\mathrm{Ra_{eff}}$, convection is unsteady and non-periodic, Fig.18(b), (d) and (f), and variables oscillates irregularly around an average. A cluster of hot plumes forms at the bottom boundary drifting horizontally toward the main upwelling. Correspondingly, a set of cold instabilities is forming in the upper boundary layer. Progressive remelting and resolidification thus happens over a broad region where the clusters exist.

Each transition in convective style is generally accompanied by an abrupt change in the heat transfer (Malkus, 1954). The Rayleigh number at which this change occurs depends on the particular setting. In our experiments conducted at $\mathrm{Pr} = 7$ convection style changes from steady to oscillating at $\mathrm{Ra_{eff}} \sim 4{\cdot}10^4$. Such a sharp transition is not observed for experiments at high Prandtl number and steady and oscillatory experiments are treated together. A second transition to unsteady non-periodic flow happens at $\mathrm{Ra_{eff}} \sim 10^5$ for $\mathrm{Pr} = 7$ and $\mathrm{Ra_{eff}} \sim 10^6$ for infinite Prandtl.

We perform a systematic study for $\mathrm{Ra_{eff}}$ between 10^4 and 10^8. A least squares fit in the form $\mathrm{Nu_{eff}} = \beta_1 \mathrm{Ra_{eff}}^{\beta_2}$ is then applied for each of the regimes separately (Fig. 19). Coefficients β_1 and β_2 depend on the style of convection and physical parameters of the system (Pr). β_1 is around 0.2, and the exponent β_2 varies between 0.26 and 0.30 (Table 1).

Regime	Pr	β_1	Standard deviation	β_2	Standard deviation
Steady	7	0.227	0.0005	0.296	0.0005
Oscillating	7	0.229	0.0009	0.289	0.0008
Unsteady	7	0.258	0.0023	0.270	0.0016
Steady/Oscillating	∞	0.219	0.0658	0.255	0.0583
Unsteady	∞	0.116	0.0066	0.291	0.0079

Table 1: Least squares fitting of equation $\mathrm{Ra}_{\mathrm{eff}} = \beta_1 \mathrm{Nu}_{\mathrm{eff}}^{\beta_2}$.

6.2. Heat transfer and thermal evolution of the basal magma ocean (BMO)

Seismic ultra low velocity zones (ULVZ) at the bottom of the mantle have been detected for more than a decade now (Williams and Garnero, 1996; McNamara et al., 2010). These regions are non homogeneously distributed, have a variable thickness (5-40 km) and could consist of partial melt (Williams and Garnero, 1996). One scenario for their existence is that these zones are the remnants of the thick magma ocean that formed between the mantle and the core early after the Earth was formed and slowly solidified since (Labrosse et al., 2007). Using our parametrization of heat transfer developed in the previous subsection we infer the impact of the presence of the BMO on the thermal history of the Earth.

To obtain the typical value of the Stefan number, cf. Eq.(7), we need the estimation of ΔT_{t}, the total temperature difference over the solid and the liquid. As we show below, high convective vigor of the liquid layer maintains a small temperature difference across it. Thus ΔT_{t} is approximately equal to the temperature jump over the mantle boundary layer that is around 1000 K. Using this value results in a Stefan number of the order of unity. This implies

that timescales of resolidification/remelting are short and the system adjusts nearly instantly to the position of the hot/cold plumes.

Combining Eqs. (21) and (22) for the Nusselt and Rayleigh numbers, together with the fitting relation, we obtain

$$Q = \beta_1 k \left(\frac{\alpha g \rho_0}{\kappa \eta_{\mathrm{L}}} \right)^{\beta_2} \langle h \rangle^{3\beta_2 - 1} \, {\Delta T_{\mathrm{L}}}^{1+\beta_2} \,, \tag{23}$$

where coefficients β_1 and β_2 were determined experimentally (Table 1). Since β_2 is close to 1/3, the expression is only weakly sensitive to the depth of the liquid layer $\langle h \rangle$.

Eq.(23) is used to determine the temperature jump ΔT_{L}, which embodies the super-isentropic temperature difference across the BMO. In order to estimate its value, we use parameters listed in Table 2. The most critical but uncertain parameter determining the dynamics of the whole system is the viscosity. There are no experimental results for the viscosity at the pressure conditions pertaining to the bottom of the mantle and extrapolations are not reliable since the pressure effects are nonmonotonic (Liebske et al., 2005). It is assumed that it can be very low, varying between 10^{-2} and 1 Pa s (Solomatov, 2007). Hence, the Prandtl number is between unity and several thousand and $\mathrm{Ra}_{\mathrm{eff}}$ exceeds 10^{16}. Due to high convective vigour it is appropriate to use the values of coefficients β_1 and β_2 derived for unsteady flow. This results in ΔT_{L} lower than 0.1 K for $Q = 100\,\mathrm{mW\,m^{-2}}$. Hence, the superisentropic temperature difference maintained across the top and the bottom boundary layers of the BMO is minute and the temperature of the core follows the evolution of the liquidus temperature at the bottom of the mantle. The rate at which the BMO cools is approximately the same as that of the Earth's core, which explains why it can be maintained for so long.

Variable	Notation	Value	Unit
Gravitational acceleration	g	10	$\mathrm{m\,s^{-2}}$
Density	ρ_0	5500	$\mathrm{kg\,m^{-3}}$
Viscosity range	η_L	$10^{-2} - 1$	$\mathrm{Pa\,s}$
Coefficient of thermal expansion	α	10^{-5}	$\mathrm{K^{-1}}$
Heat capacity	C_P	1000	$\mathrm{J\,kg^{-1}K^{-1}}$
Thermal conductivity	k	5.5	$\mathrm{W\,m^{-1}K^{-1}}$
Heat flux into the solid mantle	Q	50-150	$\mathrm{mW\,m^{-2}}$

Table 2: Typical values of the basal magma ocean properties.

7. Conclusions

We have presented and tested two approaches to compute the evolution of convection with a solid-liquid phase transition. The moving grid method involves explicit tracking of the phase change interface position at each time. We have implemented it in the finite element code `Elmer` presented here to the geodynamics community. The melting/freezing front is assigned to nodes that follow its motion, deforming the whole mesh. It demands that the topology of the phase transition stays approximately aligned along one of the axes, so that a bijection between the phase change position and the coordinate always exists. This method is particularly suited for simulations with large Stefan number, in which the front is moving slowly and continuously compared to simulations with low Stefan number where quick jumps between two consecutive timesteps can exist.

We also implemented a fixed grid method, called the enthalpy method,

in the 3D finite volume code `StagYY` . In this case, the solid and the liquid, respectively, are treated together in a single non-deforming domain and the latent heat effects are implicitly included in the enthalpy variable. To account for the phase change, suitable functions depending on temperature must be prescribed to describe the liquid phase fraction and the viscosity. Because an abrupt change of material properties is difficult to model with such a method, a transition zone of a given width has to be introduced. This drawback can turn into a benefit if the considered material is not a pure pole. Indeed, a system with multiple components involves a mushy zone (Worster, 1997) which is approximately modeled through the zone of transition between the solid and the liquid. Compositional effects associated with the crystallisation of multi-component systems are important for the dynamics of both the mushy layer and the liquid but were not addressed in this simplifying first approach. They should be included in the future.

The phase transformation is incorporated by modifying the heat capacity that, due to temperature dependence, is non-constant. For a given grid, the accuracy of the solution can be enhanced by increasing the viscosity ratio between the solid and the liquid, which is ultimately needed to prevent deformation of the solid, thus limiting the velocities in the mushy region. However, large viscosity gradients are numerically challenging and also significantly increase the computational time.

Both moving and fixed grid codes display a good agreement in the benchmark tests.

We have used the two numerical tools to derive scaling laws for the heat flux as a function of the Rayleigh number in the molten region of the two-

phase system, depending on the convective vigour. We have applied the scaling law for unsteady flow to determine the temperature contrast between the base of the mantle and core in the presence of a deep magma ocean. We found that the temperature difference across the top and bottom boundary layers of the BMO is lower than 0.1 K, hence negligible, implying that the potential temperatures at the CMB for both the BMO and core are equal, therefore the BMO and core cool at the same rate.

References

Alboussière, T., Deguen, R., Melzani, M., 2010. Melting-induced stratification above the Earth's inner core due to convective translation. Nature 466, 744–747.

Baiocchi, C., Brezzi, F., Franca, L.P., 1993. Virtual bubbles and Galerkin-least-squares type methods (Ga.L.S.). Comput. Meth. Appl. Mech. Engrg. 105, 125–141.

Bertrand, O., Binet, B., Combeau, H., Couturier, S., Delannoy, Y., Gobin, D., Marcel Lacroix, M., Le Quéré, P., Médale, M., Mencinger, J., Sadat, H., Vieira, G., 1999. Melting driven by natural convection A comparison exercise: first results. Int. J. Therm. Sci. 38, 5 – 26.

Brandeis, G., Jaupart, C., 1986. On the interaction between convection and crystallization in cooling magma chambers. Earth Planet. Sci. Lett. 77, 345–361.

Brandeis, G., Marsh, B.D., 1989. The convective liquidus in a solidifying magma chamber: a fluid dynamic investigation. Nature 339, 613–616.

Christensen, U.R., Yuen, D.A., 1985. Layered convection induced by phase transitions. J. Geophys. Res. 901, 10291.

Coltice, N., Moreira, M., Hernlund, J., Labrosse, S., 2011. Crystallization of a basal magma ocean recorded by Helium and Neon. Earth Planet. Sci. Lett. 308, 193–199.

Crank, J., 1984. Free and Moving Boundary Problems. pp. 424. Oxford, UK: Oxford University Press.

Crank, J., Nicolson, P., 1947. A practical method for numerical evaluation of solutions of partial differential equations of the heat–conduction type. Proc. Cambridge Philos. Soc. 43, 50–67.

CSC – IT Center for Science, 2010. `http://www.csc.fi/english/pages/elmer`.

Davaille, A., Jaupart, C., 1993. Transient high-Rayleigh-number thermal convection with large viscosity variations. J. Fluid Mech. 253, 141–166.

Davies, D.R., Wilson, C.R., Kramer, S.C., 2011. Fluidity: A fully unstructured anisotropic adaptive mesh computational modeling framework for geodynamics. Geochem. Geophys. Geosyst. 120, 6001.

Davis, S.H., 2001. Theory of Solidification. Cambridge University Press, New York, 400pp.

Davis, S.H., Muller, U., Dietsche, C., 1984. Pattern selection in single-component systems coupling Bénard convection and solidification. J. Fluid Mech. 144, 133–151.

834 Davis, T.A., 2004. A column pre-ordering strategy for the unsymmetric-
835 pattern multifrontal method. ACM Trans. Math. Softw. 30, 165–195.

836 Deubelbeiss, Y., Kaus, B.J.P., 2008. Comparison of Eulerian and Lagrangian
837 numerical techniques for the Stokes equations in the presence of strongly
838 varying viscosity. Phys. Earth Planet. Inter. 171, 92–111.

839 Donea, J., Huerta, A., Ponthot, J.P., Rodríguez-Ferran, A., 2004. Arbitrary
840 Lagrangian-Eulerian Methods. Encyclopedia of Computational Mechan-
841 ics (Volume 1: Fundamentals), edited by E. Stein and R. De Borst and
842 T. J. R. Hughes.. chapter 14. pp. 413–437.

843 Franca, L.P., Frey, S.L., 1992. Stabilized finite element methods: II. The in-
844 compressible Navier-Stokes equations. Comput. Meth. Appl. Mech. Engrg.
845 99, 209–233.

846 Franca, L.P., Frey, S.L., Hughes, T.J.R., 1992. Stabilized finite element
847 methods: I. Application to the advective-diffusive model. Comput. Meth.
848 Appl. Mech. Engrg. 95, 253–276.

849 Gobin, D., Le Quéré, P., 2000. Melting from an isothermal vertical wall .
850 Synthesis of a numerical comparison exercise. Comp. Ass. Mech. Eng. Sc.
851 7, 289–306.

852 Hughes, T.J.R., 1987. The Finite Elment Method. Prentice Hall Inc., En-
853 glewood Cliffs, NJ, 803pp.

854 Jarvis, G.T., 1984. Time-dependent convection in the Earth's mantle. Phys.
855 Earth Planet. Inter. 36, 305–327.

856 Jellinek, A.M., Kerr, R.C., 2001. Magma dynamics, crystallization, and
857 chemical differentiation of the 1959 Kilauea Iki lava lake, Hawaii, revisited.
858 J. Volcan. Geotherm. Res. 110, 235–263.

859 Krishnamurti, R., 1970a. On the transition to turbulent convection. Part
860 1. The transition from two- to three-dimensional flow. J. Fluid Mech. 42,
861 295–307.

862 Krishnamurti, R., 1970b. On the transition to turbulent convection. Part 2.
863 The transition to time-dependent flow. J. Fluid Mech. 42, 309–320.

864 Labrosse, S., Hernlund, J.W., Coltice, N., 2007. A crystallizing dense magma
865 ocean at the base of the Earth's mantle. Nature 450, 866–869.

866 Liebske, C., Schmickler, B., Terasaki, H., Poe, B.T., Suzuki, A., Funakoshi,
867 K.I., Ando, R., Rubie, D.C., 2005. Viscosity of peridotite liquid up to 13
868 GPa: Implications for magma ocean viscosities. Earth Planet. Sci. Lett.
869 240, 589–604.

870 Malkus, W.V.R., 1954. Discrete Transitions in Turbulent Convection. Proc.
871 R. Soc. Lond. A 225, 185–195.

872 McNamara, A.K., Garnero, E.J., Rost, S., 2010. Tracking deep mantle reser-
873 voirs with ultra-low velocity zones. Earth Planet. Sci. Lett. 299, 1–9.

874 Notz, D., Worster, M.G., 2006. A one-dimensional enthalpy model of sea ice.
875 Ann. Glaciol. 44, 123–128.

876 Schmeling, H., Babeyko, A.Y., Enns, A., Faccenna, C., Funiciello, F., Gerya,
877 T., Golabek, G.J., Grigull, S., Kaus, B.J.P., Morra, G., Schmalholz, S.M.,

van Hunen, J., 2008. A benchmark comparison of spontaneous subduction models–Towards a free surface. Phys. Earth Planet. Inter. 171, 198–223.

Solomatov, V., 2007. Magma Oceans and Primordial Mantle Differentiation. Treatise on Geophysics: Evolution of the Earth, edited by editor–in–chief G. Schubert and volume editor D. Stevenson. Elsevier Ltd.. volume 9. pp. 92–119.

Tackley, P.J., 1993. Effects of strongly temperature-dependent viscosity on time-dependent, three-dimensional models of mantle convection. Geophys. Res. Lett. 20, 2187–2190.

Tackley, P.J., 1996. Effects of strongly variable viscosity on three-dimensional compressible convection in planetary mantles. J. Geophys. Res. 101, 3311–3332.

Tackley, P.J., 2002. Strong heterogeneity caused by deep mantle layering. Geochem. Geophys. Geosyst. 3.

Tackley, P.J., 2008. Modelling compressible mantle convection with large viscosity contrasts in a three-dimensional spherical shell using the yin-yang grid. Phys. Earth Planet. Inter. 171, 7–18.

Taylor, C., Hood, P., 1973. Numerical solution of the Navier-Stokes equations using the finite element technique. Computers & Fluids 1, 1–28.

Viswanath, R., Jaluria, Y., 1993. A comparison of different solution methodologies for melting and solidification problems in enclosures. Numer. Heat Transf. B 24, 77–105.

900 Voller, V.R., 1985. Implicit Finitedifference Solutions of the Enthalpy For-
901 mulation of Stefan Problems. IMA J. Numer. Anal. 5, 201–214.

902 Voller, V.R., 1996. An Overview of Numerical Methods for Solving Phase
903 Change Problems. Advances in Numerical Heat Transfer (Volume 1),
904 edited by W. J. Minkowycz and E. M. Sparrow.. chapter 9. pp. 341–375.

905 Voller, V.R., Swaminathan, C.R., Thomas, B.G., 1990. Fixed grid techniques
906 for phase change problems: A review. Int. J. Numer. Meth. Engng. 30,
907 875–898.

908 Van der Vorst, H.A., 1992. Bi-CGSTAB: A fast and smoothly converging
909 variant of Bi-CG for the solution of nonsymmetric linear systems. SIAM
910 J. Sci. Stat. Comp. 13, 631–644.

911 Williams, Q., Garnero, E.J., 1996. Seismic Evidence for Partial Melt at the
912 Base of Earth's Mantle. Science 273, 1528–1530.

913 Worster, M.G., 1997. Convection in Mushy Layers. Ann. Rev. Fluid. Mech.
914 29, 91–122.

915 Worster, M.G., Huppert, H.E., Sparks, R.S.J., 1993. The Crystallization of
916 Lava Lakes. J. Geophys. Res. 98, 15891–15901.

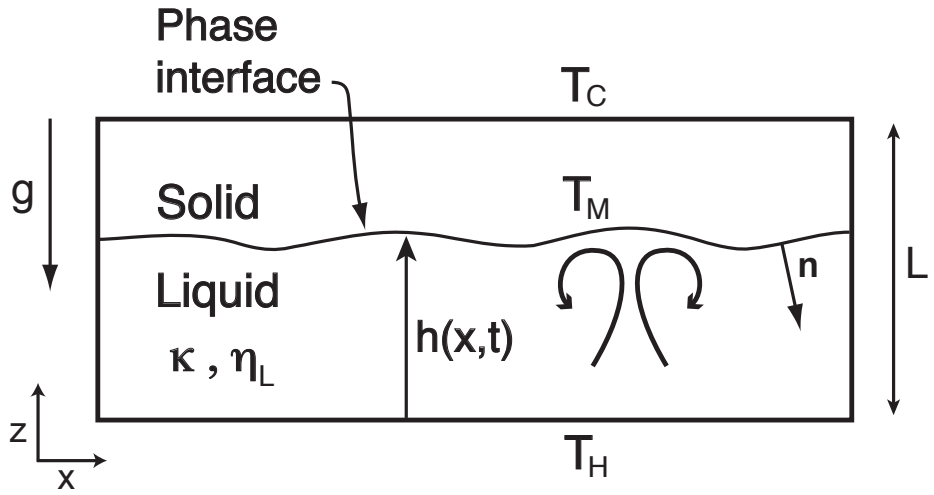

Figure 1: Schematic picture of a convecting liquid layer that solidifies/melts. The layer is heated from below and cooled from above so that the upper part is frozen and the phase transformation remains in the computing domain.

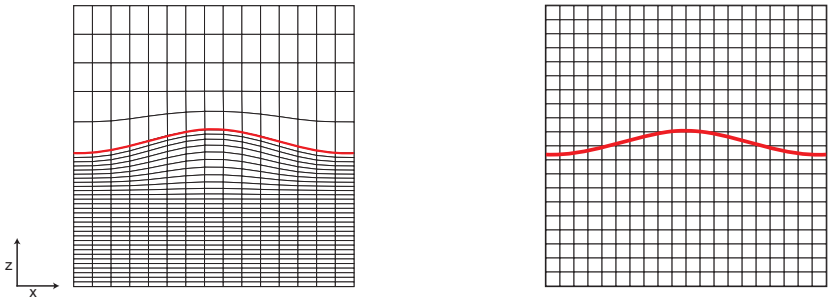

(a) Distorted mesh (b) Fixed grid mesh

Figure 2: Schematic pictures of moving and non-moving mesh for single component Stefan problem in configuration depicted in Fig.1. The melting front is denoted by the solid red line.

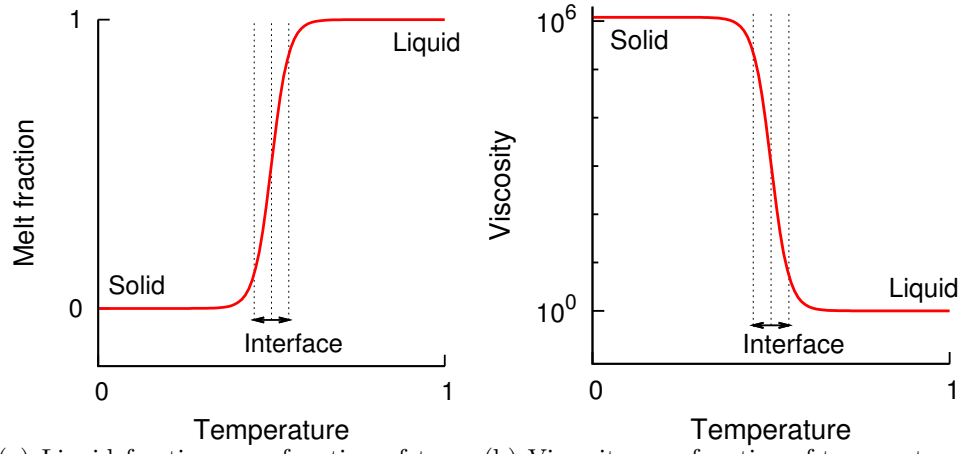

(a) Liquid fraction as a function of temperature. (b) Viscosity as a function of temperature.

Figure 3: Melt fraction and viscosity as a function of temperature for the enthalpy method. Dashed vertical lines denote the interval of phase transformation, in this case being 10% of the total temperature range ($\epsilon = 0.05$).

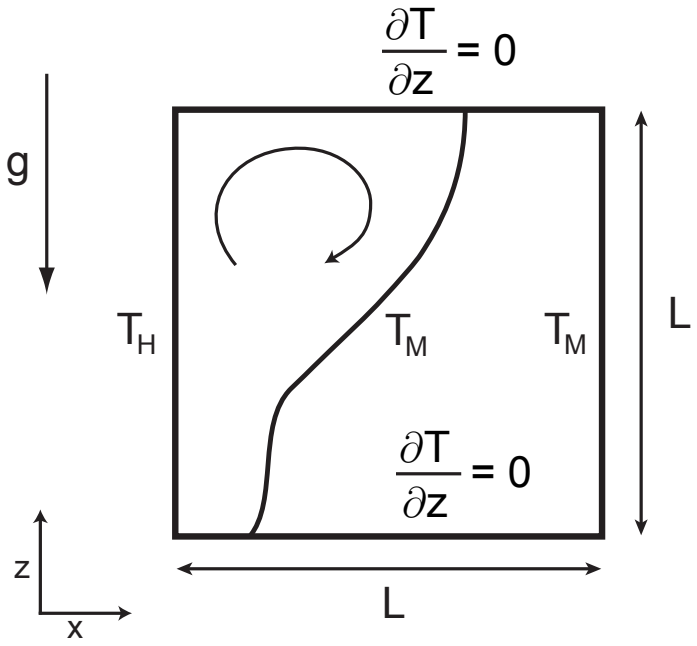

Figure 4: Schematic view of the test case after Bertrand et al. (1999). The enclosure is heated from the left vertical wall, which causes a progressive melting. After an initial state of pure conduction, natural convection occurs in the liquid and results in more extensive melting in the upper part of the cavity. Horizontal walls are kept insulated and the right vertical wall is maintained at the melting temperature T_{M}.

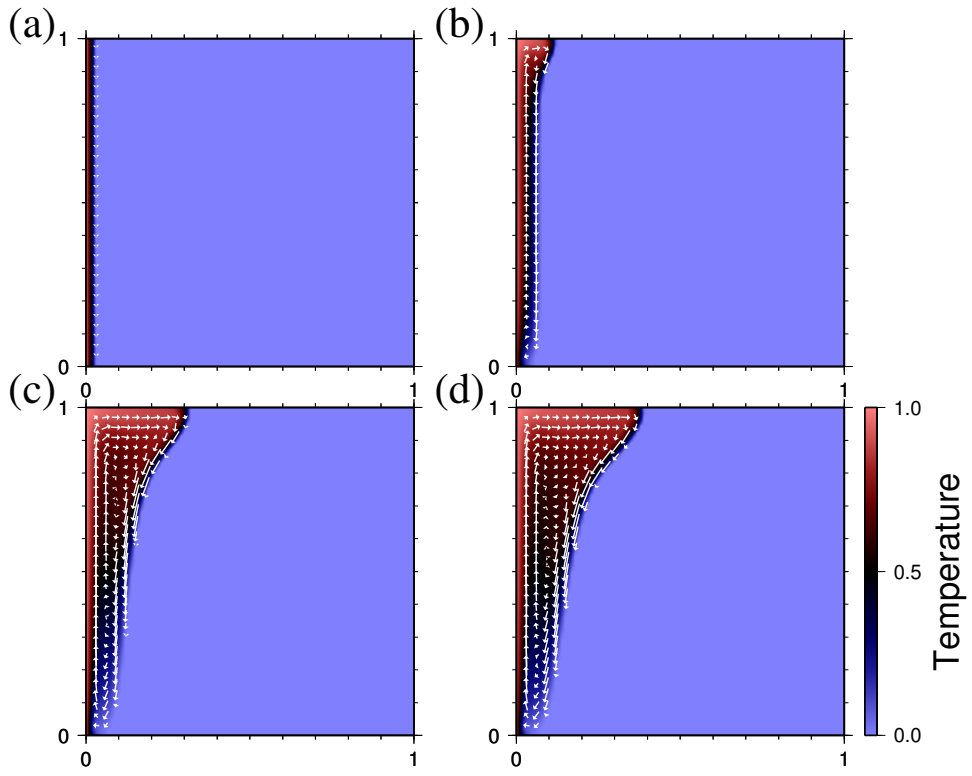

Figure 5: Snapshots of temperature (color scale) and velocity field (vectors) at times (a) $t = 0.005$ (b) $t = 0.03$ (c) $t = 0.08$ (d) $t = 0.1$. In an initially nearly completely solid cavity with temperature equal to the zero melting temperature ($T_{\mathrm{M}} = 0$), progressive melting occurs from the hot left vertical wall. (Case with Pr = 50, Ra = 10^7, St = 10.) Results were obtained with the moving mesh grid code.

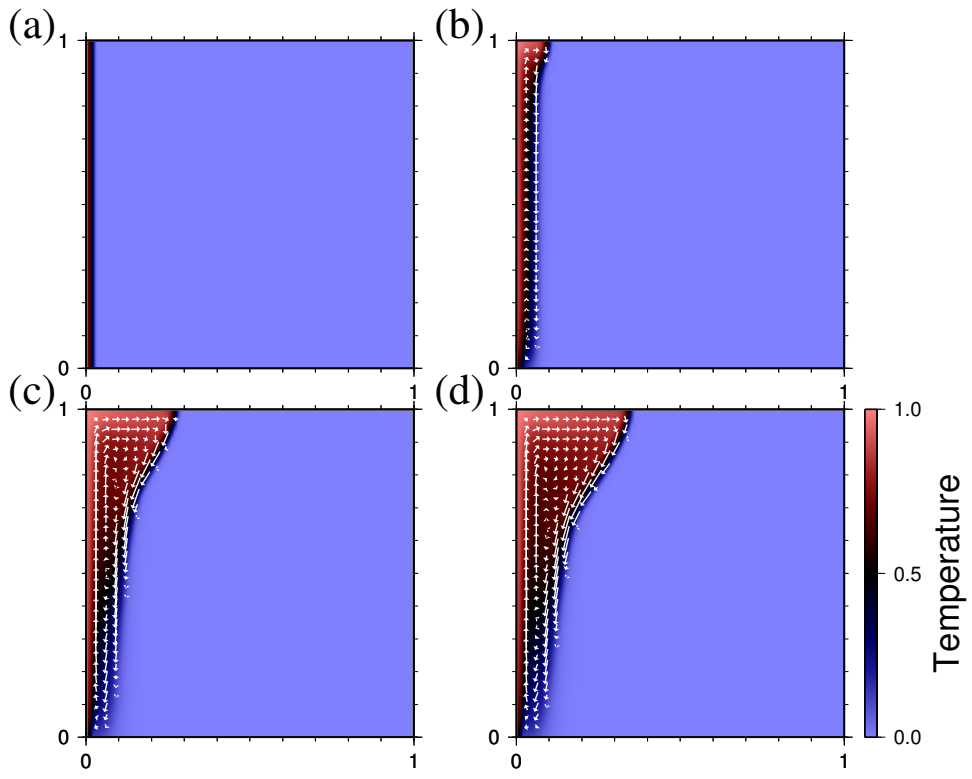

Figure 6: The same caption as for Fig.5, but the results were obtained with the fixed grid StagYY code.

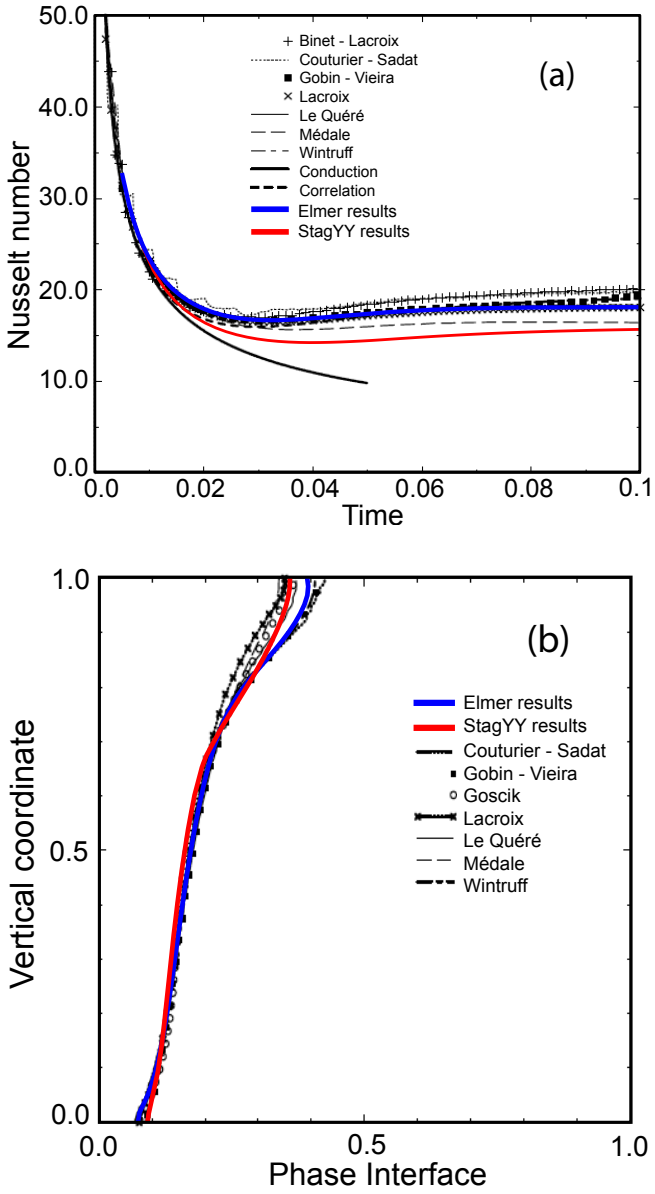

Figure 7: Comparison of melting driven by natural convection test case with results published in Gobin and Le Quéré (2000). (Case with $\mathrm{Pr} = 50$, $\mathrm{Ra} = 10^7$, $\mathrm{St} = 10.$) (a) Time evolution of flux over the hot wall. (b) The interface position at time $t = 0.1$.

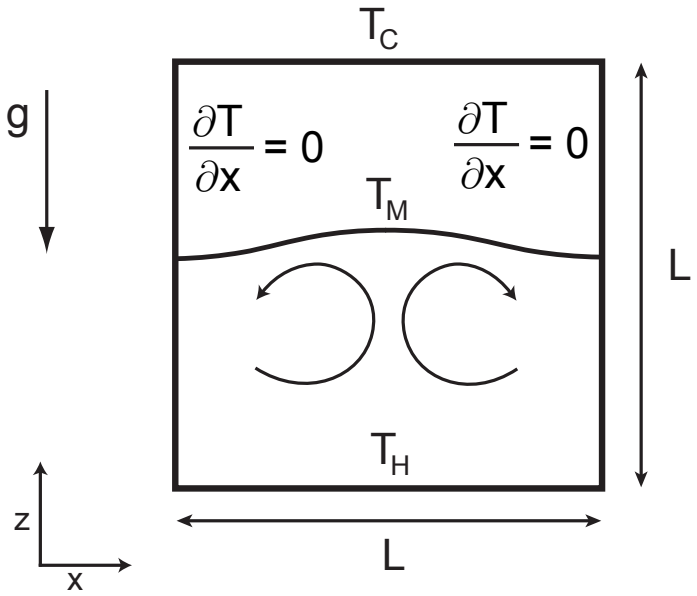

Figure 8: Schematic picture of the set up for the second test case with solidification/melting of a liquid layer with developed Rayleigh-Bénard convection. The phase change front is maintained at a fixed temperature T_{M} whose value lies between the temperature of the bottom boundary T_{H} and upper boundary T_{C}. Vertical walls are insulating and no-slip boundary conditions are applied on all boundaries.

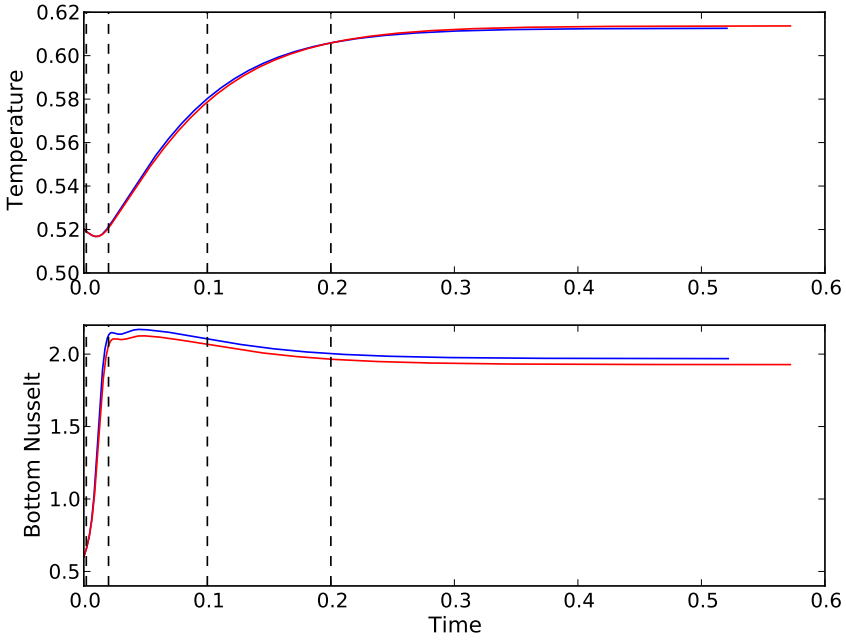

Figure 9: Time evolution of mean temperature in the cavity (upper figure) and mean Nusselt number over the hot bottom boundary (lower figure). Solid blue lines represent solutions obtained by the front distorted grid. Solid red lines result from the fixed grid enthalpy method. Vertical dashed lines indicate times when snapshots of Fig.10–Fig.13 were taken. (Case with $\mathrm{Pr} = 1000$ (blue) and $\mathrm{Pr} = \infty$ (red), $\mathrm{Ra} = 10^5$, $\mathrm{St} = 0.1$.)

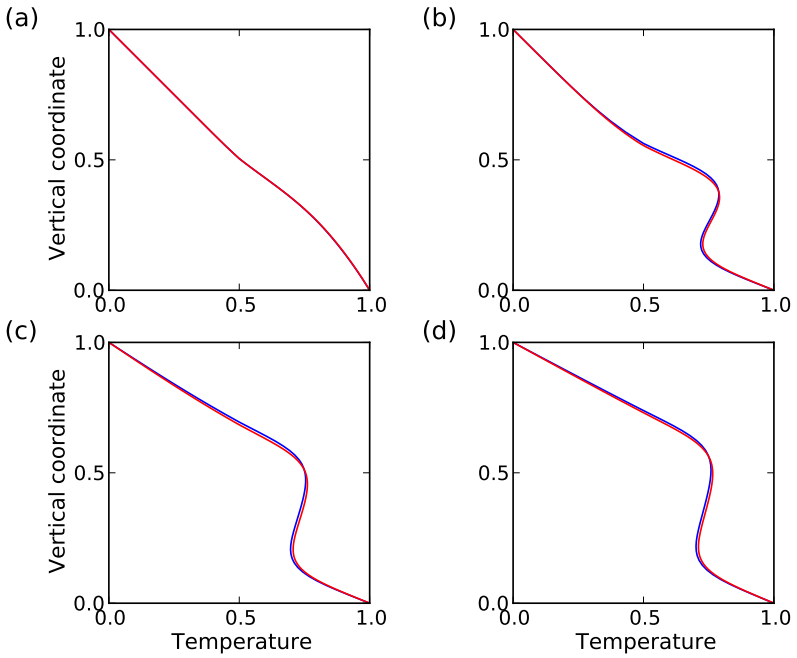

Figure 10: Vertical profiles of horizontal temperature at $x = 0.25$ for four different times (a) $t = 0.002$ (b) $t = 0.02$ (c) $t = 0.1$ and (d) $t = 0.2$. Solid blue lines represent solutions obtained with the distorted grid code. Solid red lines result from the fixed grid enthalpy code. (Case with $\mathrm{Pr} = 1000$ (blue) and $\mathrm{Pr} = \infty$ (red), $\mathrm{Ra} = 10^5$, $\mathrm{St} = 0.1$.)

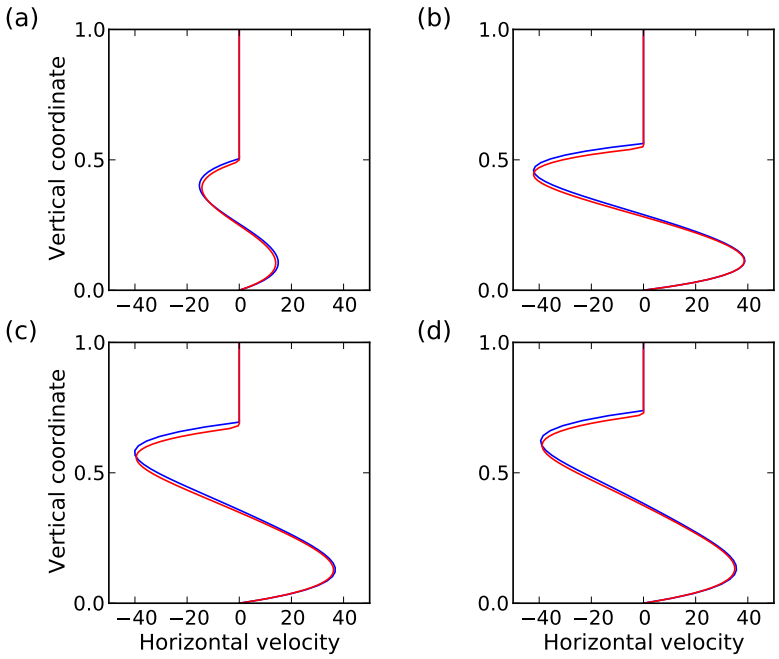

Figure 11: Vertical profiles of horizontal velocity at $x = 0.25$ for four different times (a) $t = 0.002$ (b) $t = 0.02$ (c) $t = 0.1$ and (d) $t = 0.2$. Solid blue lines represent solutions obtained with the distorted grid code. Solid red lines result from the fixed grid enthalpy code. (Case with $\mathrm{Pr} = 1000$ (blue) and $\mathrm{Pr} = \infty$ (red), $\mathrm{Ra} = 10^5$, $\mathrm{St} = 0.1$.)

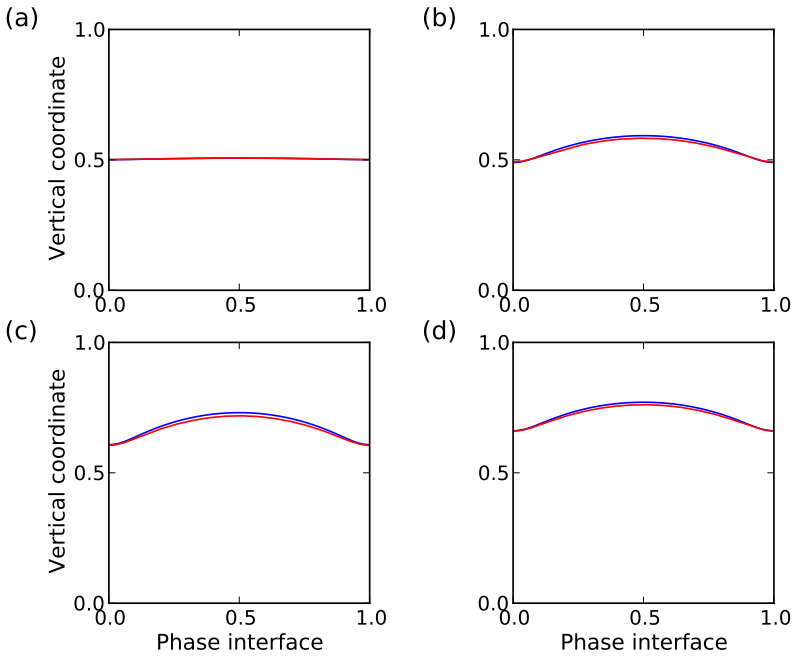

Figure 12: Positions of the phase change interface at four different times (a) $t = 0.002$ (b) $t = 0.02$ (c) $t = 0.1$ and (d) $t = 0.2$. Solid blue lines represent solutions obtained with the distorted grid code. Solid red lines result from the fixed grid enthalpy code. (Case with $\mathrm{Pr} = 1000$ (blue) and $\mathrm{Pr} = \infty$ (red), $\mathrm{Ra} = 10^5$, $\mathrm{St} = 0.1$.)

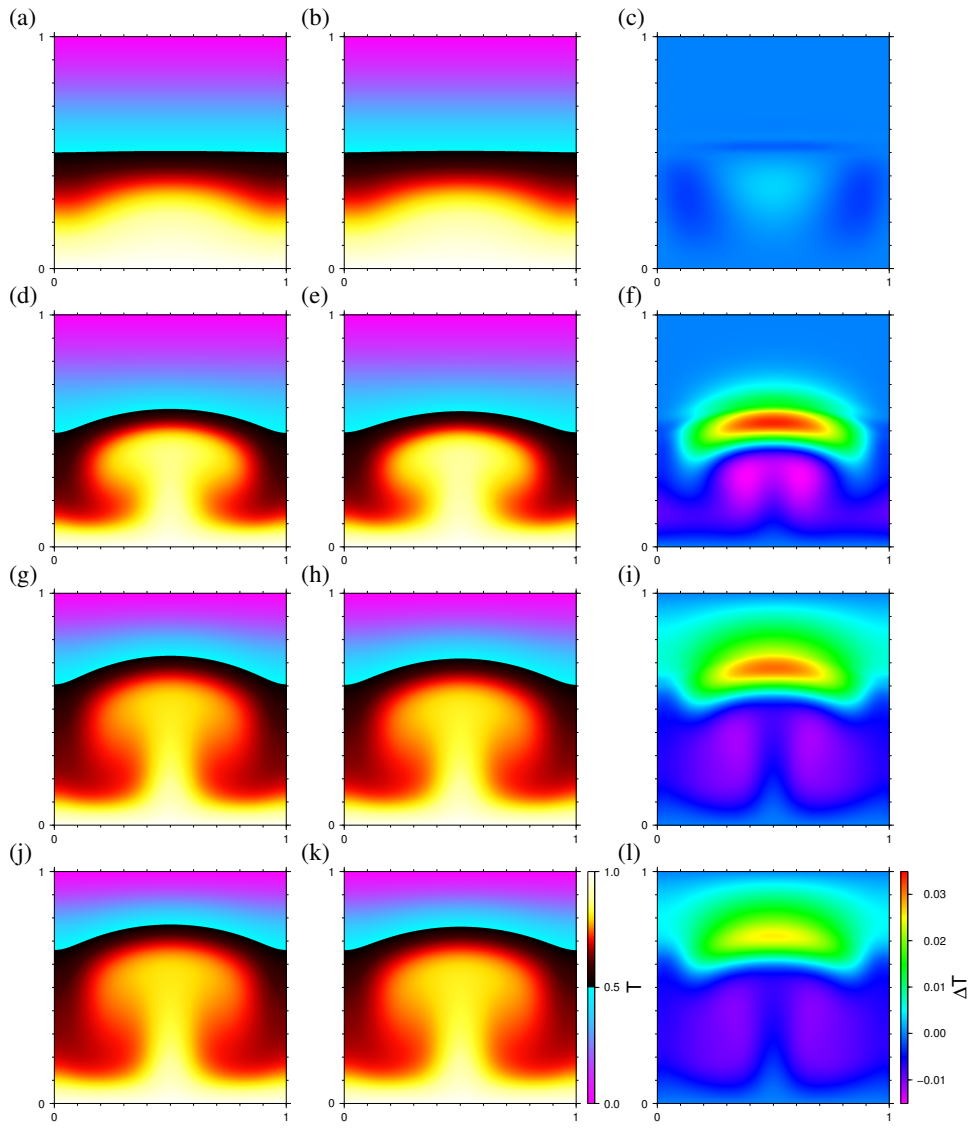

Figure 13: Temperature field at four different times corresponding to snapshots of Fig.12 and dashed lines of Fig. 9. In the first column, solutions obtained with the moving mesh grid code are displayed. The second column depicts resulted obtained with the fixed grid enthalpy code. The third column shows the absolute difference between the two solutions at a given time. The melting temperature is $T_{\mathrm{M}} = 0.5$. (Case with $\mathrm{Pr} = 1000$ (first column) and $\mathrm{Pr} = \infty$ (second column), $\mathrm{Ra} = 10^5$, $\mathrm{St} = 0.1$.)

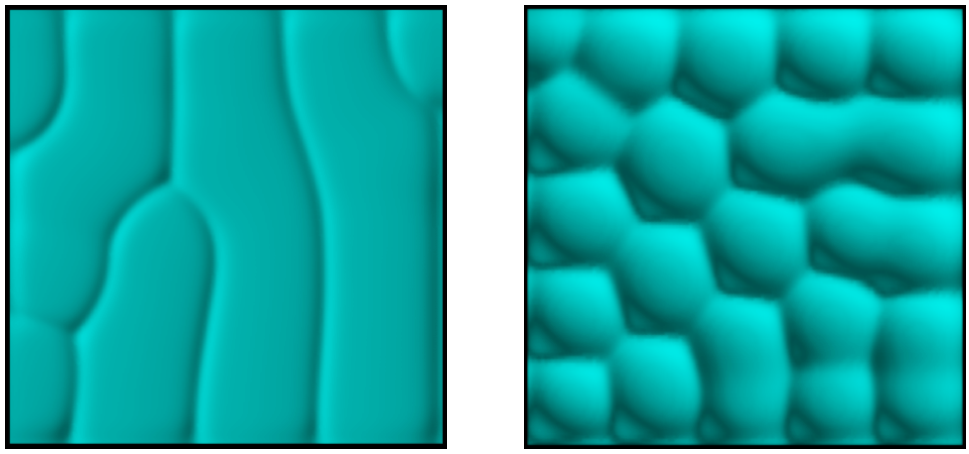

(a) Roll-like patterns.

(b) Hexagonal patterns.

Figure 14: 3D corrugated phase change interface in two different configurations corresponding to the results of Davis et al. (1984) Figures 3(a) and 3(c), depicting the roll and hexagonal planforms, respectively. Computed with the `StagYY` code in a cavity with an aspect ratio of 8 in both horizontal directions for St = 1 and (a) $\mathrm{Ra} = 8.4 \cdot 10^3$ (b) $\mathrm{Ra} = 1.1 \cdot 10^4$.

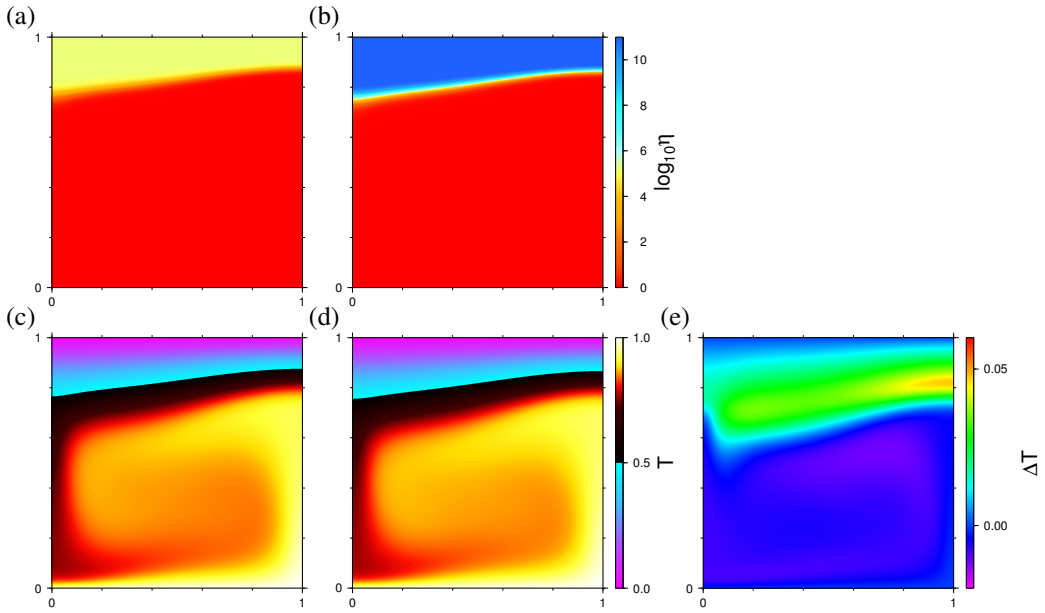

Figure 15: Influence of the viscosity contrast between the solid and the liquid in the fixed grid code. Viscosity field (a) $B = 6$ (b) $B = 13$ and (c)-(d) corresponding temperature fields at steady state. (e) difference between the two temperature solutions. (Case with $\mathrm{Pr} = \infty$, $\mathrm{Ra} = 3 \cdot 10^5$, $\mathrm{St} = 0.1$.)

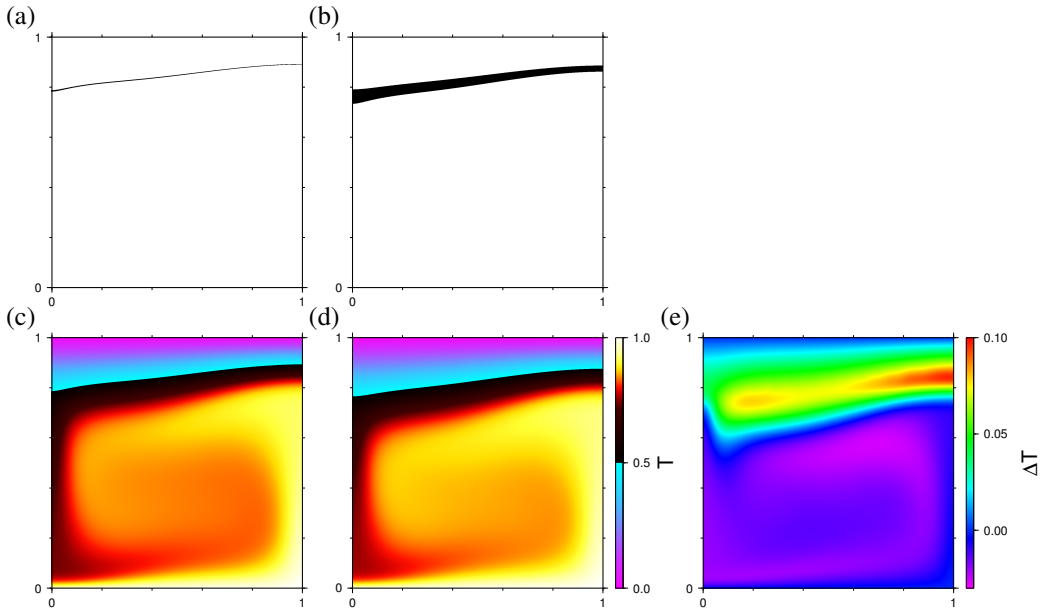

Figure 16: Influence of the width of the phase change interval for the code using the enthalpy method. Interval where phase change occurs (a) $\epsilon = 0.005$, (b) $\epsilon = 0.05$. (c)-(d) corresponding temperature fields at steady state. (e) difference between the two temperature solutions. (Case with $\mathrm{Pr} = \infty$, $\mathrm{Ra} = 3 \cdot 10^5$, $\mathrm{St} = 0.1$.)

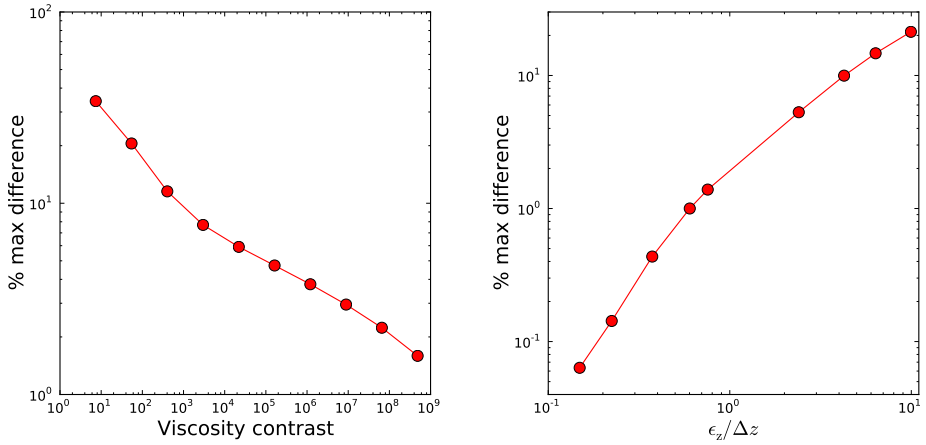

(a) Reference solution with $B = 13$ (corresponds to viscosity contrast $2 \cdot 10^{11}$)

(b) Reference solution with $\epsilon = 0.001$.

Figure 17: Maximum difference between the temperature and that of a reference solution as a function of (a) the viscosity ratio between the solid and the liquid and (b) phase change width. The mesh step is fixed for all experiments, $\Delta z = 0.0078125$ (corresponds to grid with 128×128 cells).

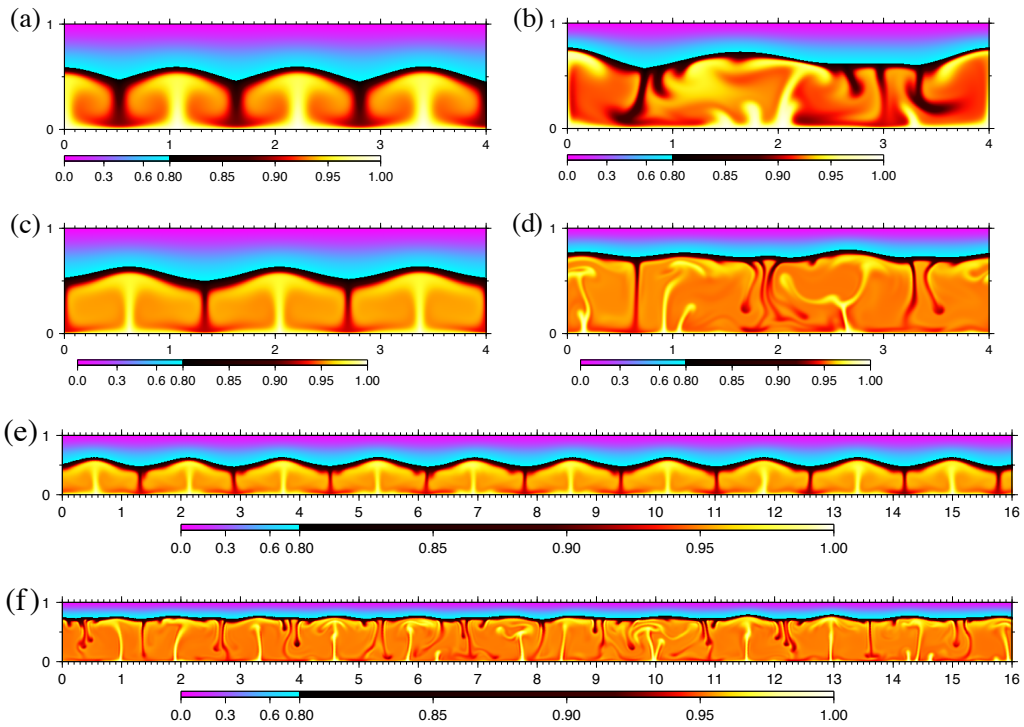

Figure 18: Snapshots of temperature field in Rayleigh-Bénard convection coupled with solidification/melting at two different Prandtl numbers and different Rayleigh numbers (a) $\mathrm{Pr} = 7$, $\mathrm{Ra}_{\mathrm{eff}} = 3 \cdot 10^4$ ($\mathrm{Ra} = 9.6 \cdot 10^5$); (b) $\mathrm{Pr} = 7$, $\mathrm{Ra}_{\mathrm{eff}} = 4 \cdot 10^5$ ($\mathrm{Ra} = 6.4 \cdot 10^6$); (c) $\mathrm{Pr} = \infty$, $\mathrm{Ra}_{\mathrm{eff}} = 4 \cdot 10^5$ ($\mathrm{Ra} = 10^7$) (d); $\mathrm{Pr} = \infty$, $\mathrm{Ra}_{\mathrm{eff}} = 8 \cdot 10^6$ ($\mathrm{Ra} = 10^8$); (e) $\mathrm{Pr} = \infty$, $\mathrm{Ra}_{\mathrm{eff}} = 3 \cdot 10^5$ ($\mathrm{Ra} = 10^7$) (f); $\mathrm{Pr} = \infty$, $\mathrm{Ra}_{\mathrm{eff}} = 8 \cdot 10^6$ ($\mathrm{Ra} = 10^8$).

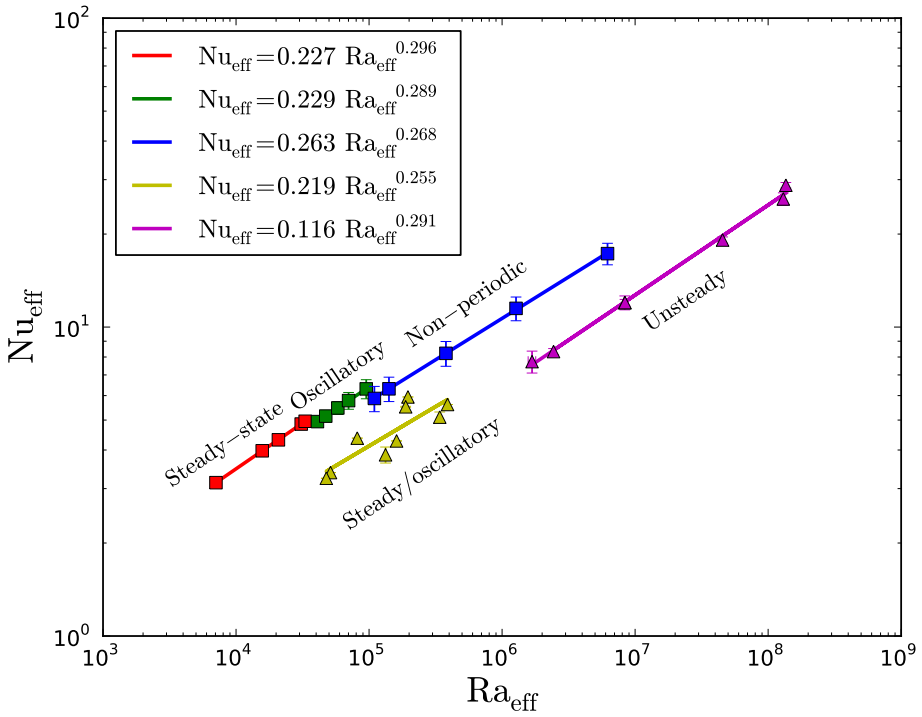

Figure 19: Effective Nusselt number as a function of the effective Rayleigh number. Two Prandtl numbers are used: Pr = 7 (square symbols) and infinite Prandtl (triangles). Different colors correspond to different convection styles observed. Change from steady to oscillating and unsteady flow is accompanied by the jump in the heat transfer. Lines are the least squares fits obtained for each convecting regime.

Chapter 4

Heat transfer

In order to reconstruct the thermal history of the Earth in the presence of the BMO, we study, using analytical and numerical methods, the physics of heat transfer through a crystallizing/melting layer that is heated from below and cooled from above (Figure 4.1). In particular, we investigate the coupling between convective motions in the melt and phase change transformation. The melting temperature T_{M} is chosen such that the upper part of the cavity is always frozen.

In the goal of understanding the dynamics of the convecting layer that changes its phase state from liquid to solid, we first focus on a qualitative description of the system that is based on the numerous simulations performed. This is followed by a quantitative study of heat transported across a solidifying convecting melt.

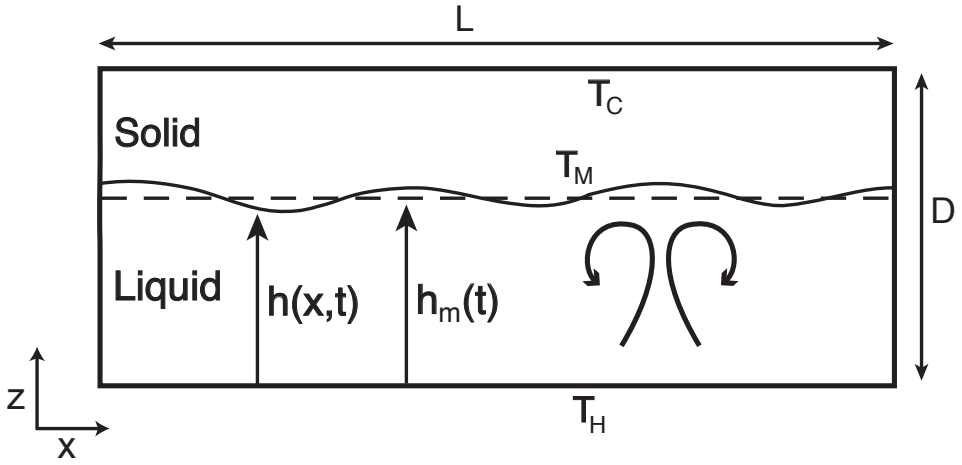

Figure 4.1: Schematic picture of the system under study. The upper part of the cavity is frozen and the lower one is liquid since we impose $T_{\mathrm{c}} < T_{\mathrm{M}} < T_{\mathrm{h}}$. The position of the phase change interface is at $h(x,t)$ with a spatial average $h_{\mathrm{m}}(t)$.

4.1 Descriptive analysis of the physics

Description of the system under study (Figure 4.1) is based on a number (around 50) of numerical simulations with various parameters. Each simulation is conducted with a balanced energy budget when (statistical) steady state is reached since we aim to simulate the short term evolution of the BMO.

We explore only cases with small St (under unity) and two Prandtl numbers (7 and ∞), since these are the plausible parameters for the BMO. $\mathrm{Ra}_{\mathrm{eff}}$ is explored over a wide interval from 10^4 to 10^8. Simulation at $\mathrm{Pr} = 7$ are performed with Elmer code in 2D Cartesian geometry. Experiments at $\mathrm{Pr} = \infty$ are conducted with StagYY code in 2D and 3D Cartesian geometries.

4.1.1 Temperature profiles

A profile of mean temperature in the system (averaged horizontally in space and also temporally) at (statistically) steady state consists of linearly varying temperature in the solid where heat conduction dominates (Figure 4.2). In the liquid, where well developed convection is set up, the mean temperature profile is the same as in the classical Bénard problem. Isothermal convective core is surrounded by the two boundary layers of thicknesses δ^+ (upper boundary) and δ^- (bottom boundary) where most of the temperature variations occurs (Figure 4.2). δ^+ and δ^- are either with similar thicknesses (when boundary conditions at the melting front and at the bottom are identical, i.e. bottom boundary has fixed temperature and is noslip) or differ significantly (when boundary conditions at the phase interface and at the bottom differ, i.e. free-slip condition is employed at the bottom). The exact identical size of the boundary layers is strictly not possible when convection is developed in the liquid since it implies corrugated top boundary, and thus breaking the symmetry.

Also, we are interested in the minimum and maximum temperature profiles in the cavity (Figure 4.3). A value of the maximum temperature gradually decreases from the hottest bottom boundary over the liquid. Its steep drop is then observed in the upper part of the liquid and the solid. On the other hand, the structure of the minimum temperature profile changes gradually in the upper part of the cavity till the bottom where a boundary layer exists with a thickness inferior to δ^-.

When the system achieves statistical steady state, there is no mean heat flux discontinuity across the phase change front apparent in the temperature profile since at the phase change interface latent heat is neither liberated nor consumed on average. Also, we note that the profile across the whole cavity (i.e. in the solid and the liquid) corresponds to a mean temperature profile of a system where viscosity is strongly temperature dependent and a thick stagnant lid develops (White, 1988).

4.1.2 Thermal regimes

As we saw before, the system is fully controlled by three dimensionless parameters: Pr, Ra and St. When the system does not change in time, i.e. eulerian time derivatives are zero, the heat transported across the liquid does not depend on the Stefan number. So the heat transfer is given by a couple: Pr, Ra and we decide to perform two sets of experiments for two different Pr numbers, $\mathrm{Pr} = 7$ and $\mathrm{Pr} = \infty$. This

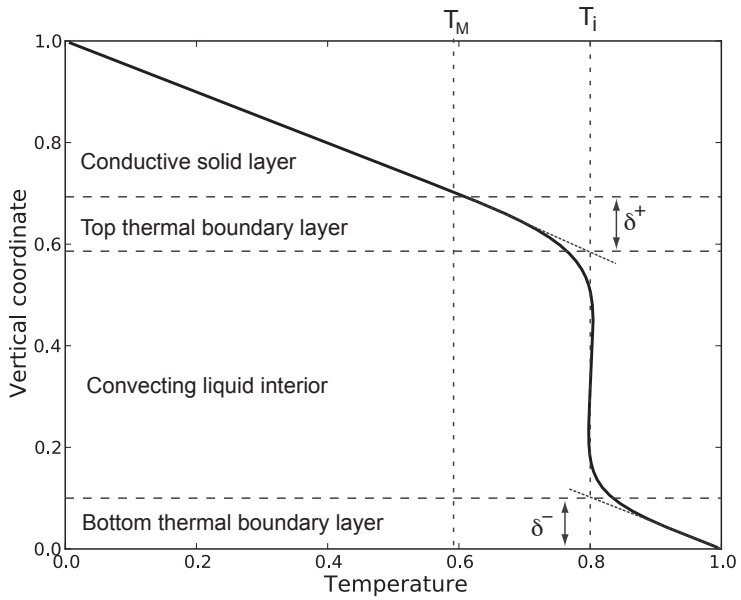

Figure 4.2: Thermal structure of the convecting system undergoing solidification/melting. Horizontally and temporally averaged temperature is plotted against vertical coordinate. (3D simulation with Ra = $3 \cdot 10^5$ and $T_{\mathrm{M}} = 0.59$)

choice is motivated by our intention to use the scalings laws for the BMO whose Pr is estimated to lie between 1 and 1000 (cf. Chapter 2). For a given Pr, only one parameter is left and it is Ra.

We are particularly interested in the mean bottom and surface heat fluxes which are equal in the absence of internal heating, the mean temperature in the cavity and also in the position of the phase front. Several convective regimes have been distinguished depending on time evolution of relevant variables (mean temperature, mean interface position, mean heat fluxes and mean effective Rayleigh number). An experiment starts either from a given initial conditions (zero velocity everywhere, a linearly varying temperature profile in the solid and an isothermal interior in the liquid with boundary layers at top and bottom, plus small random perturbations) or we start from the temperature field obtained in another simulation. First of all, a transition period occurs when the system adjusts for an imposed Ra parameter at given Pr. Then three different permanent states can be attained depending on Ra. Similarly to the case without phase change, the evolution with increasing Ra is toward more complex time dependence. The first regime for small Ra, termed steady state, is when all variables stay constant in time at each point. In the second regime for intermediate Ra (termed oscillatory regime), variables oscillate periodically around a mean value. In the third regime for high Ra (termed statistically steady state or unsteady) mean variables (mean temperature, heat flux, etc.) vary unevenly around an average value with no long term evolution. The Earth is in another state where in addition to short scale variations there is a long term evolution. But we assume that there is a good separation of long and short time scales so that the long

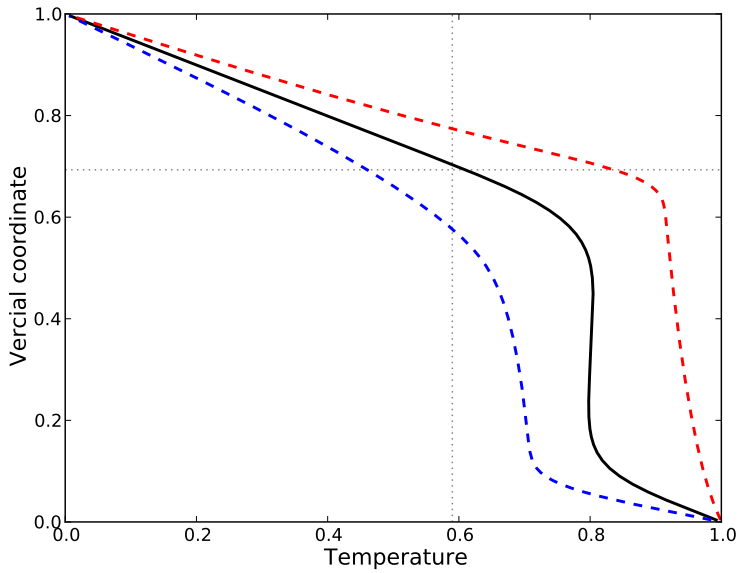

Figure 4.3: Horizontally and temporally averaged minimum temperature (blue dashed line), maximum temperature (red dashed line) and mean temperature (solid black line) are plotted against vertical coordinate. The horizontal dotted line represents the mean (spatial and temporal) position of the phase interface. The vertical dotted line represents the imposed melting temperature $T_{\mathrm{M}} = 0.59$. (3D simulation with $\mathrm{Ra} = 3 \cdot 10^5$)

term evolution can be understood from the scaling obtained for statistically steady state.

At which Ra the transition between the regimes occurs depends on the Prandtl number, the boundary conditions at vertical as well as horizontal walls, and the size of the box. We estimate its values later in the manuscript. Snapshots of the temperature field for $\mathrm{Pr} = 7$ simulations and for several Ra are depicted in Figure 4.4 where the transition to more complex flows with increasing Ra is apparent (insulating vertical walls and free slip vertical and bottom walls). Temperature snapshots of simulations conducted at $\mathrm{Pr} = \infty$ are shown in Figure 4.5 (2D geometry) and Figures 4.6 and 4.7 (3D geometry).

An example of the time evolution of several diagnostic quantities in the unsteady regime is depicted in Figure 4.8. Temperature and heat flux evolutions are given together with a mean position of the liquid/solid phase change interface. As the mean thickness of the liquid layer changes in time, the effective Rayleigh number also changes with time (Figure 4.8(f)). Comparing Figure 4.8(a) and (c) we note that the small variations in mean temperature induce large variations in average heat flux. Also, the largest amplitudes of mean temperature variations occurs on long periods, whereas the mean heat flux over the bottom boundary fluctuates with large amplitude at high frequencies. Figures 4.8(c), (d) and (e) show a mean heat flux across the bottom boundary, the phase interface and the top boundary. In these figures we observe a filtering of high frequency signals and a significant reduction of amplitude

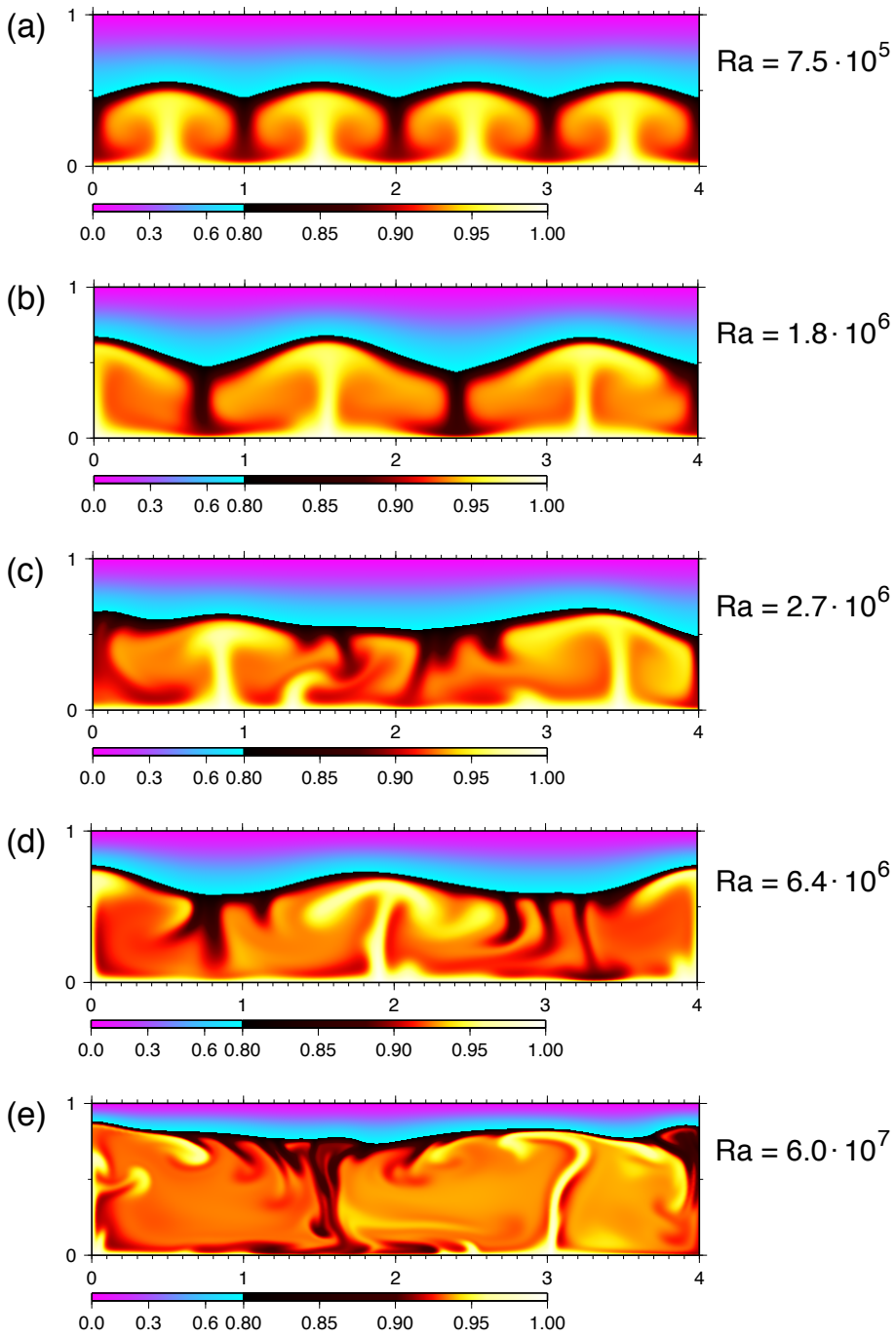

Figure 4.4: Snapshots of the temperature field at (a) steady state (b) oscillatory regime (c)-(e) statistically steady states. Pink to cyan color scale represents temperatures in the solid. Black to yellow colors represent temperatures in the liquid. (Cases $\mathrm{Pr} = 7$, $T_{\mathrm{M}} = 0.8$ and $\mathrm{St} = 0.9$)

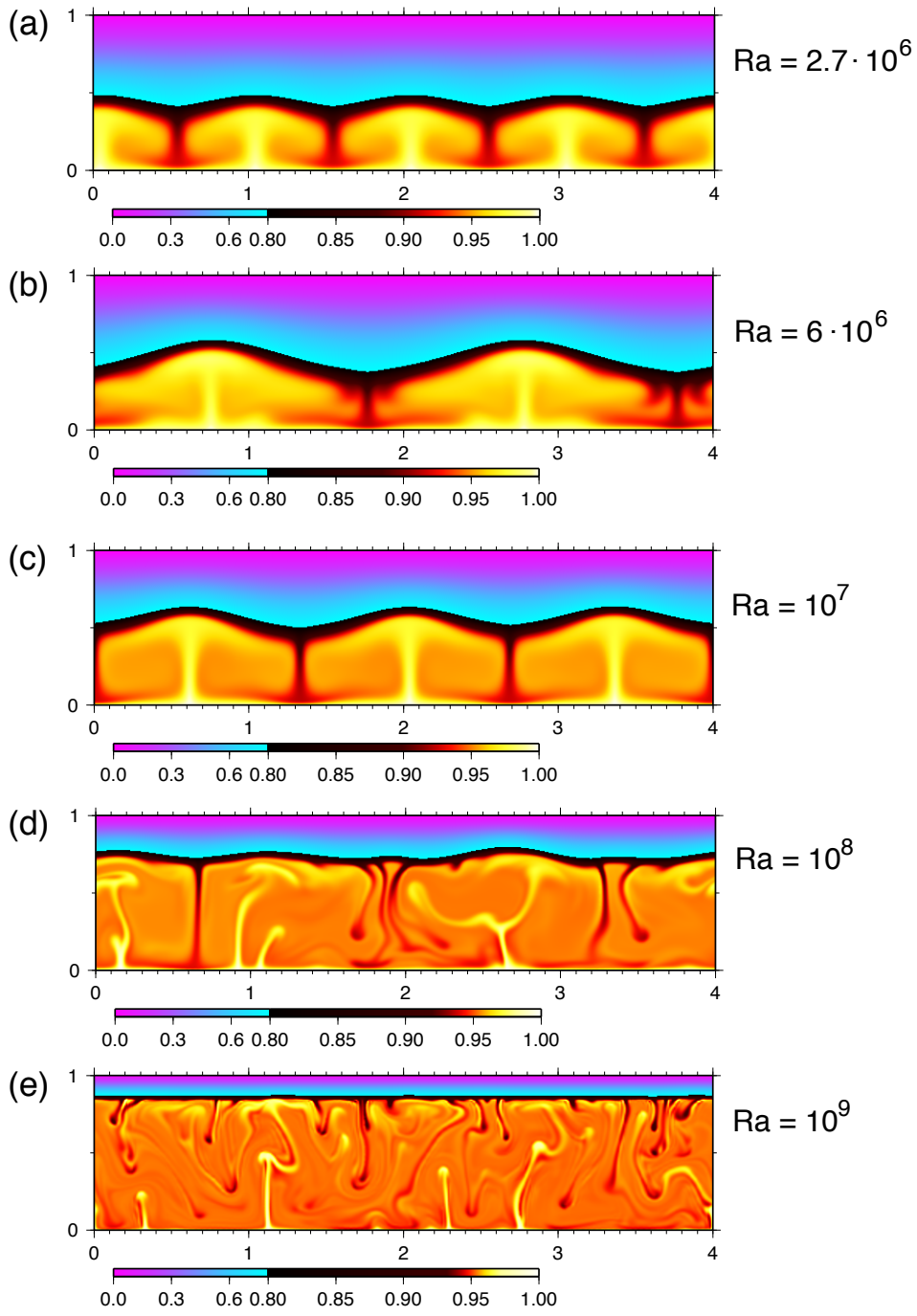

Figure 4.5: Snapshots of the temperature field at (statistically) steady states. Pink to cyan color scale represents temperatures in the solid. Black to yellow colors represent temperatures in the liquid. (Cases $\mathrm{Pr} = \infty$, $T_{\mathrm{M}} = 0.8$ and $\mathrm{St} = 0.1$)

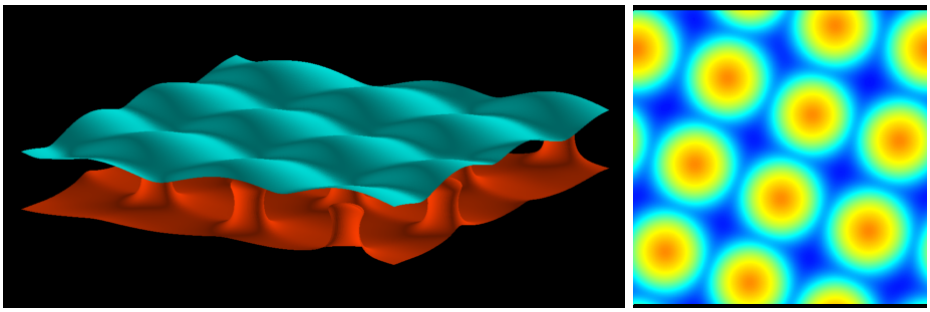

(a) $\mathrm{Ra} = 1.4 \cdot 10^5$ ($\mathrm{Ra}_{\mathrm{eff}} = 1.4 \cdot 10^4$), $T_{\mathrm{M}} = 0.59$ (b)

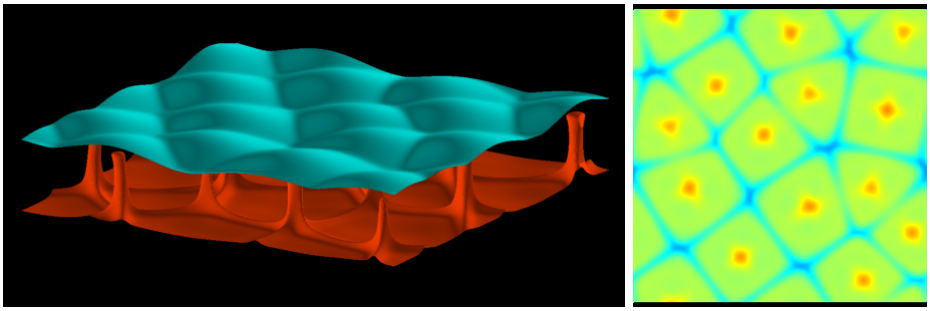

(c) $\mathrm{Ra} = 5 \cdot 10^5$ ($\mathrm{Ra}_{\mathrm{eff}} = 7.9 \cdot 10^4$), $T_{\mathrm{M}} = 0.59$ (d)

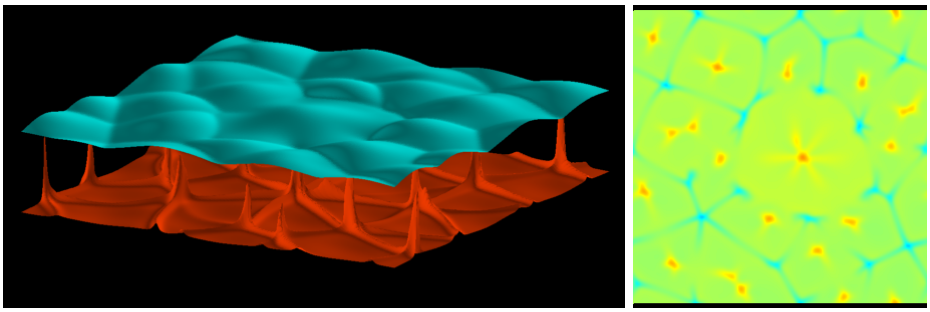

(e) $\mathrm{Ra} = 2 \cdot 10^6$ ($\mathrm{Ra}_{\mathrm{eff}} = 4.3 \cdot 10^5$), $T_{\mathrm{M}} = 0.59$ (f)

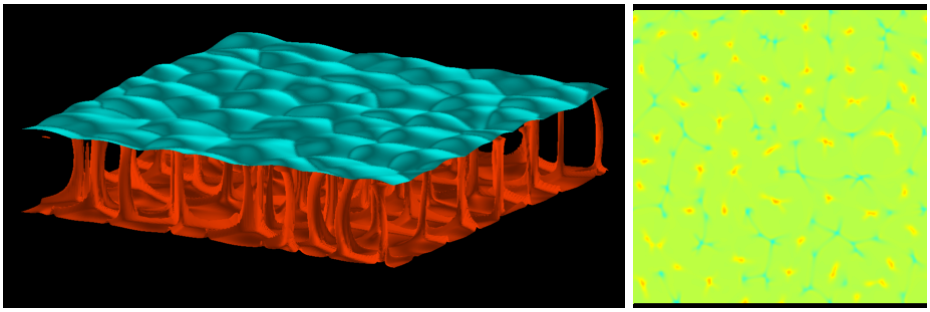

(g) $\mathrm{Ra} = 2 \cdot 10^7$ ($\mathrm{Ra}_{\mathrm{eff}} = 3.3 \cdot 10^6$), $T_{\mathrm{M}} = 0.7$ (h)

Figure 4.6: (Left column) Isotherms of temperature field at (statistically) steady states. Cyan isotherm represents the phase change front (temperature of melting), red isotherm represents the hot upwelling ($T = 0.9$). (Right column) Snapshots of temperature field at horizontal cross-section at mid-depth. The red is hot, the blue is cold. (Cases with $\mathrm{Pr} = \infty$, $\mathrm{St} = 0.14$ and no-slip bottom velocity boundary conditions. Boundary conditions at vertical walls are periodic. Domain size is $4 \times 4 \times 1$.)

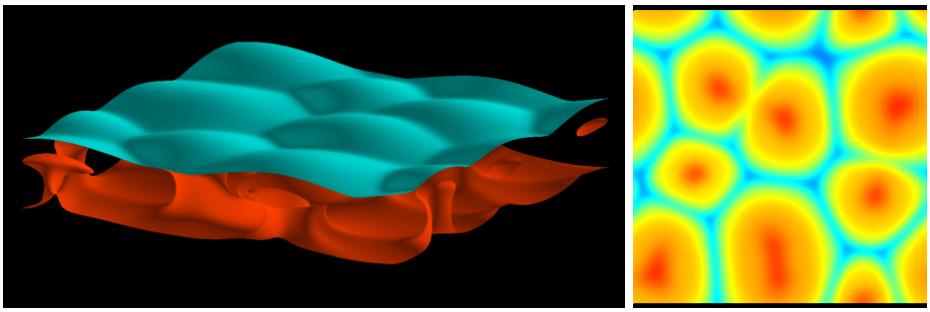

(a) $\mathrm{Ra} = 1.4 \cdot 10^5$ ($\mathrm{Ra}_{\mathrm{eff}} = 2.0 \cdot 10^4$), $T_{\mathrm{M}} = 0.59$ (b)

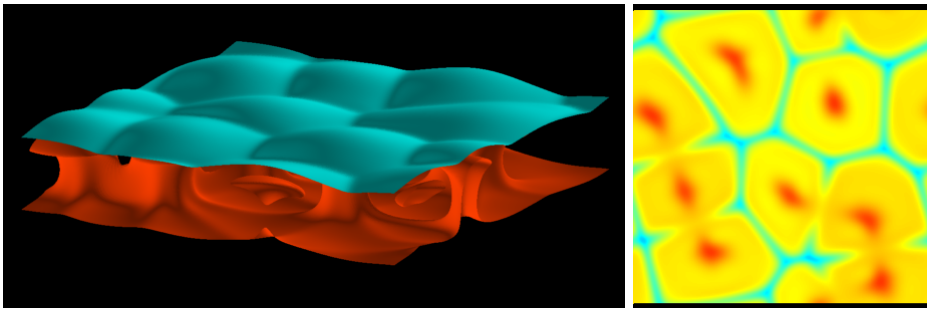

(c) $\mathrm{Ra} = 3 \cdot 10^5$ ($\mathrm{Ra}_{\mathrm{eff}} = 5.3 \cdot 10^4$), $T_{\mathrm{M}} = 0.59$ (d)

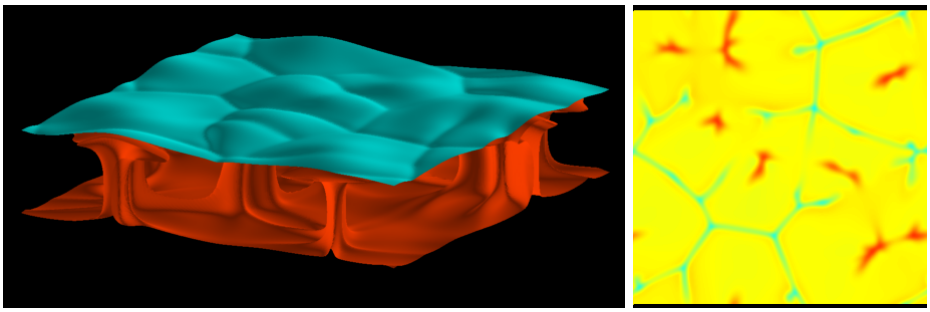

(e) $\mathrm{Ra} = 2 \cdot 10^6$ ($\mathrm{Ra}_{\mathrm{eff}} = 4.9 \cdot 10^5$), $T_{\mathrm{M}} = 0.59$ (f)

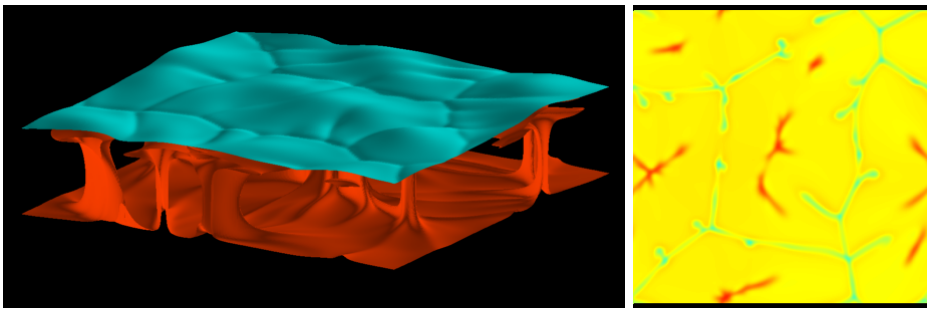

(g) $\mathrm{Ra} = 4 \cdot 10^6$ ($\mathrm{Ra}_{\mathrm{eff}} = 1.1 \cdot 10^6$), $T_{\mathrm{M}} = 0.59$ (h)

Figure 4.7: The same caption as for Figure 4.6, but experiments were performed with free-slip bottom velocity boundary conditions.

when passing from the bottom boundary to the top of the computational domain.

4.1.3 Form and amplitude of corrugations

When a liquid layer is melting without any flow developed in it, the interface between the solid and the melt stays planar, perpendicular to the direction of heat flow. Heat is transported by conduction and depends on the thickness of the layer (solid or liquid), the temperature drop across the layer and the thermal conductivity. Some of the authors chose this state as a reference and relate all results to it (Davis et al., 1984; Dietsche and Müller, 1985). This is a good choice when the Rayleigh number is not too high but might be rather poor at high Ra.

As soon as convection sets up in the liquid, deflection of the phase front occurs as the heat flux in the vicinity of the melting interface varies along the phase change front. A higher heat flux, where hot upwelling currents reach the top, induces a higher rate of melting. The roots of cold descending currents induce more extensive solidification due to a low heat flux. Corrugations, i.e. distinctive undulations of the melting front, are created. These have forms of caps at small Rayleigh numbers when steady flow is developed in the liquid (Figures 4.4(a), 4.5(a) for 2D examples, Figure 4.6(a) for 3D example). For unsteady flows at high Ra, multiple clusters of localized plumes exist (e.g. Figure 4.4(e)) and the topography of the interface becomes irregular.

The convective vigour determines the size and amplitudes of corrugations. We observe a significant decrease of the corrugation's amplitude Δh for unsteady flows (Figure 4.9(bottom)). Δh is determined as a difference between the maximum and minimum of the melting front position. This leads to higher values of Δh than if they were determined for each corrugation separately and averaged as was done e.g. in the work of Hill (1996). In Figure 4.9 we see indeed that Hill (1996) reported lower values of Δh for highly unsteady flows where the difference between the shape of individual corrugations (and so the size of Δh for separate cells) is very different.

At small Ra we see a more complex behaviour: Δh increases with increasing Ra and then starts to decrease (Figure 4.9(top)). This could be possibly explained by forcing the convective cells to have a wavelength given by the size of the box and thus implicitly also forcing Δh. However, we would need more experiments at small supercritical Ra in order to confirm this hypothesis.

The decrease in Δh with increasing Ra can be explained by unsteadiness of the flow in the liquid. Numerous time dependent currents reduce the temperature differences when temporally averaged at a given space. In a limiting case at very high Ra, the number of hot and cold plumes passing at a certain point will be the same after a long time elapsed (typically several convective times). Also, if the characteristic time scales of solidification/melting are much superior to the convective times, corrugations will not develop. We thus expect $\Delta h \to 0$ for very large Ra and/or St.

4.2 Parametrization: general scaling laws

Here, we give a quantitative study of heat transfer across a solidifying/melting layer using the results of the numerical simulations. We thus explore a relation between the heat flux and the Rayleigh and Prandtl numbers at steady state. Results for all experiments are given in Tables 4.1, 4.2, 4.3 and 4.4.

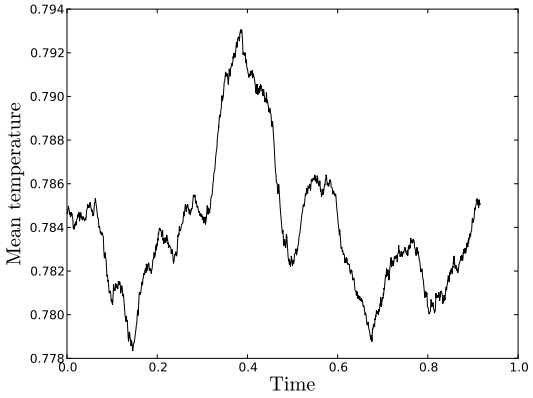

(a) Mean temperature in the whole domain

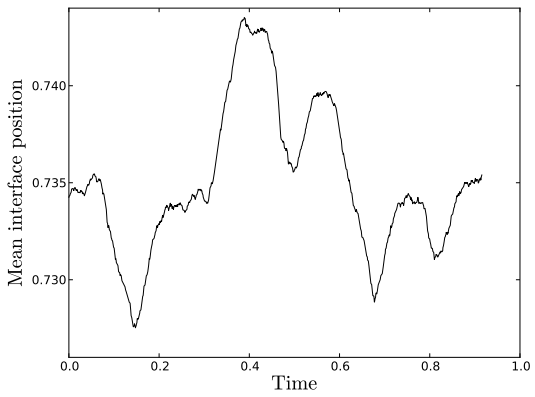

(b) Mean interface position

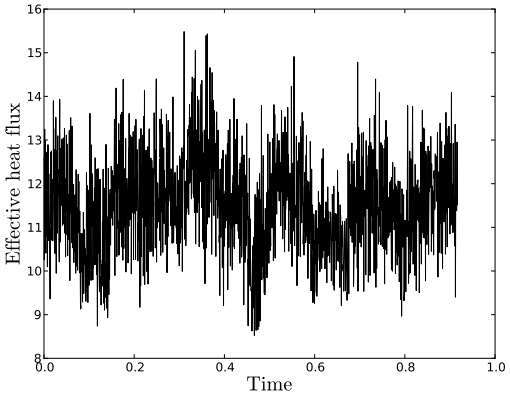

(c) Mean effective heat flux at the bottom

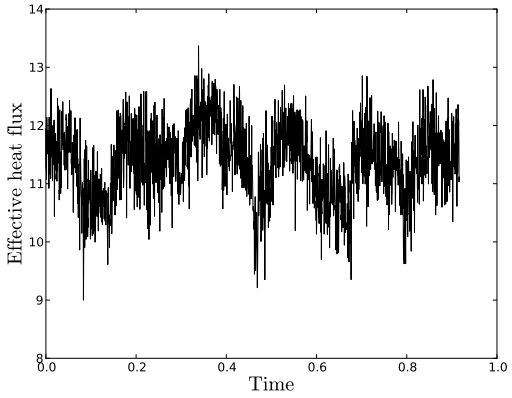

(d) Mean effective heat flux across the phase interface

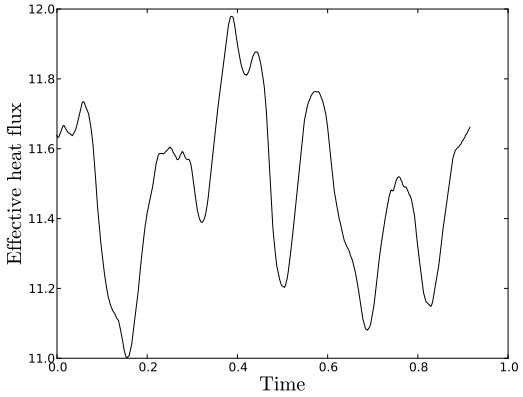

(e) Mean effective heat flux at the top

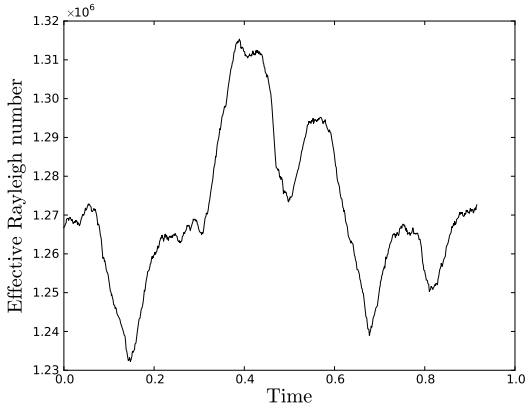

(f) Mean Rayleigh number

Figure 4.8: Time evolution of the temperature, mean interface position, effective heat flux (termed effective since its definition is written with variables applying to the liquid layer) and effective Rayleigh number. Changes in the liquid thickness induce changes in the effective Rayleigh number. 2D simulation with $\mathrm{Pr} = 7$, $\mathrm{Ra} = 1.6 \cdot 10^7$ and $\mathrm{St} = 0.9$.

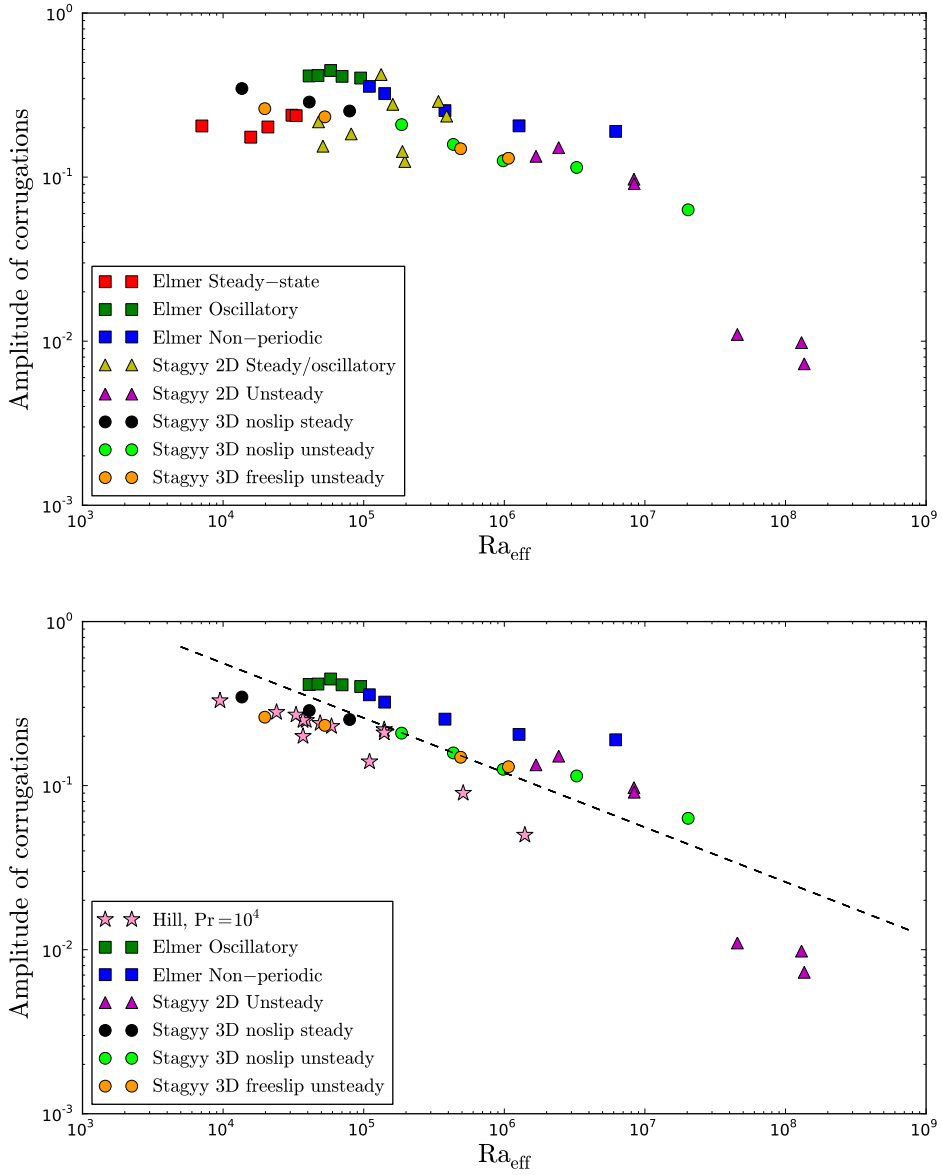

Figure 4.9: Amplitude of corrugations (scaled with the thickness of the liquid layer) as a function of the effective Rayleigh number. The size of corrugation is determined as a difference between the maximum and minimum positions of the phase front and is thus generally higher than results of Hill (1996) (pink stars). (top) All numerical experiments. Note the increase in amplitude when passing from steady to oscillatory regime for Elmer results. Also, no apparent trend is observed for StagYY 2D steady/oscillatory regime (yellow triangles). (bottom) Selected numerical data (2D steady regimes are omitted) are depicted together with experimental results of Hill (1996). The black dashed line represents $-1/3$ power law.

Several resolution tests are carried out to verify the numerical solutions. Results together with mesh resolutions for individual experiments are reported in Appendix A.

For an imposed Ra we obtain a mean bottom and top heat fluxes coming in and out, $Q_{\rm bot}$ and $Q_{\rm top}$,

$$Q_{\rm bot} = \frac{\iint q_{\rm bot}(x)\,{\rm d}x\,{\rm d}t}{t_{\rm s}L}\,, \tag{4.1}$$

where a time integration happens over an interval of length $t_{\rm s}$ when the system is in (statistically) steady state and space integration is over a bottom boundary L (similarly for $Q_{\rm top}$). $Q_{\rm bot}$ and $Q_{\rm top}$ can be calculated directly from a temperature gradient as velocities normal to the external boundaries are zero at all horizontal walls. Since we examine permanent states, $Q_{\rm bot}$ should be the same as $Q_{\rm top}$ in order to conserve energy in the system. Indeed, in all our experiments difference between the two fluxes is inferior to 1%.

$Q_{\rm bot}$ and $Q_{\rm top}$ are not directly related to the convecting liquid layer (they are defined with variables applying to the whole cavity) and we thus define their effective values that are written with variables applying to the liquid layer (the thickness of the liquid and the temperature difference across the melt). In addition, we also give the effective Rayleigh number $\mathrm{Ra}_{\rm eff}$ that is time dependent and is not known a priori due to dependence on $h_{\rm m}$ (given as well in the tables with results).

The heat flux can also be estimated from the energy conservation equation. Integrating Eq.(2.15) over a volume Ω of a domain bordered by the bottom boundary ($z = 0$), the horizontal surface at height $z = d$ and vertical walls we obtain

$$\int_\Omega \frac{{\rm D}T}{{\rm D}t}\,{\rm d}\Omega = \int_\Omega \nabla^2 T\,{\rm d}\Omega\,. \tag{4.2}$$

Using the incompressibility condition and applying the boundary conditions we rewrite (4.2)

$$Q_{\rm bot} \equiv \frac{\overline{\partial T}}{\partial z}(z=0) = \frac{\overline{\partial T}}{\partial z}(z=d) - \overline{w\theta}(z=d) - \int_0^d \frac{\partial \overline{T}}{\partial t}\,{\rm d}z\,, \tag{4.3}$$

where overbars stand for horizontally averaged variables at a given depth and w is the vertical velocity. We also introduced a temperature perturbation θ, $T = \overline{T} + \theta$, for which it holds $\overline{w\theta} = \overline{w(T-\overline{T})} = \overline{wT}\,$.

Eq. (4.3) represents the energy balance in a volume Ω. In a steady state the time derivative disappears ($\int_0^d \frac{\partial \overline{T}}{\partial t}\,{\rm d}z = 0$) and the mean bottom heat flux is composed of two terms: the heat conducted at height $z = d$ and the heat advected through a horizontal plane at $z = d$. The same applies also for statistical steady state. If Eq.(4.3) is averaged over the time interval long enough compared to the periods in the system, the time derivative also disappears. Then, the overbar would be defined as the average over the horizontal surface and this timescale.

Eq. (4.3) is valid for all $d \in (0, D)$ and can be used to verify the conservation of energy in the cavity. Figure 4.10 shows individual terms of Eq. (4.3) for one particular simulation at high Ra and indeed we conclude that the conservation of energy is verified at each depth.

nb	Ra	Q_{bot}	Q_{top}	$\mathrm{Ra}_{\mathrm{eff}}$	$Q_{\mathrm{bot}}^{\mathrm{eff}}$	$Q_{\mathrm{top}}^{\mathrm{eff}}$	$\langle h_{\mathrm{m}} \rangle$	Δh	$\Delta h / h_{\mathrm{m}}$	A
09	$4.2 \cdot 10^5$	1.43	1.43	$7.1 \cdot 10^3$	3.14	3.14	0.44	0.090	0.205	1.283
01	$6.4 \cdot 10^5$	1.60	1.60	$1.6 \cdot 10^4$	3.98	3.98	0.50	0.087	0.175	1.012
12	$7.5 \cdot 10^5$	1.67	1.68	$2.1 \cdot 10^4$	4.32	4.34	0.52	0.105	0.202	0.931
07	$9.6 \cdot 10^5$	1.78	1.79	$3.1 \cdot 10^4$	4.85	4.86	0.54	0.130	0.238	0.839
13	$1.0 \cdot 10^6$	1.81	1.81	$3.3 \cdot 10^4$	4.96	4.96	0.55	0.130	0.237	0.822
08	$1.3 \cdot 10^6$	1.82 (0.08)	1.82 ($3.5 \cdot 10^{-4}$)	$4.1 \cdot 10^4$ (9)	4.94 (0.21)	4.95 ($7.40 \cdot 10^{-4}$)	0.54 ($4.1 \cdot 10^{-5}$)	0.225	0.414	0.843
14	$1.4 \cdot 10^6$	1.86 (0.08)	1.87 ($2.9 \cdot 10^{-4}$)	$4.7 \cdot 10^4$ (9)	5.15 (0.22)	5.15 ($1.00 \cdot 10^{-3}$)	0.55 ($3.7 \cdot 10^{-5}$)	0.230	0.416	0.810
02	$1.6 \cdot 10^6$	1.93 (0.09)	1.93 ($1.7 \cdot 10^{-4}$)	$5.8 \cdot 10^4$ (10)	5.47 (0.26)	5.47 ($7.15 \cdot 10^{-4}$)	0.57 ($3.2 \cdot 10^{-5}$)	0.253	0.447	0.765
15	$1.8 \cdot 10^6$	1.99 (0.12)	1.99 ($2.9 \cdot 10^{-4}$)	$7.0 \cdot 10^4$ (13)	5.78 (0.36)	5.78 ($9.16 \cdot 10^{-4}$)	0.58 ($3.6 \cdot 10^{-5}$)	0.239	0.412	0.725
16	$2.2 \cdot 10^6$	2.10 (0.15)	2.10 ($9.4 \cdot 10^{-4}$)	$9.5 \cdot 10^4$ (41)	6.31 (0.45)	6.31 ($3.12 \cdot 10^{-3}$)	0.60 ($8.8 \cdot 10^{-5}$)	0.241	0.402	0.666
11	$2.7 \cdot 10^6$	2.00 (0.17)	2.00 (0.06)	$1.1 \cdot 10^5$ (7700)	5.87 (0.55)	5.87 (0.31)	0.59 ($1.4 \cdot 10^{-2}$)	0.211	0.358	0.693
03	$3.2 \cdot 10^6$	2.09 (0.18)	2.08 (0.04)	$1.4 \cdot 10^5$ (5600)	6.31 (0.57)	6.28 (0.20)	0.60 ($8.2 \cdot 10^{-3}$)	0.195	0.323	0.656
04	$6.4 \cdot 10^6$	2.47 (0.23)	2.47 (0.04)	$3.8 \cdot 10^5$ (9500)	8.22 (0.76)	8.21 (0.17)	0.67 ($5.5 \cdot 10^{-3}$)	0.169	0.254	0.501
05	$1.6 \cdot 10^7$	3.13 (0.27)	3.12 (0.05)	$1.3 \cdot 10^6$ ($2.0 \cdot 10^4$)	11.5 (1.01)	11.49 (0.24)	0.74 ($3.9 \cdot 10^{-3}$)	0.151	0.205	0.360
18	$6.0 \cdot 10^7$	4.31 (0.34)	4.19 (0.04)	$6.2 \cdot 10^6$ ($3.7 \cdot 10^4$)	17.3 (1.38)	16.83 (0.17)	0.80 ($1.6 \cdot 10^{-3}$)	0.153	0.190	0.246

Table 4.1: Results obtained with moving mesh grid code Elmer. Three regimes were observed: steady (top part of the table), oscillating (middle part of the table) and unsteady (bottom). All experiments are two dimensional and are performed at $\mathrm{Pr} = 7$, $T_{\mathrm{M}} = 0.8$, $\mathrm{St} = 0.9$ and for aspect ratio 4. Standard deviations (if exist) are given in parentheses.

nb	Ra	Q_{bot}	Q_{top}	$\mathrm{Ra}_{\mathrm{eff}}$	$Q_{\mathrm{bot}}^{\mathrm{eff}}$	$Q_{\mathrm{top}}^{\mathrm{eff}}$	$\langle h_{\mathrm{m}} \rangle$	Δh	$\Delta h/h_{\mathrm{m}}$	A
02	$2.7 \cdot 10^6$	1.48	1.48	$5.1 \cdot 10^4$	3.38	3.37	0.46	0.070	0.154	1.194
10	$6.0 \cdot 10^6$	1.61 (0.1)	1.59	$1.3 \cdot 10^5$ $(5.9 \cdot 10^1)$	3.86 (0.23)	3.82	0.48	0.203	0.422	1.081
01	$6.4 \cdot 10^5$	3.5	3.5	$2.0 \cdot 10^5$	5.94	5.94	0.85	0.106	0.124	0.177
03	$1.0 \cdot 10^7$	1.94	1.94	$3.9 \cdot 10^5$	5.62	5.61	0.58	0.137	0.236	0.726
04	$3.0 \cdot 10^7$	2.36 (0.16)	2.36 (0.11)	$1.7 \cdot 10^6$ $(1.1 \cdot 10^5)$	7.73 (0.63)	7.72 (0.53)	0.65 $(1.39 \cdot 10^{-2})$	0.088	0.134	0.528
05	$1.0 \cdot 10^8$	3.21 (0.16)	3.20 (0.03)	$8.4 \cdot 10^6$ $(7.3 \cdot 10^4)$	11.99 (0.62)	11.97 (0.16)	0.75 $(2.18 \cdot 10^{-3})$	0.073	0.097	0.338
06	$1.0 \cdot 10^9$	5.99 (0.28)	6.01 (0.01)	$1.3 \cdot 10^8$ $(1.2 \cdot 10^5)$	25.98 (1.22)	26.03 (0.04)	0.87 $(2.59 \cdot 10^{-4})$	0.008	0.010	0.154

Table 4.2: Results obtained with the fixed grid StagYY code for 2D domain with aspect ratio 4. Standard deviations (if exist) are given in parentheses. $\mathrm{St} = 0.1$ is chosen for all experiments and $T_{\mathrm{M}} = 0.8$ is fixed for all experiments but case 01 where $T_{\mathrm{M}} = 0.5$.

nb	Ra	Q_{bot}	Q_{top}	$\mathrm{Ra}_{\mathrm{eff}}$	$Q_{\mathrm{bot}}^{\mathrm{eff}}$	$Q_{\mathrm{top}}^{\mathrm{eff}}$	$\langle h_{\mathrm{m}} \rangle$	Δh	$\Delta h / h_{\mathrm{m}}$	A
02a2	$2.7 \cdot 10^6$	1.46	1.45	$4.8 \cdot 10^4$	3.24	3.23	0.445	0.097	0.217	1.249
02a	$1.0 \cdot 10^6$	2.03	2.02	$8.2 \cdot 10^4$	4.37	4.37	0.648	0.119	0.184	0.544
10a	$6.0 \cdot 10^6$	1.67	1.67	$1.6 \cdot 10^5$ $(3.1 \cdot 10^0)$	4.28	4.28	0.512 $(3.31 \cdot 10^{-6})$	0.142	0.278	0.953
01a	$6.4 \cdot 10^5$	3.30 (0.01)	3.29	$1.9 \cdot 10^5$ $(2.0 \cdot 10^1)$	5.52 (0.02)	5.52	0.838 $(2.94 \cdot 10^{-5})$	0.120	0.143	0.193
03a	$1.0 \cdot 10^7$	1.84 (0.07)	1.84	$3.4 \cdot 10^5$ $(4.3 \cdot 10^2)$	5.11 (0.20)	5.10	0.554 $(2.35 \cdot 10^{-4})$	0.160	0.289	0.805
04a	$4.0 \cdot 10^7$	2.48 (0.06)	2.48 (0.01)	$2.4 \cdot 10^6$ $(1.1 \cdot 10^4)$	8.33 (0.19)	8.34 (0.05)	0.673 $(9.78 \cdot 10^{-4})$	0.102	0.151	0.486
05a	$1.0 \cdot 10^8$	3.21 (0.08)	3.21 (0.01)	$8.4 \cdot 10^6$ $(1.6 \cdot 10^4)$	12.00 (0.29)	12.03 (0.04)	0.749 $(4.72 \cdot 10^{-4})$	0.068	0.091	0.336
06a	$4.0 \cdot 10^8$	4.62 (0.11)	4.66	$4.5 \cdot 10^7$ $(3.1 \cdot 10^4)$	19.13 (0.45)	19.30 (0.02)	0.828 $(1.87 \cdot 10^{-4})$	0.009	0.011	0.207
07a	$1.0 \cdot 10^9$	6.55 (0.14)	6.62	$1.4 \cdot 10^8$ $(4.6 \cdot 10^4)$	28.78 (0.60)	29.12 (0.02)	0.879 $(9.98 \cdot 10^{-5})$	0.006	0.007	0.137

Table 4.3: Results obtained with the fixed grid StagYY code for 2D domain with aspect ratio 16. Standard deviations (if exist) are given in parentheses. $\mathrm{St} = 0.1$ for all experiments. $T_{\mathrm{M}} = 0.8$ is fixed for all experiments except for case 02a that has $T_{\mathrm{M}} = 0.7$ and case 01a that has $T_{\mathrm{M}} = 0.5$.

nb	Ra	$Q_{\rm bot}$	$Q_{\rm top}$	$\mathrm{Ra}_{\rm eff}$	$Q_{\rm bot}^{\rm eff}$	$Q_{\rm top}^{\rm eff}$	$\langle h_{\rm m}\rangle$	Δh	$\Delta h/h_{\rm m}$	A
01	$1.4\cdot10^5$	1.61	1.61	$1.36\cdot10^4$	2.43	2.43	0.619	0.215	0.347	0.614
06	$3.0\cdot10^5$	1.99	1.99	$4.10\cdot10^4$	3.37	3.37	0.693	0.199	0.287	0.443
02	$5.0\cdot10^5$	2.26	2.26	$7.94\cdot10^4$	4.01	4.01	0.729	0.184	0.253	0.372
03	$1.0\cdot10^6$	2.65 (0.03)	2.64 (0.03)	$1.86\cdot10^5$ $(1.71\cdot10^3)$	4.96 (0.06)	4.96 (0.06)	0.769 $(2.35\cdot10^{-3})$	0.161	0.209	0.301
07	$2.0\cdot10^6$	3.19 (0.02)	3.19 (0.02)	$4.34\cdot10^5$ $(1.98\cdot10^3)$	6.29 (0.04)	6.29 (0.05)	0.809 $(1.23\cdot10^{-3})$	0.128	0.158	0.236
04	$4.0\cdot10^6$	3.87 (0.03)	3.86 (0.03)	$9.82\cdot10^5$ $(4.14\cdot10^3)$	7.95 (0.06)	7.94 (0.07)	0.843 $(1.19\cdot10^{-3})$	0.106	0.126	0.186
08	$2.0\cdot10^7$	3.87 (0.02)	3.88 (0.02)	$3.27\cdot10^6$ $(9.51\cdot10^3)$	10.54 (0.07)	10.56 (0.06)	0.817 $(7.93\cdot10^{-4})$	0.093	0.114	0.225
09	$1.0\cdot10^8$	5.80 (0.05)	5.81 (0.05)	$2.03\cdot10^7$ $(6.41\cdot10^4)$	16.98 (0.16)	17.01 (0.16)	0.878 $(9.24\cdot10^{-4})$	0.055	0.063	0.139
15	$1.4\cdot10^5$	2.05 (0.01)	2.05 (0.01)	$1.98\cdot10^4$ $(1.53\cdot10^2)$	3.50 (0.03)	3.50 (0.03)	0.701 (0.002)	0.183	0.261	0.426
12	$3.0\cdot10^5$	2.51 (0.03)	2.51 (0.03)	$5.29\cdot10^4$ $(6.07\cdot10^2)$	4.62 (0.07)	4.62 (0.06)	0.755 (0.003)	0.176	0.233	0.325
11	$2.0\cdot10^6$	3.94 (0.04)	3.94 (0.04)	$4.89\cdot10^5$ $(2.81\cdot10^3)$	8.09 (0.08)	8.09 (0.09)	0.842 (0.002)	0.125	0.149	0.188
13	$4.0\cdot10^6$	4.70 (0.04)	4.69 (0.05)	$1.07\cdot10^6$ $(4.43\cdot10^3)$	9.93 (0.09)	9.93 (0.11)	0.867 (0.001)	0.113	0.130	0.153

Table 4.4: Results obtained with the fixed grid StagYY code in 3D cartesian geometry with dimensions $4\times4\times1$. Top and bottom parts of the table, respectively, contain results with noslip and freeslip velocity condition, respectively, at the base of the computation domain. Standard deviations (if exist) are given in parentheses. $\mathrm{St}=0.14$ was chosen for all experiments. $T_{\rm M}=0.59$ was fixed for all experiments except for cases 08 and 09 where $T_{\rm M}=0.7$ was imposed.

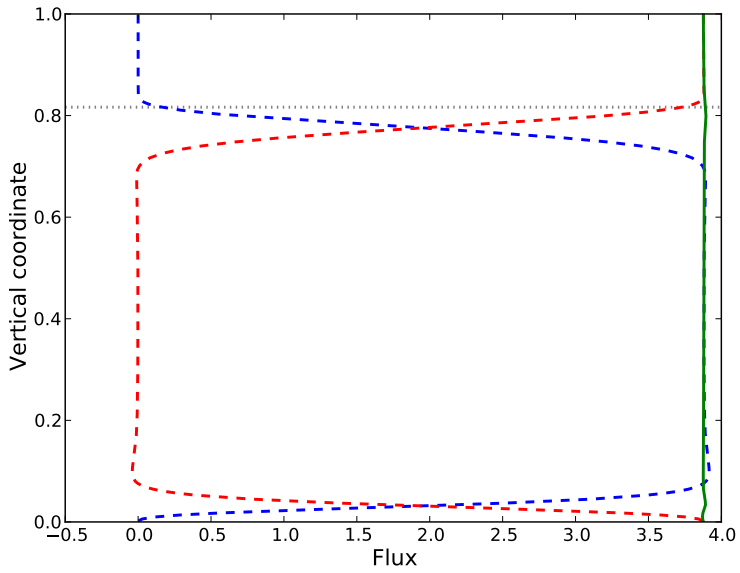

Figure 4.10: Profiles of horizontally and temporally averaged advective flux (blue dashed line), conductive flux (red dashed line) and their sum (solid green line). The horizontal dotted line represents the mean (spatial and temporal) position of the phase interface. We distinguish the frozen upper part of the cavity where conduction prevails as the solid in non-deformable with zero advective transport. The liquid layer contains a well mixed interior where heat is transported by advection and conduction is negligible. At the bottom and at the phase interface, advection vanishes and conduction prevails. The conservation of energy is indeed verified as the sum of the advective and conductive fluxes is constant at all depths. (3D simulation using StagYY with $\mathrm{Ra} = 2 \cdot 10^7$ and $T_\mathrm{M} = 0.7$)

We proceed by quantifying the relation between the Nusselt and the Rayleigh numbers. As was noted in Chapter 2, the general scaling law has the form

$$\mathrm{Nu}_\mathrm{eff} = \beta_1 \mathrm{Ra}_\mathrm{eff}^{\beta_2}\,, \tag{4.4}$$

where β_1 depends among other things on the boundary conditions. Some authors argue, that β_1 does not depend on Pr for $\mathrm{Pr} > 1$ (e.g King et al., 2012). For β_2, one of the theories based on marginal stability analysis predicts β_2 equal to 1/3 for large Ra (Malkus, 1954b). This implies that the dimensional heat flux transfered across a convecting layer does not depend on its thickness and also that the dynamics of the bottom and top boundary layers are independent.

Theoretical scalings based on the dynamical equations both in the bulk and in the boundary layers have been derived in Grossmann and Lohse (2000) and discussed for Earth's systems in Jaupart and Mareschal (2010). Several regimes in the (Ra,Pr) parameter space were proposed depending on whether the boundary layer or the bulk dominates the global thermal and kinetic energy dissipation.

A collection of our results is plotted in Figure 4.11 (top) where the numerical data points are depicted

together with experimental data of Rossby (1969) and Hill (1996). Rossby (1969) performed laboratory experiments of classical Rayleigh-Bénard convection with water (Pr = 7) and silicon oil (Pr = 200). We notice that our results obtained at Pr = ∞ in 3D geometry and with a no-slip bottom boundary condition correspond remarkably well to his results (for both the steady and unsteady regimes). This suggests that a convecting layer undergoing a solidification/melting follows the same laws as Rayleigh-Bénard convection. In addition, due to this agreement we conclude as well that we made a right choice in the selection of scaling parameters (we use the depth of a liquid layer and the temperature difference across the convecting liquid). However, note that the physics is not exactly the same although the exponents are close. Also note that the thickness of the layer used as a scaling dimension is a simulation outcome and depends itself in a way on Ra.

Hill (1996) has conducted a series of laboratory experiments in the same set up as ours, i.e. he studied a system with a frozen upper part of the cavity lying above a convecting liquid. His experiments were done with glycerol (Pr = $4 \cdot 10^4$) in a domain with aspect ratio (horizontal to vertical dimension) varying from 4 to 8. His data points fall also in the same range of results.

Considering only 3D experiments that were performed for two different bottom horizontal boundary conditions (no shear stress and vanishing velocities) we see immediately that the heat transfer is more efficient when free-slip is imposed.

As was discussed earlier, there are several transitions in the convective style (Malkus, 1954a; Krishnamurti, 1970a). When searching for a $\mathrm{Nu_{eff}}(\mathrm{Ra_{eff}})$ relationship each of the regimes must be fitted separately so that only experiments following the same convective regime are handled together. Results of regression are gathered in Table 4.5 and are plotted in Figure 4.11 (bottom). For unsteady regimes the β_2 exponent varies from 0.26 for 3D experiments at Pr = ∞ to 0.29 for 2D experiments for the same Prandtl number. In any case we obtain an exponent inferior to 1/3.

Also, the transition from steady to time dependent convective mode is accompanied by the decrease of β_2 (Table 4.5) at both Prandtl numbers and we are receding from a theoretical value 1/3. However, this is consistent to that of what would be expected. The discrete transitions toward turbulence at finite Prandtl number generally decrease the slope in the Nu(Ra) dependence (Grossmann and Lohse, 2000).

We should not overlook that the results can probably slightly change with the different domain size (the best way would be to work on a sphere). Indeed, fixing an aspect ratio of the cavity determines the wavelength of convective cells. The horizontal size of the domain must be an integer multiple of the size of a convective cell. Since the thickness of the liquid layer changes with time and is an outcome of a simulation, the final aspect ratio of the liquid layer is also not known until the (statistically) steady state is reached and changes for each experiment. Resulting aspect ratios are given in Table 4.6.

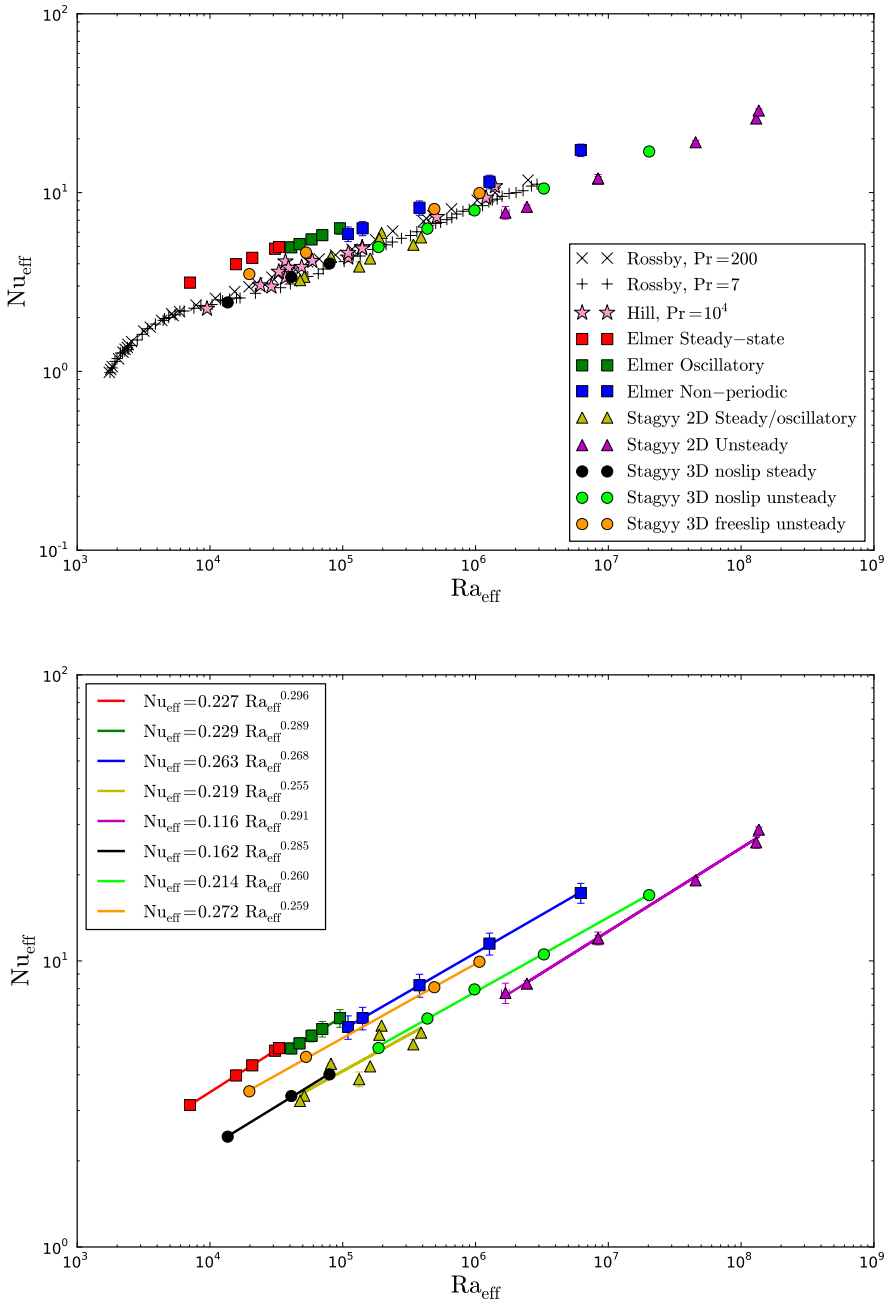

Figure 4.11: Nusselt number as a function of the Rayleigh number. (top) Numerical data with experimental results of Rossby (1969) and Hill (1996). (bottom) Numerical fits. Different convective regimes are fitted separately.

Regime	Domain	Pr	β_1	β_2	Ra range
Steady	2D	7	0.227 (0.0005)	0.296 (0.0005)	$7 \cdot 10^3 < \mathrm{Ra}_{\mathrm{eff}} < 4 \cdot 10^4$
Oscillating	2D	7	0.229 (0.0009)	0.289 (0.0008)	$4 \cdot 10^4 < \mathrm{Ra}_{\mathrm{eff}} < 10^5$
Unsteady	2D	7	0.263 (0.0033)	0.268 (0.0022)	$10^5 < \mathrm{Ra}_{\mathrm{eff}} < 10^7$
Steady/Oscillating	2D	∞	0.219 (0.0658)	0.255 (0.0583)	$4 \cdot 10^4 < \mathrm{Ra}_{\mathrm{eff}} < 4 \cdot 10^5$
Unsteady	2D	∞	0.116 (0.0066)	0.291 (0.0079)	$10^6 < \mathrm{Ra}_{\mathrm{eff}} < 10^8$
Steady	3D	∞	0.162 (0.0065)	0.285 (0.0088)	$10^4 < \mathrm{Ra}_{\mathrm{eff}} < 10^5$
Unteady	3D *	∞	0.214 (0.0062)	0.260 (0.0047)	$2 \cdot 10^5 < \mathrm{Ra}_{\mathrm{eff}} < 2 \cdot 10^7$
Unteady	3D †	∞	0.272 (0.0051)	0.259 (0.0036)	$2 \cdot 10^4 < \mathrm{Ra}_{\mathrm{eff}} < 10^6$

Table 4.5: Least squares fitting of equation $\mathrm{Ra}_{\mathrm{eff}} = \beta_1 \mathrm{Nu}_{\mathrm{eff}}^{\beta_2}$ with standard deviations of the regression in the parentheses. *computed with no-slip velocity boundary conditions at the bottom of the domain. †free-slip velocity conditions at the bottom were imposed.

Pr	box size	$\mathrm{Ra}_{\mathrm{eff}}$ range	A range	aspect ratio range
7	4×1	$7 \cdot 10^3 - 6 \cdot 10^6$	$0.25 - 1.28$	$5.0 - 9.1$
∞	4×1	$2 \cdot 10^5 - 10^8$	$0.15 - 1.19$	$4.6 - 8.8$
∞	16×1	$5 \cdot 10^4 - 10^8$	$0.14 - 1.25$	$18 - 36$
∞	$4 \times 4 \times 1$ *	$10^4 - 2 \cdot 10^7$	$0.14 - 0.61$	$4.6 - 6.5$
∞	$4 \times 4 \times 1$ †	$2 \cdot 10^4 - 10^6$	$0.15 - 0.43$	$4.6 - 5.7$

Table 4.6: Range of parameters for different experiments. A is a ratio of mean solid and liquid thicknesses once the permanent state is reached. The aspect ratio is computed as a ratio of the horizontal size of the domain and the liquid layer thickness. *computed with no-slip velocity boundary conditions at the bottom of the domain. † free-slip velocity conditions at the bottom were imposed.

4.3 Analytical model: physical quantities as function of wavelength of convection

Previously we explored the dependence of the heat transport (given by the effective Nusselt number) on the convective vigour (quantified by the effective Rayleigh number) and gave parameters (determined numerically) β_1 and β_2 in the general scaling $\mathrm{Nu}_{\mathrm{eff}} = \beta_1 \mathrm{Ra}_{\mathrm{eff}}^{\beta_2}$, cf. Table 4.5. From our results, we obtain, that β_2 is slightly smaller than 1/3. This means that the heat flux at the interface (with dimensions) is dependent on the total depth of the convecting liquid layer (although only weakly) and it also means that the dynamics of the boundary layer is dependent on the flow in the bulk.

In the next section we conduct a finer analysis where instead of focusing on β_2 we explore the dependence of β_1 on the size of convective cells to further explain the measured heat flux. We compare the synthetic numerical data with an analytical model derived below (called the fluid loop model). Such models were presented e.g. by Turcotte and Oxburgh (1967), Guillou and Jaupart (1995) or Grigné et al. (2005) and also were discussed in Jaupart and Mareschal (2010) but we make some modifications to suit our particular set-up.

4.3.1 Loop model

We consider one convective cell (thickness h_m, length L_c) in Cartesian 2D geometry that underlies a diffusive layer (thickness h_s). The hot upwelling current occurs beneath the lid on the left and the cold downwelling current on the right hand sides. The interior of the cell is well mixed and has a temperature T_i, cf. Figure 4.12.

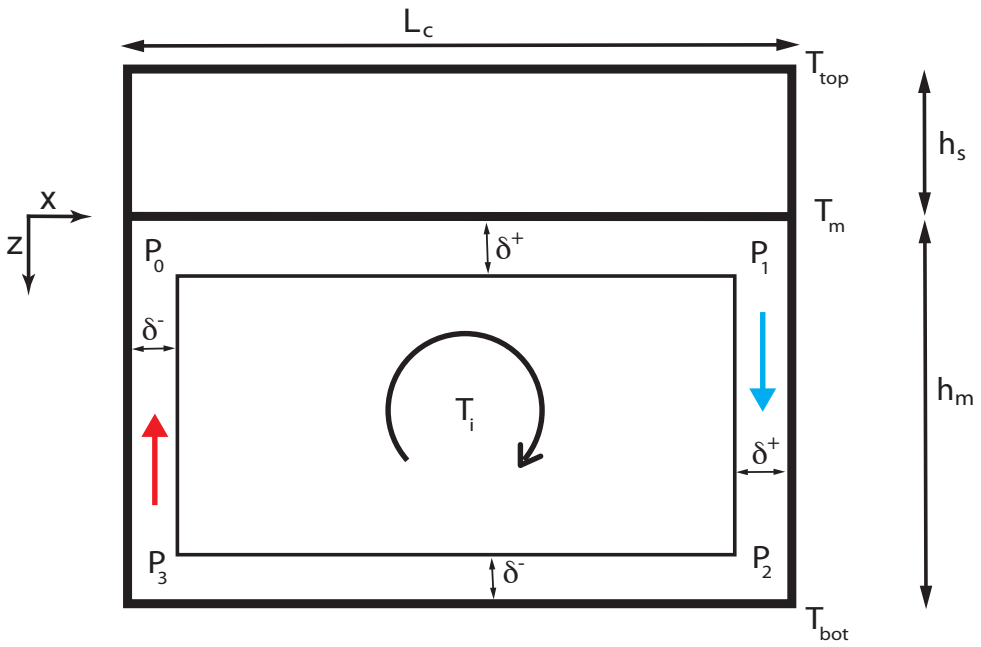

Figure 4.12: Schematic picture of the loop model setup.

The uniform temperature T_bot at the bottom of the cell is imposed. The temperature prescribed at the melting front (that is considered to be planar) is T_M. The vertical sides are thermally insulated with fixed temperatures of T_hot in the hot upwelling and T_cold in the cold downwelling, respectively.

Heat transfer in the upper and lower thin boundary layers in the cell proceeds by conduction, the temperature distribution can be thus obtained from a model of cooling of a semi-infinite space. For the lower boundary layer we have for the temperature distribution $T(t,z)$

$$\frac{T(t,z)-T_\mathrm{i}}{T_\mathrm{bot}-T_\mathrm{i}} = \mathrm{erfc}\left(\frac{h_\mathrm{m}-z}{2\sqrt{\kappa t}}\right), \tag{4.5}$$

where the time t is measured following a parcel of fluid starting from the bottom right corner and moving horizontally to the left. Considering a uniform horizontal velocity u at the bottom of the box, we replace

a time dependence by a spatial dependence, i.e. $t = (L_\mathrm{c} - x)/u$. Then, the mean heat flux is given by

$$\overline{Q_\mathrm{bot}} = \frac{1}{L_\mathrm{c}} \int_0^{L_\mathrm{c}} q_\mathrm{bot}(x)\,\mathrm{d}x = \frac{1}{L_\mathrm{c}} \int_0^{L_\mathrm{c}} k \frac{\partial T(x,z)}{\partial z}\bigg|_{z=h_\mathrm{m}} \mathrm{d}x = \frac{2k(T_\mathrm{bot} - T_\mathrm{i})}{\sqrt{\pi\kappa L_\mathrm{c}}}\sqrt{u}\,. \tag{4.6}$$

In order to determine the velocity u we consider the balance of work of shear stresses and buoyancy forces over the cell volume V that reads as

$$0 = \int_V \boldsymbol{F}\cdot\boldsymbol{v}\,\mathrm{d}V + \int_V (\nabla\cdot\tau)\cdot\boldsymbol{v}\,\mathrm{d}V\,. \tag{4.7}$$

Using the identity $\nabla\cdot(\tau\cdot\boldsymbol{v}) = (\nabla\cdot\tau)\cdot\boldsymbol{v} + \tau^T : \boldsymbol{\nabla v}$ and the divergence theorem we can rewrite Eq.(4.7) as

$$\int_V \boldsymbol{F}\cdot\boldsymbol{v}\,\mathrm{d}V = \int_V \tau : \nabla\boldsymbol{v}\,\mathrm{d}V - \int_S \tau\cdot\boldsymbol{v}\,\mathrm{d}\boldsymbol{S}\,, \tag{4.8}$$

where S is the surface that bounds the volume V. Transposition of the shear stress τ was removed because of the symmetry of the tensor. The second term on the right hand side vanishes due to the boundary conditions since at the phase boundary the velocity is zero and at sides and bottom shear stress acting on the boundary must be zero. We thus obtain a balance equation

$$\int_V \boldsymbol{F}\cdot\boldsymbol{v}\,\mathrm{d}V = \int_V \tau : \nabla\boldsymbol{v}\,\mathrm{d}V\,, \tag{4.9}$$

that expresses that the work of buoyancy forces is entirely converted into dissipation (e.g. Hewitt et al., 1975)

$$\tau : \boldsymbol{\nabla v} = \tau_{ij}\frac{\partial v_i}{\partial x_j}\,. \tag{4.10}$$

In order to compute the viscous tensor

$$\tau = \eta_\mathrm{L}\left(\boldsymbol{\nabla v} + (\boldsymbol{\nabla v})^T\right)\,, \tag{4.11}$$

we approximate the velocity profiles by piecewise continuous linear functions (Figure 4.13) that would meet the boundary condition requirements. The horizontal profile of vertical velocity varies linearly with the largest velocity w at vertical sides. Since convective cells are not always square, a free parameter λ appears, that is the distance in the horizontal cross section over which velocity changes (Grigné et al., 2005). The vertical profile of horizontal velocity is composed of piecewise linear functions corresponding to a zero velocity boundary condition at the melting front, having the maximum value $\gamma_2 u$ at the distance $\gamma_1 h_\mathrm{m}/2$ from the phase change interface. This choice will be discussed in more detail further in the manuscript. The lower boundary is free-slip with the maximum horizontal velocity u.

We introduced two parameters, γ_1 and γ_2, in the velocity profile, that are tied by the mass conservation condition

$$(1-\gamma_1)h_\mathrm{m}u = \gamma_1 h_\mathrm{m}\gamma_2 u \quad\Rightarrow\quad \gamma_1 = \frac{1}{1+\gamma_2}\,. \tag{4.12}$$

Since the viscosity is approximately constant in the liquid, velocity profiles lead to a horizontal shear

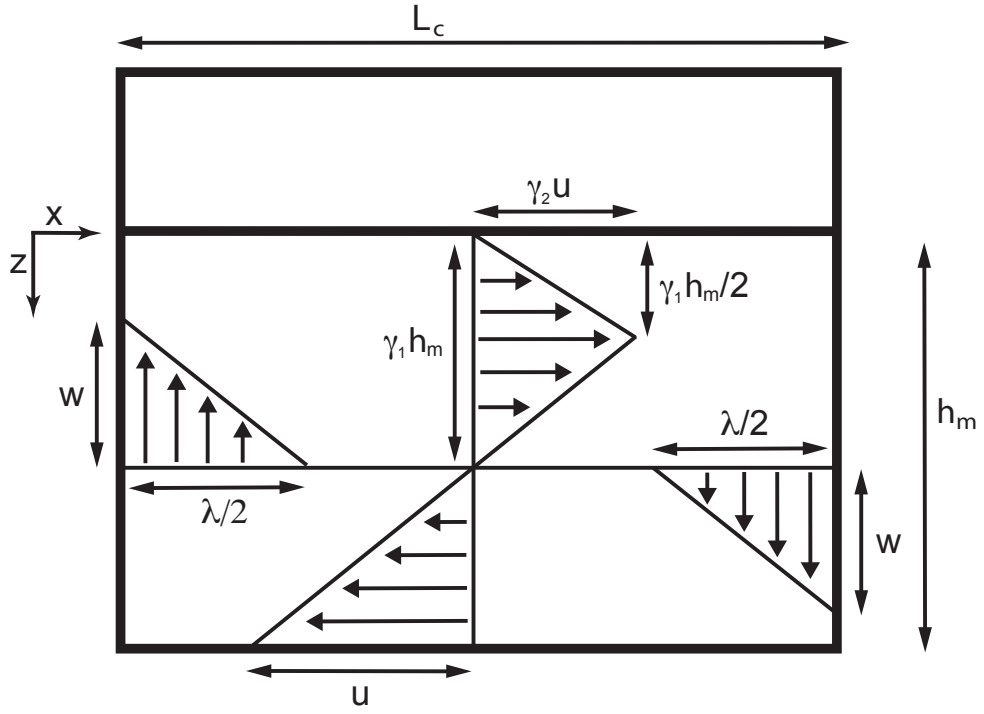

Figure 4.13: Schematic picture of velocity profiles in one convecting cell.

stress for $z \in (0, \gamma_1 h_\mathrm{m}/2)$

$$\tau_\mathrm{h}^\mathrm{top} = -\eta_\mathrm{L} \frac{2\gamma_2 u}{\gamma_1 h_\mathrm{m}}\,, \tag{4.13}$$

and for $z \in (\gamma_1 h_\mathrm{m}/2, h_\mathrm{m})$ to

$$\tau_\mathrm{h}^\mathrm{bot} = \eta_\mathrm{L} \frac{u}{h_\mathrm{m}(1-\gamma_1)}\,. \tag{4.14}$$

Vertical shear stress is

$$\tau_\mathrm{v} = -\eta_\mathrm{L} \frac{2w}{\lambda}\,. \tag{4.15}$$

The dissipation in Eq.(4.9) is approximately calculated by separating horizontal and vertical parts of the shear stress

$$\int_V \tau : \boldsymbol{\nabla v}\, \mathrm{d}V = \eta_\mathrm{L} \left(\frac{4h_\mathrm{m}}{\lambda} w^2 + \frac{2\gamma_2^2 L_\mathrm{c}}{\gamma_1 h_\mathrm{m}} u^2 + \frac{L_\mathrm{c}(2-\gamma_1)}{2h_\mathrm{m}(1-\gamma_1)^2} u^2 \right)\,, \tag{4.16}$$

and we remove the vertical velocity w dependence by considering the conservation of mass

$$w\frac{\lambda}{2} = u h_\mathrm{m}(1-\gamma_1)\,, \tag{4.17}$$

to obtain

$$\int_V \tau : \boldsymbol{\nabla v}\,\mathrm{d}V = \eta_\mathrm{L} u^2 \left((4\gamma_2\gamma_1)^2 \left(\frac{h_\mathrm{m}}{\lambda}\right)^3 + \frac{2\gamma_2^2 L_\mathrm{c}}{\gamma_1 h_\mathrm{m}} + \frac{L_\mathrm{c}(2-\gamma_1)}{2h_\mathrm{m}(1-\gamma_1)^2} \right) . \tag{4.18}$$

A buoyancy force per unit length is $f_\mathrm{c} = \alpha g \rho \delta^+ (T_\mathrm{i} - T_\mathrm{cold})$ for cold downwelling and $f_\mathrm{h} = \alpha g \rho \delta^- (T_\mathrm{hot} - T_\mathrm{i})$ for hot upwelling with T_cold the temperature of cold downwelling and T_hot the temperature of hot upwelling. The rate of heat flux per unit of length of both plumes is

$$A = A_\mathrm{c} + A_\mathrm{h} = \rho c_\mathrm{p} w \left(\delta^+ (T_\mathrm{i} - T_\mathrm{cold}) + \delta^- (T_\mathrm{hot} - T_\mathrm{i}) \right) . \tag{4.19}$$

Using Eq.(4.6) we can write for the total heat through bottom boundary

$$A = \overline{Q_\mathrm{top}} L_\mathrm{c} = \overline{Q_\mathrm{bot}} L_\mathrm{c} = 2k(T_\mathrm{bot} - T_\mathrm{i}) \sqrt{\frac{uL_\mathrm{c}}{\pi\kappa}} . \tag{4.20}$$

Combining Eqs.(4.20) and (4.19) we get

$$\delta^+ (T_\mathrm{i} - T_\mathrm{cold}) + \delta^- (T_\mathrm{hot} - T_\mathrm{i}) = 2(T_\mathrm{bot} - T_\mathrm{i}) \frac{u}{w} \left(\frac{\kappa L_\mathrm{c}}{\pi u} \right)^{1/2} , \tag{4.21}$$

that is introduced into the buoyancy force giving

$$f_\mathrm{c} + f_\mathrm{h} = 2\alpha\rho g (T_\mathrm{bot} - T_\mathrm{i}) \frac{u}{w} \left(\frac{\kappa L_\mathrm{c}}{\pi u} \right)^{1/2} . \tag{4.22}$$

The velocity can be then expressed by inserting Eq.(4.17) and (4.22) to Eq.(4.9) as

$$u = \frac{\kappa}{h_\mathrm{m}} \left(\frac{L_\mathrm{c}}{\pi h_\mathrm{m}} \right)^{1/3} \left(\frac{T_\mathrm{bot} - T_\mathrm{i}}{T_\mathrm{bot} - T_\mathrm{M}} \right)^{2/3} \left(\frac{2\mathrm{Ra}_\mathrm{eff}}{f(L_\mathrm{c})} \right)^{2/3} , \tag{4.23}$$

with $f(L_\mathrm{c})$

$$f(L_\mathrm{c}) = 16\gamma_1^2\gamma_2^2 \left(\frac{h_\mathrm{m}}{\lambda} \right)^3 + \frac{2-\gamma_1}{2(1-\gamma_1)^2} \frac{L_\mathrm{c}}{h_\mathrm{m}} + \frac{2\gamma_2^2}{\gamma_1} \frac{L_\mathrm{c}}{h_\mathrm{m}} . \tag{4.24}$$

Inserting Eq. (4.23) into Eq. (4.6) we get the mean heat flux through the bottom boundary as

$$\overline{Q_\mathrm{bot}} = \frac{k(T_\mathrm{bot} - T_\mathrm{M})}{h_\mathrm{m}} \left(\frac{T_\mathrm{bot} - T_\mathrm{i}}{T_\mathrm{bot} - T_\mathrm{M}} \right)^{4/3} \frac{2^{4/3}}{\pi^{2/3}} \left(\frac{\mathrm{Ra}_\mathrm{eff}}{f(L_\mathrm{c})} \right)^{1/3} \left(\frac{h_\mathrm{m}}{L_\mathrm{c}} \right)^{1/3} . \tag{4.25}$$

In order to compare our numerical results with analytical model derived above we use a time averaged quantities (temperature and velocity) that are computed when statistical steady states are reached. Interval over which averages are constructed is not fixed and for one particular run several time averaging periods are usually chosen.

For each simulation, first we need to determine individual convective cells. A convective cell is defined as the space in the fluid in between adjacent hot and cold plumes. For steady solutions finding cells is

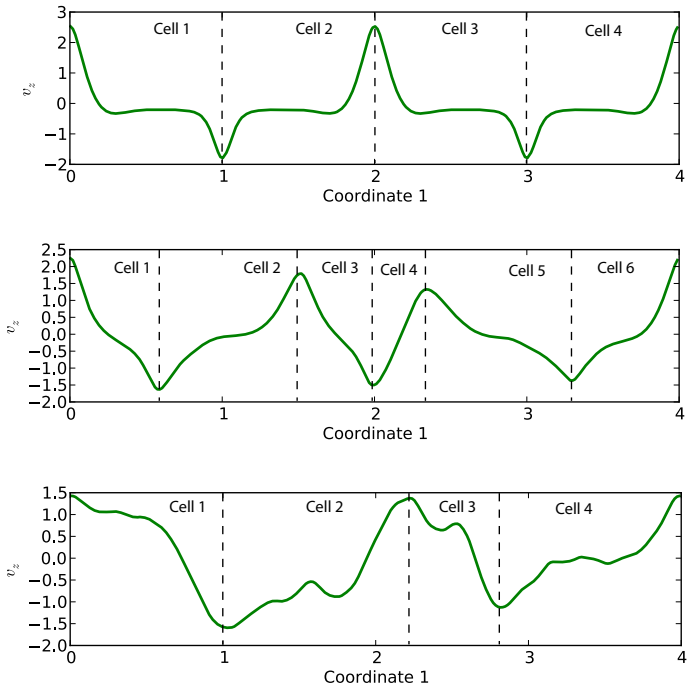

Figure 4.14: Observed horizontal profiles of vertically averaged vertical velocity v_z at (top) $\mathrm{Ra} = 6 \cdot 10^6$ ($\mathrm{Ra_{eff}} = 10^5$) (middle) $\mathrm{Ra} = 10^8$ ($\mathrm{Ra_{eff}} = 8 \cdot 10^6$) (bottom) $\mathrm{Ra} = 10^9$ ($\mathrm{Ra_{eff}} = 10^8$). Velocities are normalized using the root mean square of the velocity. Time averaged velocity fields are used for the analysis. Dashed vertical lines denote position of plumes that define the cell size. (top) 4 cells were detected (middle) 6 cells were detected (bottom) 4 convective cells were detected.

obvious, cf. e.g. Figure 4.5(c) where six convective cells are clearly present in the box. For unsteady flows, cf. e.g. Figure 4.5(e), definition of the cell is less obvious. One possibility is to use temperature threshold to detect plumes since plumes exhibit (positive or negative) thermal anomalies. However, here we prefer to use the velocity field. In order to detect individual cells we use vertically averaged vertical velocity in the box, see Figure 4.14. Zones of upwellings and downwellings, respectively, then correspond to places where the velocity profile is maximal and minimal, respectively. Thresholds are used to determine which peak is considered as plume. Distance between two adjacent peaks is read as a size of a convective cell. Within a detected cell, the mean bottom heat flux, mean temperature, effective Rayleigh number and velocity at the bottom of the cell are computed.

Figure 4.14(top) shows a horizontal profile of vertically averaged velocity for a steady state simulation. The form of the profile can be considered as, in the first approximation, a piecewise linear function. Although in reality, the horizontal gradient of vertical velocity increases closer to upwelling/downwelling (Jarvis and Peltier, 1982). We also note that cells are regular and parameter λ is the same for all cells. This is not the case for unsteady flows (Figure 4.14(middle)) where λ differs significantly for each cell. For even more unsteady flows (Figure 4.14(bottom)) the structure of the velocity

profile is less clear.

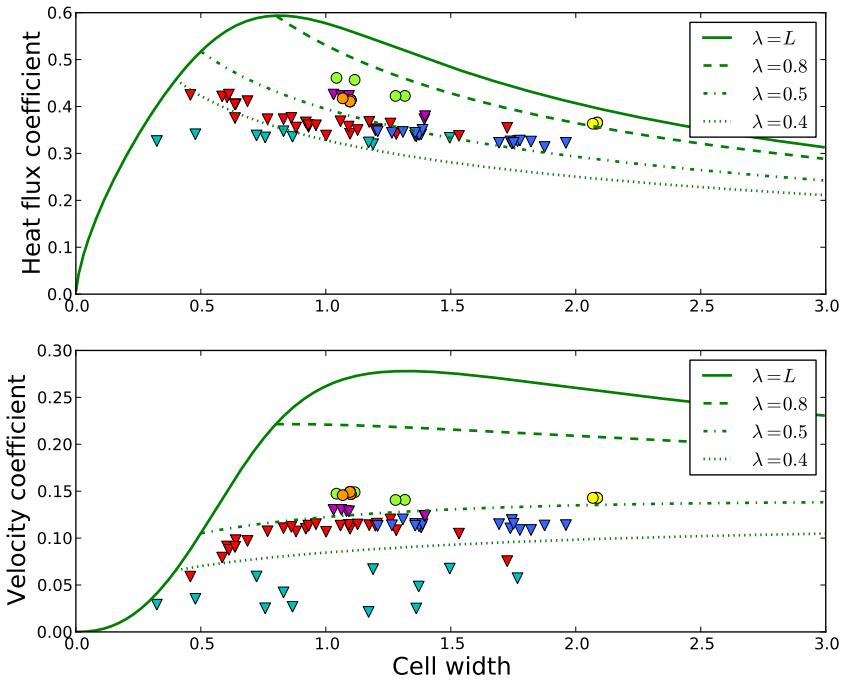

Figure 4.15: Comparison of time averaged numerical results with analytical model for high prandtl number experiments in boxes with aspect ratio 4. Circles represent experiments at steady state, inverse triangles cases with unsteady flow. Each point represents a result for one detected cell. (Orange: $\mathrm{Ra} = 2.7 \cdot 10^6\,, \mathrm{Ra}_{\mathrm{eff}} = 5.1 \cdot 10^4$; yellow: $\mathrm{Ra} = 6 \cdot 10^6\,, \mathrm{Ra}_{\mathrm{eff}} = 1.3 \cdot 10^5$; green: $\mathrm{Ra} = 6.4 \cdot 10^5\,, \mathrm{Ra}_{\mathrm{eff}} = 1.9 \cdot 10^5$; magenta: $\mathrm{Ra} = 10^7\,, \mathrm{Ra}_{\mathrm{eff}} = 3.6 \cdot 10^5$; blue: $\mathrm{Ra} = 3 \cdot 10^7\,, \mathrm{Ra}_{\mathrm{eff}} = 1.6 \cdot 10^6$; red: $\mathrm{Ra} = 10^8\,, \mathrm{Ra}_{\mathrm{eff}} = 8.4 \cdot 10^6$; cyan: $\mathrm{Ra} = 10^9\,, \mathrm{Ra}_{\mathrm{eff}} = 1.3 \cdot 10^8$.)

Once we have diagnostic quantities for each cell, we plot the heat flux coefficient in a dimensionless form (Figures 4.15(top) and 4.16(top))

$$\overline{Q_{\mathrm{bot}}}(1 - T_{\mathrm{i}})^{-4/3}\mathrm{Ra}_{\mathrm{eff}}^{-1/3}\,, \tag{4.26}$$

and the velocity coefficient in a dimensionless form (Figures 4.15(bottom) and 4.16(bottom))

$$u(1 - T_{\mathrm{i}})^{-2/3}{\mathrm{Ra}_{\mathrm{eff}}}^{-2/3}\,, \tag{4.27}$$

as a function of cell width and we compare these results with analytical model derived above that is represented in figures for several parameters λ. λ is considered to be independent of the cell width L_{c}. The parameter $\gamma_2 = 2/3$ was chosen and gives $\gamma_1 = 3/5$. We inspect 2D experiments at high Pr for two

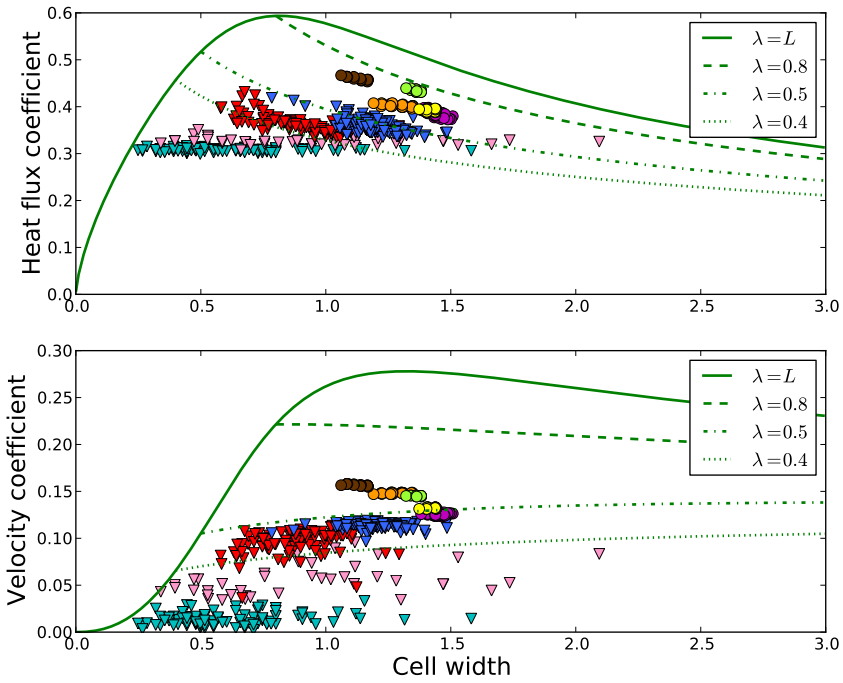

Figure 4.16: Comparison of time averaged numerical results with analytical model for high prandtl number experiments in boxes with aspect ratio 16. Circles represent experiments at steady state, inverse triangles cases with unsteady flow. Each point represents a result for one detected cell. (Brown: $\mathrm{Ra} = 10^6\,, \mathrm{Ra}_{\mathrm{eff}} = 8.1 \cdot 10^4$; orange: $\mathrm{Ra} = 2.7 \cdot 10^6\,, \mathrm{Ra}_{\mathrm{eff}} = 4.7 \cdot 10^4$; yellow: $\mathrm{Ra} = 6 \cdot 10^6\,, \mathrm{Ra}_{\mathrm{eff}} = 1.6 \cdot 10^5$; green: $\mathrm{Ra} = 6.4 \cdot 10^5\,, \mathrm{Ra}_{\mathrm{eff}} = 1.9 \cdot 10^5$; magenta: $\mathrm{Ra} = 10^7\,, \mathrm{Ra}_{\mathrm{eff}} = 3.4 \cdot 10^5$; blue: $\mathrm{Ra} = 4 \cdot 10^7\,, \mathrm{Ra}_{\mathrm{eff}} = 2.5 \cdot 10^6$; red: $\mathrm{Ra} = 10^8\,, \mathrm{Ra}_{\mathrm{eff}} = 8.4 \cdot 10^6$; pink: $\mathrm{Ra} = 4 \cdot 10^8\,, \mathrm{Ra}_{\mathrm{eff}} = 4.5 \cdot 10^7$; cyan: $\mathrm{Ra} = 10^9\,, \mathrm{Ra}_{\mathrm{eff}} = 1.4 \cdot 10^8$.)

aspect ratios of the computational domain (4 and 16). Results fall close to predicted laws although the match is not ideal. The higher the Ra, the smaller λ explains better the numerical results. Best matches are obtained for small λ ($\lambda = 0.4$). We also note, that the analytical model predicts better the mean heat flux coefficient rather than the horizontal velocity coefficient. Predicted velocities are much higher than the observed ones.

4.3.2 Amplitude of corrugation

Assuming that we know the heat flux at the phase interface as a function of horizontal coordinate $q_{\mathrm{m}}(x)$. Then using the linear dependence for the conductive flux in the solid with thickness h_{s}

$$q_{\mathrm{m}}(x) = q_{\mathrm{top}}(x) = k \frac{T_{\mathrm{M}} - T_{\mathrm{top}}}{h_{\mathrm{s}}(x)}\,, \tag{4.28}$$

we can determine the amplitude of corrugations Δh as

$$\Delta h = h_{\mathrm{s}}(x = L_{\mathrm{c}}) - h_{\mathrm{s}}(x = 0) = k(T_{\mathrm{M}} - T_{\mathrm{top}}) \left(\frac{1}{q_{\mathrm{m}}(x = L_{\mathrm{c}})} - \frac{1}{q_{\mathrm{m}}(x = 0)} \right) . \tag{4.29}$$

In order to derive $q_{\mathrm{m}}(x)$, we proceed the in same way as in the section 4.3.1 supposing that the temperature profile in the top thermal boundary can be approximated by the analytical solution of conduction in a semi-infinite space

$$\frac{T(t, z) - T_{\mathrm{i}}}{T_{\mathrm{M}} - T_{\mathrm{i}}} = \mathrm{erfc} \left(\frac{z}{2\sqrt{\kappa t}} \right) , \tag{4.30}$$

that results in the heat flux at the melting interface

$$q_{\mathrm{m}} = k \frac{\partial T(x, z)}{\partial z} \bigg|_{z=0} \mathrm{d}x = \frac{2k(T_{\mathrm{i}} - T_{\mathrm{M}})}{\sqrt{\pi \kappa t}} . \tag{4.31}$$

Time dependence can not be simply replaced by the relation $t = x/u$ since the phase change boundary imposes no-slip conditions with zero velocity. However, velocity in the vicinity of the melting front as well as the mean heat flux at the phase change interface must follow the same Ra dependence. This implies that the ratio between the two velocities, the maximum velocity in the top boundary layer of the convecting cell and the maximum velocity at the bottom of the convecting layer, must remain the same for different convective vigour. Also, the depth at which horizontal velocity in the upper part of the cell attains its maximum (denoted as depth $\gamma_1 h_{\mathrm{m}}/2$ in Figure 4.13) should not be affected by convection. Figures 4.17 and 4.18 show that indeed these two quantities stay constant for a wide range of Rayleigh numbers.

Thus, we consider that the velocity is determined to some adjustable constant c_{vel} so that we write $t = x/(c_{\mathrm{vel}} u)$ resulting in

$$q_{\mathrm{m}}(x) = \frac{2k(T_{\mathrm{i}} - T_{\mathrm{M}})}{\sqrt{\pi \kappa}} \sqrt{\frac{c_{\mathrm{vel}} u}{x}} . \tag{4.32}$$

Considering the equality of the bottom and middle mean heat flux at steady state, $\overline{q_{\mathrm{bot}}} = \overline{q_{\mathrm{m}}}$, we obtain a condition for c_{vel}

$$c_{\mathrm{vel}} = \left(\frac{T_{\mathrm{bot}} - T_{\mathrm{i}}}{T_{\mathrm{i}} - T_{\mathrm{M}}} \right)^2 . \tag{4.33}$$

Fig 4.19 shows c_{vel} as a function of T_{i}.

Once we know the spatial dependence of the heat flux, Eq. (4.32), we can determine the amplitude of the phase change topography Eq. (4.29). Yet, the heat flux diverges at $x = 0$. Thus, as a measure of topography size we use

$$\Delta h = h_{\mathrm{s}}(x = L_{\mathrm{c}}) - \overline{h_{\mathrm{s}}(x)} = k(T_{\mathrm{M}} - T_{\mathrm{top}}) \left(\frac{1}{q_{\mathrm{m}}(x = L_{\mathrm{c}})} - \frac{1}{L_{\mathrm{c}}} \int_0^{L_{\mathrm{c}}} \frac{1}{q_{\mathrm{m}}(x)} \mathrm{d}x \right) . \tag{4.34}$$

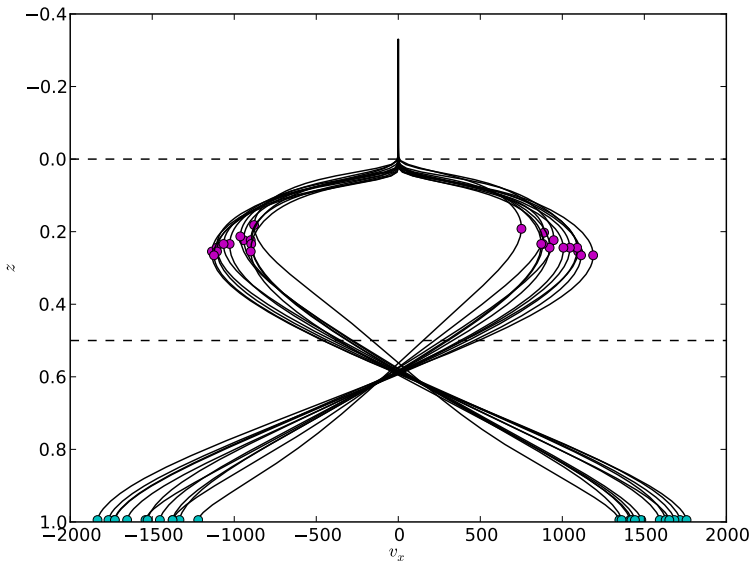

Figure 4.17: Each solid black line represents a vertical profile of horizontal velocity v_{x} in the middle of a convective cell. Magenta circles are maxima of velocity in the upper part of the cell. Cyan circles are maxima of velocity at the bottom boundary. The dashed lines at $z = 0$ and $z = 0.5$ represent a limit between the solid and the liquid layers (negative z values correspond to the solid where the velocity is zero) and a mid-depth of the liquid, respectively. (2D simulation with computation domain aspect ratio 16 and $\mathrm{Ra} = 10^8$ ($\mathrm{Ra}_{\mathrm{eff}} = 8 \cdot 10^6$))

Using Eq. (4.32) to evaluate heat flux in (4.34) we obtain

$$\Delta h = \frac{T_{\mathrm{M}} - T_{\mathrm{top}}}{T_{\mathrm{i}} - T_{\mathrm{M}}} \frac{\sqrt{\pi \kappa L_{\mathrm{c}}}}{6\sqrt{c_{\mathrm{vel}} u}}\,, \tag{4.35}$$

that can be further transformed using the expression for velocity derived earlier Eq. (4.23)

$$\Delta h = h_{\mathrm{m}} \frac{T_{\mathrm{M}} - T_{\mathrm{top}}}{T_{\mathrm{i}} - T_{\mathrm{M}}} \left(\frac{T_{\mathrm{bot}} - T_{\mathrm{i}}}{T_{\mathrm{bot}} - T_{\mathrm{M}}} \right)^{1/3} \frac{\pi^{2/3}}{2^{4/3}} \left(\frac{L_{\mathrm{c}}}{h_{\mathrm{m}}} \right)^{1/3} \frac{f(L_{\mathrm{c}})^{1/3}}{3\sqrt{c_{\mathrm{vel}}}} \mathrm{Ra}_{\mathrm{eff}}^{-1/3}\,. \tag{4.36}$$

Finally, after rescaling and using Eq.(4.33) for coefficient c_{vel} we obtain

$$\Delta h = -\frac{T_{\mathrm{top}}}{(1 - T_{\mathrm{i}})^{2/3}} \frac{\pi^{2/3} {L_{\mathrm{c}}}^{1/3}}{2^{4/3}} \frac{f(L_{\mathrm{c}})^{1/3}}{3} \mathrm{Ra}_{\mathrm{eff}}^{-1/3}\,, \tag{4.37}$$

where $f(L_{\mathrm{c}})$ is given by Eq.(4.24).

The comparison of our analytical model with numerical simulations is depicted on Figures 4.20

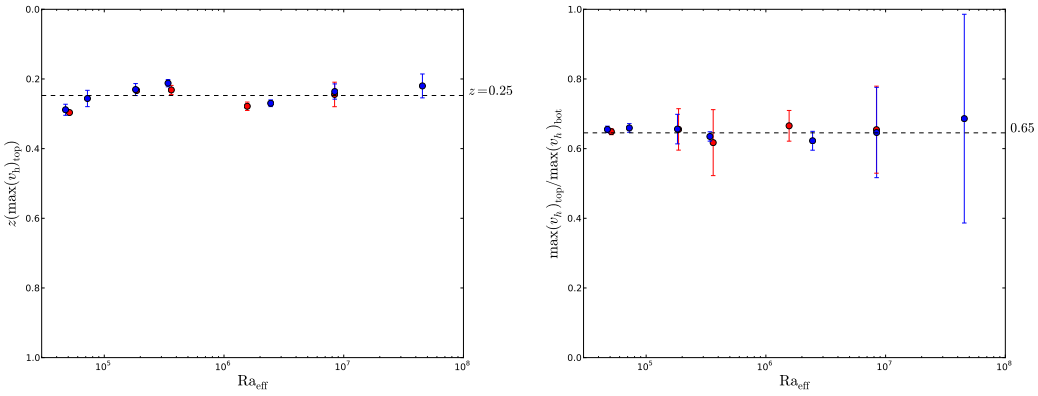

Figure 4.18: (Left) Depth at which the horizontal velocity attains its maximum in the upper part of the convective cell as a function of the Rayleigh number. The dashed horizontal line at $z = 0.25$ represents a mean value for all experiments. (Right) Ratio of maximum horizontal velocities in the upper and lower part of the cell with a mean value represented by the dashed horizontal line. Red and blue circles, respectively, denote simulations in a box with aspect ratio 4 and 16, respectively. Each symbol represents an average for all cells detected and the error bars thus give a variability of quantities observed (the largest deviations are naturally observed for the most unsteady flows, i.e. the highest $\mathrm{Ra_{eff}}$).

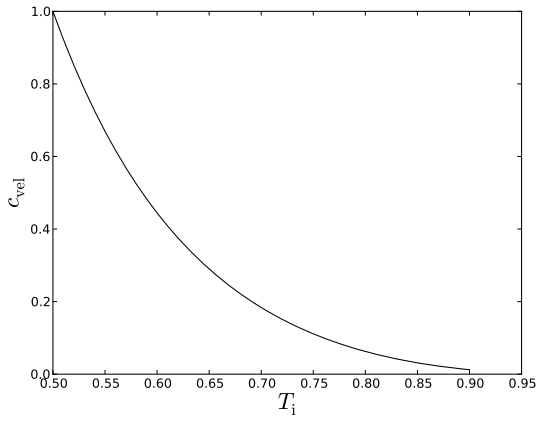

Figure 4.19: Variation of an adjustable parameter $c_{\rm vel}$ as a function of internal temperature $T_{\rm i}$

and 4.21 where for each cell we compute the value of coefficient (in a dimensionless form)

$$-\Delta h(1-T_{\rm i})^{2/3}\,\mathrm{Ra_{eff}}^{1/3}\,, \tag{4.38}$$

and plot it against cell width.

Numerical results fall in the places where theoretical predictions are lying. However, they are far from close match (even for steady cases). The loop model is built on an assumption of steady state. When

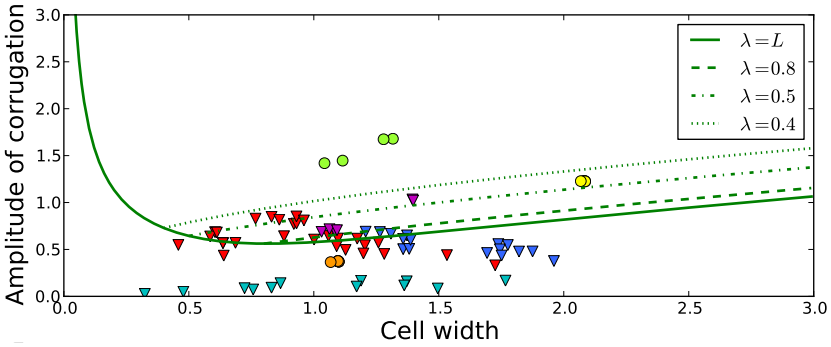

Figure 4.20: Comparison of time averaged numerical results with the analytical model for high Prandtl number experiments in boxes with aspect ratio 4. Each point represents a result for one detected cell. Circles denote experiments at steady state, inverse triangles cases with unsteady flow. (Orange: $\mathrm{Ra} = 2.7 \cdot 10^6$, $\mathrm{Ra_{eff}} = 5.1 \cdot 10^4$; yellow: $\mathrm{Ra} = 6 \cdot 10^6$, $\mathrm{Ra_{eff}} = 1.3 \cdot 10^5$; green: $\mathrm{Ra} = 6.4 \cdot 10^5$, $\mathrm{Ra_{eff}} = 1.9 \cdot 10^5$; magenta: $\mathrm{Ra} = 10^7$, $\mathrm{Ra_{eff}} = 3.6 \cdot 10^5$; blue: $\mathrm{Ra} = 3 \cdot 10^7$, $\mathrm{Ra_{eff}} = 1.6 \cdot 10^6$; red: $\mathrm{Ra} = 10^8$, $\mathrm{Ra_{eff}} = 8.4 \cdot 10^6$; cyan: $\mathrm{Ra} = 10^9$, $\mathrm{Ra_{eff}} = 1.3 \cdot 10^8$.)

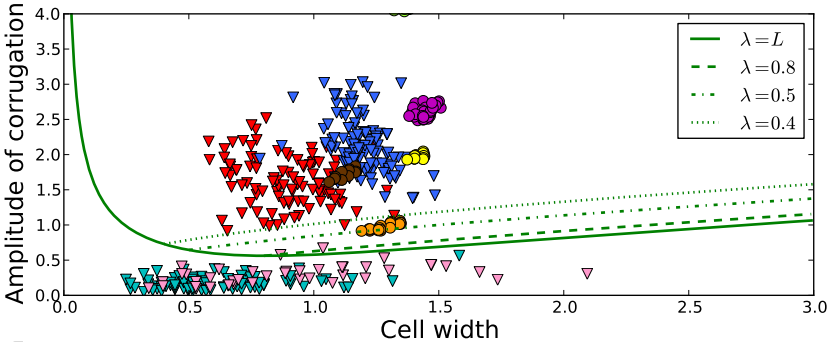

Figure 4.21: Comparison of time averaged numerical results with analytical model for high Prandtl number experiments in boxes with aspect ratio 16. Each point represents a result for one detected cell. Circles denote experiments at steady state, inverse triangles cases with unsteady flow. (Brown: $\mathrm{Ra} = 10^6$, $\mathrm{Ra_{eff}} = 8.1 \cdot 10^4$; orange: $\mathrm{Ra} = 2.7 \cdot 10^6$, $\mathrm{Ra_{eff}} = 4.7 \cdot 10^4$; yellow: $\mathrm{Ra} = 6 \cdot 10^6$, $\mathrm{Ra_{eff}} = 1.6 \cdot 10^5$; green: $\mathrm{Ra} = 6.4 \cdot 10^5$, $\mathrm{Ra_{eff}} = 1.9 \cdot 10^5$; magenta: $\mathrm{Ra} = 10^7$, $\mathrm{Ra_{eff}} = 3.4 \cdot 10^5$; blue: $\mathrm{Ra} = 4 \cdot 10^7$, $\mathrm{Ra_{eff}} = 2.5 \cdot 10^6$; red: $\mathrm{Ra} = 10^8$, $\mathrm{Ra_{eff}} = 8.4 \cdot 10^6$; pink: $\mathrm{Ra} = 4 \cdot 10^8$, $\mathrm{Ra_{eff}} = 4.5 \cdot 10^7$; cyan: $\mathrm{Ra} = 10^9$, $\mathrm{Ra_{eff}} = 1.4 \cdot 10^8$.)

convection flow is highly time dependent, progressive remelting and refreezing of the solid occur and thus we expect the theoretical model to be less accurate. This can explain why we observe for the highest Ra very low amplitudes of corrugations, lower than the loop model predictions.

4.4 Conclusions

We study a convecting melted layer that undergoes slow crystallization. The convective cells developed in the liquid are characterized by up-flows and down-flows, hence the solidification is not uniform and corrugations of the phase interface are formed. The amplitude of corrugations decreases with increasing convective vigour and it is negligible for highly time dependent flows.

It was proposed that a molten layer was formed at the base of the Earth's mantle early after formation of the core. In order to determine a thermal history of the Earth that would experience extensive melting of its deep interior, we investigate the heat transfer across a solidifying convecting liquid. We propose a scaling law for the mean heat flux coming out. Although the physics of the system differs from the classical Rayleigh-Bénard convection, scalings for these two systems are (with an eligible choice of scaling quantities) close. We further present an analytical model that includes the dependence of the heat flow on the size of the convective cells. The analysis shows that the data can be better matched with a theory when the wavelength of a convective cell is taken into account.

An analytical model has been also derived to predict a size of the BMO topography. However, a rather unsatisfactory match is observed between the predictions and synthetic data although, taken into account that the loop model is very simple, theory and data are relatively close. For the estimated BMO parameters, its topography due to convective motions in the liquid would be negligible, but can be still important due to heterogeneous mantle temperature variations.

Conclusions

In this thesis, we have explored several aspects of the dynamics of the early Earth, focusing on it's compositional and thermal evolution on multiple scales.

During the differentiation of planetary bodies, iron separates from silicates and descends to the centre of the planet to form the metallic core. Chemical equilibration proceeds between dispersed metal blobs and background silicate liquids. We build a physical framework and numerically model for the equilibration process that occurs by diffusion at the rim and is enhanced by stirring inside as well as outside the blobs. We derive scaling laws for the time it takes to reach the equilibrium. These scaling relations critically depend on the dynamic regime of the flow and on the material properties of the two liquids. In particular, the chemical exchange is enhanced when internal circulation is developed in the descending material and/or when inertia dominates the system due to significant reduction of the boundary layer thicknesses. The proposed scaling laws are applied to nickel equilibration during the Earth's core formation event and we show that the system tends to be in chemical equilibrium at all times.

Simultaneously to the differentiation of the Earth, extensive melting of its interior occurs. During the violent late accretion stages, large impacts hit the planets and part of their kinetic energy remains buried inside the impacted body. The temperature increase superimposed to the energy released by short lived radioactive nuclides and gravitational energy released due to core formation are sufficient heat sources to melt the interior of the planet at some stages of its evolution. Following this idea, we explore the evolution of a molten silicate layer, a basal magma ocean (BMO), that would form in between the Earth's mantle and the core. The initial thickness of the BMO is estimated to be up to one thousand kilometers and since the heat flow from the interior of the planet is limited by the overlying solid mantle, timescales of crystallization of this system would be very long (about the age of the Earth).

We perform numerical experiments of the system representing the crystallizing BMO underlying the solid mantle. Well developed vigorous convection in the liquid magma ocean is simulated. The solid layer, representing the bottom thermal boundary of the mantle, is modelled as a non-deformable medium with suppressed velocities. The melting/freezing front in between represents a free moving boundary that needs to be tracked. We focus on short term thermal evolution of the system and conduct a systematic study of the dynamics of the solidification process coupled with convective flow. We infer scaling laws for the heat flux coming out of the system. Parametrized relations are then used to estimate the super-

isentropic temperature difference maintained across the BMO, which happens to be minute, implying that the Earth's core must cool at the same pace as the BMO.

The style of convective motion in the liquid layer determines the size of corrugations that are developed due to non-homogeneous temperature conditions in the vicinity of the liquid-solid phase change interface. Convecting vigour tends to decrease the corrugation's amplitude. Hence, for the BMO with high convective vigour, the topography due to unsteady flow in the liquid is negligible, but might be important due to large scale heterogeneous temperature variations in the solid mantle.

Perspectives

All our numerical simulations have been performed with constant top temperature boundary conditions. Yet, large scale convection in the solid mantle imposes laterally varying temperature/heat flux conditions. Convection in the BMO can change the way these lateral variations at the bottom of the solid mantle are transmitted to the core. To mimic the effect of convection in the overlying solid mantle, laterally varying temperature should be imposed at the top surface in the computation domain. A systematic study with large ratio boxes and laterally varying top temperature boundary condition should be conducted. This would allow to estimate the buffering effect of the BMO on the lateral variations imposed by the solid mantle as seen by the core.

Preliminary simulations have been run. Figure 4.22 shows two snapshots of temperature field: one with constant top temperature boundary conditions and the second one with variable top temperature conditions (imposed temperature variations are represented on Figure 4.23(top)). Imposing variable top temperature conditions results in development of important topography of the phase change interface. Large scale modulation of the heat flux at the bottom and top of the cavity appears (Figure 4.23(bottom)).

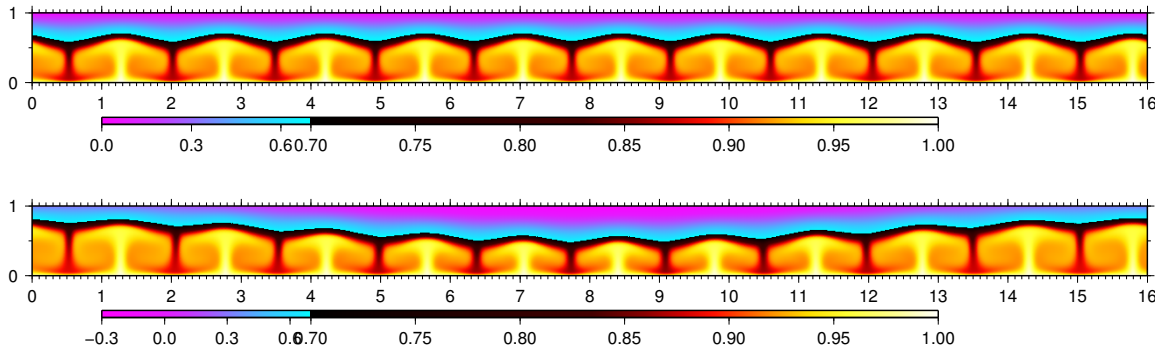

Figure 4.22: Snapshots of the temperature field for cases with a spatially varying temperature imposed at the top boundary. Pink to cyan color scale represents temperatures in the solid. Black to yellow colors represent temperatures in the liquid. (top) constant temperature at the top of the cavity is imposed (bottom) amplitude of temperature variations is 0.6. (Case $\mathrm{Pr} = \infty$, $\mathrm{Ra} = 10^6$, $T_\mathrm{M} = 0.7$)

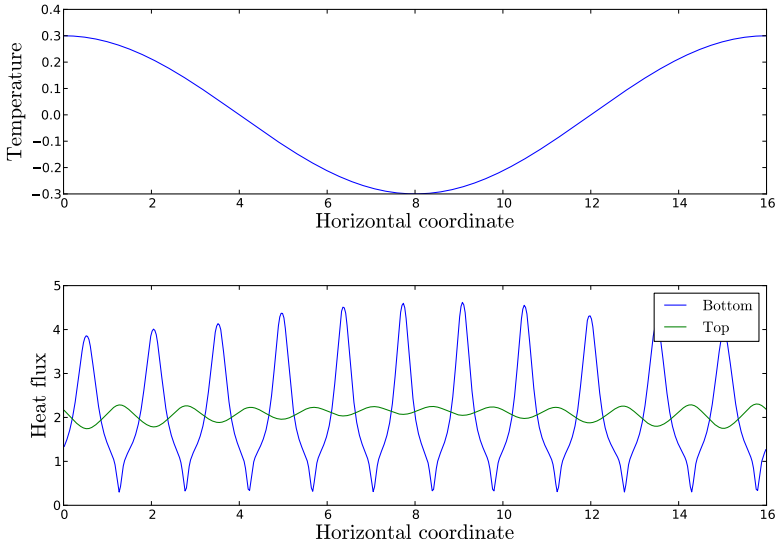

Figure 4.23: (top) temperature variations imposed at the top of the cavity. (bottom) resulting heat flux at the top and bottom. Corresponding temperature snapshot at steady state is represented in Figure 4.22 (bottom). (Case $\mathrm{Pr} = \infty$, $\mathrm{Ra} = 10^6$, $T_\mathrm{M} = 0.7$)

Laterally varying heat flux boundary condition at the top of the cavity could be implemented. This would be probably more representative for the conditions solid mantle imposes in its lowermost parts. However, this would imply that the whole cavity might end up in solid or liquid state and from preliminary tests it seems to be the case for most experiments. It is very difficult to obtain a steady solution, even in the statistical sense, where the solid and liquid layers would remain in the cavity. As a remedy, melting temperature of the material should be adjusted in time so as to keep the phase change position within the domain.

Including compositional buoyancy would be also a possible step to cover more complex physics and be able to model thermo-chemical convection and multi-component phase change. This would certainly be more realistic for a lot of natural phenomenons since geophysical systems such as sea-ice, lava lakes or magma chambers are always composed of multiple components. As a result, more complex behaviour could be modelled such as super-cooling at the solid-liquid interface or dynamics and formation of mushy layers. Also, this would allow us to have a melting temperature that depends on the material composition.

A numerical model accounting for the thermal evolution of the whole planet could be developed. It should couple dynamics of the core, the BMO and the mantle. The thermal history of the system over the age of the Earth would then be simulated.

More systems that undergo crystallization/melting while vigorously convecting should be studied and derived scaling relations could be applied to them. These include for example icy satellites. Space missions *Galileo* and *Cassini* have revealed that large scale subsurface water oceans could be present on icy satellites of Jupiter and Saturn (Anderson et al., 1998; Kivelson et al., 2000; Sohl et al., 2002; Porco et al., 2006; Schubert et al., 2007). Internal structure being still great debated, our model can contribute to constrain the internal dynamics of these objects.

Appendix A

Mesh resolution

Here, a grid resolution of individual simulations is given in Tables A.1 and A.2.

nb	Aspect ratio	Ra	nx	ny	nz
02	4	$2.7 \cdot 10^6$	256		64
10	4	$6 \cdot 10^6$	512		128
01	4	$6.4 \cdot 10^5$	1024		512
03	4	10^7	1024		256
04	4	$3 \cdot 10^7$	512		256
05	4	10^8	512		256
06	4	10^9	512		256
02a2	16	$2.7 \cdot 10^6$	1024		64
02a	16	10^6	1024		128
10a	16	$6 \cdot 10^6$	1024		128
01a	16	$6.4 \cdot 10^5$	1024		128
03a	16	10^7	1024		128
04a	16	$4 \cdot 10^7$	1024		128
05a	16	10^8	1024		128
06a	16	$4 \cdot 10^8$	1024		128
07a	16	10^9	1024		128
01b	4×4	$1.4 \cdot 10^5$	256	256	128
06	4×4	$3 \cdot 10^5$	256	256	128
02b	4×4	$5 \cdot 10^5$	256	256	128
03	4×4	10^6	256	256	128
07	4×4	$2 \cdot 10^6$	256	256	128
04	4×4	$4 \cdot 10^6$	256	256	128
08	4×4	$2 \cdot 10^7$	256	256	256
09	4×4	10^8	256	256	256
15	4×4	$1.4 \cdot 10^5$	256	256	128
12	4×4	$3 \cdot 10^5$	256	256	128
11	4×4	$2 \cdot 10^6$	256	256	128
13	4×4	$4 \cdot 10^6$	256	256	128

Table A.1: Grid resolution for experiments performed with StagYY code. nx, ny and nz are number of volumes in the two horizontal and vertical directions.

nb	Ra	nx	nz_{liq}	nz_{sol}
09a	$4.2 \cdot 10^5$	200	30	10
01a	$6.4 \cdot 10^5$	200	30	10
12a	$7.5 \cdot 10^5$	200	30	10
07a	$9.6 \cdot 10^5$	300	45	10
13a	10^6	300	45	10
08a	$1.3 \cdot 10^6$	300	45	10
14a	$1.4 \cdot 10^6$	300	45	10
02a	$1.6 \cdot 10^6$	300	45	10
15a	$1.8 \cdot 10^6$	400	50	10
16a	$2.2 \cdot 10^6$	400	50	10
11a	$2.7 \cdot 10^6$	300	45	10
03a	$3.2 \cdot 10^6$	300	45	10
04a	$6.4 \cdot 10^6$	300	45	10
05a	$1.6 \cdot 10^7$	500	85	10
18a	$6 \cdot 10^7$	500	85	10

Table A.2: Grid resolution for experiments performed with Elmer code in 2D Cartesian geometry in boxes with aspect ratio 4. nx is a number of elements in the horizontal direction. nz_{liq} and nz_{sol} are number of elements in the vertical direction in the liquid and solid.

nx	nz_{liq}	nz_{sol}	Ra_{eff}	Q_{bot}	Q_{top}	% ΔQ
250	45	8	$1.2748 \cdot 10^6$ $(2.67 \cdot 10^4)$	11.40 (0.97)	11.55 (0.28)	1.37
500	85	10	$1.2732 \cdot 10^6$ $(2.01 \cdot 10^4)$	11.50 (1.01)	11.49 (0.24)	0.06

Table A.3: Resolution test at $\text{Ra} = 1.6 \cdot 10^7$ for moving mesh method in the box with aspect ratio 4. In parenthesis standard devations of a given quantity are given. nx is a number of elements in the horizontal direction. nz_{liq} and nz_{sol} are number of elements in the vertical direction in the liquid and solid.

Several resolution tests were carried out, cf. Tables A.3 and A.4. Considering a simulation with moving mesh method (Table A.3), when approximately doubling the number of elements in the horizontal and vertical directions in the liquid, the heat flux changes about 0.9%.

Resolution tests for the enthalpy method all show a small difference between the top and bottom heat fluxes (inferior to 1%), that verifies the conservation of energy in the system. At Rayleigh number 10^7, the mean heat flux changes about 1.1% when passing from 512×128 resolution to 1024×256 grid.

nx	nz	Ra	$\mathrm{Ra}_{\mathrm{eff}}$	Q_{bot}	Q_{top}	$\%\Delta Q$
128	32	$2.7 \cdot 10^6$	$4.33 \cdot 10^4$	3.06	3.04	0.64
256	64	$2.7 \cdot 10^6$	$5.13 \cdot 10^4$	3.38	3.37	0.29
128	32	$6.4 \cdot 10^5$	$1.87 \cdot 10^5$	5.31	5.30	0.16
256	64	$6.4 \cdot 10^5$	$1.93 \cdot 10^5$	5.73	5.72	0.11
512	128	$6.4 \cdot 10^5$	$1.95 \cdot 10^5$	5.90	5.89	0.04
1024	512	$6.4 \cdot 10^5$	$1.96 \cdot 10^5$	5.94	5.94	0.01
256	64	10^7	$3.61 \cdot 10^5$	5.32	5.29	0.50
512	128	10^7	$3.83 \cdot 10^5$	5.55	5.54	0.17
1024	256	10^7	$3.89 \cdot 10^5$	5.62	5.61	0.06
256	64	10^9	$1.20 \cdot 10^8$	5.06	5.11	0.9
512	256	10^9	$1.30 \cdot 10^8$	5.99	6.01	0.19

Table A.4: Resolution test for the enthalpy method for four different Ra numbers. Aspect ratio of the computation domain is 4.

Appendix B

Article: A model of metal-silicate separation on growing planets

During my master project and first months of my thesis I developed a finite volume numerical model solving for the equation of conservation of chemical species in axisymmetric spherical geometry. Subsequently, this code has been integrated into more complex model describing the evolution of metal-silicate separation on growing planets. Results have been published in an international journal (Monteux et al., 2009) and the paper is attached below. With its governing topic describing the evolution of the primitive Earth, it naturally complements the work presented in this manuscript.

A Model of Metal-Silicate Separation on Growing Planets

J. Monteux[a], Y. Ricard[a], N. Coltice[a], F. Dubuffet[a], and M. Ulvrova[a]

[a] *Université de Lyon, Lyon, F-69003, France ; Université Lyon 1, Lyon, F-69003, France ; Ecole Normale Supérieure de Lyon, Lyon, F-69364, France ; CNRS, UMR5570, Laboratoire de Sciences de la Terre, Villeurbanne, F-69622, France.*

Abstract

The thermal evolution of planets during their accretionary growth is strongly influenced by impact heating. The temperature increase following a collision takes place mostly below the impact location in a volume a few times larger than that of the impactor. Impact heating depends essentially on the radius of the impacted planet. When this radius exceeds $\sim$ 1000 km, the metal phase melts and forms a shallow and dense pool that penetrates the deep mantle as a diapir. To study the evolution of a metal diapir we propose a model of thermo-chemical readjustment that we compare to numerical simulations in axisymmetric spherical geometry and with variable viscosity. We show that the metallic phase sinks with a velocity of order of a Stokes velocity. The thermal energy released by the segregation of metal is smaller but comparable to the thermal energy buried during the impact. However as the latter is distributed in a large undifferentiated volume and the former potentially liberated into a much smaller volume (the diapir and its close surroundings) a significant heating of the metal can occur raising its temperature excess by at most a factor 2 or 3. When the viscosity of the hot differentiated material decreases, the proportion of thermal energy transferred to the undifferentiated material increases and a protocore is formed at a temperature close to that of the impact zone.

Key words: core formation; meteoritical impacts; early earth; numerical modeling; differentiation.

1. Introduction

Core formation is the most important differentiation event that occured during Earth's history. Metal/silicates separation is a rapid event (< 60 My) (Yin et al., 2002; Kleine et al., 2002; Touboul et al., 2007) contemporaneous with Earth accretion and involving gravitational mechanisms such as percolation, negative diapirism and Rayleigh-Taylor instabilities (Stevenson, 1990; Honda et al., 1993). In the homogeneous accretion hypothesis, metal segregation and thereby core formation need significant heating to exceed the melting temperature of iron alloys or of silicates. During the early stages of planetesimals formation, heating by decay of short lived radionuclides is a potential energy source to enhance early differentiation (Yoshino et al., 2003). As a planetesimal grows, its gravity increases and it will increasingly attract the other surrounding planetesimals. The dissipation of the kinetic energy of the impacts provides a later shallow source of heat.

Impacts of large planetesimals have strongly influenced the late accretionary and thermal state of nearly fully-formed planetary bodies (Tonks and Melosh, 1992; Senshu et al., 2002). During an impact, when the relative velocity between a planet and an impactor overcomes the seismic velocities of the medium, a shock wave develops. The shock pressure is nearly uniform in a spherical region next to the impact (the isobaric core), and strongly decays away from it (Croft, 1982; Pierazzo et al., 1997). In this isobaric core, the kinetic energy of the impact is dissipated and leaves a temperature anomaly of several hundred degrees on Moon to Mars size bodies (Senshu et al., 2002; Monteux et al., 2007). The temperatures reached are mostly related to the properties (density and radius) of the impacted body, and only weakly to those of the impactor (Monteux et al., 2007). The melting temperature of iron alloys is lower than the silicates solidus (Fei et al., 1997; Agee, 1997; Ghosh and McSween, 1998). On large impacted

planets, a local differentiation may occur between heavy metal and light silicates in the heated anomaly (Tonks and Melosh, 1992). Hence, a thermo-chemical readjustment follows, associated with the sinking of the metallic component toward the center of the impacted protoplanet (Fig. 1).

For large planets, gravitational energy release due to core formation can induce melting of the whole planet (Stevenson, 1989; Ricard et al., 2009). This subsequent melting depends on the mechanisms of the metal descent (Samuel and Tackley, 2008; Golabek et al., 2008). The aim of this study is to determine the thermal evolution of metal during descent and the thermal state of the core.

First, we propose analytical and numerical isoviscous models of segregation of a purely spherical iron diapir. As the viscosity contrast between molten metal and undifferentiated cold material can reach several orders of magnitude, we then focus on more realistic models of segregation of metal after a large impact with temperature dependent rheologies. We show that the size of impactors and viscosities involved largely determine the inner thermal state of a young planet.

2. Thermo-chemical state after large impact

2.1. Thermal state

After a meteoritical impact, heating is localized in a spherical region called the isobaric core just beneath the impact site. The radius of the isobaric core R_{ic} is comparable to the radius of the impactor R_{imp} and depends on energy conversion during the shock. With a minimal set of assumptions, we get $R_{ic} = 3^{1/3}\ R_{imp}$ following Senshu et al. (2002) and Pierazzo et al. (1997). Just after the adiabatic pressure release, the isobaric core is isothermal and we call ΔT_0 the shock induced temperature increase. The lower script 0 indicates that we consider this instant as the origin of our time variable. Outside the isobaric core, the temperature anomaly decays as $\Delta T_0(r) = \Delta T_0 \left(R_{ic}/r\right)^m$ with $m \sim 4.4$

as proposed by Senshu et al. (2002). Assuming that the kinetic energy of the impactor is controlled by the escape velocity of the impacted body and that impactor and impacted body have the same densities (i.e., $\rho_{ic} = \rho_{imp} \equiv \rho_0$), a simple energy balance (see e.g., Monteux et al., 2007), indicates that

$$\Delta T_0 = \frac{4\pi}{9} \frac{\gamma}{h(m)} \frac{\rho_0^2 G R^2}{\overline{\rho C_p}}, \tag{1}$$

where $\overline{\rho C_p}$ is the average heat capacity of the impacted body that is plausibly a mixture of silicate and metal, G is the gravitational constant, ρ_0 is the density of the undifferentiated material, R is the radius of the impacted planet and where the function $h(m)$ represents the volume effectively heated normalized by the volume of the isobaric core (typically $h(m) \sim 2 - 3$ (Monteux et al., 2007)). The empirical coefficient γ is the fraction of the kinetic energy of the impactor dissipated as heat. From shock experiments, γ ranges between 0.2 and 0.4 depending on material properties and shock velocities (O'Keefe and Ahrens, 1977) (i.e., 20 to 40% of the kinetic energy is buried at depth, the rest rapidly radiated away during or shortly after the impact). The shock-induced temperature excess, ΔT_0, strongly increases with the radius of the impacted body. According to the set of parameters of Table 1, $\Delta T_0(\mathrm{K}) = 4.7 \times 10^{-5} R^2(\mathrm{km})$; for a Moon size body ΔT_0 is 140 K while it is 1925 K for an Earth size body.

The thermal state of a protoplanet before an impact depends on its growth history and on its initial heating caused by short lived radionuclides like ^{26}Al and ^{60}Fe. This early radioactive heating can eventualy cause melting and differentiation of planetesimals that have quickly grown (Yoshino et al., 2003). The impact heating superimposed to a sufficiently hot protoplanetary interior can trigger melting of the Fe-FeS system (the eutectic temperature is close to 1250 K at 1 bar) (Fei et al., 1997) and potentially of silicates (solidus temperature is around 1500 K at 1 bar) (Agee, 1997). In these cases, a fraction of the thermal

energy is converted to latent heat during the phase transformations.

2.2. Compositional state

An impact on a large enough undifferentiated protoplanet composed of a mixture of metals and silicates can trigger phase transformations and initiate differentiation. The first component that melts is the metal phase. In the region where metal melting occurs, the liquid metal can percolate through the solid silicate matrix. Percolation is only possible for small dihedral angles ($< 60°$) or for large melt volume fraction above a percolation threshold. The dihedral angle of liquid iron alloy within silicates is large ($\sim 100°$) in the upper mantle but decreases with increasing pressure (Shannon and Agee, 1996). However, the volume fraction of liquid alloy is typically larger than 10% if melting is complete, which overcomes the percolation threshold (Von Bargen and Waff, 1986). On Earth the core represents 17% of the volume of the planet, Mars has likely a slightly smaller core but Mercury's core is 43% of the planet. The metal is collected at the bottom boundary of the melted zone forming a diapir that ultimately sinks within the interior of the impacted protoplanet (Ricard et al., 2009).

If the temperature exceeds the silicate solidus and eventually the liquidus, the separation of metal and silicates can occur as a metal rainfall through a turbulent magma (Stevenson, 1990; Höink et al., 2005). Small droplets of heavy metal sediment at the bottom of the melted region. This scenario may not be the generic one, as it would imply that a planet embryo maintains a melted metal component without differentiating until the silicates start melting. It has been suggested that the metal may segregate per percolation, as soon as it melts, while the silicates are still mostly solid (Ricard et al., 2009). Locally, however, the impact of an undifferentiated planetesimal on an already differentiated large planetary embryo, may of course, be energetic enough to melt (or even vaporize)

the silicate and metal contents of the impactor and the silicates of the impacted body inside the isobaric core.

The two processes (percolation or metal "rain") lead to a local differentiation within the melted region between light silicates and heavy metals on a short timescale compared to that of the slow viscous deformation (Tonks and Melosh, 1992). The melted region is as large as or a few times larger than the isobaric core (Pierazzo et al., 1997). Here, we identify the initially differentiated zone to the isobaric core, metal being overlaid by pure silicates shortly after the impact (see Fig.1).

3. Dynamic model of differentiation

The setting described in the previous section is gravitationally unstable and the metal phase sinks toward the center of the impacted planetesimal while the silicates (lighter than undifferentiated material) spread underneath the surface. To study the global dynamics of this differentiation event, we develop a thermo-mechanical model in spherical axisymmetrical geometry, of viscous flow with three chemical components. Using a viscous and linear rheology during the segregation of the core is clearly a large approximation. The large deviatoric stress generated by the metallic diapirs should lead to a non-linear rheology (Samuel and Tackley, 2008), elasto-plastic deformations (Gerya and Yuen, 2007) or even to hydrofracturation if they exceed the ultimate strength of rocks which is $\sim 1-2$ GPa (Davies, 1982). Pressure dependence of the rheology can also influence the metal sinking time but is not considered here since we focus on small growing planets. During the early stages of accretion, the interior of the growing planets may have been colder or hotter than the outer layers depending on the ratio of radioactive and impact heating and on the history of accretion. For simplicity, we assume in our models an homogenous temperature on the

158 growing planet before the impact.

159 *3.1. Physical model*

160 Sinking occurs under the action of gravity in a spherical homogeneous pro-
161 toplanetary body. We neglect for simplicity the changes of gravity during the
162 differentiation. Hence gravitational acceleration $g(r)$ increases linearly with ra-
163 dius r:

$$g(r) = \frac{4}{3} G\pi\rho_0 r = g_0 \frac{r}{R}, \tag{2}$$

164 where g_0 the surface gravity. The density of undifferentiated material is $\rho_0 =$
165 $f_0\rho_{Fe} + (1 - f_0)\rho_{Si}$ where f_0 is the volume fraction of metal and ρ_{Fe}, ρ_{Si}, the
166 densities of the metallic phase and the pure silicates, respectively (see typical
167 numerical values in Table 1.)

168 The dynamics of segregation potentially involves a series of multiscale physi-
169 cal processes, especially to take the effects of melting into account and a realistic
170 multiphase dynamics (Golabek et al., 2008; Ricard et al., 2009). No numerical
171 models can handle simultaneously all these complexities and as a consequence,
172 we follow the approach of Samuel and Tackley (2008) and consider a thermo-
173 chemical system with infinite Prandtl limit, with no possible subsequent phase
174 separation within the undifferentiated material except that caused by the im-
175 pact (e.g., the volumes of pure metal and pure silicates remain constant during
176 the simulations and equal to 17% and 83% of the initial isobaric core).

177 The necessary approximations are somewhat different from the classic treat-
178 ment of thermal convection (see e.g., Ricard, 2007). We non-dimensionalize the
179 lengths by the planetary radius R, the velocities by a Stokes velocity $\Delta\rho_0 g_0 R^2/\eta_0$
180 (where $\Delta\rho_0 = \rho_{Fe} - \rho_{Si}$ and η_0 is the reference viscosity of cold material far from
181 the impact site), the temperature by ΔT_0 (see Eq.1). The governing mechanical
182 non-dimensionnal equations are the conservation of mass

$$\boldsymbol{\nabla} \cdot \mathbf{v} = 0, \tag{3}$$

and the conservation of momentum

$$-\boldsymbol{\nabla} P + \boldsymbol{\nabla} \cdot \left(\frac{\eta}{\eta_0} \left[\boldsymbol{\nabla} \mathbf{v} + [\boldsymbol{\nabla} \mathbf{v}]^T \right] \right) + \left(\frac{T}{B} - f \right) r \mathbf{e_r} = 0, \tag{4}$$

where $\mathbf{v}$, P, T and r are the non-dimensional velocity, pressure, temperature and radius, η the viscosity, T_0 the temperature (assumed uniform) before the impact and $\mathbf{e_r}$ the radial unit vector. The buoyancy ratio B (Christensen and Yuen, 1985) is:

$$B = \frac{\Delta \rho_0}{\rho_0 \alpha \Delta T_0}. \tag{5}$$

The downward buoyancy force that drives the flow increases with the volume fraction of metal f that varies between 0 (pure silicates) and 1 (pure metal), 0.17 being that of undifferentiated material. A depth dependent and constant in time gravity has been used in the momentum equation Eq.4 although, in principle, gravity should have been computed self-consistently from the time-dependent density distribution. We assume a temperature dependent viscosity such as $\eta = \eta_0 \lambda^T$ with λ being the viscosity factor (lower than 1) which is equivalent to the viscosity ratio between the hottest and coldest material at the start of the experiment. Such a viscosity decreases sharply with temperature and is simpler to implement than the usual Arrhenius law (Ratcliff et al., 1997; Ziethe and Spohn, 2007).

The conservation of energy writes

$$\frac{DT}{Dt} = \frac{\nabla^2 T}{Ra_\chi} + D_\chi \frac{\eta}{\eta_0} \Phi + \frac{1}{B} \frac{\Delta \rho}{\rho} \frac{T}{\Delta T_0} D_\chi \frac{DP}{Dt}. \tag{6}$$

The importance of diffusion is controlled by the compositional Rayleigh num-

ber Ra_χ,

$$Ra_\chi = \frac{\Delta\rho_0 g_0 R^3}{\kappa\eta_0}, \tag{7}$$

the chemical dissipation number is

$$D_\chi = \frac{\Delta\rho_0 g_0 R}{\overline{\rho C_p}\Delta T_0}, \tag{8}$$

considering for simplicity that $\overline{\rho C_p} = \rho_{Fe} C_p^{Fe} = \rho_{Si} C_p^{Si}$ (truely, see Table 1, $\rho_{Fe} C_p^{Fe} = 4 \times 10^3$ kJ K^{-1} m^{-3}, $\rho_{Si} C_p^{Si} = 3.85 \times 10^3$ kJ K^{-1} m^{-3}, and we use $\overline{\rho C_p} = 4 \times 10^3$ kJ K^{-1} m^{-3}). As g_0 is proportional to R and ΔT_0 to R^2, see Eq.1, the chemical dissipation is independent of the planet radius and amounts to 36.6 (see Table 1).

An important energy source is provided by the dimensionless dissipation function Φ that expresses the conversion of potential energy into heat

$$\Phi = 2\,\underline{\boldsymbol{\epsilon}} : \underline{\boldsymbol{\epsilon}}. \tag{9}$$

where $\underline{\boldsymbol{\epsilon}}$ is the dimensionless strain rate tensor. For simplicity, we make the approximation that the thermal conductivities of the metal, silicates and undifferentiated materials are the same (truely k_{Fe}=10 W m^{-1} K^{-1}>k_{Si}=3 W m^{-1} K^{-1}).

The metal volume fraction is then simply advected by the flow,

$$\frac{Df}{Dt} = 0. \tag{10}$$

3.2. Model approximations

The equations of momentum and energy conservations, Eq.4 and Eq.6, are similar to those classically used for mantle convection simulation but a number of differences should be discussed. As the buoyancy number B is very large (the

density difference between metal and silicates is 40 to 620 times larger than the thermal density variations), the thermal buoyancy T/B can be safely neglected in the momemtum equation.

Neglecting the terms in $1/B$ implies to omit the adiabatic heat transfer (the term in (DP/Dt)) in Eq.6 but to keep the dissipation term $D_\chi(\eta/\eta_0)\Phi$. The differentiation of the planet liberates a large amount of potential energy converted into heat by the dissipation term but the adiabatic heating remains small. This is very different from the typical convection situation in which there is no time variation of the potential energy, and where the dissipation is on average, balanced by the work due to compression and expansion over the convective cycle (Hewitt et al., 1975).

3.3. Numerical model

We implement a finite volume numerical model to solve Eq.3, Eq.4, Eq.6 and Eq.10 in axi-symmetric spherical geometry. We use a stream function formulation for the equations of motion with a direct implicit inversion method (Schubert et al., 2001). Eq.6 and Eq.10 are solved by an Alternating Direction Implicit (ADI) scheme (Peaceman and Rachford, 1955; Douglas, 1955). The stream function, temperature and compositional fields are described by a second-order approximation in space. To limit numerical diffusion when solving the transport equations, especially for the compositional field, we use a Total Variation Diminishing Superbee scheme (Roe, 1986; Laney, 1998) implemented in an implicit way (Sramek, 2007) which enables a high resolution of pure advective fields. We use at least 200×200 grid points. Velocity boundary conditions are free-slip at the surface and along the symmetry axis. Thermal boundary conditions are isothermal at the surface and insulating along the symmetry axis. We benchmark the viscous flow solver with variable viscosity and the transport scheme against several analytical solutions (Monteux, 2009).

4. Thermal evolution of sinking metallic diapir: Analytical considerations

Before showing the results of complex numerical simulations with temperature dependent rheologies, we develop a simple model describing the thermal evolution of the sinking metal diapir, by approximating the metal diapir by a spherical drop falling into undifferentiated medium of uniform viscosity with a Stokes-like velocity. The radius of the metal drop R_{Fe}, can be related to the radius R_{ic} of the volume initially differentiated after impact heating, by $R_{Fe}^3 = f_0 R_{ic}^3$ and to the radius of the impactor by $R_{Fe}^3 = 3 f_0 R_{imp}^3$.

4.1. Sinking velocity

The velocity V of the metallic diapir in an undifferentiated medium is comparable to the Stokes velocity of a sphere of similar volume. The density difference between the metal and the undifferentiated material is a function of temperature and composition but the temperature contribution is minor. Hence, we consider $\Delta\rho = (1 - f_0)\Delta\rho_0$. Because gravity is a linear function of depth, the velocity of the sphere decreases during sinking as

$$V = \frac{dr}{dt} = -c_1(1 - f_0)\frac{\Delta\rho_0 g_0 R_{Fe}^2}{\eta_S}\frac{r}{R}. \tag{11}$$

In equation Eq.11, the dimensionless constant c_1 depends on the geometry of the system and on the viscosity contrast between the falling sphere and the surrounding medium.

The viscosity of the surrounding undifferentiated material η_S controls the sinking velocity. In the case of a sphere sinking in an infinite medium, the coefficient c_1 is given by the Hadamard-Rybczynski equation and varies from $4/15 = 0.27$ (isoviscous) to $1/3 = 0.33$ for an inviscid sphere (Hadamard, 1911; Rybczynski, 1911). In the situation described in this paper, the boundary condi-

tions are applied at a finite distance (the planetary surface) and the Hadamard and Rybczynski equation is thus only an approximation (Honda et al., 1993; Samuel and Tackley, 2008). The exact value of the constant c_1 will be obtained later through numerical experiments.

The position of the metallic drop obtained by solving Eq.11 varies from an initial position r_0 ($r_0 = R - R_{Fe} \sim R$) as

$$r(t) = r_0 \exp(-\frac{t}{\tau_S}), \tag{12}$$

with a characteristic time equal to

$$\tau_S = \frac{\eta_S R}{c_1 \Delta\rho_0 g_0} \frac{1}{(1-f_0)} \frac{1}{R_{Fe}^2}. \tag{13}$$

As g_0 is proportional to the planetary radius R (Eq.2), the time τ_S is independent of the planetary radius but depends only on the diapir size R_{Fe}. Of course, no segregation occurs, i.e., $\tau_S \rightarrow +\infty$, for a planet of pure silicates ($f_0 = 0$ which means $R_{Fe} = 0$) or of pure metal ($f_0 = 1$). This characteristic sinking time is strongly dependent of the viscosity of the surrounding undifferentiated material which is poorly constrained. With the typical values of Table 1, this time can be computed from the size R_{imp} of the impactor and we find $\tau_S(\text{kyr}) = 2.7 \times 10^9 (\eta_S/\eta_0) R_{imp}^{-2}(\text{km})$.

4.2. Global energy conversion

As we assume that gravity remains constant with time (albeit non-uniform), the energy equation Eq.6 integrated over the whole planet with the use of the momentum equation Eq.4 and neglecting the adiabatic decompression of the planet during the core segregation is simply

$$\frac{d}{dt}(\Delta E_p + \Delta E_T) = F, \tag{14}$$

where the total potential and thermal energies changes are

$$\Delta E_p = \int_\Omega \frac{1}{2} \left[\rho(\mathbf{r},t) - \rho(\mathbf{r},0)\right] g_0 \frac{r^2}{R}\, dV, \tag{15}$$

(Ω is the planetary volume),

$$\Delta E_T = \int_\Omega \overline{\rho C_p} \left[T(\mathbf{r},t) - T(\mathbf{r},0)\right]\, dV, \tag{16}$$

and the heat flux F is ,

$$F = \int_\Sigma k \frac{\partial T}{\partial r}\, dS, \tag{17}$$

(Σ is the planetary surface).

As we neglect the term in $1/B$ in the energy equation Eq.4, the budget Eq.14 misses the energy variation ΔE_a due to the changes in pressure (the subscript a means that this term is related to changes in adiabatic compression)

$$\frac{d\Delta E_a}{dt} = \int_\Omega \alpha T \frac{\partial P}{\partial t}\, dV \sim \alpha T_0 \frac{d}{dt} \int_\Omega \left[P(\mathbf{r},t) - P(\mathbf{r},0)\right]\, dV \tag{18}$$

(where the last approximation assumes that the temperature remains close to T_0). The difference of pressure between a homogeneous and a differentiated planet is easy to compute analytically and is of order $\alpha T_0 \Delta E_p$, i.e., a few percent of the changes in potential energy. This confirms that the energy change due to pressure changes is a minor effect.

4.3. Maximum temperature

The maximum temperature that the sinking metal can reach can be estimated by assuming that the whole variation of potential energy is only used to heat up the metal, without any heat transfer to the surrounding material.

Let us consider a melted zone of radius R_{ic} underneath and tangent to the planetary surface that differentiates ultimately forming a metallic core of volume V_{Fe} and radius R_{Fe} (with $R_{Fe}^3 = f_0 R_{ic}^3$) and a silicate layer of volume V_{Si} within a shell surrounding the whole planet with inner shell radius R_S and outer shell radius R i.e., $R_S^3 = R^3 - (1-f_0)R_{ic}^3$. The change of potential energy is according to Eq.15 (see also Flasar and Birch, 1973):

$$\Delta E_p = \frac{2\pi}{5R} g_0 \left((\rho_{Fe} - \rho_0) R_{Fe}^5 + (\rho_{Si} - \rho_0)(R^5 - R_S^5) \right). \tag{19}$$

Assuming $R_{ic} << R$, a Taylor expansion of Eq.19 leads to

$$\Delta E_p \sim -\frac{1}{2}\Delta\rho_0 g_0 R f_0 (1-f_0) V_{ic} = -\frac{1}{2}(\rho_{Fe} - \rho_0) g_0 R V_{Fe} = -\frac{1}{2}(\rho_0 - \rho_{Si}) g_0 R V_{Si}, \tag{20}$$

where V_{ic} is the volume of the isobaric core. The change of potential energy is thus equivalent to that released by the sinking of the isobaric volume V_{ic} and excess density $f_0(1-f_0)\Delta\rho_0$. Alternatively it corresponds to the energy released by a metal sphere of volume V_{Fe} sinking, or of a silicate sphere rising, through undifferentiated material. If only the metal heats up, the change of thermal energy according to Eq.16 is $\Delta E_T = \overline{\rho C_p} f_0 \Delta\Theta V_{ic}$ where $\Delta\Theta$ is the temperature increase (just after the impact, the metal temperature is $T_0 + \Delta T_0$, then it reaches at most $T_0 + \Delta T_0 + \Delta\Theta$). A scaling value for the temperature increase during segregation is thus

$$\Delta\Theta = \frac{1-f_0}{2} \frac{1}{\overline{\rho C_p}} \Delta\rho_0 g_0 R. \tag{21}$$

As g_0 is proportional to R (Eq.2), the core segregation can increase the temperature by a quantity proportional to R^2 (in agreement with Flasar and Birch, 1973; Ricard et al., 2009). The ratio of $\Delta\Theta$ to the post impact temperature

ΔT_0 is, according to Table 1 and Eq.1,

$$\frac{\Delta\Theta}{\Delta T_0} = \frac{3h(m)}{2\gamma}(1-f_0)\frac{\Delta\rho_0}{\rho_0} \sim 11.8 \tag{22}$$

or, $\Delta\Theta(\mathrm{K}) = 11.8\ \Delta T_0(\mathrm{K}) = 5.6\times10^{-4}R^2(\mathrm{km})$ which rapidly becomes a large quantity as R increases. Of course, in a real situation not all energy will remain within the metal, and we will see that, when the metal diapir is too small, the metal can even cool off rather than warm up during its motion.

4.4. Thermal regime of the metallic sphere

While the hot metallic sphere is sinking, it warms up by shear heating but it also cools down by diffusion. In the reference frame of the sinking drop, the conservation of energy integrated over the volume V_{Fe} of the metallic drop (or through its surface S_{Fe}) indicates that

$$\overline{\rho C_p} V_{Fe}\frac{d\Delta T}{dt} = -k\frac{\Delta T}{\delta}S_{Fe} + \underline{\boldsymbol{\tau}} : \boldsymbol{\nabla}\mathbf{v}\ V_{Fe}, \tag{23}$$

where we assume that the temperature and the dissipation are at first order uniform in the metal. The difference ΔT is the difference between the diapir and the undifferentiated material. We assume that $\Delta T = T - T_0$, i.e., that the hot diapir sinks into a medium that keeps its initial temperature outside the boundary thickness δ. Even when the diapir viscosity is low and when the dissipation occurs significantly outside it, our numerical simulations shows that the maximum temperature is reached inside the diapir.

The thickness δ over which the temperature diffuses should be written as R_{Fe} times a dimensionless function c_2 of the various parameters of the problem. The thickness of the diffusive boundary layer, c_2, should decrease with the sinking velocity of the diapir (i.e., with the Peclet number VR_{Fe}/κ) as a power law with exponent -1/2 or -1/3, depending on the viscosity ratio between the metal

and the undifferentiated material (see e.g., Ribe, 2007). We can also write the dissipation $\underline{\boldsymbol{\tau}} : \boldsymbol{\nabla}\mathbf{v} = \eta_e V^2/R_{Fe}^2$ where η_e is the effective viscosity of the region where dissipation occurs. In this case, Eq.23 using the expressions of the time dependent position, Eq.12, and of the maximum temperature increase, Eq.21, can be recast as

$$\frac{d\Delta T}{dt} = -\frac{\Delta T}{\tau_D} + 2a\left(\frac{r_0}{R}\right)^2 \frac{\Delta\Theta}{\tau_S} \exp\left(-2\frac{t}{\tau_S}\right), \tag{24}$$

where the dimensionless constant

$$a = c_1 \frac{\eta_e}{\eta_S} \tag{25}$$

characterizes the proportion of heat effectively dissipated in the metal and τ_D the characteristic time of diffusion

$$\tau_D = \frac{c_2 R_{Fe}^2}{3\kappa}, \tag{26}$$

where c_2, measuring in terms of R_{Fe} the thickness of the thermal boundary layer around the metal, $\delta = c_2 R_{Fe}$, is a dimensionless number.

Eq.24 cannot be used predictively in a complex situation as it requires the knowledge of various parameters c_1, c_2 and a. The dependences of these parameters with more fundamental quantities (mostly with the temperature dependence of the viscosity) have to be determined empirically. We will see however, that for a given choice of the rheology, Eq.24 captures the evolution of the metallic diapir temperature as a function of time and the dependence of this temperature with the diapir size. For example, Eq.24 suggests that the diffusion term decreases with R_{Fe} (as R_{Fe}^{-2} if one considers c_2 as a constant) while the dissipation term increases with R_{Fe}^2. We can also use Eq.24 qualitatively by

assuming $a \sim c_1 \sim 4/15$ (using Stokes law) and $c_2 \sim 1$.

The expression Eq.24 shows that the temperature is not necessarily an increasing function of time. More precisely, according to Eq.24 the metal temperature increases just after the impact ($t \sim 0$), if

$$-\frac{\Delta T_0}{\tau_D} + 2a \left(\frac{r_0}{R}\right)^2 \frac{\Delta\Theta}{\tau_S} > 0 \tag{27}$$

Using the expressions for the temperature increase upon impact ΔT_0 (see Eq.1), the maximum temperature increase during segregation $\Delta\Theta$ (see Eq.21) and for the two time constant τ_S and τ_D (see Eq.13 and Eq.26), this condition implies that dissipative heating overcomes the conductive diffusion when

$$R_{Fe} > R_{Fe,min} \tag{28}$$

where $R_{Fe,min}$ involves the properties of the planet, but not its radius since ΔT_0 is proportional to R^2:

$$R_{Fe,min}^4 = \frac{9}{8\pi} \left(\frac{r_0}{R}\right)^2 \frac{1}{c_1 c_2 a} \frac{\Delta T_0}{\Delta\Theta} \frac{\eta_S \kappa}{G\rho_0(1-f_0)\Delta\rho_0}. \tag{29}$$

According to the set of parameters shown in Table 1, $R_{Fe,min} \sim 45$ km (using $c_1 \sim a \sim 4/15$, $r_0 \sim R$ and $c_2 \sim 1$ but using values fitted from experiments does not change this radius very much for the moderate level of viscosity variations used in our simulations heraftер). Such a diapir corresponds to an impactor of radius $R_{imp} \sim 60$ km ($R_{imp} = R_{ic}/3^{1/3} = R_{Fe}/(3f_0)^{1/3}$). Therefore, only impactors larger than $R_{imp} = 60$ km generate metallic diapirs that heat up during sinking, although their initial temperature set by the impact is not dependent on the size of the impactor.

Integration of Eq.24 leads to:

$$\Delta T = \Delta T_0 \exp(-\frac{t}{\tau_D}) + a \left(\frac{r_0}{R}\right)^2 \Delta\Theta \frac{2\tau_D}{2\tau_D - \tau_S} \left(\exp(-\frac{t}{\tau_D}) - \exp(-2\frac{t}{\tau_S}) \right). \quad (30)$$

The initial temperature anomaly ΔT_0 decreases exponentially with time while the interplay between diffusion and dissipation controls the general temperature evolution. For the diapir to heat up, the heating time $\tau_S/2$ must be shorter than the diffusive time τ_D. Typically $r_0 \sim R$ and in the regime where the diapir heats up, the dissipation occurs before the diffusion, $\tau_S/2 << t << \tau_D$; the temperature rapidly increases to $\Delta T = \Delta T_0 + a\,(r_0/R)^2\,\Delta\Theta$, and the physical interpretation of a is therefore the percentage of heat dissipated inside the metal. According to Eq.25, a should be lower than the coefficient c_1 of the Rybczinski-Hadamard velocity as the effective viscosity of the hot diapir η_e is likely lower than the average viscosity η_S. For a numerical application we take however $a \sim c_1 = 4/15 \sim 0.27$ as obtained for the isoviscous Rybczinski-Hadamard velocity. As $\Delta\Theta$ and ΔT_0 are simultaneously proportional to R^2, the maximum temperature of the diapir is at most $\Delta T = 4.2\,\Delta T_0$ and is independent of the planet size.

Dissipation decreases as $\exp(-2t/\tau_s) = (r/r_0)^2$ according to Eq.12. Hence, the dissipation term in Eq.24 decreases with depth. When a diapir heats up, its temperature increases therefore to the maximum ΔT_{max} reached at the radius r that satisfies $d\Delta T/dt = 0$ or

$$0 = -\frac{\Delta T_{max}}{\tau_D} + 2a\frac{\Delta\Theta}{\tau_S}\left(\frac{r}{R}\right)^2, \quad (31)$$

which implies

$$\left(\frac{r}{r_0}\right)^2 = \frac{\Delta T_{max}}{\Delta T_0}\left(\frac{R_{Fe,min}}{R_{Fe}}\right)^4. \quad (32)$$

The factor $\Delta T_{max}/\Delta T_0$ varies between 1 (no heating) and 4.2 (maximum esti-

mated temperature). As an example, an impactor of radius 120 km, generates a metallic diapir of 96 km (two times $R_{Fe,min}$) that heats up until it reaches half the radius of the impacted planet. The expression Eq.32 is only valid when $R_{Fe} > R_{Fe,min}$, otherwise the diapir temperature simply decreases.

5. Numerical simulations

We compare the predictions of the analytical model to spherical axisymmetric calculations of a sinking metallic drop, especially to extract the diffusive and sinking times τ_D and τ_S and the fraction of heat trapped in the metallic phase (e.g., the constants c_1, c_2 and a, that we expect to be close to 4/15, 1 and 4/15). We then compare these results to more complex numerical experiments where a compositional anomaly is generated in the isobaric core after a large impact. The effect of variable viscosity is also studied in these models.

5.1. Numerical models of sinking metallic drops

5.1.1. Sinking velocity

We solve numerically a set of problems in which we introduce metallic spheres ($f_0 = 1$) of different sizes, tangent to the surface, in undifferentiated planets ($f_0 = 0.17$) of various radii. From this set of experiments, we compare the temporal evolution of the sphere position to what is predicted by Eq.12. The calculations presented here are isoviscous for simplicity but variable viscosity will be introduced in more complex cases. Fig.2 shows that the values of τ_S obtained by fitting the center of the diapir position to an exponential in the numerical models, vary as $1/R_{Fe}^2$ as expected from the analytical model, with $c_1 = 0.187$ (almost 70% of the Hadamard-Rybczynski velocity for a homogenous viscosity 4/15=0.27). For large sphere radii, boundary effects are stronger and the sinking times are slightly larger.

5.1.2. Temperature evolution

Large sinking diapirs heat up before cooling down by diffusion when the velocity of the metal decreases sufficiently towards the center. Our theoretical predictions given by Eq.30 are in good agreement with the computed evolutions with the value c_1 obtained previously. Fig.3 shows the consistency between the numerical results and the theory when the parameters c_2 and a are fitted ($c_2 = 0.72$, $a = 0.2$ which is reasonably close to $c_1 = 0.187$). The value of a , indicates that 20% of the released heat is trapped in the metal. The maximum temperature value, $2.2\,\Delta T_0$, is in rough agreement with the estimate $\Delta T = \Delta T_0 + a\,(r_0/R)^2\,\Delta\Theta = 2.88\,\Delta T_0$. This value is obtained for sufficiently large impactors (> 200 km) since smaller ones can cool off very early upon sinking as seen from Eq.32.

We monitor the temperature evolution for various diapir radii. Fitting the temperature evolution with Eq.30 leads to values of τ_D and a for each diapir radius. The corresponding characteristic diffusive times are plotted in Fig.4. These times are consistent with analytical predictions from Eq.26 and increase with the square of the diapir size. For all the experiments, the fraction of heat a trapped in the metal is therefore reasonably constant ($\sim 22 \pm 5\%$) and close to c_1.

To verify condition Eq.32 that predicts the radius for which dissipation overcomes diffusion, we computed the rate of heating or cooling of metallic spheres as a function of their radius and depths. Various planetary radii have been used and, as predicted, the heating always occur in the external part of the planet (filled symbols). Near the center of the impacted planet, when the gravity decreases, diffusion dominates (open symbols) and the temperature of the sinking metallic phase decreases. As shown in Fig.5, the transition between heating and cooling occurs consistently within the shaded area predicted by the analytical

457 expressions Eq.32. For small diapirs ($R_{Fe} \leq 45$ km), diffusion dominates and
458 prevents heating. Large diapirs reach their maximum temperature and start
459 cooling near the high temperature estimate of the analytical model.

460 *5.2. Application to global evolution after an impact*

461 The thermo-chemical initial conditions after an impact differ from a simple
462 hot metallic sphere sinking within an undifferentiated material. Indeed, the
463 denser metallic pond collected at the bottom of the isobaric core is not spher-
464 ical and above it, a volume of light silicates rises and spreads underneath the
465 surface until it covers the entire surface of the planet. These deviations from
466 our analytical model potentially modify the results obtained from the sinking
467 metallic drop model. Here we show numerical simulations of segregation after
468 an impact and compare them to the analytical model previously developed.

469 Fig.6 depicts the thermal and compositional evolution after an impact of
470 a large impactor ($R = 4000$ km, $R_{imp} = 600$ km and $R_{Fe} = 480$ km). The
471 four rows correspond to real time snapshots at 0, 1.4, 3.8 and 546 Myrs. The
472 temperature field is depicted in the left column, and the composition in the right
473 column (undifferentiated material in light blue, metal in red, silicates in green).
474 The metallic pond sinks towards the center of the planet while heating. This
475 heating is in agreement with our previous findings that dissipation is larger than
476 diffusion for large impacts. However, the metal develops a tail through sinking
477 and is significantly deformed. In the meantime, the light silicates rise upward
478 and heat up as well, while stretching laterally to cover the whole surface of the
479 planet. Of course, the diffusion of heat out of the silicate layer near the surface,
480 is much faster than that out of the deep protocore and this shallow hot silicate
481 layer cools rapidly. On a much longer time scale (assuming irrealistically that
482 no other impact occurs, hot thermal plumes should start from the proto core-
483 mantle boundary and deliver the protocore heat to the surface (Behounkova and

Choblet, 2009).

Fig.7 illustrates the evolution of the conversion from potential to thermal energy with time. During the thermo-chemical reequilibration, the potential energy (thick line) decreases as the metal approaches the center and as the silicates spread beneath the surface. Viscous heating induces an increase of thermal energy (grey line). Once the metal has reached the center of the impacted protoplanet, the thermal energy can only decrease. During this whole process, heat is slowly removed by diffusion through the surface of the planet and the cumulative heat flux (dotted line) balances the total energy budget. This global balance (sum of potential energy, thermal energy and cumulative heat flux (see Eq.14)) is closely satisfied which illustrates the good accuracy of the numerical code.

We now introduce a temperature-dependence of the viscosity in the calculations. Experimental results suggest that the viscosity contrast between melt iron and solid silicates can reach 20 orders of magnitude (Vocadlo et al., 2000). Such a viscosity contrast is difficult to handle numerically and we use much smaller values.

In our models, the viscosity varies as $\eta = \eta_0 \lambda^T$ and as the temperature of metal may increase while sinking by a factor up to 2, it implies maximum viscosity contrasts up to $1/\lambda^2$ orders of magnitude between cold and hot materials. Using a composition dependent viscosity would have been more realistic but viscous fronts are too difficult to handle numerically. We compare the thermo-chemical states at the same time, $t = 3.2$ Myr for different viscosity factors in Figure 8. We use $\lambda = 0.25$ (Figure 8 second row), $\lambda = 0.1$ (Figure 8 third row) and $\lambda = 2.5 \times 10^{-2}$ (Figure 8 bottom row), the top row being the reference isoviscous case.

Increasing the temperature-dependence of the viscosity softens the surround-

ing material around the metallic drop and the metallic diapir, at a given time, is closer to the center when its viscosity is decreased, as shown in Fig.8. However, this effect remains small. Because the metallic pond becomes less viscous, its shape becomes more spherical and the tail developed in isoviscous experiments becomes thinner. Increasing the sinking velocity increases the rate of shear heating but not the total release of thermal energy which is only related to the change in gravitational energy. Lowering the viscosity in the surrounding material and within the metallic pond has also the effect of diminishing η_e. The dissipation is therefore increased in the undifferentiated material and decreased in the hot and less viscous metallic diapir. This effect combined with the faster spreading of the hot silicate that removes the heat more rapidly lead to lower maximum temperatures (see Fig.8).

We monitor the position of the inertia center of the metallic diapir as a function of time and compute the sinking times τ_S (see Figure 9). The position of the diapir obeys reasonably to the exponential law predicted by Eq.12. In the isoviscous case, the observed normalized time is $\tau_S = 563$ which is twice longer than what is predicted by Eq.13. This is due to the fact that the initial diapir shape is not spherical and to the presence of the rising volume of silicates. When the viscosity decreases with temperature the sinking is faster, $\tau_S = 249$, 170 and 114, for $\lambda = 0.25$, 0.1 and 2.5×10^{-2} (see Fig.9 and Tab.2). This is due to two effects: the reduction of viscosity inside the metal (the Rybczinski-Hadamard formula predicts an increase of the velocity factor c_1 from 0.27 to 0.33 when the interior viscosity of the diapir decreases) and the decrease of viscosity of the heated surrounding material.

In the experiments depicted in Fig.6 and Fig.8, the metal temperature increases and reaches a value close to twice the initial temperature of the isobaric core (Fig.10). However, heating within the metal is less pronounced with vari-

able viscosity and decreases with the viscosity contrast. Fitting the computed temperature evolutions in the metallic diapirs with our theoretical model gives values of c_2 in the isoviscous case and the variable viscosity cases (see Tab.2 and Fig.10). The thickness of the thermal boundary measured by c_2 decreases with the sinking velocity (the Peclet number). The values of c_2 and of τ_D are therefore related to $Pe^{-n} \propto \tau_S^n$ with an exponent $\sim 1/3$ in the range of values, $n = 1/2 - 1/3$ predicted in Ribe (2007).

When the temperature dependence of the viscosity increases, the proportion of energy heating the metal diapir, a, decreases (see Tab.2). As a consequence, the heat release of the gravitational energy becomes increasingly efficient in the surrounding undifferentiated material. This suggests that a diapir of very small viscosity does not heat much during its motion while most of the release of gravitational energy occurs in the undifferentiated materials. A low viscosity diapir keeps basically its initial temperature because its characteristic diffusive time is larger than its sinking time and also because of the buffering effect of the temperature dependent viscosity (i.e., a too large cooling would increase the viscosity and would bring back the dissipation within the diapir itself).

6. Discussion and conclusion

Core formation events induced by meteoritical impacts play a major role in determining the early thermo-chemical state of growing planets. Large meteoritical impacts can trigger a local differentiation between metal and silicates in a spherical zone above the surface called the isobaric core. The segregation of dense and light phases through the undifferentiated material of the impacted protoplanet induces a large viscous heating.

We followed the dynamics of the metal phase after a large impact with numerical experiments in axisymmetrical spherical geometry. The sinking velocity

of the metal phase is Stokes-like and is function of the viscosity contrast between the metal phase and the undifferentiated crossed media. The velocity increases when viscous heating decreases the viscosity of the surrounding material. A stress dependent viscosity (not considered here) would also increase this velocity (Samuel and Tackley, 2008). The sinking process in a planet with a cold interior compared to its surface would eventually imply higher viscosity contrasts between the metal and the surrounding material and would lead to longer sinking times.

The gravitational energy release during the segregation is converted into viscous heating in the metal and in the silicates. Our results show that a net viscous heating of the metallic phase only occurs for large metallic diapirs ($R_{Fe} > 45$ km). This metallic volume at the bottom of the isobaric core would be produced by an impactor of order $R_{imp} > 60$ km. This result underlines the importance of accretion conditions on the inner thermal state of planetary bodies. Small metallic diapirs cool while sinking and may ultimately bring the metal in a solid state to the core of the impacted planet.

The heat repartition between the metal phase, the silicates and the undifferentiated material is not only a function of the size of the metallic diapir but also of the rheology of the various phases. For low viscosity of the metal and of the sheared zone around the metallic diapir, the metal phase is weakly heated. Hence, gravitational energy release will mainly lead to the heating of the surrounding undifferentiated material and ultimately to its differentiation.

The viscosity variations that we explore in our simulations are of order $\lambda^{\Delta T_{max}}$ which in the most extreme cases reach about four orders of magnitude over very short distances. This is certainly modest relative to the viscosity contrasts of 20 orders of magnitude that exists between liquid metal and solid silicates (Vocadlo et al., 2000). Viscosity contrasts based on composition rather

than temperature would be more realistic but would have occurred on even shorter distances (the computation grid itself) that could not be resolved with classical numerical methods. Our model is therefore an end-member of possible models on heating modes during core formation. However the description of the physics of the processes would still be valid for larger viscosity contrasts.

As soon as a growing planet reaches a few 1000 km in radius R, the heating by impacts becomes significant (the temperature increase varies as R^2 and reaches 400 K for $R = 3000$ km, (Monteux et al., 2007)). This temperature increase superimposed on the fossil temperature T_0 from short half-life radionucleides (^{26}Al and ^{60}Fe) and previous impacts can lead to a temperature larger than the melting temperature of the metallic phase. Our analytical models confirmed by numerical experiments show that the metallic drop reaches the planet center in a time depending on the size of the metallic drop and the background viscosity of the planet but not of its radius (see Eq.13). Even in the case where the impacted planet is relatively cold and with a high viscosity of 10^{22} Pa s, this time is smaller than a few million years for an impactor of 300 km. The sinking timescales obtained in our models are comparable to those obtained with an Arhenius rheology (Ziethe and Spohn, 2007) and within the timeframe required for an early core formation (< 60 My). The temperature increase in the undifferentiated material localized along the sinking path of the metallic diapir could provide a prefential low viscosity chanel for the following differentiation events.

Proposing predictive models for the thermal consequences of differentiation after an impact is fundamental in order to understand the thermal state of the interior of growing planets. As shown in Ricard et al. (2009), core formation of terrestrial protoplanets could be the consequence of a runaway segregation induced by a large enough impact on undifferentiated material. These results also underline the importance of accretionary conditions (size and temporal

repartition of impacts) on the thermal energy repartition and, hence, on the magnetic history of growing planets (Elkins-Tanton et al., 2005).

Acknowledgements

The authors thank H. Samuel and M. Jellinek for helpfull discussions. The authors also thank and H. Schmeling, T. Spohn and anonymous reviewers for constructive comments. This project was funded by the A.N.R. ETHER.

References

Agee, C. B., 1997. Melting temperatures of the Allende meteorite: implications for a Hadean magma ocean. Phys. Earth Planet. Int. 100, 41–47.

Behounkova, M., Choblet, G., 2009. Onset of convection in a basally heated spherical shell, application to planets. Earth Planet. Sci. Lett., submitted.

Christensen, U. R., Yuen, D. A., 1985. Layered convection induced by phase transitions. J. Geophys. Res. 90, 10291–10300.

Croft, S. K., 1982. A first-order estimate of shock heating and vaporization in oceanic impacts. Vol. 190. Geological Implications of Impacts of Large Asteroids and Comets on Earth, edited by T.L. Silver and P.H. Schultz,Spec. Pap. Geol. Soc. Am.

Davies, G. F., 1982. Ultimate strength of solids and formation of planetary cores. Geophys. Res. Lett. 9, 1267–1270.

Douglas, J., 1955. On the numerical integration of $\frac{\partial^2 u}{\partial x^2} + \frac{\partial^2 u}{\partial y^2} = \frac{\partial u}{\partial t}$ by implicit methods. J. Soc. Ind. Appl. Math. 3, 42–65.

Elkins-Tanton, L. T., Zaranek, S. E., Parmentier, E. M., Hess, P. C., 2005. Early magnetic field and magmatic activity on Mars from magma ocean cumulate overturn. Earth Planet. Sci. Lett. 236, 1–12.

Fei, Y., Bertka, C. M., Finger, L. W., 1997. High-Pressure Iron-Sulfur Compound, Fe3S2, and Melting Relations in the FeFeS System. Science 275, 1621–1623.

Flasar, F. M., Birch, F., 1973. Energetics of core formation: A correction. J. Geophys. Res. 78, 6101–6103.

Gerya, T. V., Yuen, D. A., 2007. Robust characteristics method for modelling multiphase visco-elastic thermo-mechanical problems. Phys. Earth Planet. Int. 163, 83–105.

Ghosh, A., McSween, H. Y., 1998. A Thermal Model for the Differentiation of Asteroid 4 Vesta, Based on Radiogenic Heating. Icarus 134, 187–206.

Golabek, G. J., Schmeling, H., Tackley, P. J., 2008. Earth's core formation aided by flow channelling instabilities induced by iron diapirs. Earth Planet. Sci. Lett. 271, 24–33.

Hadamard, J., 1911. Mouvement permanent lent d'une sphère liquide et visqueuse dans un liquide visqueux. C. R. Acad. Sci. 152, 1735–1738.

Hewitt, J. M., McKenzie, D. P., Weiss, N. O., 1975. Dissipative heating in convective flows. Journal of Fluid Mechanics 68, 721–738.

Höink, T., Schmalzl, J., Hansen, U., 2005. Formation of compositional structures by sedimentation in vigorous convection. Phys. Earth Planet. Int. 153, 11–20.

Honda, R., Mizutani, H., Yamamoto, T., 1993. Numerical simulation of Earth's core formation. J. Geophys. Res. 98, 2075–2090.

Kleine, T., Münker, C., Mezger, K., Palme, H., 2002. Rapid accretion and early core formation on asteroids and the terrestrial planets from Hf-W chronometry. Nature 418, 952–955.

Laney, C. B., 1998. Computational gasdynamics. Cambridge University Press, Cambridge.

Monteux, J., 2009. Modélisation numérique de la formation du noyau terrestre : contribution des impacts météoritiques. Ph.D. thesis, Université Claude Bernard Lyon 1.

Monteux, J., Coltice, N., Dubuffet, F., Ricard, Y., 2007. Thermo-mechanical adjustment after impacts during planetary growth. Geophys. Res. Lett. 34, 24201–24205.

O'Keefe, J. D., Ahrens, T. J., 1977. Impact-induced energy partitioning, melting, and vaporization on terrestrial planets. In: Merril, R. B. (Ed.), Lun. Planet. Sci. Conf. Vol. 8. pp. 3357–3374.

Peaceman, D. W., Rachford, H. H., 1955. The numerical solution of parabolic and elliptic differential equations. J. Soc. Ind. Appl. Math. 3, 28–41.

Pierazzo, E., Vickery, A. M., Melosh, H. J., 1997. A Reevaluation of Impact Melt Production. Icarus 127, 408–423.

Ratcliff, J. T., Tackley, P. J., Schubert, G., Zebib, A., 1997. Transitions in thermal convection with strongly variable viscosity. Phys. Earth Planet. Int. 102, 201–212.

Ribe, N. M., 2007. Analytical Methods in Mantle Dynamics, Treatise of Geophysics. Vol. 7. Schubert, G. editor in Chief, Elsevier.

Ricard, Y., 2007. Physics of Mantle Convection, Treatise of Geophysics. Vol. 7. Schubert, G. editor in Chief, Elsevier.

Ricard, Y., Sramek, O., Dubuffet, F., 2009. A multi-phase model of runaway core-mantle segregation in planetary embryos. Earth Planet. Sci. Lett., in press.

Roe, P. L., 1986. Characteristic-based schemes for the Euler equations. Annual Review of Fluid Mechanics 18, 337–365.

Rybczynski, W., 1911. über die fortschreitende bewegung einer flüssigen kugel in einen medium. Bull. Acad. Sci. Cracovie 1, 40–46.

Samuel, H., Tackley, P. J., 2008. Dynamics of core formation and equilibration by negative diapirism. Geochem. Geophys. Geosyst. 9, 6011–6026.

Schubert, G., Turcotte, D. L., Olson, P., Sep. 2001. Mantle convection in the Earth and planets. Cambridge University Press.

Senshu, H., Kuramoto, K., Matsui, T., 2002. Thermal evolution of a growing Mars. J. Geophys. Res. 107, 1–13.

Shannon, M. C., Agee, C. B., 1996. High pressure constraints on percolative core formation. Geophys. Res. Lett. 23, 2717–2720.

Sramek, O., 2007. Modèle d'écoulement biphasé en sciences de la terre: fusion partielle, compaction et différenciation,. Ph.D. thesis, Ecole Normale Supérieure de Lyon.

Stevenson, D. J., 1989. Formation and early evolution of the Earth. in Mantle convection and plate tectonics, W.R. Peltier, ed.

Stevenson, D. J., 1990. Fluid dynamics of core formation. Origin of the Earth edited by H. E. Newsom and J. H. Jones, eds., Oxford Univ., New York.

Tonks, W. B., Melosh, H. J., 1992. Core formation by giant impacts. Icarus 100, 326–346.

Touboul, M., Kleine, T., Bourdon, B., Palme, H., Wieler, R., 2007. Late formation and prolonged differentiation of the Moon inferred from W isotopes in lunar metals. Nature 450, 1206–1209.

715 Vocadlo, L., Alfè, D., Price, G. D., Gillan, M. J., 2000. First principles calcula-
716 tions on the diffusivity and viscosity of liquid fe-s at experimentally accessible
717 conditions. Phys. Earth Planet. Int. 120, 145–152.

718 Von Bargen, N., Waff, H. S., 1986. Permeabilities, interfacial areas and cur-
719 vatures of partially molten systems: Results of numerical computations of
720 equilibrium microstructures. J. Geophys. Res. 91, 9261–9276.

721 Yin, Q., Jacobsen, S. B., Yamashita, K., Blichert-Toft, J., Télouk, P., Al-
722 barède, F., 2002. A short timescale for terrestrial planet formation from Hf-W
723 chronometry of meteorites. Nature 418, 949–952.

724 Yoshino, T., Walter, M. J., Katsura, T., 2003. Core formation in planetesimals
725 triggered by permeable flow. Nature 422, 154–157.

726 Ziethe, R., Spohn, T., 2007. Two-dimensional stokes flow around a heated cylin-
727 der: A possible application for diapirs in the mantle. J. Geophys. Res. 112,
728 1–13.

Table 1: Typical parameter values for numerical models

Planet radius	R	1000 - 4000 km
Impactor radius	R_{imp}	100 - 400 km
Silicate density	ρ_{Si}	3500 kg m^{-3}
Iron density	ρ_{Fe}	8000 kg m^{-3}
Density difference	$\Delta\rho_0 = \rho_{Fe} - \rho_{Si}$	4500 kg m^{-3}
Average density	ρ_0	4270 kg m^{-3}
Heat capacity	$\overline{\rho C_p}$	4×10^3 kJ K^{-1} m^{-3}
Heat diffusivity	κ	10^{-6} m^2 s^{-1}
Thermal conducivity	k	4 W m^{-1} K^{-1}
Initial temperature	T_0	K
Metal content	f_0	0.17
Viscosity	η_0	10^{22} Pa s
Viscosity factor	λ	$2.5 \times 10^{-2} - 1$
Gravity	$g_0 = 4\pi G\rho_0 R/3$	m s^{-2}
Stokes velocity scale	$\Delta\rho_0 g_0 R^2/\eta_0$	$\sim$100 m/yr
Time scale	$\eta_0/\Delta\rho_0 g_0 R$	$\sim$20 kyr
Rayleigh number Ra_χ	$\overline{\rho C_p}\Delta\rho_0 g_0 R^3/\eta_0 k$	$\sim10^8$
Buoyancy B	$\Delta\rho_0/\alpha\rho_0\Delta T_0$	25-250
Dissipation number D_χ	$\Delta\rho_0 g_0 R/\overline{\rho C_p}\Delta T_0$	36.6
Impact energy conversion coefficient	γ	0.3
Volume effectively heated by impact	$h(m)$	2.7
Stokes velocity coefficient	c_1	0.1-0.2
Heat diffusion coefficient	c_2	0.3-1.05

Table 2: Values obtained fitting numerical experiments with theoretical predictions (Eq.12 and Eq.30) for different values of λ (with $R = 2000$ km and $R_{imp} = 300$ km)

	$\lambda = 1$	$\lambda = 0.25$	$\lambda = 0.1$	$\lambda = 2.5 \times 10^{-2}$
τ_S	563	249	170	114
τ_D	20 054	16 520	13 316	8974
a	19%	14.7%	11%	7%

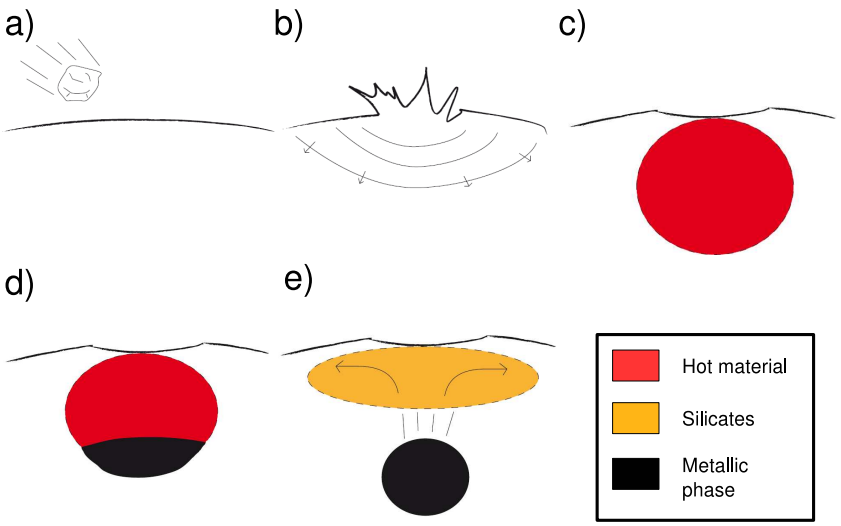

Figure 1: Schematic view of the chemical equilibration following a large impact on an undifferentiated protoplanet. In the isobaric core resulting from the dissipation of the shock wave (a,b), the temperature increase (c) melts the metal that segregates rapidly (d), then sinks toward the planetary embryo center by a diapiric instability (e).

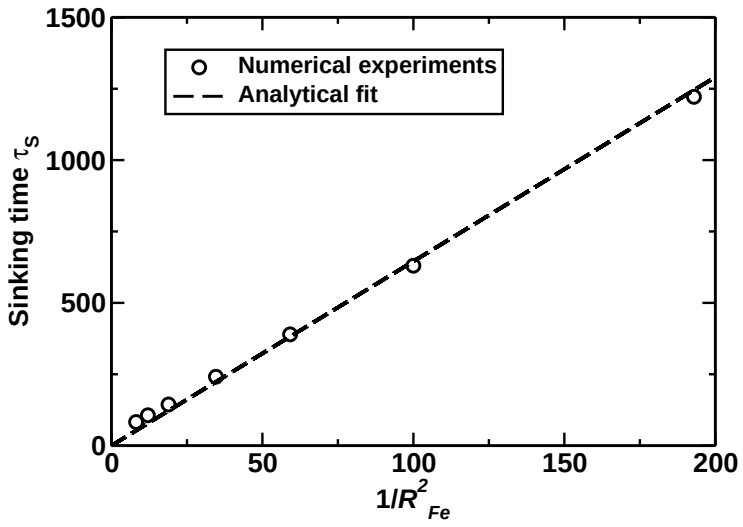

Figure 2: Characteristic sinking time τ_S as a function of $1/R^{*2}_{Fe}$, where R^*_{Fe} is the non-dimensionalized metallic sphere radius. Results from numerical experiments (with uniform viscosity $\eta_S = 10^{22}$ and $R = 1000$ km) are representated with black circles. Theoretical fit from Eq.13 is shown by the dashed line with $c_1 = 0.187$.

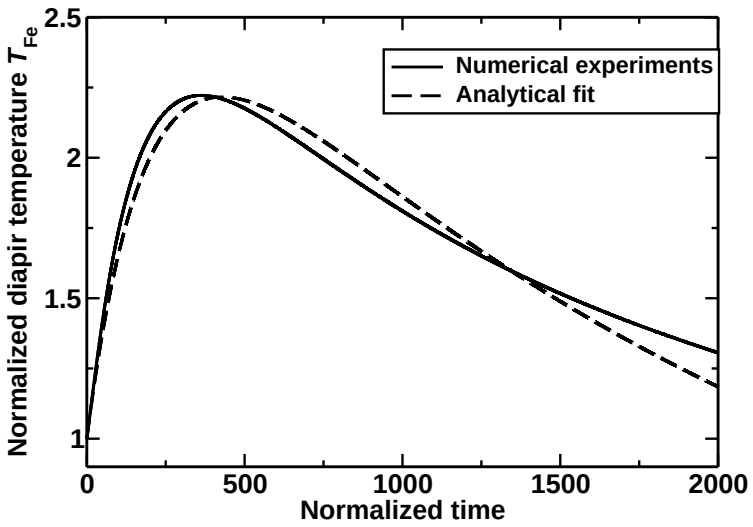

Figure 3: Temperature evolution (black line) of a metallic sphere ($R_{Fe} = 130$ km) falling in an undifferentiated planet with $R = 1000$ km. Theoretical evolution from Eq.30 is shown with a dashed line ($c_1 = 0.187$, $c_2 = 0.72$ and $a = 20\%$).

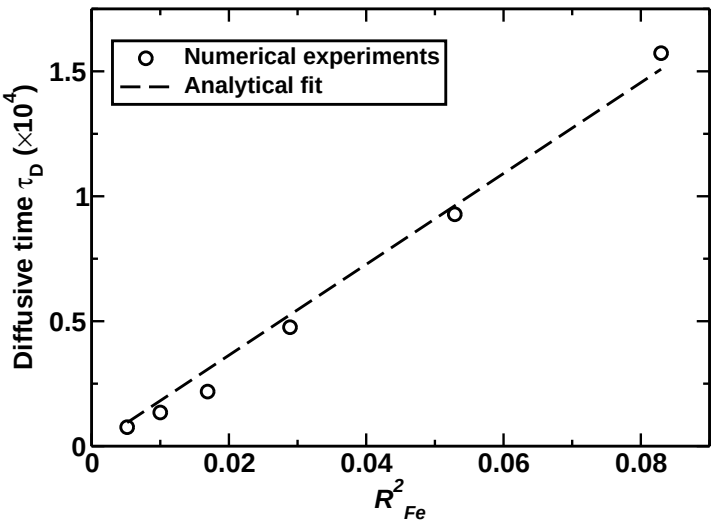

Figure 4: Non-dimensional characteristic time of diffusion τ_D as a function of the non-dimensionalized metallic sphere radius. Results from numerical experiments (with a uniform viscosity and $R = 1000$ km) are represented with black circles. Theoretical fit from Eq.26 is shown in dashed line with $c_2 = 1.01$.

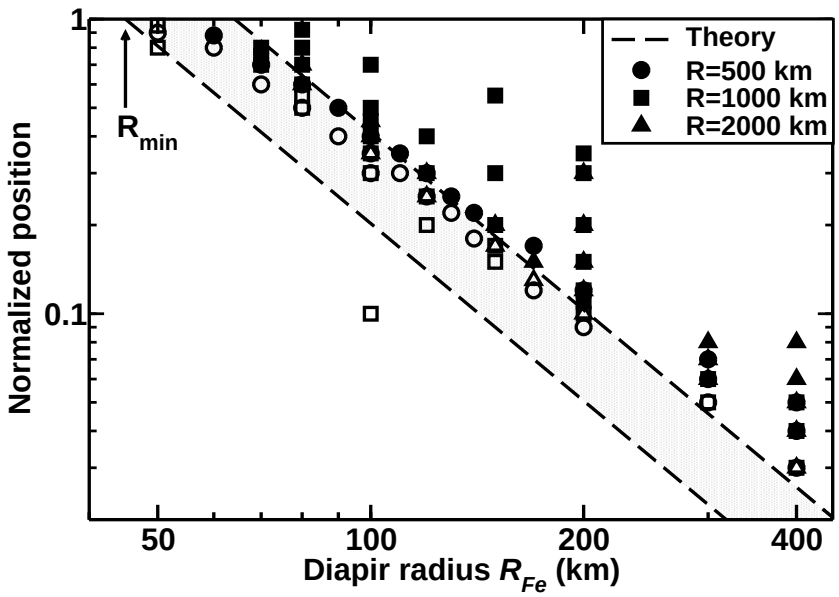

Figure 5: Thermal behaviour of a sinking metal sphere in an undifferentiated media as function of position and sphere radius. Each symbol represents the instantaneous thermal behaviour of an hot metallic sphere with radius R_{Fe} for a given initial position. Filled symbols represent numerical experiments with viscous heating and open symbols represent numerical experiments with only cooling. Different symbols characterize different planets radii. The analytical transition between heating and cooling is predicted within the shaded area and the boarders of this area are defined with $\Delta T_{max}/\Delta T_0$ between 1 (no heating) and 4.2 (maximum heating)(see, Eq.32).

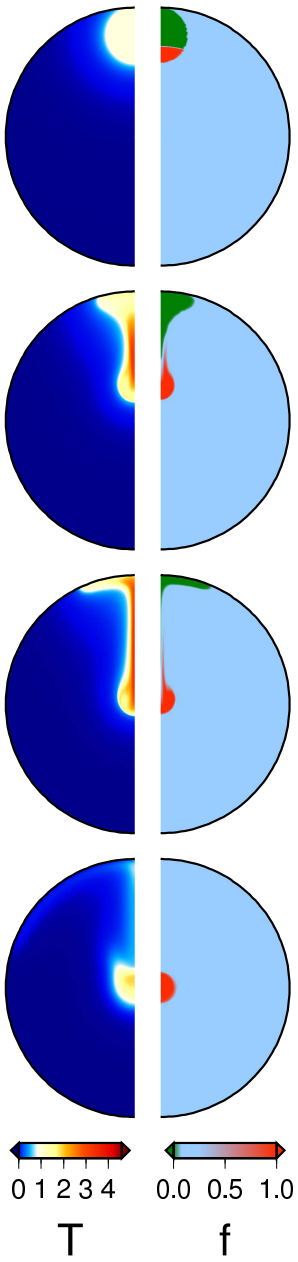

Figure 6: Non dimensional temperature (left) and composition (right) at times $t = 0$ (first line), $t = 1.4$ My (second line), $t = 3.8$ My (third line) and $t = 546$ My (fourth line) (computed for a uniform viscosity with $R = 4000$ km, $R_{imp} = 600$ km and 200×200 grid points)

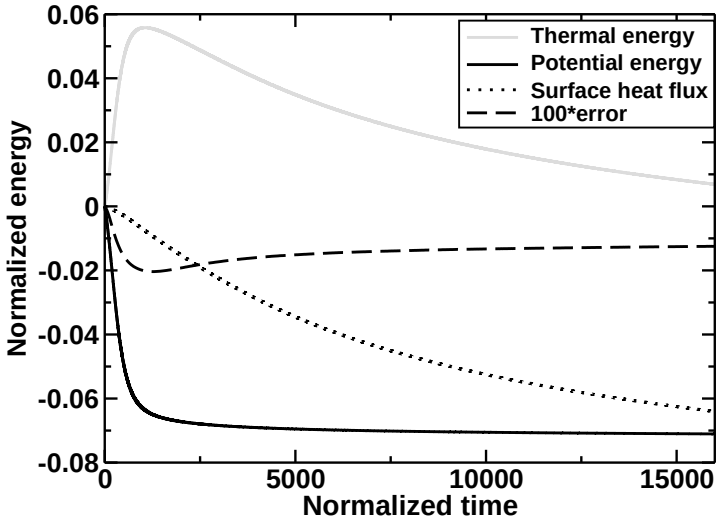

Figure 7: Non dimensionalized potential (solid black line) and thermal (solid grey line) energies and time integrated surface heat flow (dotted black line) as functions of time. The sum of these three quantities times 100 is shown in dashed black line. Its difference to zero is indicative of the accuracy of the energy conservation of the numerical code (for $R = 2000$ km, $R_{imp} = 300$ km and $R_{Fe} = 240$ km and uniform viscosity).

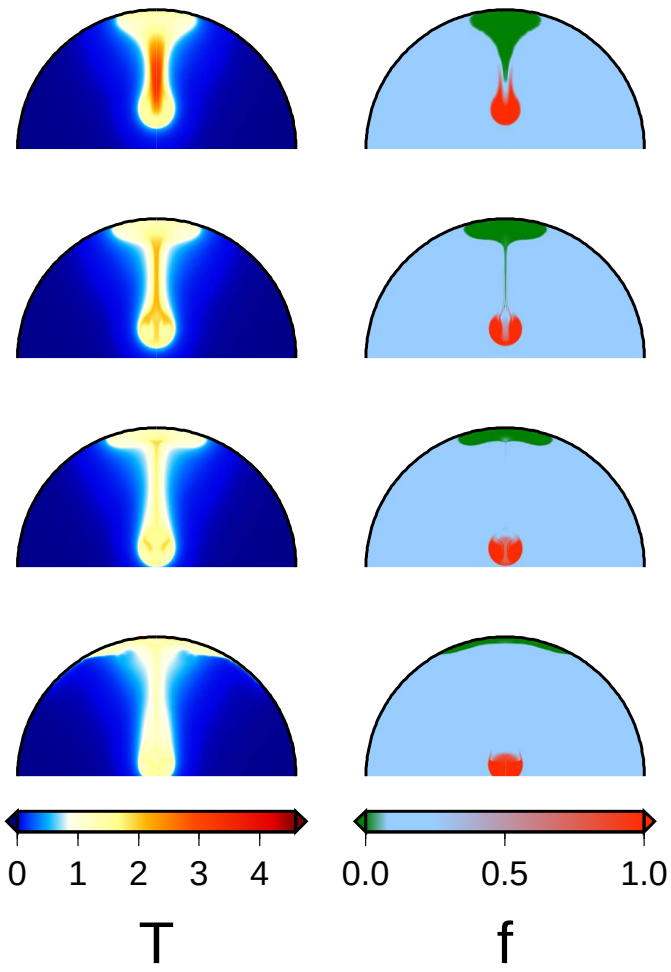

Figure 8: The four rows depict the temperature (left) and the composition (right) at $t = 3.2$ My (with $R = 2000$ km and $R_{imp} = 300$ km), for a uniform viscosity (top) and for variable viscosities (contrast of ~ 16 (second row), ~ 100 (third row) and ~ 1600 (bottom row)). As expected, the sinking velocity of the metallic diapir and the rising velocity of the silicates, both increase when their viscosity is decreased.

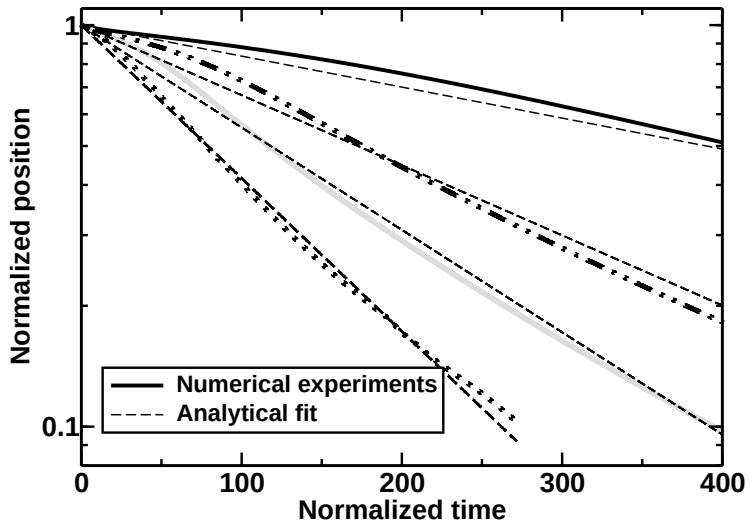

Figure 9: Position of the inertia center of the metal phase as a function of time for a uniform viscosity (black line) and for temperature-dependent viscosities with $\lambda = 0.25$ (dashed dotted line), $\lambda = 0.1$ (grey line) and $\lambda = 2.5 \times 10^{-2}$ (dotted line) ($R = 2000$ km and $R_{imp} = 300$ km). Thin dashed lines correspond to simple exponential fittings from which the sinking times are extracted (see Tab.2).

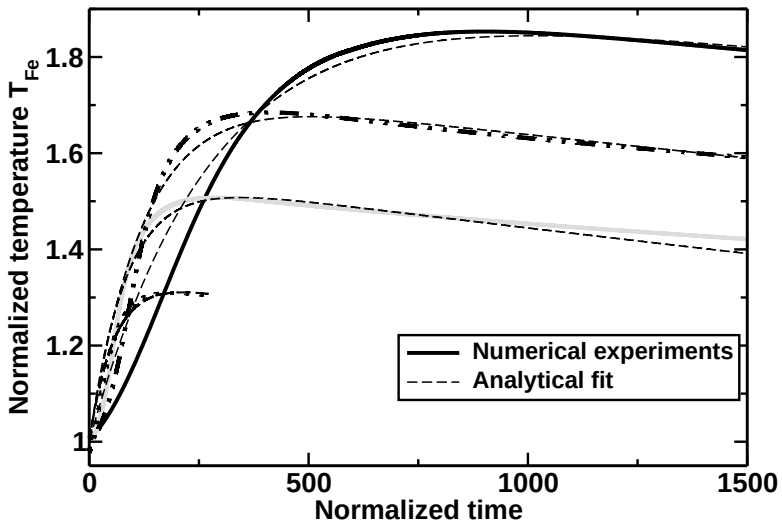

Figure 10: Temperature evolution of the metal phase as a function of time for a uniform viscosity (solid black line) and for temperature-dependent viscosities with $\lambda = 0.25$ (dashed dotted line), $\lambda = 0.1$ (grey line) and $\lambda = 2.5 \times 10^{-2}$ (dotted line) ($R = 2000$ km and $R_{imp} = 300$ km). Thin dashed lines correspond to theoretical results from Eq.30 from which the diffusive times and the proportion of energy heating the metal diapir are extracted (see Tab.2).

Bibliography

Abe, Y., 1997. Thermal and chemical evolution of the terrestrial magma ocean. Physics of the Earth and Planetary Interiors 100, 27–39.

Anderson, J.D., Schubert, G., Jacobson, R.A., Lau, E.L., Moore, W.B., Sjogren, W.L., 1998. Europa's Differentiated Internal Structure: Inferences from Four Galileo Encounters. Science 281, 2019.

Batchelor, G.K., 1967. An Introduction to Fluid Dynamics.

Bénard, H., 1900a. Les tourbillons cellulaires dans une nappe liquide. Deuxième partie: procédé mécaniques et optiques d'examen. Lois numériques des phénomènes. Rev. Gén. Sci. Pures App. 11, 1309–1328.

Bénard, H., 1900b. Les tourbillons cellulaires dans une nappe liquide. Première partie: description générale des phénomènes. Rev. Gén. Sci. Pures App. 11, 1261–1271.

Bertrand, O., Binet, B., Combeau, H., Couturier, S., Delannoy, Y., Gobin, D., Marcel Lacroix, M., Le Quéré, P., Médale, M., Mencinger, J., Sadat, H., Vieira, G., 1999. Melting driven by natural convection A comparison exercise: first results. Int. J. Therm. Sci. 38, 5 – 26.

Blankenbach, B., Busse, F., Christensen, U., Cserepes, L., Gunkel, D., Hansen, U., Harder, H., Jarvis, G., Koch, M., Marquart, G., Moore, D., Olson, P., Schmeling, H., Schnaubelt, T., 1989. A benchmark comparison for mantle convection codes. Geophys. J. Int. 98, 23–38.

Block, M.J., 1956. Surface tension as the cause of benard cells and surface deformation in a liquid film. Nature 178, 650–651.

Bouvier, A., Wadhwa, M., 2010. The age of the Solar System redefined by the oldest Pb-Pb age of a meteoritic inclusion. Nature Geoscience 3, 637–641.

Burchfield, J., 1975. Lord Kelvin and the age of the earth. Science History Publications.

Busse, F.H., Christensen, U., Clever, R., Cserepes, L., Gable, C., Giannandrea, E., Guillou, L., Houseman, G., Nataf, H.C., Ogawa, M., 1994. 3D convection at infinite Prandtl number in Cartesian geometry: A benchmark comparison. Geophysical and Astrophysical Fluid Dynamics 75, 39–59.

Canup, R.M., Righter, K., et al., 2000. Origin of the earth and moon.

Canuto, V.M., Dubovikov, M.S., 1998. Two scaling regimes for rotating rayleigh-bénard convection. Phys. Rev. Lett. 80, 281–284.

Carslaw, H.S., Jaeger, J.C., 1959. Conduction of heat in solids.

Chabot, N.L., Draper, D.S., Agee, C.B., 2005. Conditions of core formation in the earth: Constraints from Nickel and Cobalt partitioning. Geochim. Cosmochim. Acta 69, 2141–2151.

Chambers, J.E., 2004. Planetary accretion in the inner Solar System. Earth and Planetary Science Letters 223, 241–252.

Chandrasekhar, S., 1961. Hydrodynamic and hydromagnetic stability. International series of monographs on physics, Dover Publications.

Christensen, U.R., 1984. Heat transport by variable viscosity convection and implications for the earth's thermal evolution. Phys. Earth Planet. Inter. 35, 264 – 282.

Christensen, U.R., Hofmann, A.W., 1994. Segregation of subducted oceanic crust in the convecting mantle. J. Geophys. Res. (Solid Earth) 99, 19867–19884.

Coltice, N., Moreira, M., Hernlund, J., Labrosse, S., 2011. Crystallization of a basal magma ocean recorded by Helium and Neon. Earth Planet. Sci. Lett. 308, 193–199.

Coltice, N., Ricard, Y., 1999. Geochemical observations and one layer mantle convection. Earth Planet. Sci. Lett. 174, 125–137.

Crisp, J., 1984. Rates of magma emplacement and volcanic output. Journal of Volcanology and Geothermal Research 20, 177–211.

Croft, S.K., 1982. A first-order estimate of vaporization in oceanic impacts, in: Silver, T.L., Schultz, P. (Eds.), Geological Implications of Impacts of Large Asteroids and Comets on Earth, pp. 143–152.

CSC – IT Center for Science, 2010. `http://www.csc.fi/english/pages/elmer`.

Davaille, A., 1999a. Simultaneous generation of hotspots and superswells by convection in a heterogeneous planetary mantle. Nature 402, 756–760.

Davaille, A., 1999b. Two-layer thermal convection in miscible viscous fluids. J. Fluid Mech. 379, 223–253.

Davaille, A., Jaupart, C., 1993. Transient high-Rayleigh-number thermal convection with large viscosity variations. J. Fluid Mech. 253, 141–166.

Davis, S.H., 2001. Theory of Solidification. Cambridge University Press, New York, 400pp.

Davis, S.H., Müller, U., Dietsche, C., 1984. Pattern selection in single-component systems coupling Bénard convection and solidification. J. Fluid Mech. 144, 133–151.

Deparis, V., Legros, H., 2000. Voyage à l'intérieur de la terre: de la géographie antique à la géophysique moderne : une histoire des idées. CNRS.

Dietsche, C., Müller, U., 1985. Influence of Benard convection on solid-liquid interfaces. J. Fluid Mech. 161, 249–268.

Dormy, E., Soward, A.M., Jones, C.A., Jault, D., Cardin, P., 2004. The onset of thermal convection in rotating spherical shells. J. Fluid Mech. 501, 43–70.

Dziewonski, A.M., Anderson, D.L., 1981. Preliminary reference Earth model. Phys. Earth Planet. Inter. 25, 297–356.

England, P., 2007. John Perry's neglected critique of Kelvin's age for the Earth: A missed opportunity in geodynamics. GSA Today 17, 4–9.

Flasar, F.M., Birch, F., 1973. Energetics of Core Formation: A Correction. J. Geophys. Res. 78, 6101–6103.

Fowler, A.C., 1985a. Fast thermoviscous convection. Stud. Appl. Math. 72, 189–219.

Fowler, A.C., 1985b. A simple model of convection in the terrestrial planets. Geophysical & Astrophysical Fluid Dynamics 31, 283–309.

Garnero, E., Revenaugh, J., Williams, Q., Lay, T., Kellogg, L., 1998. Ultralow velocity zone at the core-mantle boundary. The Core-Mantle Boundary, edited by M. Gurnis, M. Wysession, E. Knittle, B. Buffet, Washington, DC: American Geophysical Union. pp. 319–334.

Garnero, E.J., Helmberger, D.V., 1996. Seismic detection of a thin laterally varying boundary layer at the base of the mantle beneath the central-Pacific. Geophys. Res. Lett. 23, 977–980.

Garnero, E.J., Thorne, M.S., McNamara, A., Rost, S., 2007. Fine scale ultra-low velocity zone layering at the core-mantle boundary and superplumes. Superplumes: Beyond Plate Tectonics, edited by D. Yuen, S. Maruyama, S. Karato, B. Windley. New York: Springer. pp. 139–157.

Garnero, E.J., Vidale, J.E., 1999. ScP; a probe of ultralow velocity zones at the base of the mantle. Geophys. Res. Lett. 26, 377–380.

Ghosh, A., McSween, H.Y., 1998. A Thermal Model for the Differentiation of Asteroid 4 Vesta, Based on Radiogenic Heating. Icarus 134, 187–206.

Gobin, D., Le Quéré, P., 2000. Melting from an isothermal vertical wall . Synthesis of a numerical comparison exercise. Comp. Ass. Mech. Eng. Sc. 7, 289–306.

Grigné, C., Labrosse, S., Tackley, P.J., 2005. Convective heat transfer as a function of wavelength: Implications for the cooling of the Earth. J. Geophys. Res. (Solid Earth) 110, 3409–+.

Grossmann, S., Lohse, D., 2000. Scaling in thermal convection: a unifying theory. J. Fluid Mech. 407, 27–56.

Guillou, L., Jaupart, C., 1995. On the effect of continents on mantle convection. J. Geophys. Res. 100, 24217–24238.

Heaviside, O., 1899. Electromagnetic Theory, Vol. II, Chap. V: Mathematics and the age of the Earth. SPON, London.

Hernlund, J.W., Labrosse, S., 2007. Geophysically consistent values of the perovskite to post-perovskite transition Clapeyron slope. Geophys. Res. Lett. 34, 5309.

Hernlund, J.W., Thomas, C., Tackley, P.J., 2005. A doubling of the post-perovskite phase boundary and structure of the Earth's lowermost mantle. Nature 434, 882–886.

Hewitt, J.M., McKenzie, D.P., Weiss, N.O., 1975. Dissipative heating in convective flows. J. Fluid Mech. 68, 721–738.

Hill, X., 1996. La convection sous un solide. Applications aux planètes. Ph.D. thesis. Institut de Physique du Globe de Paris, Université de Paris 7.

Hofmann, A.W., 1997. Mantle geochemistry: the message from oceanic volcanism. Nature 385, 219–229.

Hostetler, C.J., Drake, M.J., 1980. On the early global melting of the terrestrial planets, in: Bedini, S.A. (Ed.), Lunar and Planetary Science Conference Proceedings, pp. 1915–1929.

Huppert, H.E., 1990. The fluid mechanics of solidification. Journal of Fluid Mechanics 212, 209–240.

Huppert, H.E., Sparks, R.S.J., 1988. Melting the roof of a chamber containing a hot, turbulently convecting fluid. Journal of Fluid Mechanics 188, 107–131.

Jarvis, G.T., Peltier, W.R., 1982. Mantle convection as a boundary layer phenomenon. Geophysical Journal 68, 385–424.

Jaupart, C., Mareschal, J., 2010. Heat Generation and Transport in the Earth. Cambridge University Press.

Jaupart, C., Parsons, B., 1985. Convective instabilities in a variable viscosity fluid cooled from above. Physics of the Earth and Planetary Interiors 39, 14 – 32.

Jeffreys, H., 1942. On the Radioactivities of Rocks. Mon. Nitices Roy. astr. Soc. Geophys. Supp. 5, 37–40.

Jellinek, A.M., Manga, M., 2002. The influence of a chemical boundary layer on the fixity, spacing and lifetime of mantle plumes. Nature 418, 760–763.

Jones, C.A., Soward, A.M., Mussa, A.I., 2000. The onset of thermal convection in a rapidly rotating sphere. Journal of Fluid Mechanics 405, 157–179.

Karato, S.I., Murthy, V.R., 1997. Core formation and chemical equilibrium in the Earth-I. Physical considerations. Phys. Earth Planet. Inter. 100, 61–79.

Karki, B.B., Stixrude, L.P., 2010. Viscosity of mgsio$_3$ liquid at earth's mantle conditions: Implications for an early magma ocean. Science 328, 740–742.

Kaula, W.M., 1979. Thermal evolution of earth and moon growing by planetesimal impacts. J. Geophys. Res. 84, 999–1008.

Kellogg, L.H., Hager, B.H., van der Hilst, R.D., 1999. Compositional Stratification in the Deep Mantle. Science 283, 1881.

King, E.M., Stellmach, S., Aurnou, J.M., 2012. Heat transfer by rapidly rotating Rayleigh-Bénard convection. J. Fluid Mech. 691, 558–582.

King, E.M., Stellmach, S., Noir, J., Hansen, U., Aurnou, J.M., 2009. Boundary layer control of rotating convection systems. Nature 457, 301–304.

Kivelson, M.G., Khurana, K.K., Russell, C.T., Volwerk, M., Walker, R.J., Zimmer, C., 2000. Galileo Magnetometer Measurements: A Stronger Case for a Subsurface Ocean at Europa. Science 289, 1340–1343.

Kleine, T., Mezger, K., Palme, H., Münker, C., 2004. The W isotope evolution of the bulk silicate Earth: constraints on the timing and mechanisms of core formation and accretion. Earth Planet. Sci. Lett. 228, 109–123.

Kleine, T., Münker, C., Mezger, K., Palme, H., 2002. Rapid accretion and early core formation on asteroids and the terrestrial planets from Hf-W chronometry. Nature 418, 952–955.

Krishnamurti, R., 1970a. On the transition to turbulent convection. Part 1. The transition from two- to three-dimensional flow. J. Fluid Mech. 42, 295–307.

Krishnamurti, R., 1970b. On the transition to turbulent convection. Part 2. The transition to time-dependent flow. J. Fluid Mech. 42, 309–320.

Labrosse, S., 2003. Thermal and magnetic evolution of the Earth's core. Phys. Earth Planet. Inter. 140, 127–143.

Labrosse, S., Hernlund, J.W., Coltice, N., 2007. A crystallizing dense magma ocean at the base of the Earth's mantle. Nature 450, 866–869.

Labrosse, S., Poirier, J.P., Le Mouël, J.L., 2001. The age of the inner core. Earth Planet. Sci. Lett. 190, 111–123.

Lamé, G., Clapeyron, B., 1831. Mémoire sur la solidification par refroidissement d'un globe solide. Ann. Chem. Phys. 47, 250–256.

Landau, L.D., Lifshitz, E.M., 1959. Fluid mechanics.

Lay, T., Garnero, E.J., Williams, Q., 2004. Partial melting in a thermo-chemical boundary layer at the base of the mantle. Phys. Earth Planet. Inter. 146, 441–467.

Lay, T., Hernlund, J., Garnero, E.J., Thorne, M.S., 2006. A Post-Perovskite Lens and D" Heat Flux Beneath the Central Pacific. Science 314, 1272–1276.

Lay, T., Williams, Q., Garnero, E.J., 1998. The core-mantle boundary layer and deep Earth dynamics. Nature 392, 461–468.

Le Quéré, P., Gobin, D., 1999. A note on possible flow instabilities in melting from the side. Int. J. Therm. Sci. 38, 595 – 600.

Lee, D.C., Halliday, A.N., 1997. Core formation on Mars and differentiated asteroids. Nature 388, 854–857.

Li, J., Agee, C.B., 2001. The effect of pressure, temperature, oxygen fugacity and composition on partitioning of nickel and cobalt between liquid Fe-Ni-S alloy and liquid silicate: implications for the earth's core formation. Geochim. Cosmochim. Acta 65, 1821–1832.

Lin, D.N.C., 2008. The Chaotic Genesis of Planets. Scientific American .

Malkus, W.V.R., 1954a. Discrete Transitions in Turbulent Convection. Proc. R. Soc. Lond. A 225, 185–195.

Malkus, W.V.R., 1954b. The Heat Transport and Spectrum of Thermal Turbulence. Proc. R. Soc. Lond. A 225, 196–212.

Mann, U., Frost, D.J., Rubie, D.C., 2009. Evidence for high-pressure core-mantle differentiation from the metal-silicate partitioning of lithophile and weakly-siderophile elements. Geochim. Cosmochim. Acta 73, 7360–7386.

Marsh, B., 2007. Magmatism, magma, and magma chambers, in: in Chief: Gerald Schubert, E. (Ed.), Treatise on Geophysics. Elsevier, Amsterdam, pp. 275 – 333.

McNamara, A.K., Garnero, E.J., Rost, S., 2010. Tracking deep mantle reservoirs with ultra-low velocity zones. Earth Planet. Sci. Lett. 299, 1–9.

McNamara, A.K., Zhong, S., 2005. Thermochemical structures beneath Africa and the Pacific Ocean. Nature 437, 1136–1139.

Melosh, H.J., 1990. Giant impacts and the thermal state of the early Earth. pp. 69–83.

Monteux, J., Coltice, N., Dubuffet, F., Ricard, Y., 2007. Thermo-mechanical adjustment after impacts during planetary growth. Geophys. Res. Lett. 34, 24201.

Monteux, J., Ricard, Y., Coltice, N., Dubuffet, F., Ulvrova, M., 2009. A model of metal-silicate separation on growing planets. Earth Planet. Sci. Lett. 287, 353–362.

Moresi, L.N., Solomatov, V.S., 1995. Numerical investigation of 2D convection with extremely large viscosity variations. Physics of Fluids 7, 2154–2162.

Mori, J., Helmberger, D.V., 1995. Localized boundary layer below the mid-Pacific velocity anomaly identified from a PcP precursor. J. Geophys. Res. 100, 20359–20366.

Mosenfelder, J.L., Asimow, P.D., Ahrens, T.J., 2007. Thermodynamic properties of Mg_2SiO_4 liquid at ultra-high pressures from shock measurements to 200 GPa on forsterite and wadsleyite. J. Geophys. Res. (Solid Earth) 112, 6208.

Mosenfelder, J.L., Asimow, P.D., Frost, D.J., Rubie, D.C., Ahrens, T.J., 2009. The $MgSiO_3$ system at high pressure: Thermodynamic properties of perovskite, postperovskite, and melt from global inversion of shock and static compression data. J. Geophys. Res. (Solid Earth) 114, 1203.

Murakami, M., Hirose, K., Kawamura, K., Sata, N., Ohishi, Y., 2004. Post-perovskite phase transition in $MgSiO_3$. Science 304, 855–858. `http://www.sciencemag.org/content/304/5672/855.full.pdf`.

Murthy, V.R., Karato, S.i., 1997. Core formation and chemical equilibrium in the earthii: Chemical consequences for the mantle and core. Physics of the Earth and Planetary Interiors 100, 81–95.

Nakagawa, T., Tackley, P.J., 2010. Influence of initial CMB temperature and other parameters on the thermal evolution of Earth's core resulting from thermochemical spherical mantle convection. Geochem. Geophys. Geosyst. 11, 6001.

Nataf, H.C., Richter, F.M., 1982. Convection experiments in fluids with highly temperature-dependent viscosity and the thermal evolution of the planets. Phys. Earth Planet. Inter. 29, 320–329.

Nield, D.A., 1964. Surface tension and buoyancy effects in cellular convection. J. Fluid Mech. 19, 341–352.

Niemela, J.J., Skrbek, L., Sreenivasan, K.R., Donnelly, R.J., 2000. Turbulent convection at very high Rayleigh numbers. Nature 404, 837–840.

Nomura, R., Ozawa, H., Tateno, S., Hirose, K., Hernlund, J., Muto, S., Ishii, H., Hiraoka, N., 2011. Spin crossover and iron-rich silicate melt in the Earth's deep mantle. Nature 473, 199–202.

Oganov, A.R., Ono, S., 2004. Theoretical and experimental evidence for a post-perovskite phase of $MgSiO_3$ in Earth's D" layer. Nature 430, 445–448. `0911.3184`.

Oliver, D.S., Booker, J.R., 1983. Planform of convection with strongly temperature-dependent viscosity. Geophys. Astrophys. Fluid Dyn 27, 73–85.

Palm, E., 1960. On the tendency towards hexagonal cells in steady convection. J. Fluid Mech. 8, 183–192.

Patankar, S.V., 1980. Numerical heat transfer and fluid flow. Series in computational methods in mechanics and thermal sciences, Hemisphere Publishing Corporation.

Pearson, J.R.A., 1958. On convection cells induced by surface tension. J. Fluid Mech. 4, 489–500.

Perry, J., 1895a. On the Age of the Earth. Nature 51, 341–342.

Perry, J., 1895b. The Age of the Earth. Nature 51, 582–585.

Pierazzo, E., Vickery, A.M., Melosh, H.J., 1997. A Reevaluation of Impact Melt Production. Icarus 127, 408–423.

Porco, C.C., Helfenstein, P., Thomas, P.C., Ingersoll, A.P., Wisdom, J., West, R., Neukum, G., Denk, T., Wagner, R., Roatsch, T., Kieffer, S., Turtle, E., McEwen, A., Johnson, T.V., Rathbun, J., Veverka, J., Wilson, D., Perry, J., Spitale, J., Brahic, A., Burns, J.A., Del Genio, A.D., Dones, L., Murray, C.D., Squyres, S., 2006. Cassini Observes the Active South Pole of Enceladus. Science 311, 1393–1401.

Quitté, G., Halliday, A.N., Meyer, B.S., Markowski, A., Latkoczy, C., Günther, D., 2007. Correlated Iron 60, Nickel 62, and Zirconium 96 in Refractory Inclusions and the Origin of the Solar System. Astrophys. J. 655, 678–684.

Quitté, G., Latkoczy, C., Schönbächler, M., Halliday, A.N., Günther, D., 2011. ^{60}Fe-^{60}Ni systematics in the eucrite parent body: A case study of Bouvante and Juvinas. Geochim. Cosmochim. Acta 75, 7698–7706.

Quitté, G., Markowski, A., Latkoczy, C., Gabriel, A., Pack, A., 2010. Iron-60 Heterogeneity and Incomplete Isotope Mixing in the Early Solar System. Astrophys. J. 720, 1215–1224.

Rayleigh, L., 1916. On convection currents in a horizontal layer of fluid, when the higher temperature is on the under side. Philosophical Magazine Series 6 32, 529–546.

Ribe, N., 2007. Analytical approaches to mantle dynamics, in: Schubert, G. (Ed.), Treatise on Geophysics. Elsevier, Amsterdam, pp. 167 – 226.

Ricard, Y., 2007. 7.02 - physics of mantle convection, in: in Chief:Gerald Schubert, E. (Ed.), Treatise on Geophysics. Elsevier, Amsterdam, pp. 31 – 87.

Ricard, Y., Šrámek, O., Dubuffet, F., 2009. A multi-phase model of runaway core-mantle segregation in planetary embryos. Earth Planet. Sci. Lett. 284, 144–150.

Richter, F.M., 1978. Experiments on the stability of convection rolls in fluids whose viscosity depends on temperature. J. Fluid Mech. 89, 553–560.

Righter, K., 2011. Prediction of metal-silicate partition coefficients for siderophile elements: An update and assessment of PT conditions for metal-silicate equilibrium during accretion of the Earth. Earth Planet. Sci. Lett. 304, 158–167.

Ritsema, J., Heijst, H.J.v., Woodhouse, J.H., 1999. Complex shear wave velocity structure imaged beneath africa and iceland. Science 286, 1925–1928.

Ritsema, J., van Heijst, H.J., Woodhouse, J.H., 2004. Global transition zone tomography. J. Geophys. Res. (Solid Earth) 109, 2302.

Romanowicz, B., 2003. Global Mantle Tomography: Progress Status in the Past 10 Years. Annual Review of Earth and Planetary Sciences 31, 303–328.

Rossby, H.T., 1969. A study of Benard convection with and without rotation. J. Fluid Mech. 36, 309–335.

Rost, S., Garnero, E.J., Williams, Q., Manga, M., 2005. Seismological constraints on a possible plume root at the core-mantle boundary. Nature 435, 666–669.

Rubie, D.C., Melosh, H.J., Reid, J.E., Liebske, C., Righter, K., 2003. Mechanisms of metal–silicate equilibration in the terrestrial magma ocean. Earth Planet. Sci. Lett. 205, 239–255.

Rubie, D.C., Nimmo, F., Melosh, H.J., 2007. Formation of Earth's Core. Treatise on Geophysics: Evolution of the Earth, edited by editor–in–chief G. Schubert and volume editor D. Stevenson. Elsevier Ltd.. volume 9. pp. 51–90.

Rugel, G., Faestermann, T., Knie, K., Korschinek, G., Poutivtsev, M., Schumann, D., Kivel, N., Günther-Leopold, I., Weinreich, R., Wohlmuther, M., 2009. New measurement of the ^{60}Fe half-life. Phys. Rev. Lett. 103, 072502.

Russell, S.A., Lay, T., Garnero, E.J., 1998. Seismic evidence for small-scale dynamics in the lowermost mantle at the root of the Hawaiian hotspot. Nature 396, 255–258.

Safronov, V.S., 1972. Evolution of the protoplanetary cloud and formation of the earth and planets.

Safronov, V.S., 1978. The heating of the earth during its formation. Icarus 33, 3–12.

Samuel, H., 2012. A re-evaluation of metal diapir breakup and equilibration in terrestrial magma oceans. Earth Planet. Sci. Lett. 313, 105–114.

Samuel, H., Tackley, P.J., Evonuk, M., 2010. Heat partitioning in terrestrial planets during core formation by negative diapirism. Earth Planet. Sci. Lett. 290, 13–19.

Schubert, G., Anderson, J.D., Travis, B.J., Palguta, J., 2007. Enceladus: Present internal structure and differentiation by early and long-term radiogenic heating. Icarus 188, 345–355.

Schubert, G., Turcotte, D.L., Olson, P., 2001. Mantle Convection in the Earth and Planets.

Senshu, H., Kuramoto, K., Matsui, T., 2002. Thermal evolution of a growing Mars. Journal of Geophysical Research (Planets) 107, 5118.

Siebert, J., Badro, J., Antonangeli, D., Ryerson, F.J., 2012. Metal-silicate partitioning of Ni and Co in a deep magma ocean. Earth Planet. Sci. Lett. 321, 189–197.

Smolarkiewicz, P., 1998. MPDATA: A Finite-Difference Solver for Geophysical Flows,. Journal of Computational Physics 140, 459–480.

Sohl, F., Spohn, T., Breuer, D., Nagel, K., 2002. Implications from Galileo Observations on the Interior Structure and Chemistry of the Galilean Satellites. Icarus 157, 104–119.

Solomatov, V., 2007. Magma Oceans and Primordial Mantle Differentiation. Treatise on Geophysics: Evolution of the Earth, edited by editor–in–chief G. Schubert and volume editor D. Stevenson. Elsevier Ltd.. volume 9. pp. 92–119.

Solomatov, V.S., 1995. Scaling of temperature- and stress-dependent viscosity convection. Physics of Fluids 7, 266–274.

Solomatov, V.S., 2000. Fluid Dynamics of a Terrestrial Magma Ocean. Origin of the Earth and Moon, edited by R.M. Canup and K. Righter and 69 collaborating authors. Tucson: University of Arizona Press., p. 323–338. pp. 323–338.

Solomatov, V.S., Moresi, L.N., 1997. Three regimes of mantle convection with non-Newtonian viscosity and stagnant lid convection on the terrestrial planets. Geophys. Res. Lett. 24, 1907–1910.

Solomon, S.C., 1979. Formation, history and energetics of cores in the terrestrial planets. Phys. Earth Planet. Inter. 19, 168–182.

Stefan, J., 1891. Über die Theorie der Eisbildung, insbesondere über die Eisbildung im Polarmeere. Annalen der Physik und Chemie 42, 269–286.

Stevenson, D.J., 1990. Fluid Dynamics of a core formation. Origin of the Earth, edited by H. E. Newsom and J. H. Jones. New York: Oxford Univ. Press. pp. 231–249.

Stixrude, L., de Koker, N., Sun, N., Mookherjee, M., Karki, B.B., 2009. Thermodynamics of silicate liquids in the deep Earth. Earth and Planetary Science Letters 278, 226–232.

Stixrude, L., Karki, B., 2005. Structure and freezing of $MgSiO_3$ liquid in earth's lower mantle. Science 310, 297–299. http://www.sciencemag.org/content/310/5746/297.full.pdf.

Tackley, P.J., 1993. Effects of strongly temperaturedependent viscosity on time-dependent, threedimensional models of mantle convection. Geophys. Res. Lett. 20, 2187–2190.

Tackley, P.J., 1996. Effects of strongly variable viscosity on three-dimensional compressible convection in planetary mantles. J. Geophys. Res. 101, 3311–3332.

Tackley, P.J., 1998. Three-Dimensional Simulations of Mantle Convection with a Thermo-Chemical Basal Boundary Layer: D"?, in: Gurnis, M., Wysession, M.A., Knittle, E., Buffett, B.A. (Eds.), The Core-Mantle Boundary Region, AGU, Washington DC. pp. 231–253.

Tackley, P.J., 2002. Strong heterogeneity caused by deep mantle layering. Geochem. Geophys. Geosyst. 3.

Tackley, P.J., 2008. Modelling compressible mantle convection with large viscosity contrasts in a three-dimensional spherical shell using the yin-yang grid. Phys. Earth Planet. Inter. 171, 7–18.

Tackley, P.J., 2012. Dynamics and evolution of the deep mantle resulting from thermal, chemical, phase and melting effects. Earth Science Reviews 110, 1–25.

Thompson, W. (Lord Kelvin), 1864. On the secular cooling of the earth. Trans. Royal Soc. Edinburgh XXIII, 295–311.

Tonks, W.B., Melosh, H.J., 1992. Core formation by giant impacts. Icarus 100, 326–346.

Turcotte, D.L., Oxburgh, E.R., 1967. Finite amplitude convective cells and continental drift. J. Fluid Mech. 28, 29–42.

Ulvrová, M., Coltice, N., Ricard, Y., Labrosse, S., Dubuffet, F., Velímský, J., Šrámek, O., 2011. Compositional and thermal equilibration of particles, drops, and diapirs in geophysical flows. Geochem. Geophys. Geosyst. 12, 10014.

Ulvrová, M., Labrosse, S., Coltice, N., Råback, P., Tackley, P.J., 2012. Numerical modelling of convection interacting with a melting and solidification front: Application to the thermal evolution of the basal magma ocean. Phys. Earth Planet. Inter. 206-207, 51 – 66.

Šrámek, O., Milelli, L., Ricard, Y., Labrosse, S., 2012. Thermal evolution and differentiation of planetesimals and planetary embryos. Icarus 217, 339–354.

Wen, L., Helmberger, D.V., 1998. Ultra-Low Velocity Zones Near the Core-Mantle Boundary from Broadband PKP Precursors. Science 279, 1701.

Wetherill, G.W., 1985. Occurrence of giant impacts during the growth of the terrestrial planets. Science 228, 877–879.

White, D.B., 1988. The planforms and onset of convection with a temperature-dependent viscosity. J. Fluid Mech. 191, 247–286.

Wicks, J.K., Jackson, J.M., Sturhahn, W., 2010. Very low sound velocities in iron-rich (Mg,Fe)O: Implications for the core-mantle boundary region. Geophys. Res. Lett. 37, 15304.

Williams, Q., Garnero, E.J., 1996. Seismic Evidence for Partial Melt at the Base of Earth's Mantle. Science 273, 1528–1530.

Wood, B.J., Walter, M.J., Wade, J., 2006. Accretion of the Earth and segregation of its core. Nature 441, 825–833.

Wood, J.A., 1972a. Fragments of Terra Rock in the Apollo 12 Soil Samples and a Structural Model of the Moon. Icarus 16, 462.

Wood, J.A., 1972b. Thermal History and Early Magmatism in the Moon. Icarus 16, 229.

Wood, J.A., Dickey, Jr., J.S., Marvin, U.B., Powell, B.N., 1970. Lunar anorthosites and a geophysical model of the moon. Geochimica et Cosmochimica Acta Supplement 1, 965.

Yano, J.I., 1992. Asymptotic theory of thermal convection in rapidly rotating systems. J. Fluid Mech. 243, 103–131.

Zhong, S., Hager, B.H., 2003. Entrainment of a dense layer by thermal plumes. Geophys. J. Int. 154, 666–676.